

Multilayer optical switches by photopolymerization-induced phase separation

Citation for published version (APA):

Kjellander, B. K. C. (2006). *Multilayer optical switches by photopolymerization-induced phase separation*. [Phd Thesis 1 (Research TU/e / Graduation TU/e), Applied Physics and Science Education]. Technische Universiteit Eindhoven. <https://doi.org/10.6100/IR615488>

DOI:

[10.6100/IR615488](https://doi.org/10.6100/IR615488)

Document status and date:

Published: 01/01/2006

Document Version:

Publisher's PDF, also known as Version of Record (includes final page, issue and volume numbers)

Please check the document version of this publication:

- A submitted manuscript is the version of the article upon submission and before peer-review. There can be important differences between the submitted version and the official published version of record. People interested in the research are advised to contact the author for the final version of the publication, or visit the DOI to the publisher's website.
- The final author version and the galley proof are versions of the publication after peer review.
- The final published version features the final layout of the paper including the volume, issue and page numbers.

[Link to publication](#)

General rights

Copyright and moral rights for the publications made accessible in the public portal are retained by the authors and/or other copyright owners and it is a condition of accessing publications that users recognise and abide by the legal requirements associated with these rights.

- Users may download and print one copy of any publication from the public portal for the purpose of private study or research.
- You may not further distribute the material or use it for any profit-making activity or commercial gain
- You may freely distribute the URL identifying the publication in the public portal.

If the publication is distributed under the terms of Article 25fa of the Dutch Copyright Act, indicated by the "Taverne" license above, please follow below link for the End User Agreement:

www.tue.nl/taverne

Take down policy

If you believe that this document breaches copyright please contact us at:

openaccess@tue.nl

providing details and we will investigate your claim.

Multilayer optical switches by photopolymerization-induced phase separation

PROEFSCHRIFT

ter verkrijging van de graad van doctor aan de
Technische Universiteit Eindhoven, op gezag van de
Rector Magnificus, prof.dr.ir. C.J. van Duijn, voor een
commissie aangewezen door het College voor
Promoties in het openbaar te verdedigen
op maandag 4 december 2006 om 16.00 uur

door

Birgitta Katarina Charlotte Kjellander

geboren te Kristianstad, Zweden

Dit proefschrift is goedgekeurd door de promotoren:

prof.dr. D.J. Broer
en
prof.dr. J.W. Niemantsverdriet

Copromotor:
dr. L.J. van IJzendoorn

CIP-DATA LIBRARY TECHNISCHE UNIVERSITEIT EINDHOVEN

Kjellander, B. K. Charlotte

Multilayer optical switches by photopolymerization-induced phase separation./ by B. K. Charlotte Kjellander. - Eindhoven : Technische Universiteit Eindhoven, 2006. - Proefschrift.

ISBN-10 : 90-386-2142-6

ISBN-13 : 978-90-386-2142-5

NUR 926

Trefwoorden: vloeibare kristallen / fasescheiding / elektro-optische schakelaars / polymeren / reactie-diffusiesystemen / statistische analyse

Subject headings: liquid crystals / phase separation / electro-optical devices / statistical analysis / polymer dispersed liquid crystal / reaction-diffusion systems / secondary ion mass spectrometry

Copyright © 2006, B. K. C. Kjellander, Printed by University Press Facilities, Eindhoven, The Netherlands. Cover design by Chris van Heesch. This research was financially supported by the Dutch Polymer Institute (DPI); project 277.

Contents

Summary	v
1 Introduction	1
1.1 Background	1
1.2 Liquid crystal optical switches	2
1.3 Holographic stratified PDLC gratings	6
1.4 The cholesteric self-stratification process	8
1.5 Theoretical model of photopolymerization-induced phase separation	11
1.6 Outline of thesis	11
1.7 References	12
2 Photopolymerization-induced phase separation	15
2.1 Introduction	15
2.2 Phase separation mechanisms	16
2.2.1 Isotropic mixing	17
2.2.2 Network elasticity	19
2.2.3 Nematic ordering	20
2.3 Reaction-diffusion mechanisms	24
2.3.1 Radical photopolymerization	24
2.3.2 Diffusion	28
2.4 Ternary conversion-phase diagrams	30
2.5 Combined phase separation and reaction-diffusion model for holo- graphic stratified films	31
2.5.1 Formalism	31
2.5.2 Procedure for obtaining phase separation line	32
2.5.3 Procedure for obtaining reaction-diffusion line	33
2.6 Holographic reflection gratings	35
2.7 Experimental	37
2.7.1 Stratified gratings by laser beam holography	37
2.7.2 Monomer conversions	39
2.7.3 Constants for polymerization kinetics	41
2.7.4 Diffusion constants	42
2.8 Results and discussion	42
2.8.1 Holographic reflection gratings	42

2.8.2	Monomer conversion versus double bond conversion	44
2.8.3	Cross-linking probability and efficiency	48
2.8.4	Weight of effects in the combined phase separation model	49
2.8.5	Simulation results: phase separation lines	51
2.8.6	Simulation results: reaction-diffusion lines	57
2.8.7	Combination of the models	65
2.9	Conclusions	68
2.10	References and notes	70
3	Secondary ion mass spectrometry and multivariate statistical analysis	73
3.1	Introduction	73
3.2	Multivariate statistical analyses	74
3.2.1	Principle component analysis	75
3.2.2	Discriminant function analysis	77
3.2.3	Significance and multivariate normal distribution	79
3.3	Predicting concentrations from SIMS spectra with PCA and DFA	80
3.4	Experimental	81
3.4.1	Materials	81
3.4.2	Analysis techniques	83
3.5	Results and discussion	83
3.5.1	Polymer dispersed liquid crystal samples	88
3.5.2	Depth resolution of stratified PDLC films	91
3.6	Conclusions	94
3.6.1	Improvements to interpret SIMS depth profiles of stratified polymer dispersed liquid crystals	94
3.7	References and notes	95
4	Liquid crystal concentrations in stratified PDLCs	97
4.1	Introduction	97
4.2	Experimental	99
4.2.1	Combined phase separation and reaction-diffusion model	101
4.3	Results and discussion	103
4.3.1	Analyzed LC concentrations	103
4.3.2	Simulated liquid crystal concentrations	109
4.4	Conclusions	110
4.5	References	111
5	Cholesteric self-stratification process: Simulations	113
5.1	Introduction	113
5.2	Absorbed intensity profile	115
5.3	Phase separation mechanisms	119
5.4	Reaction-diffusion mechanisms	121
5.5	Experimental	122
5.5.1	Materials	122

5.5.2	Ellipsometry and birefringence measurements	124
5.5.3	Light propagation through cholesteric films	127
5.5.4	Phase separation and reaction-diffusion model parameters	129
5.6	Results and discussion	130
5.6.1	Absorbed light intensity profile	130
5.6.2	Combined phase separation - reaction diffusion model	138
5.7	Conclusions	147
5.8	References and notes	148
6	Materials selection for the cholesteric self-stratification process	151
6.1	Introduction	151
6.2	Experimental	153
6.2.1	Materials	153
6.2.2	Experimental techniques	154
6.3	Results and discussion	155
6.3.1	Nematic liquid crystal host	155
6.3.2	Chiral dopants	156
6.3.3	Cross-linking monomers	158
6.3.4	Difunctional monomers	161
6.3.5	Towards photopolymerization-induced stratified films	166
6.4	Conclusions	171
6.5	References	174
A	SIMS spectra identification	177
	Technology Assessment	189
	Acknowledgements	193
	Curriculum Vitae	195

Summary

Large, light and flat are currently key words manufacturing liquid crystal displays (LCDs). However with the conventional cell-technology the size limits for LCDs are approached. In order to further stretch the boundaries new process routes are necessary. This thesis introduces such a novel route, the cholesteric self-stratification process, with the potential to produce large area stratified electro-optical switches using continuous processing manufacturing. Moreover, having access to such a production methodology would enormously expand the application field ranging from light-controlling devices in e.g. homes, offices, cars, greenhouses to ambient-intelligent related devices such as electronic wall papers, smart paints, etc.

The cholesteric self-stratification process is a promising method to produce multilayer optical films in a single polymerization step. The advantages are unlimited device size and easily manipulated layer periodicity, stretching from nanometers to millimeters. Furthermore, the experimental curing set-up is simple; a normal UV-light source combined with a polarizer. In contrast, the reaction method is considerably more complicated. The formation of the periodic layers of polymers and liquid crystals is based on photopolymerization-induced phase separation, and the layer periodicity is determined by a periodic modulation of the reaction rate in depth of the reaction mixture. The liquid crystalline (LC) reaction mixture is self-organized in the chiral nematic LC phase, all components in the reaction mixture, including a dichroic photoinitiator, align in the cholesteric LC phase. The modulated reaction rates obtained by an absorbed intensity profile created with linearly polarized light and dichroic photoinitiators. The initiators are elongated, rod-like molecules with transition dipole moment for UV absorption parallel to the molecular long axis. The initiators mainly absorb linearly polarized light at every depth where the light polarization direction is parallel to the molecular length direction. During polymerization periodic layers are formed by phase separation between the polymer network and the unreactive LCs. To predict the photopolymerization-induced phase separation process a model was introduced which was verified on holographic stratified polymer dispersed liquid crystals (PDLCs).

The phase separation model is based on the Gibbs free energy (in form of the chemical potentials). The influences on the phase separation caused by isotropic mixing, network elasticity and nematic ordering were investigated. The elasticity of densely cross-linked polymer networks was found the most important mechanism to induce and enhance phase separation. Interestingly, simulations of the reaction-

diffusion behavior during the polymerization was found to be diffusion independent for diffusion constants applicable for the current systems ($> 10^{-10} \text{ m}^2\text{s}^{-1}$). Only for lower values effects on the reaction-diffusion behavior was found. Increasing, or decreasing, the polymerization rate did not show any effects on the diffusion behavior for the pitches ($< 200 \text{ nm}$) studied in this thesis.

By combining the phase separation model with simulations of the reaction-diffusion behavior, compositions of the film at the moment of phase separation are predicted. The results from the modeled holographic reflection gratings agree well with the experimental results. However, verifying the combined models with imaging techniques (as e.g. scanning electron microscopy) that depend on the contrast between the layers is difficult. Therefore, to validate the combined models, analysis technique(s) that can detect the small concentration changes in depth of the sample are assumed to be more valuable.

Dynamic secondary ion mass spectrometry (SIMS) is such a method. SIMS depth profiles of phase separated films result in complex fingerprint spectra. By applying multivariate statistical analysis to the SIMS spectra, we could identify different polymers, LCs and their blends. Quantification of the concentrations of liquid crystals in PDLCs was complicated by evaporation of the nematic liquid crystals. Evaporation was suppressed by capping the PDLC samples with poly(vinyl alcohol) before inserting samples into the SIMS vacuum system. To suppress further evaporation of the LCs, cryogenic temperatures during analysis are required. Only then, layer concentrations of liquid crystal-polyacrylate stratified gratings were possible to be correctly determined. Small concentration differences between the layers of the holographic recorded gratings were obtained from the SIMS depth profiles and the discriminant function analysis. These results agree with the results from the phase separation model, and support further use of the model to be applied on the cholesteric self-stratification process.

The absorption profile in the cholesteric reaction mixture was investigated. Dichroic photoinitiators were experimentally tested on their preferential light absorption (along the long axis), and their alignment with the chiral nematic liquid crystals. Three suitable candidates were found. The influence on the propagating curing light by the anisotropic LCs in the cholesteric phase was studied by light propagation simulations using Berreman's 4x4 matrix method. Simulations revealed that the curing light of 351 nm remains linearly polarized for cholesteric pitches below 1100 nm, and the dichroic photoinitiators absorb light with a periodicity comparable to half the cholesteric pitch. The estimated absorption profile was applied in the phase separation model.

Predictions of the phase separation behavior of the cholesteric self-stratification process showed that the reaction temperature, compared to the clearing temperature of the mixture, is critical. First, the reaction mixture is required to be liquid crystalline. Secondly, the relation between the clearing temperatures of the pure monomers respectively the unreactive LCs, also influences the phase separation behavior. For example, a large difference between the clearing temperatures induced phase separation at an earlier stage (at lower monomer conversions). Reaction-diffusion simulations reveal that the reaction kinetics did not influence the layer

formation process: by altering the curing light intensity from 0.05 to 250 mW/cm², identical reaction-diffusion lines were simulated. However, with a higher curing intensity, phase separation is reached faster.

From the phase separation simulations experimental parameters for the cholesteric self-stratification process, as e.g. the reaction temperature and composition of the reaction mixture, can be estimated. The composition of the reaction mixture before polymerization, should preferably have a LC concentration corresponding to the solubility limit (i.e. the highest LC concentration that can be held within the polymer network without phase separating). The simulations in chapter 5 revealed that large amounts of monomers (> 50 %) are required in the cholesteric reaction mixture to obtain polymerization-induced phase separated layers. Based on these results, and that the reaction mixture for the cholesteric self-stratification must keep a stable liquid crystalline phase before polymerization, materials were selected for the process.

Two alternative monomers for the cholesteric self-stratification were found to be suitable for the reaction mixtures (that also contain unreactive LCs, chiral dopants, cross-linkers and dichroic photoinitiators): reaction mixtures with large amounts of liquid crystalline monoacrylates, or reaction mixtures with isotropic monoacrylates (<10% 2-phenoxyethyl acrylate) in which the monomer content was increased by liquid crystal cross-linkers (~ 40%). The latter reaction mixture was investigated for the process and thus polymerized by linearly polarized UV-light. However, due to the large content of reactive anisotropic material (the LC cross-linker), it was not possible to conclude unambiguously whether the cholesteric LC phase was solely remained in the polymerized film, whether periodic stratified films were created, or a combination of the two. A larger contrast between the refractive indices of the polymer and the phase separated liquid crystals would facilitate the characterization.

An improved contrast between the layers remains a challenge for the cholesteric self-stratification process. The absorption profile depends mainly on materials parameters as the extinction and concentration of the photoinitiator, and the periodic absorption contrast. The latter, the absorption contrast, influences the reaction-diffusion behavior significantly, which was shown by simulations. Adding radical scavengers to the reaction mixture the polymerization can be inhibited at the positions with low absorbed light intensity, while at the depths with high intensity are the scavengers consumed faster and polymerization will start. As a result, the layer formation process becomes less dependent on the concentration of the reaction mixture and the temperature.

To summarize, the cholesteric self-stratification process is a promising tool for the next generation liquid crystal optical switches. In spite of the understanding of the phase separation mechanism as studied in this thesis, still experimental parameters are difficult to control. In particular the construction of a functional device based on switchable selective reflection by periodic layers of polymers and LCs remains to be proven. Solving the final intricacy of the cholesteric self-stratification process offers versatile multilayer optical switches.

List of abbreviations

A_{\parallel}	absorption of light parallel to the long axis of the dichroic photoinitiator
A_{\perp}	absorption of light perpendicular to the long axis of the dichroic photoinitiator
B	between groups matrix of sums and squares of cross products
C	correlation matrix
C_{eff}	network efficiency factor
$[C=C]$	double bond concentration
c	concentration of chiral dopant
D	diagonal matrix of eigenvalues
DFA	discriminant function analysis
DSC	differential scanning calorimetry
D_m	diffusion constant of monomers in polymer
F-test	statistical significance test
f	monomer functionality
G	Gibbs free energy
G	holographic grating vector
HTP	helical twisting power
I_a	absorbed intensity (by the photoinitiators)
In	photoinitiator
$[In]$	photoinitiator concentration
k_p	propagation rate constant
k_t	termination rate constant
LC	liquid crystal
LCD	liquid crystal display
M, m	monomer
MF	mean field theory
MVA	multivariate statistical analysis
m_c	average polymer chain length between two cross-links
m/z	mass over charge; mass channel
N_i	number of lattice unit cells that one molecule of species i occupies
$n_{average}$	average refractive index
n_e	extraordinary refractive index
n_i	number of molecules of species i
n_o	ordinary refractive index
\bar{n}	director of the nematic LC phase
Δn	birefringence
P, p	polymer
P_{chol}	cholesteric pitch
PCA	principle component analysis
PC	principle component
PDLC	polymer dispersed liquid crystal
RPI	relative peak intensity

S	sample population matrix
SEM	scanning electron microscopy
SIMS	secondary ion mass spectrometry
s	order parameter
T	total sums and squares of cross product matrix
ToF	time-of-flight (detector)
T_{ni}	phase transition temperature between nematic and isotropic phase; clearing temperature
T_{n^*i}	phase transition temperature between chiral nematic and isotropic phase; clearing temperature
T_p	polymerization temperature
V	matrix of eigenvectors
V	holographic fringe constant
V_{abs}	absorption contrast
W	within groups matrix of sums and squares of cross products
$X_{C=C/M}$	average number of double bonds reacted per monomer
x	double bond conversion

Greek characters

α	monomer conversion
ϵ_{In}	extinction coefficient of the photoinitiator
κ	cross-linking efficiency factor
Λ	holographic pitch
λ_{ref}	central wavelength of reflection
μ	chemical potential
ν	nematic interaction parameter
Σ	covariance matrix
Φ_{In}	quantum efficiency of the photoinitiator
ϕ_i	volume fraction of species i
χ_{ij}	Flory-Huggins interaction parameter between molecule i and j
χ^2 -test	statistical significance test

Chapter 1

Introduction

1.1 Background

More than a century ago, in 1888, liquid crystals (LCs) were discovered by the Austrian botanist Friedrich Reinitzer. He observed that the molecule cholesteryl benzoate had two, what he called, “melting points”¹. By melting the solid sample the crystals changed into a hazy liquid. As he increased the temperature further, the material changed again into a clear, transparent liquid. The formation of the hazy meso-state, or what we now call the liquid crystal phase, is promoted by the anisotropic shape of the cholesteryl benzoate molecules in their lowest energy conformation. The self-organization and the shape anisotropy lead to anisotropic optical and dielectrical properties, which are qualities used in liquid crystalline optical switches.

Liquid crystalline switches are applied in a wide range of devices, of which the liquid crystal display (LCD) is by far the most known. In the last decade mid-sized LCDs (15-10 inch screen diagonal) became market leader for applications as desktop computer monitors because of their slim form factor and high resolution. Recently also larger sized LCDs became available competing with cathode ray tube (CRT) and plasma screens for the television market. The development of notebook computers with high performance screens would not have been possible without the LCD development.

Among the principles of LCDs, the switching of polarized light on pixel level is the best known. The liquid crystals confined in a cell respond to an electric field because of their dielectric anisotropy, and change the state of polarization of the transposing light depending on the applied electrical field. Light passes through a polarizer before entering the LC cell. The linearly polarized light experiences the anisotropy of the liquid crystals, which leads to transmission or extinction by the analyzer situated after the LC cell. LCDs are available in numerous applications including mobile phone displays, supermarket price tags and devices for technical instruments and vehicles as clocks, speedometers and navigation systems^{2,3,4}. Another application is sunscreen windows, or privacy windows, that control the transmitted light by switching between clear and scattered states⁵. Thereto the LCs are embedded as

droplets in a polymer matrix (polymer dispersed liquid crystals, PDLCs) of which the refractive index of the LCs matches the polymer either when an electric field is applied over the cross section of the film or without an electric field.

In a few years time several new devices with liquid crystal switches may appear on the market. Such devices might be control devices (non-display applications) as micro-lenses with tunable focal lengths for applications in optical beam steering and image processing⁶. Furthermore, novel proposals of LC switches are in the telecommunication and fiber optics branch where LCs and PDLCs have been studied as photonic band-gap materials^{7,8} and compact laser light sources^{9,10}.

Fixing the liquid crystals by polymerization generates passive optical films that keep their optical properties constant. Thereto the anisotropically shaped liquid crystal molecules are modified with reactive, polymerizable moieties such as acrylates. They can be processed and aligned like normal LCs but additionally can be fixed by photo-initiated polymerization^{11,12}. Polymerized liquid crystals are found in devices as filters, retarders, polarization sensitive reflection gratings and passive reflective displays^{13,14,15}.

Lately, the market has asked for wider, lighter and thinner electro-optical switches e.g. to be used as cost-effective large privacy windows (in homes and offices), effective sunscreens (for agricultural applications in e.g. greenhouses), or as wall coverage (ambient intelligence), but also for large area wall-sized displays and television sets. For the latter it is essential to find operational solutions using unpolarized light in order to enhance the brightness, weight and energy efficiency of the LCDs.

This thesis introduces a new production method for next generation liquid crystalline switches. The technique builds on the photopolymerization-induced phase separation process. Recently, paintable displays (liquid crystals covered by a phase separated polymerized coating) have been produced by this technique¹⁶. Here, the self-organization of LCs is exploited to create more complex phase separated films, serving as optical switches with wavelength selective reflection. The gain, procedure and underlying mechanism to form complex stratified optical switches by photopolymerization-induced phase separation are discussed.

1.2 Liquid crystal optical switches

Liquid crystal switches are the basic components of liquid crystal displays (LCDs). Compared to traditional cathode ray tube (CRT) screens or plasma displays, LCDs are cheaper to produce and lighter in weight, but lack image quality. Most research was focused on the latter, resulting in image qualities of today's LCDs being comparable with those of the CRTs.

The operating principles of LCDs are based on the self-organization and optical properties of the liquid crystals. LCs are mesogens, i.e. organic molecules that have intermediate phases containing both rheological properties of fluids and crystalline properties of solids. Thermotropic LCs, which are mainly used in LCDs, change phase by temperature (figure 1.1(a)). At high temperatures, the isotropic state, the molecules are totally disordered. Decreasing the temperature, more order is

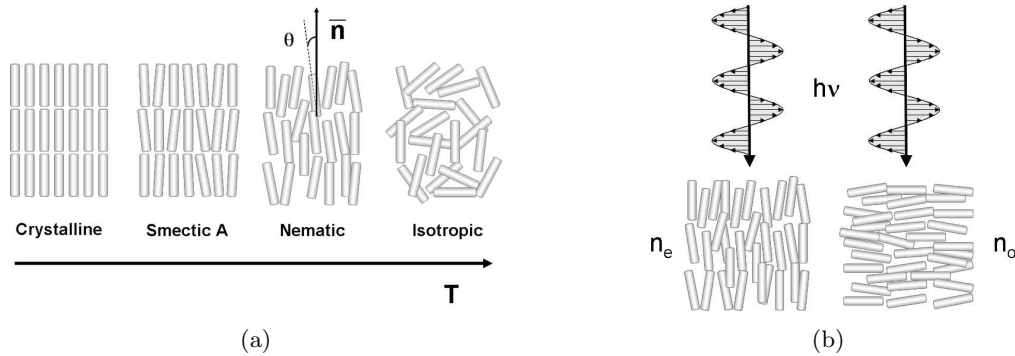


Figure 1.1: (a) The liquid crystalline phases change with temperature. The directional order of the LC molecules is given by the director \bar{n} . (b) Light polarized parallel to the long axis of the molecules experiences a different index of refraction (extraordinary refractive index, n_e) than light polarized perpendicular to the long axis (ordinary refractive index, n_o).

brought into the system and one or more mesophases can be observed depending on the nature of the LC molecules. The nematic phase has one dimensional directional order; the molecules are aligned in a preferred direction, represented by the director \bar{n} . At lower temperatures, the molecular orientation can be restricted in more dimensions and one or more smectic LC phases can appear. The intermediate phases are induced by the molecular shape-anisotropy induced by the stiff molecular core in general formed by aligned benzene rings or other organic ring formations. Two LC shapes are observed: rod-like and disc-like, however also other shapes (e.g. banana-shaped LC molecules) are reported. The molecular shape anisotropy induces differences in electron densities along the molecular axes which in turn causes anisotropic behavior of physical properties such as the dielectric constants, magnetic susceptibility, refractive indices, and electric conductivity. For optical switches, the dielectric and optical anisotropy are the most important. Generally, LCs are symmetric in two of the three molecular axes. Therefore, light polarized parallel to the length direction of the molecule experiences a different index of refraction (extraordinary refractive index, n_e) than light polarized perpendicular to the length direction (ordinary refractive index, n_o), figure 1.1(b). The birefringence is then the difference between the two refractive indices ($n_e - n_o$). In an electric field, the molecule turns to align the largest of the dielectric constants with the field direction. In this way, the orientation of LCs can be changed by applying an external electric field.

Present LCDs employ several variations of liquid crystal switches, the most common is the twisted nematic (TN-LCD)². In such a display the nematic LCs are sandwiched between two transparent substrates with transparent electrodes. Alignment layers are applied on the substrates in order to direct the long axis of the LCs in the plane of the LC cell. Since the alignment direction of the bottom and top substrates are perpendicular, a 90° twist of the LC molecules is induced (figure 1.2). On the outside of the substrates, sheets of polarizers with a direction parallel to the alignment layers are glued. Due to the 90° twist, the cell thickness and the

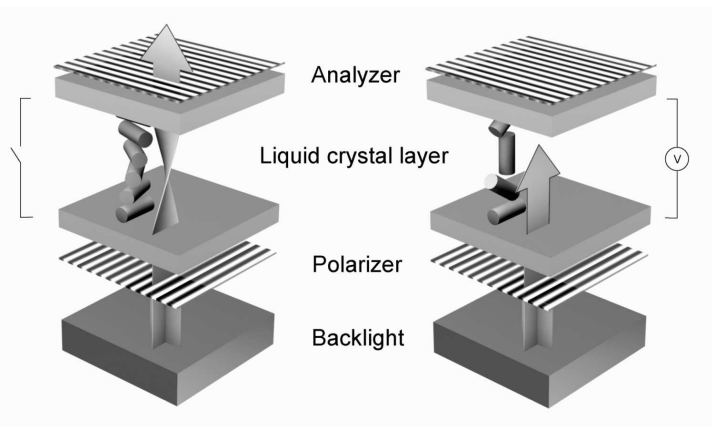


Figure 1.2: The principles of a twisted nematic liquid crystal display. Light is generated from the backlight at the bottom of the display and the light becomes linearly polarized by a polarizer before entering the LC cell. On the substrates alignment layers are applied facing the liquid crystal layer. In the left image (OFF state) the liquid crystal molecules are rotated 90° in the LC cell in order to guide the light through the display, and the light is transmitted through the analyzer. In the right image (ON state), an electrical field is applied, which aligns the LCs in the cell along the field direction, with a result that the light is no longer guided through the LCD. At the analyzer the light is absorbed and the display appears dark. (Image kindly provided by Chris van Heesch).

birefringence, the incoming light, polarized by the sheet polarizer, is guided through the twisted LCs, as is seen in figure 1.2. In this OFF state, without external field, the display appears bright. Adding a color-filter changes the black and white switch to a color display. Next, an external field applied over the cross section of the device, aligns the LC's largest dielectric constant in the field direction. In this ON state (right image in figure 1.2), the incoming light becomes totally blocked by the perpendicular polarizers (also called the dark state).

Studies of the LC switching mechanism, liquid crystalline materials and alignments have led to successful advances of the image quality of LCDs^{2,17,18,19}. Yet, the power consumption in the LCD, mainly used for powering the light source, remains an issue due to the light absorbing optical components such as polarizers and color filters. These optical components absorb large amounts of the light, decreasing the power efficiency of the device. Although research to recycle light has shown promising results, the most efficient is to totally discard the polarizers and the color-filters. In fact, color filters can be replaced by using cholesteric LCs in the switchable LC-cell⁴. The principle for such a cholesteric LC cell will be explained in next paragraph.

The cholesteric, or chiral nematic, LC phase include liquid crystal molecules with chiral centers inducing the director, \vec{n} , to rotate in depth of the film (figure 1.3). The cholesteric LCs form a helix where the 360° rotation of the molecules represents the cholesteric pitch. Since the birefringent LC molecules are rotated in depth, macroscopically linearly polarized light experiences periodic layers of material with different refractive index. Due to the helix rotation, cholesteric LCs reflect the circu-

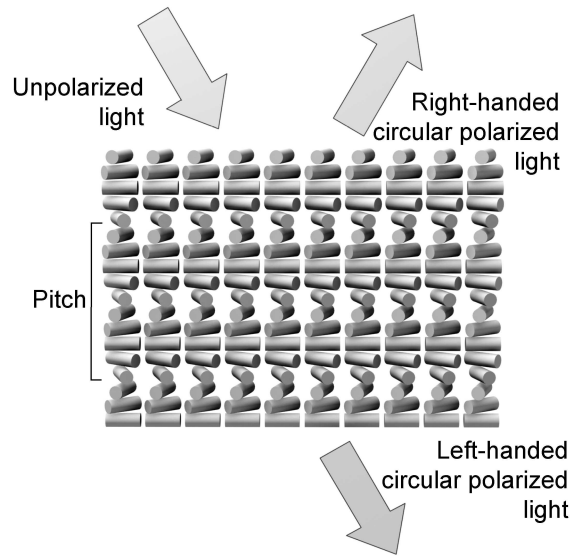


Figure 1.3: Cholesteric liquid crystals are aligned in planes that rotate in depth of the film, this is visualized by showing a cross-section of the film where the cholesteric helix is seen as rotating LC molecules. The distance at which the director has rotated 360° is called the cholesteric pitch. Cholesteric liquid crystals reflect one handedness of circularly polarized light, the same handedness as the rotation of the cholesteric pitch. The other handedness is transmitted. (Image kindly provided by Chris van Heesch).

larly polarized light component that corresponds with the cholesteric helix, the other component is transmitted. An optical switch with cholesteric LCs in a cell reflects a color in the OFF state, and appears dark in the ON state. Consequently, switchable cholesteric LC-cells replace both the color filter and the LC cell. Unfortunately also several drawbacks are reported, such as changed reflected colors with viewing angle and the need for large switching voltages. However, stabilizing the cholesteric LC by polymerization, gives bright and power efficient passive color reflectors^{14,20} which can replace a traditional (and absorbing) color filter in a modified LC cell.

Other switchable reflective films are based on the principles of Bragg-reflection as a result of alternating polymer and LC layers with different refractive indices (figure 1.4). A periodic mismatch in refractive indices between the polymer and LC layers generates reflection of light (left image in figure 1.4). Compared to cholesteric LCs, Bragg gratings reflect both handedness of light. The reflected wavelength depends on the layer periodicity and the refractive indices likewise to the cholesteric LCs. By applying an electrical field over the cross section of the device, the LCs align with the field similar to the ON state in the TN-LCD. If the refractive index of the aligned LC molecules (n_o) equals that of the polymer, the grating becomes transparent (right image in figure 1.4). Such a polarization independent switchable grating can replace not only the LC cell and the color filters in the device, but also the polarizers.

Switchable Bragg gratings can be obtained by polymerization-induced phase separation from mixtures of non-reactive liquid crystal and reactive monomers.

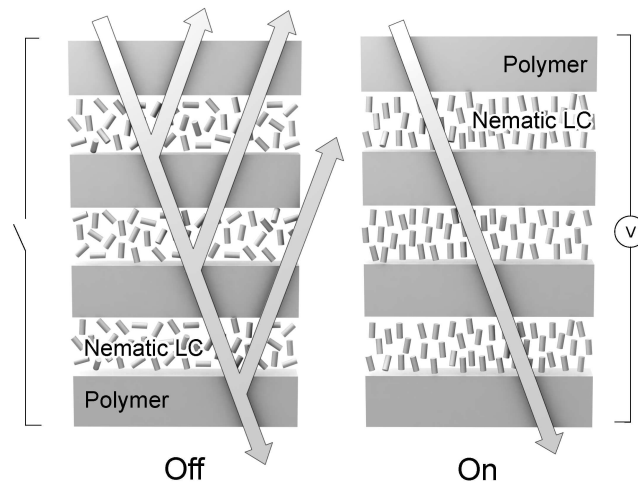


Figure 1.4: A liquid crystalline switchable Bragg grating consists of polymer layers with in between liquid crystals. The birefringence of the LCs is used to switch the optical properties. In the left image the grating reflects light due to the periodic mismatch of refractive indices in the polymer and LC layers. Applying an electric field over the cross section of the Bragg grating the LC molecules align with the field direction (right image) and the refractive indices of the LC- and the polymer-layers match resulting in a transparent grating. (Image kindly provided by Chris van Heesch).

Polymerizing monomers mixed with non-reactive liquid crystals, droplets of LCs phase separate from the polymer network forming a polymer dispersed liquid crystal (PDLC) film. By initiating the polymerization at periodic depths in the film, stratified PDLCs are obtained where LC droplets are confined into layers in the polymer matrix. Controlling photo-induced phase separation to produce the desired optical components such as complex structured PDLC films remains difficult, but is essential for the ultimate device properties. In the following sections two methods to achieve stratified PDLCs will be discussed: holographic recording and cholesteric self-stratification process. The former is a well established technique using the interference pattern of two coherent laser beams to create an intensity gradient in depth of an isotropic reaction mixture. The latter is a novel method based on the self-organization of LCs and on dichroic photoinitiators. First the holographic technique to obtain stratified PDLCs is explained, followed by the cholesteric self-stratification process. The similarities and differences between the two methods are discussed.

1.3 Holographic stratified PDLC gratings

Holography is a technique for recording and reproducing objects with the use of interference effects^{21,22}. Scattered and/or reflected light from an object, such as the plant in figure 1.5, overlaps with a reference beam to produce an interference pattern on the holographic plate. The recording material on the plate preserves the fringe information from the interference pattern. By illuminating the hologram with

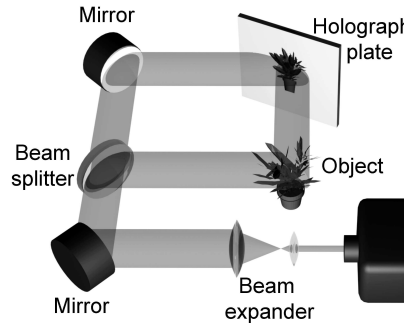


Figure 1.5: Principles of holography: light that scatters from an object, the plant, interferes with a reference beam on the holographic plate. The recorded interference pattern is the hologram. By illuminating the hologram with the reference beam, the object is reconstructed and the plant appears as an image. (Image kindly provided by Chris van Heesch).

the reference beam, the object is reconstructed, and visualized as a virtual image. When the hologram is thicker than the fringe spacing in the interference pattern, the reconstructed image is three dimensional.

Grating holograms, used for optical devices, are holograms made from interference pattern of two plane waves without using an object. Typically two coherent laser beams interfere on the recording material and create an intensity profile in the hologram (figure 1.6). By recording the interference pattern in an isotropic mixture of LCs and monomers, the intensity profile initiates the polymerization at periodic positions, producing a structured PDLC with phase separated layers of LC droplets in the polymer matrix²³. Positioning the sample with the interference profile in depth of the hologram produces a reflection grating. Turning the sample 90°, the layered planes become perpendicular to the film surface. Such a transmission grating has diffraction properties valuable for diffractive optics technology in e.g. optical data storage and integrated optic devices²⁴. Holograms with slanted periodic planes generate polarization selective out-coupling of light, which is of interest

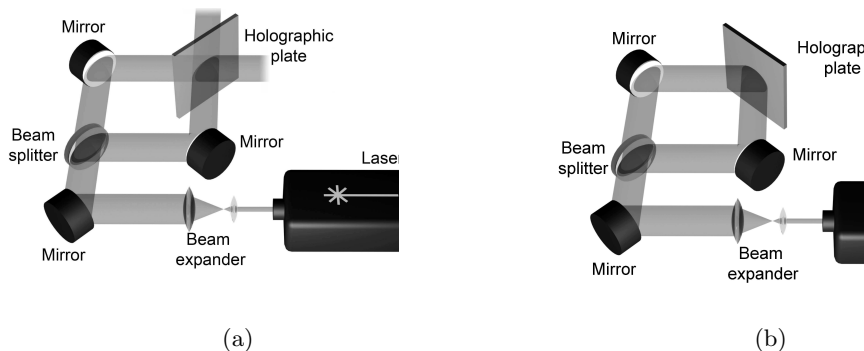


Figure 1.6: Laser beam holography setup for recording reflection gratings (a) and transmission gratings (b). (Images kindly provided by Chris van Heesch).

in lighting systems of LCDs^{25,26}. In the concept of this thesis, focus is on reflection gratings. The performance of reflective switchable PDLC gratings polymerized from a isotropic LC/photo-acrylate systems has been improved since the introduction in 1993^{27,28}, nevertheless the processing still requires a complicated optical set-up of coherent laser beams. Additionally, the device size and grating periodicity are limited by the spot size of the laser beams and the recording wavelength. The size of the interference pattern determines the device size and is generally a few square centimeters. The layer periodicity based on the intensity profile is determined by the laser wavelength and the angles between the interfering beams. Therefore, a layer periodicity smaller than the half of the laser wavelength is not physically possible. Due to these limitations laser beam holography is not a suitable production technique for large area optical reflection switches. To offer a new possibility to solve all these problems, we introduce a novel production method: the cholesteric self-stratification process.

1.4 The cholesteric self-stratification process

Cholesteric self-stratification is a novel method based on the self-organization of liquid crystals²⁹. A reaction mixture of chiral nematic LCs, monomers and photoinitiators is aligned in the cholesteric LC phase (cholesteric LC phase is shown in figure 1.3). The reaction mixture is applied on a rubbed polyimide alignment layer which in principle can be of any size; from molecular size to square meters. The purpose of the alignment layer is to organize the LC molecules at the interface in the same direction. In this way at every depth in the cell the LC molecules are aligned with respect to their horizontal neighbors.

Dichroic photoinitiators with preferential absorption of light linearly polarized to the molecular length direction are used (figure 1.7). By aligning the dichroic photoinitiators with the rotating director in the cholesteric LC reaction mixture and polymerizing with linearly polarized UV-light, light is absorbed at every depth position where the dichroic photoinitiators are parallel oriented with the linearly polarized curing light, ideally i.e. at every half cholesteric pitch (figure 1.8). In other words, an absorption profile is created in depth of the film that generates

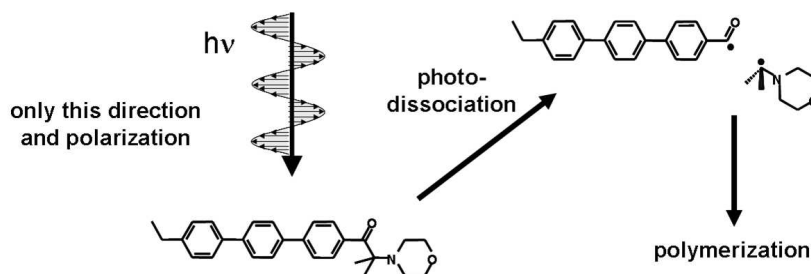


Figure 1.7: Light polarized along the length direction of the dichroic photoinitiator is absorbed, resulting in photodissociation of the initiator into two radicals. Other polarization directions of the light are not efficiently absorbed by the dichroic photoinitiator.

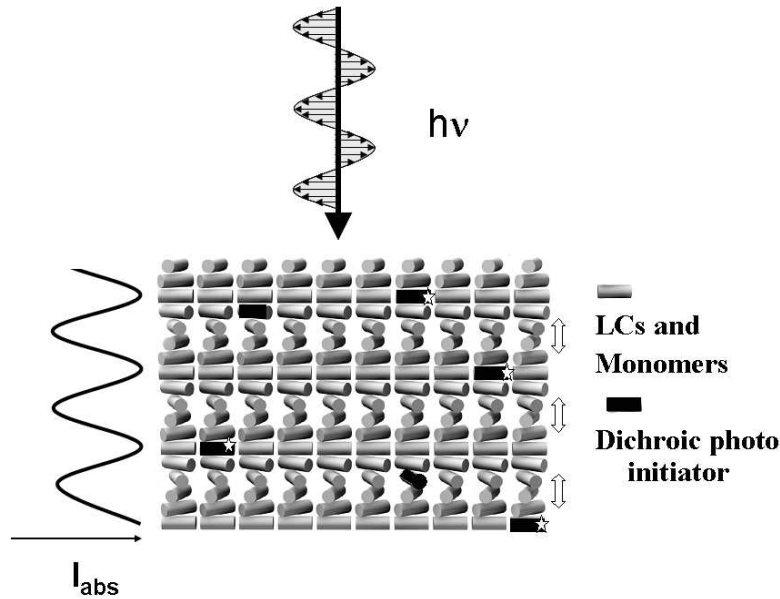


Figure 1.8: The principles of the cholesteric self-stratification process. A mixture of monomers, liquid crystals and dichroic photoinitiators are all in the chiral nematic phase (ordered in the cholesteric helices). Applying linearly polarized light on the cholesteric mixture, the dichroic photoinitiators aligned with the polarized light will most efficiently absorb the light; an absorption profile is created in depth. Polymers are predominantly formed at every half cholesteric pitch due to the absorption profile. This favors phase separation into a stratified PDLC. (Image kindly provided by Chris van Heesch).

periodic phase separated layers during polymerization.

The periodicity of the absorption profile relies on the cholesteric pitch, which is easily manipulated before polymerization by adding chiral dopants to the nematic reaction mixture. Before the polymerization also the temperature can change the cholesteric helix: at higher temperatures the cholesteric pitch is increased. After polymerization, the periodicity of the stratified film is expected to be fixed.

The advantages of the cholesteric self-stratification process are unlimited device size and easily manipulated layer periodicity, stretching from reflecting light in the deep UV to in the far IR. Furthermore this new technique overcomes the inhomogeneous reflection effects caused by localized polymerization shrinkage during the holographic exposure^{30,31}. During the holographic recording the polymerized structure shrinks while the interference pattern remains unaltered, this leads to a localized intensity disturbance which blurs the reflection from the grating. The cholesteric self-stratification process surpasses this problem since the absorbed intensity profile remains with the relative position of the aligned photoinitiators although the absolute periodicity might shift. The cholesteric order act as a spring that when being compressed the positions that initially have the highest absorption intensity remain the highest intensity and only change their periodicity. The positions with low absorbed intensity will not be subjected to higher absorbed intensity. Moreover, the experimental curing set-up is simple, with a normal UV-light source combined

with a polarizer. In contrast, the reaction method is considerably more complicated. In order to realize the stratified PDLC switch by the cholesteric self-stratification method the reaction mixture has to fulfill certain requirements:

- allowing curing light to propagate through the reaction mixture without rotation to initiate the dichroic photoinitiator at every half cholesteric pitch
- having perfectly miscible components in the cholesteric LC phase to align the dichroic photoinitiator and obtain the absorption profile
- favoring the polymerization-induced phase separation starting from the LC phase (in contrast to ordinary PDLC formation which involves phase separation from an isotropic phase)
- producing isotropic polymer layers with refractive index matching the refractive index of the aligned LCs

Cholesteric LCs reflect light with a color and polarization corresponding to the cholesteric pitch (as was discussed in section 1.2). However, if the cholesteric pitch is much larger than the wavelength of light ($P_{chol} \gg \lambda$), the light is wave-guided with the cholesteric helix (an effect used in TN-LCDs). The curing light for the cholesteric self-stratification has to be unaffected by the cholesteric pitch and remain linearly polarized while propagating through the cholesteric reaction mixture. Only then, a periodic absorption profile is obtained which initiates the polymerization. The created polymer layers should preferentially become optically isotropic. This is favored by isotropic monomers, but due to their isotropic nature they do not favor, but un-stabilize, the cholesteric LC phase. If LC monomers are used, the cholesteric LC phase of the reaction mixture will be stabilized, but the anisotropic LC properties remain in the formed polymer. Furthermore, the differences and similarities of the refractive indices of the (isotropic) polymer and the phase separated LCs must be optimized for the optical switching characteristics of the phase separated grating.

Obviously, the phase separation mechanism is crucial for the required layer formation by the cholesteric self-stratification process. Photopolymerization-induced phase separation is generally favored by a polymer network, implying that cross-linking monomers should be present. Moreover, polymer networks increase the stability of the device. On the other hand, cross-linking monomers are often bulky and therefore a disadvantage to the cholesteric LC phase of the reaction mixture.

To realize the cholesteric self-stratification process, the curing light propagation through the cholesteric reaction mixture is simulated, the miscibility of monomers and LCs is studied, and the polymerization-induced phase separation behavior is modeled. The latter lay a ground for designing the experimental conditions for the cholesteric self-stratification process, but also to understand the phase separation mechanism in a general sense.

1.5 Theoretical model of photopolymerization-induced phase separation

As discussed in the previous section, phase separation starting from a cholesteric LC phase is the requirement for the cholesteric self-stratification process. To study the conditions for such phase separation, we modeled the thermodynamic behavior during the layer formation process.

Phase separation during photopolymerization can be considered as the process where the liquid phase, containing only liquid components (monomers and LCs), emerges from the three-component phase of polymers, monomers and LCs. The latter phase is created during polymerization of the monomer-LC mixture. The two phases can coexist when the system is in thermodynamical equilibrium, expressed as a minimum in Gibbs free energy. Three effects are assumed to contribute independently to the free energy of a system: isotropic mixing, network elasticity and nematic ordering of the liquid crystalline compounds. The isotropic mixing³² takes into account the relative sizes of the molecules and the van der Waals interactions between the different species in the mixture. The elasticity of a cross-linked network can affect the phase separation considerably³³. The theory of Maier-Saupe³⁴ for nematic ordering is adopted to account for the extra energy term originating from the nematic ordering of the LC molecules.

A phase separation model based on these principles has been reported by Penterman³⁵, who considered photopolymerization-induced phase separation from an isotropic reaction mixture. The model presented in this thesis is based on Penterman's model, with the modification adapted to the fully liquid crystalline phase of the reaction mixture.

Understanding the phase separation behavior the experimental conditions for the cholesteric self-stratification process can be designed. Combining the phase separation model with dynamic polymerization-diffusion simulations, we can estimate the produced grating periodicity and composition.

1.6 Outline of thesis

The objective of this thesis is to present a novel method to produce large area stratified PDLC switches. For that purpose a phase separation model is described and verified on holographic stratified PDLCs (**chapter 2**).

To verify the phase separation model experimentally we need to accurately identify when and where phase separation occurs. Imaging techniques such as spectroscopy and scanning electron microscopy usually characterize optical devices in terms of reflected/transmitted wavelength and grating periodicity. However, these analysis techniques are dependent on the contrast between the layers thus reducing their accuracy. Moreover they do not provide information on the compositions of layers. Ion beam analysis techniques could offer such a possibility. Nuclear reaction analysis was studied for depth profiling nitrogen containing LCs in stratified PDLCs. Resonant reactions have a very narrow energy range where they are likely to occur,

and are therefore suitable for depth profiling specific elements. However, due to the small concentration differences between the layers in the grating and the low gamma yield from the liquid crystals, nuclear reaction analysis showed not to be accurate enough to depth profile stratified PDLCs³⁶.

An alternative analysis technique available for depth profiling polymers is secondary ion mass spectrometry (SIMS). The primary ion source sputters off fragments from the sample surface and secondary ions are detected. During continuous sputtering, the intensities of the fragments can be followed in depth of the sample. Since SIMS detects all elements, the layers do not need to contain specific labels. **Chapter 3** presents methods to quantify LC concentrations in stratified LC/polyacrylate samples. The necessary sample treatments and quantification methods using multivariate statistical analyses are discussed. In **chapter 4**, the LC concentrations of a holographic stratified PDLC film are quantified and compared with the modeled results.

In **chapter 5** the cholesteric self-stratification process is theoretically investigated by simulating the phase separation behavior. The phase separation model designs the ideal reaction mixtures and experimental conditions for obtaining stratified PDLC films. Since the cholesteric self-stratification process differs from the holographic grating recording by the reaction mixture initially being in the chiral nematic LC phase instead of isotropic, a phase separation model describing the former specific situation is proposed. The layer periodicity of self-stratified gratings is predicted by comparing the simulated curing light propagation and the directionality of the dichroic photoinitiators. Materials for the cholesteric self-stratification process are investigated in **chapter 6**, which ends with recommendations for further work. The potential use of the cholesteric self-stratification process is evaluated in the **Technology Assessment**.

1.7 References

1. Collings, P. J. *Liquid crystals*. IOP Publishing Ltd., Bristol, (1990).
2. Gray, G. W. and Kelly, S. M. *J. Mater. Chem.* **9**, 2037–2050 (1999).
3. Tombling, C. and Tillin, M. *Synthetic Metals* **122**, 209–214 (2001).
4. Urbas, A., Klosterman, J., Tondiglia, V., Natarajan, L., Sutherland, R., Tsutsumi, O., Ikeda, T., and Bunning, T. *Adv. Mater.* **16**(16), 1453–1456 (2004).
5. Pena, J. M. S., Vázquez, C., Pérez, I., Rodríguez, I., and Otón, J. M. *Opt. Eng.* **41**(7), 1608–1611 (2002).
6. Kyu, T. and Nwabunma, D. *Macromolecules* **34**, 9168–9172 (2001).
7. Mitov, M., Nouvet, E., and Dessaud, N. *Eur. Phys. J. E* **15**, 413–419 (2004).
8. Kikuchi, H., Yokota, M., Hisakado, Y., Yang, H., and Kajiyama, T. *Nat. Mater.* **1**, 64–68 (2002).

9. Cao, W., F., A. M., Palffy-Muhoray, P., and Taheri, B. *Mat. Res. Soc. Symp. Proc.* **776**, 159–167 (2003).
10. F., A. M., Palffy-Muhoray, P., and Taheri, B. *Opt. Lett.* **26**, 804–806 (2001).
11. Broer, D. J. and Heynderickx, I. *Macromolecules* **23**, 2474–2477 (1990).
12. Hikmet, R. A. M., Lub, J., and Broer, D. J. *Adv. Mater.* **3**(7/8), 392–394 (1991).
13. Broer, D. J., Lub, J., and Mol, G. N. *Nature* **378**, 467–469 (1995).
14. John, W. D. S., Fritz, W. J., Lu, Z. J., and Yang, D.-K. *Phys. Rev. E* **51**(2), 1191–1198 (1995).
15. van de Witte, P., Brehmer, M., and Lub, J. *J. Mater. Chem.* **9**, 2087–2094 (1999).
16. Penterman, R., Klink, S. I., de Koning, H., Nisato, G., and Broer, D. J. *Nature* **417**, 55–58 (2002).
17. Escuti, M. J., Bowley, C. C., Crawford, G. P., and Žumer, S. *Appl. Phys. Lett.* **75**(21), 3264–3266 (1999).
18. Doane, J. W., Vaz, N. A., Wu, B.-G., and Žumer, S. *Appl. Phys. Lett.* **48**, 269–271 (1986).
19. Varghese, S. *Patterned alignment of liquid crystals by microrubbing, a new route towards wide viewing angle flat panel displays*. PhD thesis, Eindhoven University of Technology, (2005).
20. Lub, J., van de Witte, P., Doornkamp, C., Vogels, J. P. A., and Wegh, R. T. *Adv. Mater.* **15**, 1420–1425 (2003).
21. Hecht, E. *Optics*, chapter 13, 623–648. Addison Wesley, San Francisco, 4th edition (2002).
22. Pedrotti, F. L. and Pedrotti, L. S. *Introduction to optics*, chapter 13, 266–279. Prentice-Hall Inc., London, 2nd edition (1993).
23. Bunning, T. J., Natarajan, L. V., Tondiglia, V. P., and Sutherland, R. L. *Annu. Rev. Mater. Sci.* **30**, 83–115 (2000).
24. Sutherland, R. L., Tondiglia, V. P., Natarajan, L. V., Bunning, T. J., and Adams, W. W. *Appl. Phys. Lett.* **64**(9), 1074–1076 (1994).
25. Sanchez, C., Escuti, M. J., van Heesch, C., Bastiaansen, C. W. M., and Broer, D. J. *Appl. Phys. Lett.* **87**(9), 094101 (2005).
26. van Heesch, C. M., Jagt, H., Cornelissen, H. J., Broer, D. J., and Bastiaansen, C. W. M. *Proc. SPIE* **5289**, 170–181 (2004).
27. Escuti, M. J., Kossyrev, P., Crawford, G. P., Fike, T. G., Colegrove, J., and Silverstein, L. D. *Appl. Phys. Lett.* **77**(26), 4262–4264 (2000).
28. Sutherland, R. L., Natarajan, L. V., Tondiglia, V. P., and Bunning, T. J. *Chem. Mater.* **5**, 1533–1538 (1993).

-
29. Kjellander, B. K. C., Broer, D. J., de Jong, A. M., and van IJzendoorn, L. *Patent PCT Int. Appl.* **WO 2006059895 A1**, 21 pp. 20060608 (2006).
 30. Sutherland, R. L., Tondiglia, V. P., Natarajan, L. V., and Bunning, T. J. *J. Appl. Phys.* **769**(10), 1420–1422 (2001).
 31. Natarajan, L. V., Shepherd, C. K., Brandelik, D. M., Sutherland, R. L., Chandra, S., Tondiglia, V. P., Tomlin, D., and Bunning, T. J. *Chem. Mater.* **15**, 2477–2484 (2003).
 32. Flory, P. J. *Principles of polymer chemistry*. Cornell University Press, London, (1971).
 33. Moerkerke, R., Koningsveld, R., Berghmans, H., Dušek, K., and Šolc, K. *Macromolecules* **28**, 1103–1107 (1995).
 34. de Gennes, P. G. and Prost, J. *The Physics of Liquid Crystals*. Clarendon Press, Oxford, 2nd edition, (1993).
 35. Penterman, R. *Photo-enforced stratification of liquid crystal/monomer mixtures, Principle, Theory and analysis of a paintable LCD concept*. PhD thesis, Eindhoven University of Technology, Eindhoven, (2005).
 36. Prenen, A. Master's thesis, Eindhoven University of Technology, Eindhoven, (2005).

Chapter 2

Photopolymerization-induced phase separation

2.1 Introduction

Optical components which contain polyacrylate - liquid crystal (LC) composites are applied in liquid crystal displays (LCD). Promising components for the new generation LCD screens are switchable reflection gratings, or switchable photonic band-gap films. Such a switchable component can be realized by a periodic structure (a Bragg grating) consisting of layers with LC droplets dispersed in a polymer matrix¹. Periodic concentration profiles in polymer dispersed liquid crystals (PDLC) can be obtained by laser beam holography where a position-dependent intensity pattern is recorded in an isotropic reaction mixture of LCs and monomers². The holographic interference pattern induces a position-dependent reaction rate, which creates local distortions in the compositional equilibrium causing diffusion of the reactive materials to the high-intensity sites. Non-reactive materials, i.e. the LC molecules, are transported to the low-intensity sites. For a given LC concentration, phase separation can take place at a critical monomer conversion. The liquid components separate from the polymer, forming periodic layers of liquid droplets (containing LCs and unreacted monomers) in the polymer matrix³.

Several theoretical models have been suggested for the formation of holographic LC-polyacrylate reflection gratings, most of them concentrating only on the reaction-diffusion kinetics^{4,5,6}. However, the phase separation mechanism is also important. Sutherland *et al.*⁷ proposed a phenomenological model explaining holographic reaction-diffusion kinetics combined with phase separation mechanisms expressed as minimum in Gibbs free energy of the system. Recently, a reaction-diffusion model combined with the phase separation mechanism for non-coherent and low intensity curing light forming stratified layers in LC/polyacrylates was proposed by Penterman *et al.*⁸. The main difference between the models is how the authors treat the formed polymer network. In Sutherland's model holes are formed during polymerization (due to polymerization shrinkage), and the hole formations and collapses explain the network elasticity of the polymer. Penterman, on the other hand, adds

a contribution to the Gibbs free energy in the form of network elasticity. We adopt Penterman's approach for our combined phase separation - reaction-diffusion model, and apply it on multilayer LC/polyacrylate systems prepared by either holographic recordings⁹ or cholesteric self-stratification processes. The model allows us to predict where phase separation starts in order to control grating configuration in terms of relative polymer/LC layer thicknesses and composition. The phase separation model is a promising tool to predict morphologies of all kinds of structured PDLCs. The ultimate goal is to simulate the experimental conditions needed for holographic stratification and to translate this later to the cholesteric self-stratification processes.

Aim of chapter

First we discuss the contributions to the Gibbs free energy: Flory's and Huggins' isotropic mixing, network elasticity and nematic ordering. We proceed with the kinetic principles of photopolymerization and diffusion applied on cross-linking polymerization. We combine the phase separation model with diffusion and reaction kinetics characteristic for holographic recordings. Simulation results are verified by experimental results on holographic reflection gratings. The thermodynamic behavior of the reaction mixture upon photopolymerization is described.

2.2 Phase separation mechanisms

Before the polymerization starts, a homogeneous and miscible two-component reaction mixture of monomers and LCs is present. For reason of simplicity we treat the LC and monomers as single components, although in practice it may contain multiple components often homologous of the same basic structure. During polymerization, monomers are converted to polymers, and the two-component system is transformed into a three-component system: monomer-polymer-LC. When the reaction has proceeded to a certain degree of polymerization, the polymer network can no longer hold the liquid components and phase separation occurs.

During polymerization a ternary system is formed of LCs, monomers and polymers in which two phases are distinguished: the polymer matrix phase (phase I) and the liquid phase (phase II). The matrix phase is a three-component phase, containing polymers, monomers and liquid crystals. The liquid phase is a two-component phase, containing monomers and liquid crystals, and is the phase present before polymerization. A description of the phase behavior of such a ternary system is presented next.

Upon polymerization, the ratio of polymer-monomer-LC is changed locally. Assuming that each reaction step induces only a local disturbance of the thermodynamic equilibrium, a thermodynamic treatment of phase separation is legitimate.

Coexistence of two phases in a system is characterized by the equality of the intensive variables (variables that are not dependent on the size of the system) in both phases. Consequently, the chemical potential $\Delta\mu$, or rather the difference in chemical potential in the mixed state and of the pure component, of all components

in both phases must be equal:

$$\Delta\mu_i^I = \Delta\mu_i^{II} \quad (2.1)$$

The chemical potential of a component is the derivative of the Gibbs free energy G of the system to the number of molecules of that component, at constant temperature (T), constant pressure (p) and constant number of molecules for the other species present¹⁰. ΔG_i is the difference in free energy of the mixed and pure state of the component i .

$$\Delta\mu_i = \left(\frac{\partial \Delta G}{\partial n_i} \right)_{T,p,n_j(j \neq i)} \quad (2.2)$$

The next sections give an overview of the thermodynamic models that describe the contributions of isotropic mixing (Flory-Huggins), network elasticity (Dušek) and nematic ordering (Maier-Saupe) to the Gibbs free energy. An important assumption is made: these three effects contribute independently to the free energy of the system.

2.2.1 Isotropic mixing

The isotropic mixing of polymers, monomers and solvents is described by the Flory-Huggins lattice model¹¹. The fundamental thermodynamic equation to describe a mixing process relates the Gibbs free energy function, ΔG , to the enthalpy, ΔH , and the entropy, ΔS :

$$\Delta G = \Delta H - T\Delta S \quad (2.3)$$

Mixtures will be homogeneous, well-mixed, when the Gibbs free energy of mixing is negative:

$$\Delta G^M \leq 0 \quad (2.4)$$

The macroscopic behavior is connected to the behavior on the molecular level of the mixture by statistical mechanics in terms of the Boltzmann relation. This relation links the entropy to the total number of distinguishable microscopic states, Ω .

$$\Delta S = k_B \ln \Omega(n, V, E) \quad (2.5)$$

n is the number of molecules in volume V at the constant energy E . k_B equals the Boltzmann's constant. Consider a mixture of two components, species 1 and 2, with respectively n_1 and n_2 molecules in the mixture, ordered in a lattice of size $n_1 + n_2$. We assume that species 1 and 2 follow Raoult's law (i.e. an ideal solution where the chemical potential of a species is related to its molar fraction), and that there is no change in volume or heat (energy) upon mixing. When all molecules have the same size, every molecule occupies one unit cell in the Flory-Huggins lattice. The number of possible configurations is:

$$(n_1 + n_2)! \quad (2.6)$$

Since two molecules of the same species are indistinguishable, the total number of characteristic states of the system becomes:

$$\frac{(n_1 + n_2)!}{n_1!n_2!} \quad (2.7)$$

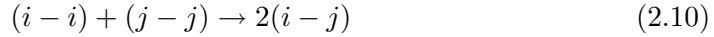
Using Stirling's approximation ($\ln x! \approx x \ln x - x$, for large x), this yields for the entropy:

$$\Delta S = -k_B \left(n_1 \ln \frac{n_1}{n_1 + n_2} + n_2 \ln \frac{n_2}{n_1 + n_2} \right) \quad (2.8)$$

Flory and Huggins independently derived expressions for Ω for mixtures of polymers and solvents^{12,13,14}. We convert their two-component system to our three-component system of monomers-polymers-LCs. The components are large and unequal in size and they can occupy different numbers of unit cells in the lattice. Therefore the number of LCs, monomers and polymers are converted into volume fractions. The number of molecules for the three components are n_{lc} , n_m and n_p , and they occupy respectively N_{lc} , N_m and N_p unit cells per molecule. The volume fraction of species i , ϕ_i , in the mixture is $\frac{n_i N_i}{n_p N_p + n_m N_m + n_{lc} N_{lc}}$. Extending equation 2.8 to a three-component system of large molecules, the entropy of mixing becomes

$$\Delta S^M = -k_B [n_m \ln \phi_m + n_{lc} \ln \phi_{lc} + n_p \ln \phi_p] \quad (2.9)$$

Up till now, no heat or energy exchange upon mixing was assumed, however this is an unrealistic situation. From regular solution theory¹⁵, an expression can be obtained for the enthalpy ΔH^M . The energy change is assumed to originate from the exchange of contacts between monomer-monomer, LC-LC and polymer-polymer with monomer-LC, polymer-LC and monomer-polymer contacts¹⁶. For two components, i and j , this can be represented by:



where the formation of an $i - j$ contact requires breaking of $i - i$ and $j - j$ contacts. The change in energy can be expressed as an interchange energy Δw_{ij} per new contact, given by:

$$\Delta w_{ij} = w_{ij} - \frac{1}{2}(w_{ii} + w_{jj}) \quad (2.11)$$

Here w_{ii} and w_{jj} are the contact energies for each species. Consequently, if the total volume remains constant upon mixing, the energy of mixing can be expressed by ΔH^M . When q new contacts are formed in the solution, the enthalpy of mixing becomes:

$$\Delta H^M = q \Delta w_{ij} \quad (2.12)$$

The average number of possible contacts can be estimated from the total number of possible contacts between molecule i and any neighbor and the probability that the neighbor is of the other species¹¹. First, the total number of any contact with i is zN_i , where z is the lattice coordination number or the number of unit cells of the closest neighbors. N_i is the number of unit cells that molecule i occupies. If N_i is large (i.e. molecule i is a chain and occupy several unit cells), it has $(z-2)N_i$ contacts per chain unit plus 2 for both chain ends, thus a total of $(z-2)N_i + 2$ neighbors. For large z the total number of neighbors approaches zN_i . The probability that one of the neighbors to i is of the other kind (j) approximates to the volume fraction

of j (ϕ_j). As a result, for n_i molecules of i the number of $i - j$ contacts become: $q = n_i \cdot z N_i \cdot \phi_j$. The expression for ΔH^M can then be written as:

$$\Delta H^M = z n_i N_i \phi_j \Delta w_{ij} \quad (2.13)$$

To eliminate z , a dimensionless parameter χ , called the interaction parameter, is introduced. It is defined¹⁷ as:

$$k_B T \chi_{ij} = z \Delta w_{ij} \quad (2.14)$$

The final expression for the enthalpy becomes:

$$\Delta H^M = k_B T \chi_{ij} n_i N_i \phi_j \quad (2.15)$$

Having calculated the entropy and enthalpy contributions to mixing, these can now be combined to give the expression for the free energy of mixing, $\Delta G^M = \Delta H^M - T \Delta S^M$. For the monomer-polymer-LC system the Gibbs free energy of mixing is:

$$\Delta G^M = k_B T \left[n_m \ln \phi_m + n_{lc} \ln \phi_{lc} + n_p \ln \phi_p + \sum_{i < j} \chi_{ij} n_i N_i \phi_j \right] \quad (2.16)$$

The chemical potentials are the derivatives of the free energy, shown here for the three components: the monomer (2.17), the LC (2.18) and the polymer (2.19)

$$\frac{\Delta \mu_m^M}{k_B T} = \frac{1}{k_B T} \left(\frac{\partial \Delta G^M}{\partial n_m} \right)_{T,P,n} = \ln \phi_m + (1 - \phi_m) - \phi_{lc} \left(\frac{N_m}{N_{lc}} \right) - \phi_p \left(\frac{N_m}{N_p} \right) \quad (2.17)$$

$$+ (\chi_{m-lc} \phi_{lc} + \chi_{m-p} \phi_p) (\phi_{lc} + \phi_p) N_m - \chi_{p-lc} \phi_{lc} \phi_p N_m$$

$$\frac{\Delta \mu_{lc}^M}{k_B T} = \frac{1}{k_B T} \left(\frac{\partial \Delta G^M}{\partial n_{lc}} \right)_{T,P,n} = \ln \phi_{lc} + (1 - \phi_{lc}) - \phi_m \left(\frac{N_{lc}}{N_m} \right) - \phi_p \left(\frac{N_{lc}}{N_p} \right) \quad (2.18)$$

$$+ (\chi_{m-lc} \phi_m + \chi_{p-lc} \phi_p) (\phi_m + \phi_p) N_{lc} - \chi_{m-p} \phi_m \phi_p N_{lc}$$

$$\frac{\Delta \mu_p^M}{k_B T} = \frac{1}{k_B T} \left(\frac{\partial \Delta G^M}{\partial n_p} \right)_{T,P,n} = \ln \phi_p + (1 - \phi_p) - \phi_{lc} \left(\frac{N_p}{N_{lc}} \right) - \phi_m \left(\frac{N_p}{N_m} \right) \quad (2.19)$$

$$+ (\chi_{p-lc} \phi_{lc} + \chi_{m-p} \phi_m) (\phi_{lc} + \phi_m) N_p - \chi_{m-lc} \phi_{lc} \phi_m N_p$$

2.2.2 Network elasticity

Phase separation is among others dependent on the elasticity of the polymer network. The network can be swollen by diffusing solvent molecules. It has been demonstrated¹⁸ that phase separation during polymerization was induced by the

increased elasticity of the growing and swollen polymer network. The elasticity of the network chains aims to resist swelling, giving an extra energy to the system. Dušek provided an expression for the contribution of the network deformation by swelling to the Gibbs free energy^{19,20,21}:

$$\frac{\Delta G^{el}}{Nk_B T} = \frac{\nu_e}{N} \left[\frac{3}{2} A \Phi_p^{2/3} (\phi_p^{-2/3} - 1) + B \ln \phi_p \right] \quad (2.20)$$

ϕ_p is the volume fraction of the polymer, in this case it is assumed that all polymer formed is part of the network. ν_e is the number of polymer chains between two cross-links in the network, and N is the total size of the lattice ($N = n_{lc}N_{lc} + n_m N_m + n_p N_p$). Thus ν_e/N reflects the fraction of polymer chains in the elastic network, this can also be expressed by ϕ_p/m_c , where m_c is the average length of the chains between two cross-links. During the polymerization m_c decreases since the probability for cross-linking increases with the monomer conversion (α). It is assumed that the lengths of the polymer chains between the cross-links have a Gaussian distribution, and can be represented by the average (m_c). An expression for m_c is proposed in section 2.8.3 where also the cross-linking efficiency is discussed. The derivatives of equation 2.20 gives the chemical potentials for the network contribution.

It is assumed that the network is created instantaneously and remains homogeneous upon polymerization, therefore the polymer volume fraction during cross-linking, Φ_p , equals ϕ_p . A and B are constants defined as¹⁸

$$A = 1 \quad B = 2/f \quad (2.21)$$

where f is the monomer functionality (one double bond has a functionality of $f = 2$).

The elastic contribution to the chemical potentials, using equation 2.20 with 2.21, becomes

$$\frac{\Delta \mu_m^{el}}{k_B T} = \frac{N_m}{m_c} \left[1 - \frac{2}{f} \right] \phi_p \quad (2.22)$$

$$\frac{\Delta \mu_{lc}^{el}}{k_B T} = \frac{N_{lc}}{m_c} \left[1 - \frac{2}{f} \right] \phi_p \quad (2.23)$$

2.2.3 Nematic ordering

Self-organized liquid crystals add an extra contribution to Gibbs free energy due to the molecular ordering. The nematic phase has one-dimensional order since the molecules are aligned in a preferred direction represented by the director \bar{n} (figure 1.1(a) in chapter 1). The order of the LC molecules can be quantified by the order parameter^{22,23,24} s , or $\langle P_2 \rangle$, defined as the average of the second-order Legendre polynomial of the orientational distribution function:

$$s = \langle P_2 \rangle = \left\langle \frac{3}{2} \cos^2 \theta - \frac{1}{2} \right\rangle \quad (2.24)$$

θ is the angle between the director and the long axis of each molecule. The time averaged cosine square of θ , $\langle \cos^2 \theta \rangle$, is defined as

$$\langle \cos^2 \theta \rangle = \int \int \cos^2 \theta f(\theta, \phi) d(\cos \theta) d\phi \quad (2.25)$$

where $f(\theta, \phi)$ is the distribution function of the orientation of the LCs, assuming each molecule having well defined long axes with the polar angles ϕ and θ . The distribution function gives the probability of finding a LC molecule in the direction at the angle θ . When $f(\theta, \phi)$ yields high probability for the directions $\theta = 0^\circ$ and $\theta = 180^\circ$, s is 1. This is the case for an ideal macroscopically ordered LC state where all molecules are perfectly aligned with the director. Contrary, with a totally random distribution function, equation 2.24 averages to 0 and s equals 0. The disordered phase, with the director in random directions, is present in the isotropic phase. The order parameter for LCs in the nematic phase have typically values²⁵ between 0.3-0.8, depending on the nature of the LCs and the temperature. Below the nematic-isotropic phase transition temperature (T_{ni}), a liquid crystal component prefers to be nematic. Above T_{ni} the isotropic phase is present.

Maier and Saupe developed a mean-field theory applied as the free energy of nematic ordering. At equilibrium, a minimum value for the thermodynamic potential, ΔG^N , is obtained²⁶.

$$\frac{\Delta G^N(p, T)}{Nk_B T} = \frac{\phi_{lc}}{N_{lc}} \int \int f \log(4\pi f) d(\cos \theta) d\phi - \frac{\phi_{lc}}{N_{lc}} \frac{1}{2} \nu \phi_{lc} s^2 \quad (2.26)$$

where N is the total number of lattice unit cells ($N = n_{lc}N_{lc} + n_m N_m + n_p N_p$). The decrease in entropy due to the anisotropic angular distribution is described by the integral. The logarithm originates from the Gibbs entropy formula:

$$S = -k_B \sum_v P_v \ln P_v \quad (2.27)$$

where P_v is the probability for the system to be in a state v . In this particular case, this probability is related to the distribution function f .

Minimizing ΔG^N with respect to all variations of f that satisfy the constraint

$$\int f d(\cos \theta) d\phi = 1 \quad (2.28)$$

gives the form of the distribution function:

$$f(\theta) = \frac{1}{Z} \exp\left(\frac{-u(\theta)}{k_B T}\right) \quad (2.29)$$

$u(\theta)$ is the energy associated with one particular orientation of a molecule to the director:

$$\frac{u(\theta)}{k_B T} = -\frac{1}{2} m (3 \cos^2 \theta - 1) \quad (2.30)$$

with m a mean-field parameter, expressing the strength of the mean field. Z is the nematic partition function; the total number of possible states of the nematic system:

$$Z = \int \exp\left(\frac{-u(\theta)}{k_B T}\right) d(\cos \theta) \quad (2.31)$$

The second term in equation 2.26, describes the effects of intermolecular interactions and the potential of the director orientation. Maier and Saupe assumed the potential being independent of temperature and that only van der Waals forces contribute (which interactions scale with $1/r^6$ or $1/V^2$ or ϕ^2 , with r radius and V volume of LC). They defined these interactions to be quadratic in the order parameter. ν is a quadrupole interaction parameter defined as

$$\nu = 4.54 \frac{T_{ni}}{T} \quad (2.32)$$

with T_{ni} the nematic to isotropic transition temperature of the liquid crystal.

The order parameter s may be evaluated based on the free energy minimization approach by deriving equation 2.26 to s :

$$-\frac{d \ln Z}{ds} + s \frac{dm}{ds} + m - \phi_{lc} \nu s = 0 \quad (2.33)$$

Since the first two terms cancel out, a simple equation remains which gives:

$$m = \phi_{lc} \nu s \quad (2.34)$$

In the Maier-Saupe theory adopted here²⁶ the mean field parameter m is linear dependent of the concentration (or volume fraction) of the LCs. In other studies the strength of the mean field is assumed to scale to the square of the concentration^{23,27} based on the assumption that the nematic interactions of van der Waals type influence not only the intermolecular forces (N_1) but also the mean field. A square dependence, $m \sim \phi_{lc}^2$ would increase the strength of the ordering of the LCs, with higher order parameters as a result. This is often found for (long) liquid crystal polymer chains²⁷.

Note that the order parameter is defined as a function of the distribution function f , which in turn depends on the mean field parameter m . Therefore s can be expressed as a function of m . However, solving m from 2.24 using 2.25, 2.30 and 2.31 is not trivial. Since Z has a form of an error function, the relation $s(m)$ becomes a sigmoidal curve²⁸. In order to obtain a simpler relation between s and m , Shen *et al.*²⁶ proposed $s(m)$ being a polynomial of m :

$$s(m) = c_1 \cdot m + c_2 \cdot m^2 + c_3 \cdot m^3 + c_4 \cdot m^4 \quad (2.35)$$

$$\ln Z = \int s(m) dm = \frac{1}{2} c_1 \cdot m^2 + \frac{1}{3} c_2 \cdot m^3 + \frac{1}{4} c_3 \cdot m^4 + \frac{1}{4} c_4 \cdot m^5 \quad (2.36)$$

$$\begin{aligned} c_1 &= 0.1983 & c_3 &= -0.01653 \\ c_2 &= 0.03768 & c_4 &= 0.001458 \end{aligned}$$

Equation 2.35 correctly predicts the values of the order parameter for lower values of m ($m < 6$ for which $s < 0.88$), but at higher m , s increases drastically above 1. Order parameters, that describe the directionality of the LCs, are physically only allowed to have values between 0 and 1. For nematic LCs (generally having values of s below 0.8)²⁵, equation 2.35 is valid to use as an approximation. However for liquid crystals with higher order parameters, which is possible for some smectic phases, Shen's equation would not yield correct results for the order parameter²⁹.

For given sets of temperatures and compositions, substitution of 2.34 in 2.35 yield a solution for s . Graphically, the possible solutions for s can be seen in figure 2.1(a) as the intersections of equation 2.34, a straight line with slope $(\frac{1}{\phi_{lc}\nu})$ and equation 2.35. At $T = T_{ni}$ the critical values ($s_c \approx 0.44$ and $m_c \approx 2.00$) are determined by the tangent point of the slope and equation 2.35²⁸. With slopes having greater values, at $T > T_{ni}$, there is no intersection except $s = 0$, implying that the system is in the isotropic state. At lower temperatures $T < T_{ni}$, the straight line (equation 2.34) intersects 2.35 at $s = 0$ and s for that temperature. The order parameter increases with decreased temperature, until the crystallization occurs and the nematic state is lost.

The critical composition ϕ_{ni} for which nematic phase is present in a mixture of an isotropic monomer and a nematic liquid crystal can be calculated from the

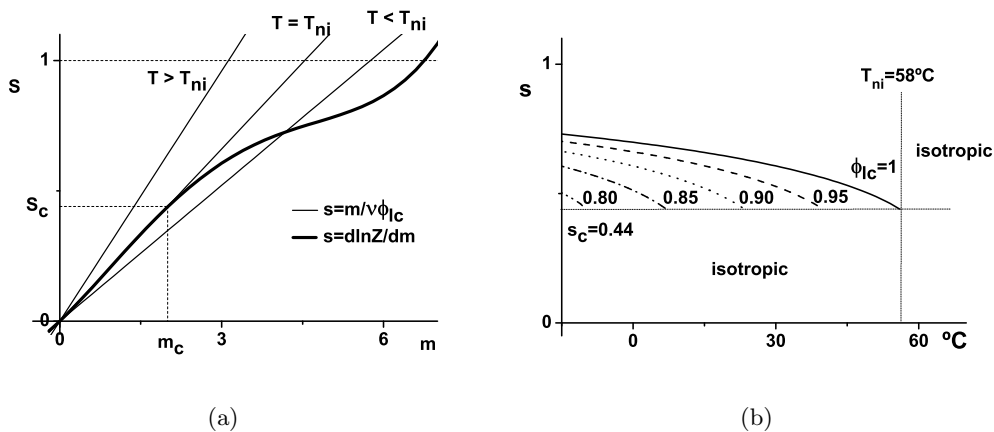


Figure 2.1: (a) Graphical presentation of the self-consistent solution for the order parameter using $s = m/(\phi_{lc}\nu)$ (equation 2.34) and $s = d \ln Z/dm$ (equation 2.35), for $\phi_{lc} = 1$. At temperatures higher than T_{ni} the slope $1/(\phi_{lc}\nu)$ only intersect with equation 2.35 at $s = 0$, implying that the system is isotropic. (b) Effects of temperature and LC volume fractions on the order parameter are shown (equations 2.34 and 2.35). At room temperature (25°C) minimum 91 volume% of LC has to be present in order to obtain a nematic phase (for $T_{ni} = 58^\circ\text{C}$). Decreasing the temperature allows more monomers being mixed in while keeping the nematic LC phase.

critical order parameter s_c (figure 2.1(b)).

$$\left(\frac{\phi \cdot s_c}{T}\right)_{\phi=\phi_{ni}} = \left(\frac{\phi \cdot s_c}{T}\right)_{T=T_{ni},\phi=1} \quad (2.37)$$

$$\phi_{ni} = \frac{T}{T_{ni}} \quad T \leq T_{ni} \quad (2.38)$$

Mixtures in the isotropic phase ($T > T_{ni}$) have no nematic contribution to the free energy.

Rewriting equation 2.26 by inserting equation 2.34, a more convenient form is obtained²⁶:

$$\frac{\Delta G^N}{Nk_B T} = \frac{\phi_{lc}}{N_{lc}} \left[-\ln Z + \frac{1}{2} \nu \phi_{lc}^2 s^2 \right] \quad (2.39)$$

where $\ln Z = \int s(m) dm$.

The chemical potentials contribution from the Maier-Saupe theory are the derivatives of 2.39:

$$\frac{\Delta \mu_{lc}^N}{k_B T} = \frac{1}{k_B T} \left(\frac{\partial \Delta G^N}{\partial n_{lc}} \right)_{T,p,n} = -\ln Z + \frac{1}{2} \nu \phi_{lc}^2 s^2 \quad (2.40)$$

$$\frac{\Delta \mu_m^N}{k_B T} = \frac{1}{k_B T} \left(\frac{\partial \Delta G^N}{\partial n_m} \right)_{T,p,n} = \frac{1}{2} \frac{N_m}{N_{lc}} \nu \phi_{lc}^2 s^2 \quad (2.41)$$

2.3 Reaction-diffusion mechanisms

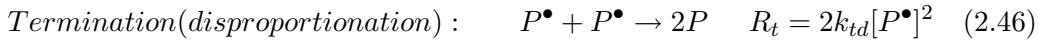
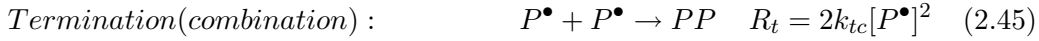
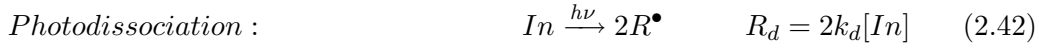
A periodic modulation of polymerization rate in depth of the reaction mixture of liquid crystals and monomers is necessary to form layered PDLC structures. The differences in polymer content caused by the modulated polymerization rates create macroscopic concentration differences in depth of the film. These are the driving force for diffusion of the monomers and liquid crystals. Here, theoretical expressions for position dependent reaction rates and diffusion will be discussed and equations derived in order to thermodynamically describe the formation of layered LC/polyacrylate structures.

2.3.1 Radical photopolymerization

Radical photopolymerization is a fast process. Polymer chains are formed by a chain addition reaction in a fraction of a second, and the whole process takes typically seconds to minutes depending on the initiator and irradiation power³⁰. The polymerization requires radicals to start the propagation and since monomers alone in general do not sufficiently absorb UV-light to dissociate into radicals, photoinitiators (I_n) are added. The radicals from the dissociated initiators (R^\bullet) react with an unsaturated double bond on the monomer (M), and the radical is transferred to the monomer unit (RM^\bullet). By addition of more unreacted double bonds, the polymer chain (P^\bullet) grows. When each monomer has one reactive bond a linear polymer is

created. The polymer chain grows until it terminates by a reaction with another radical-molecule. The termination procedure can occur by several processes: interaction of two active chain ends (combination and disproportionation), reaction of an active chain end with an initiator radical, transfer of the active center to another molecule which may be solvent, initiator or monomer, or by interaction with impurities or inhibitors. The process can also terminate by capturing radicals in unaccessible sites. The bimolecular mechanisms, combination and disproportionation, are assumed to be the dominant termination effects^{16,30}.

The reactions and the corresponding reaction rates (R) of photopolymerization are:



The photodissociation of the initiator molecules is the rate determining step, since that process is slower than the reaction between a radical and a double bond¹⁶. Further it is assumed that the reaction rate of the radicals with the monomers is independent of the type and size of the radical. The reaction rate for the initiation step is defined as:

$$R_i = k_i[R^\bullet] = 2\Phi_{In}I_a \quad (2.47)$$

where Φ_{In} is the initiation quantum yield of the photoinitiator molecules at the irradiation wavelength, and I_a is the light intensity that is effectively absorbed by the initiator. Since two radicals are formed per initiator, a factor 2 is present in equation 2.47. Using Beer's law for light absorption in thin films³¹, and assuming that the only absorption in depth of the film is from the initiators (i.e. assuming that the intensity remains almost constant), the absorbed intensity is expressed as:

$$I_a = 2.3I_0\epsilon_{In}[In]z \quad (2.48)$$

where the factor 2.3 ($= \ln 10$) indicates the use of natural logarithms of Beer's absorption law. $[In]$ and ϵ_{In} are the concentration and the molar extinction coefficient of the photoinitiator and z the thickness of the film of reaction mixture. I_0 is the light intensity applied on the reaction mixture. Structured PDLCs are formed due to a gradient in effectively absorbed light by the initiator in depth of the film, I_a .

During polymerization, if steady state conditions apply, the number of active radicals are assumed constant: $\frac{d[RM^\bullet]}{dt} = 0$. The overall polymerization rate expresses the depletion of monomers (with one reactive bond) during steady state: $-\frac{d[M]}{dt} = R_p$. In order to have a constant number of active radicals, the initiation

rate must equal the termination rate.

$$R_i = R_t \quad (2.49)$$

$$2\Phi_{In}I_a(z) = 2k_t[P^\bullet]^2 \quad (2.50)$$

$$[P^\bullet] = \sqrt{\frac{\Phi_{In}I_a(z)}{k_t}} = [RM^\bullet] \quad (2.51)$$

where $2k_t$ is the effective rate constant for all involved termination mechanisms with the factor 2 since two radicals are consumed during bimolecular termination. Combining the equations 2.44 and 2.51, the steady-state reaction rate can be expressed in terms of the monomer concentration as

$$R_p = k_p[RM^\bullet][M] = \frac{k_p}{\sqrt{k_t}}\sqrt{\Phi_{In}I_a(z)}[M] \quad (2.52)$$

The monomer conversion, α_t , at time t is defined as

$$\alpha_t = 1 - \frac{[M]_t}{[M]_0} \quad (2.53)$$

with $[M]_t$ being the monomer concentration at t time of polymerization, and $[M]_0$ the initial monomer concentration.

Equation 2.52 is only valid for diluted reaction mixtures creating linear polymers, for any form of cross linking polymerization an adapted version of 2.52 can serve as an approximation of the polymerization kinetics. This is caused by several effects arising during cross-linking polymerization.

Cross-linked polymer networks can decrease the mobility of the active polymer chains (P^\bullet) so that they are hindered to terminate the polymerization³². Locally a drastic decrease of k_t auto-accelerates the polymerization (the Trommsdorff effect) followed by a local and high polymerization and conversion rates.

Moreover, the polymer network can also vitrify the system, resulting in decreased mobility. Then monomers are hindered to diffuse to the active chains, and the polymerization terminates by trapping radicals in the network³³. Lowering the viscosity, e.g. by adding solvent or increasing the temperature, the mobility of the system increases which can favor the propagation reaction. However, unlike most other chemical reactions, increased temperature only favors polymerization kinetics to certain degree. At high temperatures the thermodynamic conditions for forming polymers are no longer fulfilled (this occurs at ca 220°C for acrylates).

Multi-functional monomers are required to create polymer networks. Since cross-linking monomers have multiple reactive groups; one, some or all reactive groups are involved when converting a monomer. Thus, the monomer conversion does most probably not equal the double bond conversion. Instead the decrease in double bond

concentration ($[C=C]$) is approximated by the steady-state polymerization rate:

$$-\frac{d[C=C]}{dt} = \frac{k_p}{\sqrt{k_t}} \sqrt{\Phi_{In} I_a(z)} [C=C] \quad (2.54)$$

$$x = 1 - \frac{[C=C]_t}{0.5f[M]_0} \quad (2.55)$$

where x is the double bond conversion and f the functionality of the monomer and $0.5f$ is the number of reactive bonds per monomer. Strictly qualitatively, equation 2.54 describes cross-linking kinetics for polymerization at low $[C=C]$ conversions before vitrification. Equations 2.54 and 2.55 assume that all reactive bonds are equally likely to react. However for cross-linking polymerization it has been suggested that pendant bonds are less reactive at high monomer conversions³⁴. It is therefore assumed that the polymerization rate decreases with increased amount of polymer formed. From experiments it is known that double bond conversions when polymerizing multi-functional monomers do not reach 100%^{30,35,36}. This is due to vitrification, where pendant double bonds are trapped in the polymer network. The vitrification decreases the polymerization rate when a certain amount of double bonds has reacted, at conversion x_{max} . Experimentally x_{max} can be measured by e.g. differential scanning calorimetry by following the reaction heat of the converted double bonds.

Also, the monomer conversion during cross-linking is often assumed not to proceed to completion. The maximum monomer conversion (α_{max}) can be experimentally determined by extracting the unreacted monomers from the polymer network. The decrease in polymerization rate is assumed to be linear with the increase in monomer conversion. At α_{max} polymerization is assumed to terminate due to the decreased mobility. The cross-linking polymerization rate can then be expressed as:

$$-\frac{d[C=C]}{dt} = \frac{k_p}{\sqrt{k_t}} \left(1 - \frac{\alpha}{\alpha_{max}}\right) \sqrt{\Phi_{In} I_a(z)} [C=C] \quad (2.56)$$

Equation 2.56 serves as a general approximation of the cross-linking kinetics. In order to gain a true description of the complex initiating, propagating and terminating reaction steps, supportive measurements and/or Monte Carlo simulations are necessary.

An expression for the monomer conversion is necessary to use equation 2.56. Until now, no valid theoretical relationship for cross-linking polymerization is available. One assumption, the mean field approximation (MF), which assumes that all double bonds are equally likely to react, is generally applied in simulations of cross-linking polymerization kinetics for diacrylate monomers⁸. The MF assumes that the double bond and the monomer conversion proceeds to completion (figure 2.2), and uses the relationship between the monomer conversion (α) to the double bond conversion (x) as

$$\alpha = 1 - (1 - x)^{f/2} \quad (2.57)$$

where f is the monomer functionality. For higher monomer functionalities, $f > 4$, the mean field approximation and experimental results deviate³⁴. It is assumed

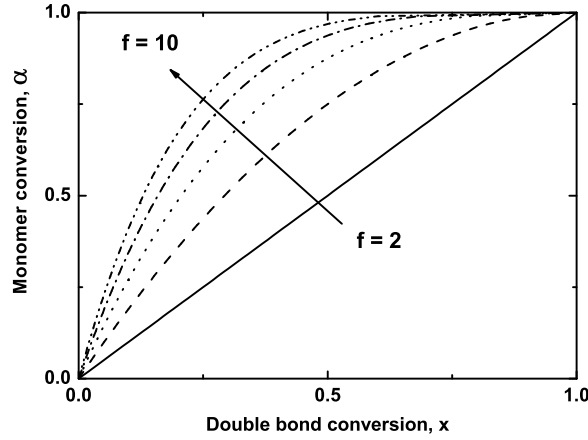


Figure 2.2: The relation between monomer and double bond conversions using the mean field approximation (equation 2.57). The conversion is plotted for monomers with one double bond ($f = 2$), two ($f = 4$), three ($f = 6$), four ($f = 8$), and five ($f = 10$) double bonds.

that the deviation is caused by the vitrification^{30,35,36}. However, at the onset of the polymerization, it is realistic to assume the double bond reactivity to be similar for all double bonds, as the MF does.

Experimentally measured values of α_{max} and x_{max} can support the mean field theory, in order to use it in simulations.

2.3.2 Diffusion

Photopolymerization with a non-uniform intensity profile induces depth dependent polymerization kinetics. The latter gives in fact rise to local distortions in concentrations that induce transport of material: diffusion. Fick's first law for steady-state diffusion states that the flux is proportional to the concentration gradient³⁷:

$$J = -D \frac{\partial c}{\partial z} \quad (2.58)$$

where J is the diffusion flux in $\text{m}^{-2}\text{s}^{-1}$, D the diffusion coefficient in m^2s^{-1} and c the concentration in particles per volume (m^3).

During the formation of PDLCS, the composition within the volume changes in time. Then Fick's second law for non-steady state diffusion applies.

$$\frac{\partial c}{\partial t} = \frac{\partial}{\partial z} \left(D \frac{\partial c}{\partial z} \right) \quad (2.59)$$

A concentration gradient manifests itself in a gradient of the chemical potential which is the driving force for diffusion¹⁰. The flux of particles is then given by:

$$J = -\frac{Dc}{kT} \frac{\partial \mu}{\partial z} \quad (2.60)$$

For ideal gaseous mixtures of non-interacting hard spheres, the chemical potential is obtained from equation 2.59 as $\mu = kT \ln c$. The LC/monomer/polymer system treated here is not consisting of ideal spheres, therefore the more general diffusion law (equation 2.62) should be applied. Furthermore, the concentration c can be replaced by the density ρ , volume fraction ϕ , and the molar weight M , of the component of interest.

$$c_i = \frac{\phi_i \rho_i}{M_i} \quad (2.61)$$

The general diffusion equation for species i with volume fraction ϕ_i and diffusion constant D_i becomes:

$$\frac{\partial \phi_i}{\partial t} = \frac{\partial}{\partial z} \left(\frac{D_i \phi_i}{kT} \frac{\partial \mu_i}{\partial z} \right) \quad (2.62)$$

The diffusion coefficient D is defined as a constant, independent of the composition and morphology of the sample. Obviously, during polymerization the mobility of the molecules decreases due to the formation of the polymer network. Therefore D has to be a function of the volume fraction ϕ_p . From the free volume theory³⁷ the following expression for D can be obtained:

$$D(\phi_m) = D_m \cdot e^{\frac{1}{K_1 \left(\frac{1}{\phi_m} + K_2 \right)}} \quad (2.63)$$

where ϕ_m is the monomer volume fraction, D_m is the monomer diffusion coefficient in the pure polymer, and K_1 and K_2 are positive constants described in the free volume theory. For any value of ϕ_m $D(\phi_m) > D_m$, $D(\phi_m)$ decreases with increased polymer content (or decreased monomer fraction).

The net change of the volume fractions has to equal zero (ignoring polymerization shrinkage) according to the material balance: $\frac{\partial \phi_{lc}}{\partial t} + \frac{\partial \phi_m}{\partial t} + \frac{\partial \phi_p}{\partial t} = 0$. The increased volume of polymer equals the decreased volume of monomer since only the monomers polymerize. Due to cross-linking polymerization the polymer is assumed to be immobile, thus not to diffuse. Even linear polymers can be assumed immobile since they have much lower diffusion coefficients compared to D_m and D_{lc} . In order to fulfill the material balance, the diffusion flux of the LCs has to be opposite and equal to the diffusion flux of the monomers (if the size and density of the two species are assumed to be equal). Therefore one of the species is assumed to be dominant in the diffusion process, and it will control the diffusion flux of the other component. Penterman⁸ found that the gradient in monomer concentration was the driving force for the diffusion for the LC-acrylate system studied. Our reaction systems are similar to Penterman's, and we assume the diffusion flux of the LCs to be determined by that of the monomers:

$$\frac{\partial \phi_{lc}}{\partial t} = -\frac{\partial \phi_m}{\partial t} = -\frac{\partial}{\partial z} \left(\frac{D_m \phi_m}{kT} \frac{\partial \mu_m}{\partial z} \right) \quad (2.64)$$

2.4 Ternary conversion-phase diagrams

A graphical representation of polymerization induced phase separation in a monomer-LC mixture was introduced by Boots *et al.*¹⁸ with the concept of ternary conversion-phase diagrams. It combines the thermodynamics of the three-component system (monomer-polymer-solvent) with the conversion of monomers into polymer.

The following relation holds between the monomer conversion α and the overall volume fractions:

$$\phi_m = (1 - \alpha)(1 - \phi_{lc}) \quad (2.65)$$

$$\phi_p = \alpha(1 - \phi_{lc}) \quad (2.66)$$

Together with the condition that the sum of all volume fractions equals one in both phases:

$$\phi_p^I + \phi_m^I + \phi_{lc}^I = 1 \quad (2.67)$$

$$\phi_m^{II} + \phi_{lc}^{II} = 1 \quad (2.68)$$

and the requirement of equality of chemical potentials in both phases for having coexistent phases,

$$\Delta\mu_m^I = \Delta\mu_m^{II} \quad (2.69)$$

$$\Delta\mu_{lc}^I = \Delta\mu_{lc}^{II} \quad (2.70)$$

all equations needed to find all possible combinations of ϕ_p^I , ϕ_m^I , ϕ_{lc}^I , ϕ_m^{II} and ϕ_{lc}^{II} for which 2 phases can coexist are available.

Figure 2.3 shows an example of a conversion-phase diagram. The gray line CD is called the phase separation line. Points to the left of this line refer to a one phase system (phase I); points to the right of the line refer to a two-phase system (phase I and II). Hence, CD is comprised of the points with the lowest conversion that satisfy the conditions 2.69 and 2.70.

Polymerization takes place on a horizontal line of constant LC-concentration, called polymerization line. At some point (X in the diagram) the polymerization line crosses the phase separation line. Phase separation occurs and phase II emerges, containing only monomers and LCs. From the fact that at the moment of phase separation the volume of phase II is infinitesimal, the composition of phase I at that point is equal to the overall composition before phase separation. The conversion at which the phase separation takes place (for a certain liquid crystal volume fraction) and the composition of the second phase can be determined as follows: Equations 2.65 and 2.66 give ϕ_p^I and ϕ_m^I as a function of the conversion α . From 2.68 ϕ_m^{II} is given as a function of ϕ_{lc}^{II} . This leaves 2 variables, ϕ_{lc}^{II} and α , which can be obtained by solving 2.69 and 2.70.

The conversion-phase diagram visualizes how the phase separation behavior depends on the initial composition of the reaction mixture. The procedure to solve 2.69 and 2.70 as described here cannot be carried out by analytical methods. A numerical solution to this set of equations will be proposed in section 2.5.

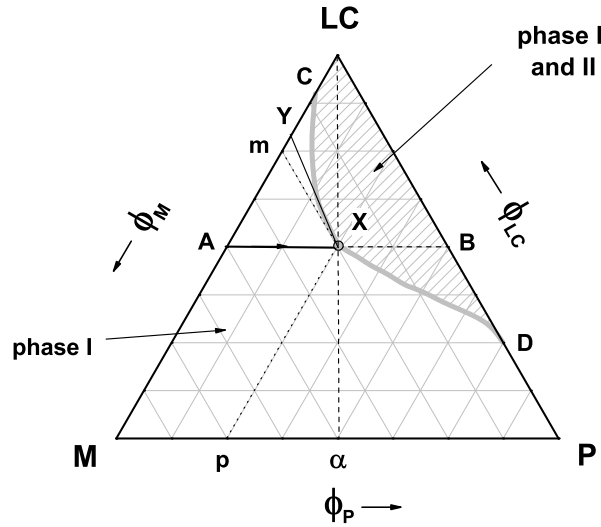


Figure 2.3: Ternary conversion-phase diagram of LC, monomer (M) and polymer (P). Starting with a composition of monomers and LCs as in point A, monomers are converted into polymers following the straight line A-B during polymerization. The formed polymer is miscible in the monomers and LCs (phase I) until a certain conversion (α) is reached. Then, at position X where the polymerization line reaches the phase separation line (the gray line CD), phase separation occurs and a liquid phase (phase II) emerges from the polymer containing phase (phase I). At phase separation the compositions of phase I (at position X) is p polymer, m monomer and B LCs, and for phase II: Y monomer and (1-Y) LCs.

It is important to realize the difference between a conversion-phase diagram and a phase diagram. In a phase diagram, the size and structure of the molecules of each component are invariable; each point represents a certain ratio of the component. During polymerization however, this is not necessarily the case. The polymer increases in weight, and also changes in molecular structure and molecular size distribution. Therefore at each point in the diagram, the composition of the system as well as the polymer itself are different.

2.5 Combined phase separation and reaction-diffusion model for holographic stratified films

2.5.1 Formalism

The expressions of the chemical potentials for monomer and liquid crystal molecules are the governing equations for both phase separation and reaction-diffusion kinetics. Isotropic mixing, network elasticity and nematic ordering are assumed to contribute independently to the Gibbs free energy. This implies that the chemical potentials due to these three effects add up independently to the total chemical potential of

both compounds.

$$\Delta\mu_m^{total} = \Delta\mu_m^M + \Delta\mu_m^{el} + \Delta\mu_m^N \quad (2.71)$$

$$\Delta\mu_{lc}^{total} = \Delta\mu_{lc}^M + \Delta\mu_{lc}^{el} + \Delta\mu_{lc}^N \quad (2.72)$$

However, in their current condition the expressions for the chemical potentials are not suitable to be used in a numerical model. In the coming paragraphs, the three terms will be discussed separately and expressions will be derived that can be exploited in a simulation program.

Expressions for the isotropic mixing, $\Delta\mu_m^M$ and $\Delta\mu_{lc}^M$, were derived in section 2.2.1. Since polymers and monomers are comprised of the same building blocks, the interaction parameter χ_{m-p} between monomer and polymer is assumed to be zero. In addition, the sizes of the monomer and liquid crystal molecules in the system under study are presumed to be comparable. Consequently, it is assumed that $N_{lc} = N_m = 1$ and that the polymer chains are infinitely long, $N_p = \infty$. Consequently, the formulation of the chemical potentials for monomers and liquid crystals are simplified considerably:

$$\begin{aligned} \frac{\Delta\mu_m^M}{k_B T} &= \ln \phi_m + \phi_p \\ &+ \chi_{m-lc} \phi_{lc} (\phi_{lc} + \phi_p) N_m \\ &- \chi_{p-lc} \phi_{lc} \phi_p N_m \end{aligned} \quad (2.73)$$

$$\begin{aligned} \frac{\Delta\mu_{lc}^M}{k_B T} &= \ln \phi_{lc} + \phi_p \\ &+ (\chi_{m-lc} \phi_m + \chi_{p-lc} \phi_p) (\phi_m + \phi_p) N_{lc} \end{aligned} \quad (2.74)$$

Polymerizing multi-functional monomers result in a cross-linked polymer network. Phase separation may occur either before or during vitrification (increased viscosity which slows down the polymerization reaction). In any case, cross-linking polymerization forms a network instantaneous and phase separation can be induced by the elasticity of the swollen network during polymerization. Therefore the network elasticity has to be taken into account.

Finally the nematic ordering contribution; $\Delta\mu_m^N$ and $\Delta\mu_{lc}^N$ are described in section 2.2.3 with equations 2.40 and 2.41. The order parameter, s , of the liquid crystal is calculated by the equation 2.35.

2.5.2 Procedure for obtaining phase separation line

In section 2.4, an analytical method for determining the points in a phase diagram where two phases can coexist was proposed. However, the set of governing equations for phase separation is not analytically solvable. Therefore, a numerical method is suggested here. The main idea is to calculate the total chemical potential for all possible compositions of phase I and phase II, and when equal the compositions of both phases at phase separation are found.

Table 2.1: Schematic representation of the procedure to calculate the phase separation line.

	Phase I	Phase II
choose:	$\phi_{lc}^I \alpha$	ϕ_{lc}^{II}
derive:	$\phi_p^I \phi_m^I$	ϕ_m^{II}
calculate:	$\Delta\mu_m^{total,I}$ $\Delta\mu_{lc}^{total,I}$	$\Delta\mu_m^{total,II}$ $\Delta\mu_{lc}^{total,II}$
check:	$\Delta\mu_m^{total,I} = \Delta\mu_m^{total,II}$	$\Delta\mu_{lc}^{total,I} = \Delta\mu_{lc}^{total,II}$
at PS:	$\phi_{lc}^I \phi_m^I \phi_p^I$	$\phi_{lc}^{II} \phi_m^{II}$

Phase I consists of polymer, monomer and liquid crystal, which gives three volume fractions to vary. Since the sum $\phi_p^I + \phi_m^I + \phi_{lc}^I = 1$, one parameter cancels. Two parameters need to be varied to obtain all possible compositions of the three-component phase. The liquid crystal volume fraction and the conversion were selected arbitrarily to do this. For phase II, the same line of reasoning leaves one variable volume fraction, ϕ_{lc}^{II} .

For every possible combination of ϕ_{lc}^I , α and ϕ_{lc}^{II} , the chemical potentials of monomer and liquid crystal in both phases ($\Delta\mu_{lc}^I, \Delta\mu_{lc}^{II}$, $\Delta\mu_m^I$ and $\Delta\mu_m^{II}$) are calculated separately. Next, the condition for phase separation, $\Delta\mu_i^I = \Delta\mu_i^{II}$ is verified. The combinations of ϕ_p^I , ϕ_m^I and ϕ_{lc}^I that satisfy the conditions $\Delta\mu_{lc}^I = \Delta\mu_{lc}^{II}$ and $\Delta\mu_m^I = \Delta\mu_m^{II}$ are the points in the conversion-phase diagram where the two phases can coexist. The composition of phase I at phase separation is equal to the overall composition of the system, since at the moment of phase separation, the volume of phase II is infinitesimal. A summary of the procedure is depicted in table 2.1.

2.5.3 Procedure for obtaining reaction-diffusion line

A reaction-diffusion model developed by Leewis *et al.*^{37,38} simulates the diffusion behavior of two reactive monomers with different reactivity in samples prepared by mask illumination. We have modified the reaction-diffusion model to apply for stratification processes.

In Leewis' reaction-diffusion model a step in the reaction is assumed to give only a small distortion of the equilibrium, which justifies a thermodynamic treatment. The mask illumination pattern is divided into discrete steps. In each reaction step, a small volume of polymer is formed, depending on the intensity and the monomer concentration in the segment. This causes an inequality in the chemical potential between segments. Chemical potential gradients are the driving force for diffusion. The discretized diffusion equation gives the change in concentration due to diffusion between segments. After this diffusion step, new volume fractions per segment are obtained. Hereafter, a new reaction step can be performed.

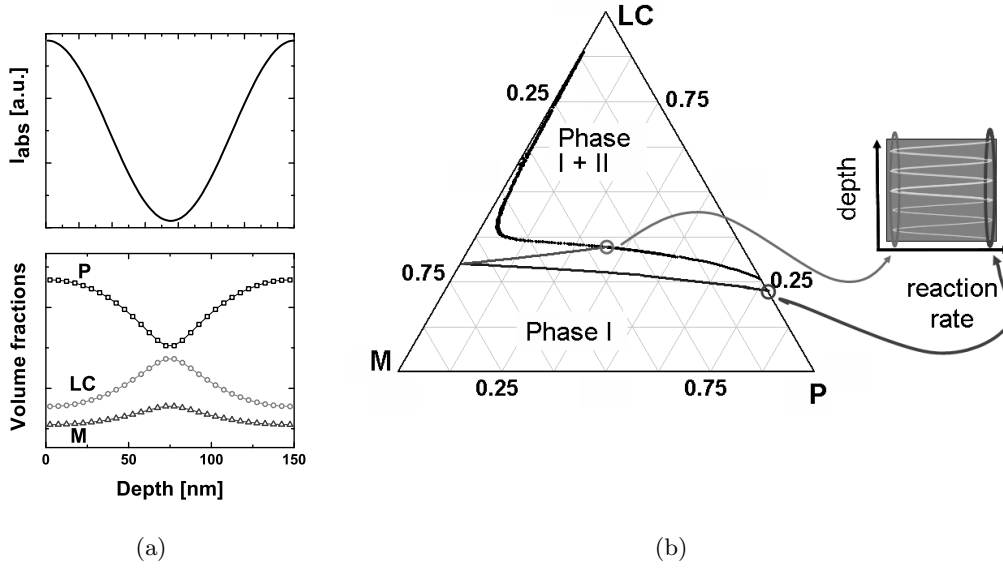


Figure 2.4: (a) Typical reaction-diffusion behavior for polymerization with a periodic modulating intensity gradient in depth. (b) High and low intensity reaction-diffusion lines of a typical holography sample.

Although this is already a very comprehensive model, polymerizations of mixtures containing both reactive and non-reactive components demand some subtle modifications.

The chemical potentials are adapted to the system of interest. Isotropic mixing, network elasticity and nematic ordering are incorporated in the chemical potentials used in the diffusion equation. Diffusion due to surface tension is omitted, since the samples prepared do not hold open surfaces.

Next, the polymerization kinetics is modified to adapt to holographic intensity profiles in depth of the sample. The polymerization rate predicts the decrease in reacted double bonds per time unit:

$$-\frac{d[C=C]}{dt} = R_p = \frac{k_p}{\sqrt{k_t}} \left(1 - \frac{\alpha}{\alpha_{max}} \right) \sqrt{\Phi_{In} I_a(z)} [C=C] \quad (2.75)$$

The diffusion behavior will be plotted in two different ways. Concentration as a function of depth will be used to visualize the in-depth profile of all volume fractions (figure 2.4(a)), and conversion-phase diagrams will be used to visualize the diffusion behavior of the components in a sample during ongoing polymerization. At every depth, the compositions are calculated by the simulation program, each composition is represented by a point in the conversion-phase diagram. Plotting all compositions of one specific depth in time gives a line in the diagram. This line will henceforth be called the reaction-diffusion line.

Figure 2.4(b) illustrates the reaction diffusion line in a ternary phase diagram for a stratified sample. For two specific points in depth, at maximum and mini-

mum intensity, reaction-diffusion lines are plotted in the ternary conversion-phase diagram. If no diffusion would occur, the lines would be horizontal (as shown in figure 2.3). Due to the faster depletion of monomers at the point of high intensity the reaction-diffusion line bends slightly downward due to diffusion of monomer to the reactive sites, which gives a higher concentration of polymer at the higher intensity side. The low intensity point shows more diffusion, the diffusion coefficient decreases less due to the less dense polymer network and larger material transport can take place. The diagram in figure 2.4(b) represents an idealized situation, and is therefore only meant to illustrate the reaction-diffusion behavior.

2.6 Holographic reflection gratings

Reflection holograms have periodic layers of materials in depth of the sample. The gratings are recorded in photosensitive material by two coherent laser beams, represented by the electric field vectors \mathbf{E}_1 and \mathbf{E}_2 (with the propagating wave vectors \mathbf{k}_1 and \mathbf{k}_2). At the intersection of the two beams, an interference pattern with dark and bright fringes (low respectively high intensity) appears. The intensity profile of the interference pattern can be obtained from the electric field vectors^{39,40} (figure 2.5(a)).

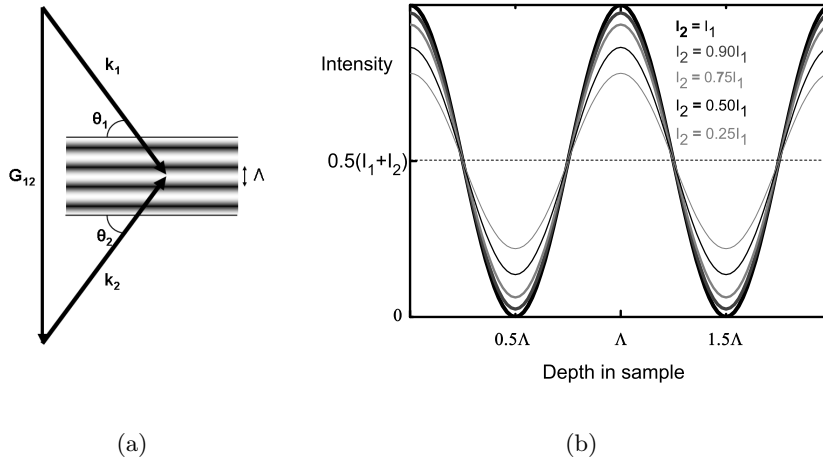


Figure 2.5: (a) Coherent laser beams with propagation vectors \mathbf{k}_1 and \mathbf{k}_2 interfere with Λ spacing between the fringes. The grating vector, \mathbf{G}_{12} , is defined as $\mathbf{k}_1 - \mathbf{k}_2$. (b) Interference profile of two coherent and plane laser beams with grating spacing Λ . When the intensity of the two beams are equal ($I_2 = I_1$) the dark fringes (at 0.5Λ) have zero intensity. With unequal intensities ($I_2 = 0.9I_1, 0.7I_1, 0.5I_1, 0.3I_1$) the "dark" fringes are not completely dark, but carry light intensity. Then polymerization is possible also in the (semi) dark fringes.

$$\mathbf{I} = \mathbf{E}_1^2 + \mathbf{E}_2^2 + 2\mathbf{E}_1\mathbf{E}_2 \cdot \cos[(\mathbf{k}_1 - \mathbf{k}_2) \cdot \mathbf{z}] \quad (2.76)$$

$$\mathbf{E}_1 = \mathbf{A}_1 \cos(\mathbf{k}_1 \cdot \mathbf{z}) \quad (2.77)$$

$$\mathbf{E}_2 = \mathbf{A}_2 \cos(\mathbf{k}_2 \cdot \mathbf{z}) \quad (2.78)$$

where \mathbf{A}_i is the amplitude of \mathbf{E}_i . $(\mathbf{k}_1 - \mathbf{k}_2)$ determines the fringe spacing, or the grating periodicity, (Λ) and is generally denoted as the grating vector ($\mathbf{G}_{12} = -\mathbf{G}_{21}$)^{41,42} with length: $|\mathbf{G}_{12}| = 2\pi/\Lambda$. According to Bragg's law, the expression for Λ is

$$\Lambda = \frac{\lambda_{rec}}{\sin \theta_1 + \sin \theta_2} \quad (2.79)$$

where λ_{rec} is the wavelength of the laser beams in the recording medium. θ_1 and θ_2 are the angles of incidence of the interfering laser beams to the sample plane, as defined in figure 2.5(a). For $\theta_1 = \theta_2 = \theta$ and $\lambda_{rec} = \lambda_{laser}/\bar{n}$ with \bar{n} the average refractive index of the recording medium, the grating period becomes

$$\Lambda = \frac{\lambda_{laser}}{2\bar{n} \sin \theta} \quad (2.80)$$

When the angle of incidence is perpendicular to the sample plane ($\theta = 90^\circ$) the interference spacing is $\lambda_{laser}/2\bar{n}$. For very small angles: $\theta \rightarrow 0$ and $\Lambda \rightarrow \infty$.

The holographic interference profile is generally given as⁴

$$I(z) = I_0(1 + V \cdot \cos[|\mathbf{G}_{12}| \cdot z]) \quad (2.81)$$

where $I_0 = I_1 + I_2$, and V is the fringe contrast. If the two laser beams have equal intensity $I_1 = I_2$, the fringe contrast becomes unity:

$$V = \frac{2\sqrt{I_1 I_2}}{I_1 + I_2} = \frac{2I_1}{2I_1} = 1 \quad (2.82)$$

If the intensities of the beams differ, there will not be any completely dark fringes with zero intensity, as is seen in figure 2.5(b).

In the reaction-diffusion model, the intensity profile is generated by inserting equation 2.81 in 2.48, and the depth profile of the absorbed intensity, I_a , becomes:

$$I_a = \int_0^z 2.3(I_1 + I_2) \left(1 + V \cos \left[\frac{4\pi\bar{n} \sin \theta}{\lambda_{laser}} z \right] \right) \epsilon_{In}[In]z dz \quad (2.83)$$

Holographic polymer dispersed liquid crystal reflection gratings

Using an isotropic mixture of LCs and monomers as the holographic recording material, holographic polymer dispersed liquid crystals (H-PDLCs) are obtained. The interfering laser beams record an intensity profile in depth of the mixture. The intensity profile initiates the polymerization of the monomers resulting in periodic layers of polymer and phase separated LCs. Having different refractive indices of the layers, certain wavelengths of light are not allowed to propagate through the film, but are reflected. Reconstructing the reflection hologram involves reflection of wavelengths fulfilling the Bragg criterium:

$$\lambda_{ref} = 2\bar{n}\Lambda \sin \beta \quad (2.84)$$

where β is the angle of the incident light reconstructing the hologram.

2.7 Experimental

2.7.1 Stratified gratings by laser beam holography

The holographic Bragg gratings were prepared from a mixture of monomers and nematic liquid crystals (E7, Merck). The monomers consisted of a blend in which 67 weight% were dipentaerythritolhydroxy pentacrylate (DPHPA, Polysciences Inc.), 15 weight% N-vinyl-2-pyrrolidone (NVP, Aldrich) and 18 weight% hexafluoro bisphenol A diacrylate (6F-bisA, Polysciences Inc.), figure 2.6. Since the monomers have different functionalities, respectively 5, 1 and 2 acrylate bonds, the average functionality was estimated to 3.6 acrylate bonds per molecule ($f = 7.2$) and the average molecular weight to 448 g/mole. One weight% of the UV-sensitive photoinitiator Irgacure 369 (IRG 369, Ciba) was added to the mixture. Structure formulas and molecular weights of the components are summed up in table 2.2.

Reflection gratings were recorded with the interference pattern of an Ar⁺ ion continuous wave laser at a wavelength 351 nm (Spectra Physics Beamlock 2085-25S). The experimental set up is presented in figure 2.7.

A time-controlled shutter (s), placed directly after the UV-laser is used to control the exposure time. The UV-beam is focused by a focusing stage consisting of a UV-lens (f1) and an aperture (a) followed by another UV-lens (f2). A linear polarizer (p1) is used as a filter to reduce the intensity of the beam. A UV mirror (r1) is used to guide the beam after which it passes a half-wave plate ($\lambda/2$) and polarizer (p2) to polarize the laser beam horizontally, in the plane of the sample. Hereafter the beam is guided to the sample surface, on which the beam spot has a diameter of approximately 1.5 cm.

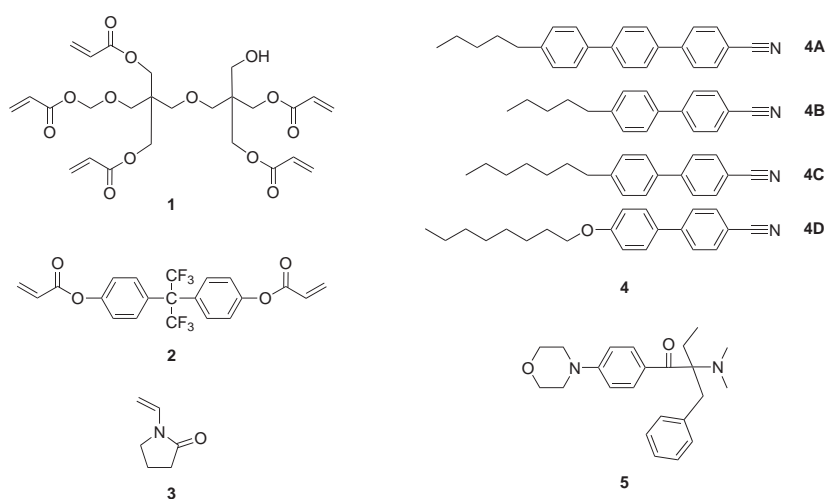


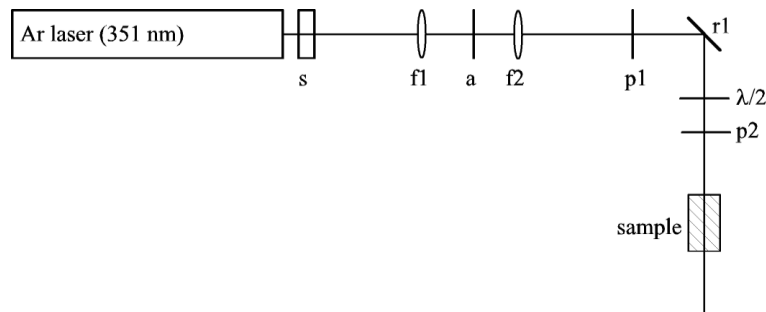
Figure 2.6: Molecular structures of **1**: dipentaerythritolhydroxy pentacrylate (DPHPA), **2**: hexafluoro bisphenol A diacrylate (6F-bisA), **3**: N-vinyl pyrrolidone (NVP), **4**: E7, components (composition of E7 mix⁴³: 8% (**4A**), 51% (**4B**), 16% (**4C**) and 25% (**4D**)), **5**: Irgacure 369.

Table 2.2: Chemical properties of the H-PDLC compounds.

Compound	Empirical formula	Molecular weight [g/mol]
E7(1)	$C_{24}H_{23}N$	325.45
E7(2)	$C_{18}H_{19}N$	249.35
E7(3)	$C_{31}H_{25}NO$	307.43
E7(4)	$C_{20}H_{23}N$	277.40
DPHPA	$C_{25}H_{32}O_{12}$	524.51
HF-bisA	$C_{21}H_{14}F_6O_4$	444.32
NVP	C_6H_9NO	111.14
IRG369	$C_{23}H_{30}N_2O_2$	366.5

The reaction mixture was sandwiched between a Si wafer coated with 150nm Ag and a cover glass slide. The interference pattern was generated by the incoming and reflected laser beams (figure 2.8(a)). The loss of intensity of the reflected beam was measured by a power meter (Newport 1815-C) by letting the incoming laser beam reflect on a clean silver coated Si-wafer (without reaction mixture). The periodicity of the interference pattern and thus the grating pitch was controlled by the angle of incidence (θ) of the laser beam to the sample plane (figure 2.8(a)). For $\theta < 60^\circ$ we coupled the laser beam onto the sample with a prism, using cyclohexane as contact liquid to reduce losses from total internal reflection (figure 2.8(b)). The intensity of the incoming laser beam (I_1) and the illumination time were varied between 0.1-4.5mWcm⁻² and 10-60s. After the holographic recording, the samples were flood exposed by non-coherent UV-light (0.3 mW cm⁻², Philips Cleo 15W) for 20 min in order to fix the grating.

The layer periodicity, Λ , was analyzed by scanning electron microscopy (SEM, XL 30 ESEM-FEG, Philips) on the cross section of the holographic sample. Thereto the samples were broken in liquid nitrogen, followed by removal of the liquid crystal at the cross section by washing with methanol. Prior to the SEM analysis, a conducting layer of 15nm gold was sputter coated (K575 XD Turbo sputter coater, Emitech, Ltd.) on the remaining polymer layers of the cross section.

**Figure 2.7:** Schematic representation of the laser setup, top view. (Image kindly provided by An Prenen).

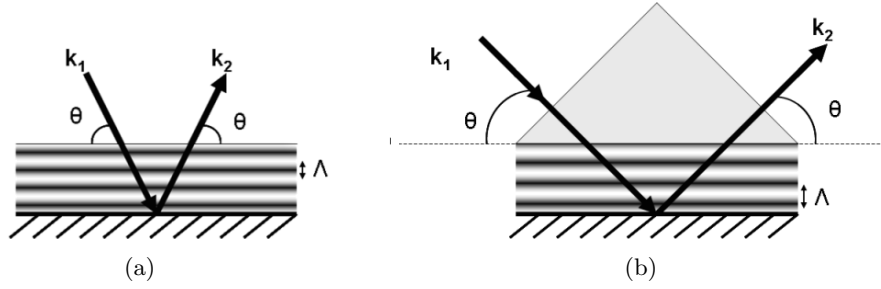


Figure 2.8: (a) Laser beam 1 reflects at the mirror, and produces an interference pattern with the reflected beam 2. (b) To couple in beams at an angle $\theta < 60^\circ$, a prism is necessary.

The wavelength of the reflected light from the H-PDLC reflection grating was measured by a UV-vis scanning spectrophotometer (Shimadzu UV-3102PC equipped with MPC-3100). The transmission as a function of wavelength was measured at normal incidence. The loss in transmission describes reflection from the film for wavelengths that are not absorbed by the sample itself (or its supporting glass plates).

2.7.2 Monomer conversions

Monomer and double bond conversions are determined for homogenous polymerization of different concentrations of for which the heat release during reaction is followed in time. This is done for reaction mixtures with different LC concentrations in order to simulate all possible concentrations in stratified gratings.

Differential scanning calorimetry (DSC) is a thermoanalytical technique in which the difference in heat release of the polymerizing sample and the reference (empty sample pan) is measured as a function of time and under isothermal conditions. Assuming that the heat capacity of the sample remains constant, the heat flow is directly related to the double-bond conversion. By observing the difference in heat flow between the sample and reference, differential scanning calorimeters measure the amount of energy released during polymerization, and the reaction heat flow during photopolymerization as a function of time, at a constant temperature, is measured.

$$\frac{dH}{dt} = V \Delta H_0 \frac{-d[C=C]}{dt} \quad (2.85)$$

Here ΔH_0 is the apparent heat per double-bond (78 kJ/mol for acrylates⁴⁴), and V the reaction volume. From the area, A , under the DSC curve, the reacted number of $C=C$ bonds can be determined.

$$A(t) = \int_0^t \frac{dH}{dt'}(t') dt' \quad (2.86)$$

The unreacted double bond concentration $[C=C]$ is given by:

$$[C=C] = [C=C]_0 - \frac{A}{V \Delta H_0} = [C=C]_0 - \frac{A}{\Delta H_0} \frac{\rho}{m} \quad (2.87)$$

with $[C=C]_0$ the initial double bond concentration, ρ the density and m the mass of the sample.

Double bond conversions were measured using a Perkin Elmer Photo-DSC 7 (Wellesley), under nitrogen atmosphere to prevent oxygen inhibition of the initiation. The samples were photopolymerized in the DSC with a UV-source (300-400 nm) with a maximum intensity at a wavelength of 365 nm (Philips TL08, 4W). Between the sample and the light source a shutter was placed. The samples were allowed for 5 minutes to obtain a thermal equilibrium before the shutter opened and started the polymerization. During 10 minutes the shutter was open to polymerize the sample and the differential heat flow rate to keep both samples at the same temperature was measured. Upon phase separation, a sample that initially was transparent became opaque due to the formation of liquid crystal droplets in the polymer matrix. A microscope (Leica Z16, Leica microsystems AG) with camera (Sony DFW-X700, Sony) was installed to determine at which time after the shutter was opened the sample became turbid.

After the polymerization, the measurement was continued in dark for another 5 minutes to allow any possible "dark-polymerization", which generally continues until the sample reaches equilibrium with (nearly) the same heat flow as before the reaction.

Since heat transfer has a finite rate, the DSC apparatus has a limited detection speed. If double bond conversion is too fast, the double bond conversion at a certain time will be underestimated. Therefore the reaction rate was lowered by decreasing the light intensity. The intensity of 0.017 mW cm^{-2} was achieved by using a pinhole and a filter in front of the 0.18 mW cm^{-2} UV-source.

DSC heat flows were measured for different ratios (30, 32, 36, 40, 50, 60, 80 weight%) LC in the monomer blend (composition of the monomer blend is described in the previous section). Photoinitiator concentration was 1 weight% for all DSC samples. The sample and reference pan were kept at constant temperature during measurement.

After the DSC measurement the sample pan with the polymerized films were weighted. Next, the LCs and unreacted monomers were removed from the polymer film by solvent extraction. Four solvents were used: methanol, cyclohexane and toluene (Biosolve) and tetrahydrofuran (THF, Normapur, VWR). The samples and pans were kept in the solvent between 1 min to 5 weeks. Thereafter the solvents were evaporated at a temperature above the transition temperature of the LCs, followed by weighting the dry polymer films and the DSC pan. The soaking and drying steps were repeated until the weight of the dry films was constant. The difference in weight before the first and after the last wash represents the weight of the LCs and unreacted monomer.

2.7.3 Constants for polymerization kinetics

The holographic interference pattern (equation 2.81) generates a gradient in polymerization kinetics, expressed as $R_p(z)$ in depth (z) of the reaction mixture.

$$R_p(z) = \frac{k_p}{\sqrt{k_t}} \sqrt{2.3 \cdot \Phi_{In} I_a(z) \epsilon_{In} [In] \Delta z \cdot [C=C]} \quad (2.88)$$

$$I_a(z) = (I_1 + I_2) \left(1 + V \cos \left(\frac{2\pi}{\Lambda} z \right) \right) \quad (2.89)$$

where I_1 and I_2 are the intensities in *Einstein* $\cdot l^{-1} s^{-1}$ of the interfering beams. Generally light intensities are measured as power per cross section: $mW cm^{-2}$. Converting the intensity ($mW cm^{-2}$) to Einstein per volume is done by first dividing the intensity by the thickness of the depth of interest (Δz) to get the irradiating power per volume. Secondly, the power per volume is divided by the energy of one mole photons of the irradiating wavelength. One mole photons has the energy

$$E_{photon} = \hbar N_A \frac{c}{\lambda_{photon}} \quad (2.90)$$

where \hbar is Planck's constant ($= 6.626 \cdot 10^{-34}$ Js), N_A Avogadro's constant ($= 6.023 \cdot 10^{23}$ mole $^{-1}$) and c the speed of light ($= 3 \cdot 10^8$ ms^{-1}). λ_{photon} is the wavelength of the photon. One mole of photons with wavelength of 351 nm, has an energy of 340 kEinstein ($= 340$ $kJ mole^{-1}$). The thickness of the simulated volume (Δz) is set in the reaction-diffusion model as a fraction of the grating pitch (Λ).

Polymerization rate constants are dependent on the functionality of the monomers. In general the initial rate increases with increasing functionality and auto acceleration is reached earlier with high functional monomers. For bulk-polymerization of DHPA monomers (nr 1 in figure 2.6) with $f = 10$, the rate constant $k_p/\sqrt{k_t}$ was determined to 0.7 ($l \cdot mole^{-1} s^{-1}$) $^{0.5}$ by Anseth *et al.*³⁵. They have also determined the rate constants for tetra-, tri- and di-acrylates to 1.8, 0.6 and 1.1 ($l \cdot mole^{-1} s^{-1}$) $^{0.5}$. It is surprising to see that the rate constants do not increased with decreasing functionality. However, the rate constants for tri- and di-acrylates are rather low; other sources report^{30,33} higher rate constants for diacrylates $k_p/\sqrt{k_t} = 13-30$ ($l \cdot mole^{-1} s^{-1}$) $^{0.5}$. Rate constants for other tetra-acrylate monomers have been measured by Selli *et al.*³⁰ to $k_p/\sqrt{k_t} = 0.4$ ($l \cdot mole^{-1} s^{-1}$) $^{0.5}$. For our holographic reaction mixture with high monomer functionality (in average 3.8 acrylate bonds per monomer), we predict $k_p/\sqrt{k_t} = 1$ ($l \cdot mol^{-1} s^{-1}$) $^{0.5}$.

The extinction coefficient of the photoinitiator (IRG 369) was found to be 4555 $l \cdot mol^{-1} cm^{-1}$ at 363 nm⁴⁵, and 17000 $l \cdot mole^{-1} cm^{-1}$ at 313 nm⁴⁶. Since the extinction coefficient is wavelength dependent, we estimated ϵ_{351} using ϵ_{363} , ϵ_{313} and information from Ciba⁴⁷ to 14000 $l \cdot mole^{-1} s^{-1}$.

Reported values of the quantum efficiency of the photo initiator IRG651 (from Ciba)^{8,48,49} are $\Phi = 0.4-0.7$. The photoinitiator used for the holographic exposures (IRG369, Ciba) has, what we know of, no reported values of its quantum efficiency. We assume its value being similar to that of IRG651, and use $\Phi_{In} = 0.5$ in the simulation model.

2.7.4 Diffusion constants

The initial diffusion coefficients of monomers and liquid crystals in the reaction mixture are estimated from values reported in literature. Monomers have in general diffusion coefficients^{8,38,50} in the order of $10^{-10} \text{ m}^2\text{s}^{-1}$. The values for LCs are reported similar to that of monomers⁴, $10^{-10} \text{ m}^2\text{s}^{-1}$, however diffusion perpendicular to the director is less than parallel²⁸. Since the holographic reaction mixtures are isotropic, the LCs are assumed to have the same diffusion behavior in all directions. Values for the initial diffusion coefficients (before polymerization) were chosen to: $D_m = 10^{-10} \text{ m}^2\text{s}^{-1}$ and $D_{lc} = D_m$.

Since the diffusion of the monomer is assumed to be dominant and determine that of the liquid crystals, only the monomer diffusion coefficients are used in the model.

The values for the constants (K_1 and K_2) in the expression describing the decrease in diffusion during polymerization (equation 4.3) have been estimated by measurements^{8,38} to

$$\begin{aligned} K_1 &= 0.21 \text{ to } 0.35 \\ K_2 &= 0 \end{aligned}$$

2.8 Results and discussion

2.8.1 Holographic reflection gratings

The stratified gratings were polymerized with a periodic intensity profile in depth from the holographic interference pattern (as shown in figure 2.8(a)). When the interference pattern is perfect, the dark fringes are dark (no light intensity). This generates the largest possible difference in monomer conversion between the bright and dark fringes. A local large compositional difference also means a large driving force for diffusion, which is preferable for creating well defined LC and polymer layers. However, the reflection is not perfect. Due to absorption at the silver mirror, the reflected beam is less intense (absorption of the monomers and LCs is neglected). The intensity loss was measured to $(54 \pm 8)\%$ after reflection. Using equation 2.82 the fringe contrast became $V = 0.93 \pm 0.04$. Due to the intensity difference between the interfering laser beams, polymerization was allowed in the low intensity regions.

Holograms were recorded with $I_0 = 0.10\text{-}4.5 \text{ mWcm}^{-2}$ during 10-60 s. With lower intensities unstructured PDLCs were obtained with large droplets of LCs scattering light in all directions. For higher intensities the holograms were transparent due to fast polymerization rate only allowing phase separated LC droplets smaller than the wavelengths of visible light. Holographic recordings in reaction mixtures with LC concentration > 40 weight% resulted in white scattering films with randomly spread phase separated LC droplets. Recordings in mixtures with lower LC concentrations (< 20 weight%) did not show phase separation and the films were

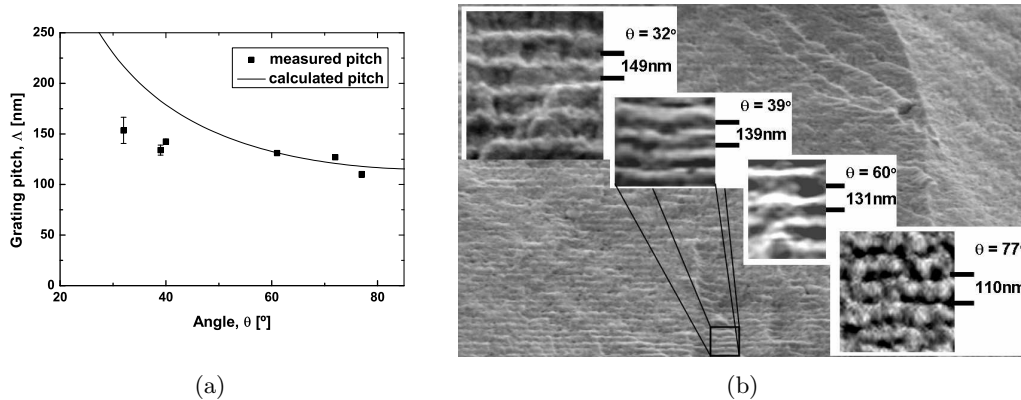


Figure 2.9: (a) Measured grating pitches versus incident angle (θ) of laser beams. (b) SEM images of cross-sections of gratings recorded with decreased fringe spacing of the interference patterns from right top to left bottom. All gratings were recorded at room temperature in a reaction mixture with 30 weight% E7.

transparent. Reflection gratings were recorded in reaction mixtures containing 30 weight% LCs.

Reflection gratings were recorded in a reaction mixture of 30 weight% E7, 69 weight% monomer blend (for composition see experimental section 2.7.1) and 1 weight% photoinitiator (IRG 369). The gratings were recorded with layer pitches of 110-164 nm, which were measured by SEM (figure 2.9(b)). The experimentally measured layer pitches for the smaller θ were in general smaller (ca 20%) than the theoretical calculated ones (using the incident angle of the interfering laser beams). Polymerization shrinkage, sample deformation during cleavage for SEM analysis, and estimated collapse of the morphology after the removal of the LCs and unreacted monomers explain the deviations (figure 2.9(a)).

The grating pitch (Λ) can also be determined from the reflected wavelength (λ_{ref}) as long as sufficient refractive index contrast between the polymer and LC layers is present (equation 2.84). Unfortunately the refractive index was relatively low and the gratings appeared transparent. However, by extracting the LCs from the gratings and replacing with air or solvent, the optical properties of the films change. The LCs were extracted by solvent; and gratings recorded by $\theta = 32^\circ$ (top left grating in figure 2.9(b)) reflected green light when swollen in methanol (figure 2.10). After having evaporated the methanol, the dry grating reflected blue light (figure 2.10). The average refractive index of the isotropic reaction mixture of 30 weight% LCs was measured by an Abbe refractometer at 589 nm wavelength to 1.52. With a rough estimation the average refractive index of the methanol swollen film to $n_{average} = 1.5$, the grating pitch was calculated to 170 nm, almost 20 nm larger than measured by SEM. As was suggested before, the differences in the measured pitches are due to pitch deformation during sample preparation for SEM analysis and/or collapsed layers after LC removal.

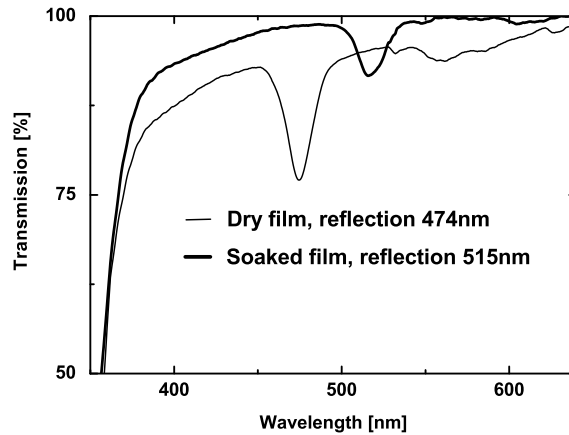


Figure 2.10: Reflection of grating where the LCs are removed. Thin line: grating where LCs are replaced by air. Bold line: grating swollen with methanol. The reflection grating was made from reaction mix of 30 weight% E7, laser intensity of the incoming beam (I_1) 1.7 mWcm^{-2} , 30 s exposure at RT. (Identical results for 60s holographic exposure).

2.8.2 Monomer conversion versus double bond conversion

In this paragraph we determine the maximum double bond conversion (x_{max}) and the corresponding maximum monomer conversion (α_{max}). Effects on the polymerization rate such as reaction mixture concentration, temperature, vitrification and intensity, are investigated and discussed. Double bond conversions at phase separation were measured, and an experimental phase separation line is proposed.

The double bond conversions during polymerization of several mixtures with different LC-monomer concentrations were measured with DSC. Reaction mixtures with low LC concentrations converted more double bonds per unit time during the polymerization, this is seen in the measured heat flows during the polymerization (figure 2.11). All samples showed a rapid increase in heat flow during the first seconds of illumination, this is caused by the Trommsdorff effect and is characteristic for cross-linking polymerization³¹. Since the Trommsdorff effect was present immediately, the kinetic constants (as $k_p/\sqrt{k_t}$) could not be determined from the DSC measurements. After 600 s of light exposure, the shutter closed and heat flow during dark polymerization was measured. Hardly any additional double bond conversions were detected; indicating that the polymer films were cross-linked and the mobility in the network was low.

During the polymerization of the DSC samples phase separation occurred, the compositions in the two phases are different which induce local polymerization rates. The maximum double bond conversion (x_{max}) after 600 s illumination ranged from 0.25-0.36 which is higher than reported values for bulk polymerization at room temperature³⁵. The two phases and the plasticizing effect of the LCs are probably the cause. Increasing the polymerization temperature, The end conversion increased

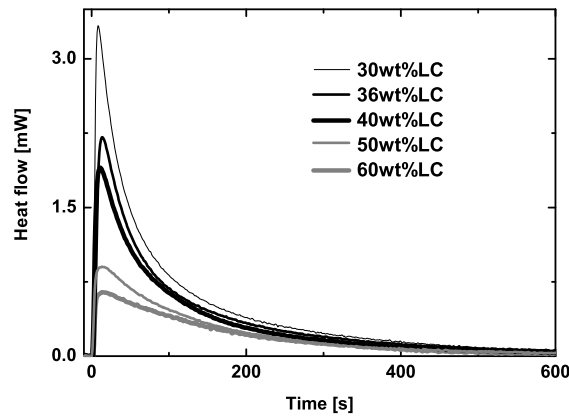
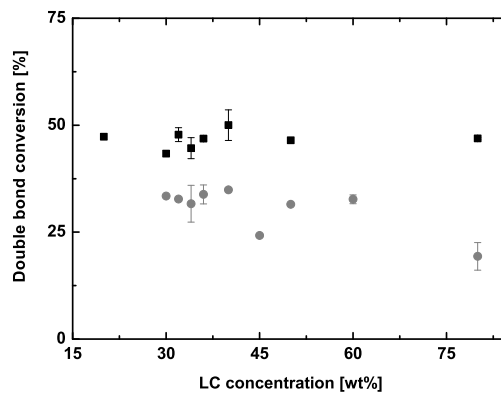


Figure 2.11: Heat flows measured by differential scanning calorimetry during photopolymerization. The heat flows for five different compositions are plotted, highest peak has the mixture of 30 weight% LCs followed by 36, 40, 50, 60 weight% LCs.

with higher polymerization temperature or higher curing light intensity (figure 2.12), which was expected^{30,35,46,51}.

The maximum monomer conversions were experimentally determined by washing out the LCs and the unreacted monomers from the polymer film. Table 2.3

LC [weight%]	x [%]	T [°C]
30	33.4 ± 0.0	20
30	37.3 ± 0.3	65
30	39.2 ± 0.4	80



(a)

(b)

Figure 2.12: (a) Double bond conversions, x , at the end of DSC measurements at different polymerization temperatures. Illumination with 0.017 mWcm^{-2} UV light intensity. (b) Double bond conversions measured at the end of the DSC measurements during polymerization with 0.017 mWcm^{-2} and 0.18 mWcm^{-2} UV intensity at 20°C .

Table 2.3: The double bond conversion, x , is measured with DSC and is the end conversion after 10 min polymerization and 5 min dark polymerization. The experimental measured monomer conversions, α , were obtained from residue after washing out liquid components from the polymer. The solvents used were methanol (MeOH), cyclohexane (c-C₆H₁₂), tetrahydrofuran (THF) and toluene. For comparison the monomer conversions calculated by the mean field approximation (equation 2.57) with $f = 7.2$.

LC [weight%]	DSC x_{max} [%]	Exp. α_{max} [%]	$X_{C=C/M}$	solvent	MF approx. α_{max} [%]	f = 7.2 $X_{C=C/M}$
30	33.4	95.4	1.3	MeOH	76.9	1.6
34	25.3	89.6	1.1	THF	65.0	1.4
36	32.2	79.7	1.5	MeOH	75.3	1.5
36	31.3	97.3	1.2	c-C ₆ H ₁₂ MeOH c-C ₆ H ₁₂	74.1	1.5
40	35.5	90.8	1.5	MeOH	79.4	1.6
40	34.3	93.5	1.4	c-C ₆ H ₁₂ MeOH c-C ₆ H ₁₂	78.0	1.6
60	34.2	85.4	1.5	toluene	77.8	1.6

shows the results from the monomer conversion measurements compared with the DSC measured double bond conversions at the end of DSC measurements (after 10 minutes of polymerization plus 5 minutes of dark polymerization). The average number of reacted double bonds per monomer ($X_{C=C/M}$) was determined to 1.4 from the experimental values. This value can seem to be low for cross-linking polymerization, but was confirmed by the mean field approximation (MF) that computed an average of 1.6 double bonds reacted per monomer for the experimentally measured x_{max} (table 2.3). The mean field approximation estimates a lower monomer conversion than the one experimentally measured. Even though it can be discussed whether the mean field approximation predicts a correct monomer conversion (commonly it is assumed that MF underestimates α), there are two main reasons that the experimentally determined monomer conversions are overrated. First, the removal of unreacted monomers and LCs are hindered by the cross-linked polymer network. Secondly, is it possible that double bond reaction proceeds after the DSC measurements, which underestimates the true double bond conversion.

At the start of the polymerization it is reasonable to assume that all double bonds are equally reactive, as the mean field approximation predicts. Since the average number of double bonds reacted per monomer ($X_{C=C/M}$) for both the MF approximation and experimentally determined resemble, we choose to use the MF approximation to link α to x using equation 2.57.

Monomer conversions at phase separation

Phase separation is favored by the formation of polymer networks (as described in section 2.2.2), and was in the DSC detected almost instantaneously after the start

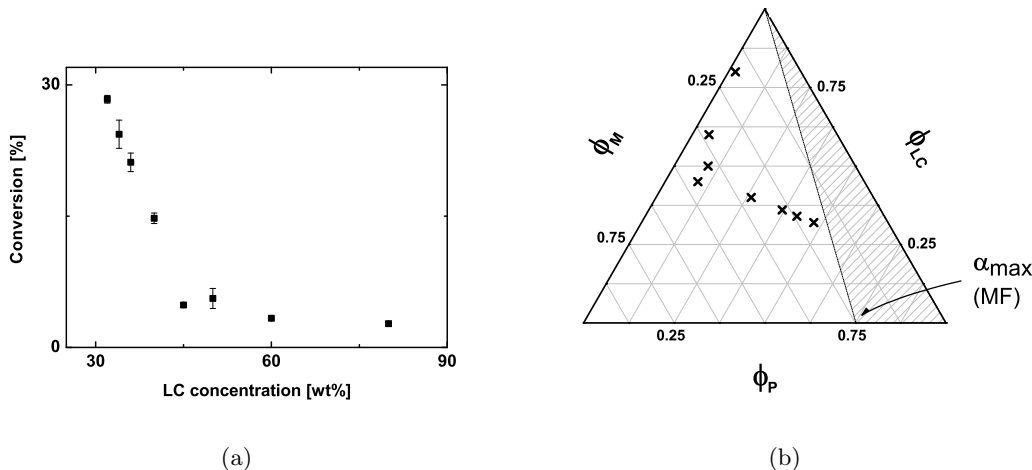


Figure 2.13: (a) Double bond conversion at phase separation measured by DSC when polymerizing with 0.017 mWcm^{-2} UV intensity. (b) Monomer, polymer and LC compositions at phase separation (\times) calculated from the measured double bond conversions using the mean field approximation. At $\alpha_{max} = 0.75$ the polymerization stops due to decreased mobility, as a result the compositions in the shaded area are never reached.

of the polymerization. Since fast polymerization rates are difficult to follow in the DSC, low curing intensity (0.017 mWcm^{-2}) was needed to enable accurate determination of the double bond conversion at phase separation. The onset of phase separation was determined visually in the optical microscope, coupled to the DSC, by noting the time at which the sample became turbid during polymerization. The double bond conversions at the moments of phase separation are plotted for reaction mixtures with different LC concentrations (figure 2.13(a)). Reaction mixtures with initial LC concentrations below 32 weight% LCs did not show phase separation during or after polymerization. If any phase separation actually occurred, the liquid droplets were smaller than the wavelengths of visible light. In figure 2.13(a) it is seen that phase separation occurs at lower x when more LC is present. Moreover, reaction mixtures with LC concentrations above 60 weight% phase separated rapidly after polymerization started. Due to difficulties visually determining phase separations at short reaction times in the microscope, combined with the limited accuracy of measurement rate of the DSC, the measurement points for the high LC concentrations have large error margins.

The experimentally measured double bond conversions at phase separation are converted to monomer conversions with equation 2.57 and plotted in the conversion phase diagram in figure 2.13(b). The polymer and monomer compositions, determined experimentally, have possible errors, while the liquid crystal content is certain

since it does not change during the (homogeneous) polymerization. Additionally, when the maximum monomer conversion ($\alpha_{max} = 0.75$, table 2.3) is reached, the polymerization reaction terminates (as discussed in section 2.3.1). Compositions with $\alpha > 0.75$ are not observed, and the compositions in the shaded triangle are never attained.

2.8.3 Cross-linking probability and efficiency

In order to predict the experimentally observed phase separation with our model the elasticity of a cross-linked network formed by multi-functional monomers has to be revisited. The elasticity of the network is one of the contributions to the Gibbs free energy (section 2.2.2) which we use to predict the compositions at phase separation. To simulate the network contribution an expression for m_c has to be established.

Before polymerization begins, there are y number of monomers (with functionality f) on which $0.5fy$ number of double bonds are available for reaction. When x double bonds and α monomers have been converted, αy double bonds are necessary to link the monomers to the polymer chains. The other double bonds, $0.5fxy - \alpha y$, are assumed to be involved in the cross-linking reaction. Consequently, the fraction of reacted double bonds that are cross-linked is $\frac{0.5fx - \alpha}{0.5fx}$.

During the polymerization densely cross-linked microgel particles containing polymer rings are likely to form. These do not contribute to the elastic network, and decrease the fraction of cross-links contributing to the elastic behavior of the network. Additionally, cross-linking polymerization does not necessarily produce a homogenous polymer network. Locally, highly cross-linked polymers can be surrounded with less densely cross-linked or even linear polymers, this effect has been suggested by simulations where non-homogenous cross-linked polymer networks were formed according to the percolation theory³⁴. In our model we insert an overall efficiency factor $\kappa(\alpha) \leq 1$, to account for the ineffective elastic network chains. We assume that the cross-linking efficiency increases linearly with the monomer conversion: $\kappa(\alpha) = C_{eff} \cdot \alpha$. Then the average chain length between cross-links (m_c) can be obtained with

$$m_c = \frac{\alpha}{\frac{0.5fx - \alpha}{0.5fx} \cdot \kappa(\alpha)} \quad (2.91)$$

The fraction of cross-links corresponds to the probability that a cross-link is formed ($P(cross)$). Logically, monomers with many double bonds (high functionality) have a larger probability to form cross-links than low functional monomers. This behavior is plotted in figure 2.14 using the mean field approximation introduced in the photopolymerization section 2.3.1. At a certain double bond conversion in figure 2.14 all monomers are converted and $P(cross)$ reaches one. Depending on the polymerization monomer functionality, this double bond conversion is equal to, or higher than, the double bond conversion necessary to create a linear polymer. At higher x the reacted double bonds are only involved in cross-linking and $P(cross) = 1$.

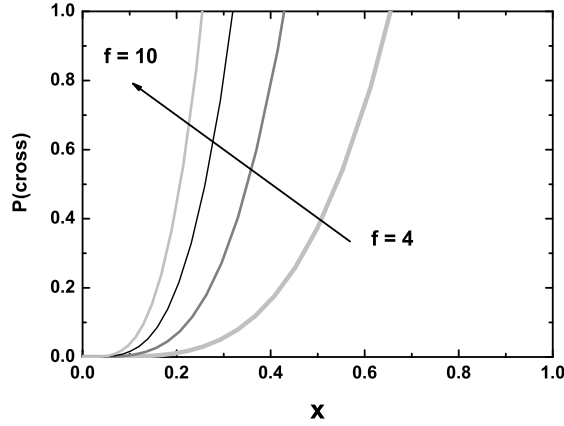


Figure 2.14: The cross-linking probability increases with the monomer functionality. At a certain double bond conversion (x) $P(\text{cross})$ reaches 1. For higher double bond conversions the cross-linking probability remains 1 since all monomers are converted. $C_{eff} = 0.5$. The mean field theory expresses the monomer conversion in double bond conversion.

The elastic contribution to the chemical potentials are equal for both the monomers and the LCs assuming that $N_m = N_{lc} = 1$. Inserting $\kappa(\alpha)$ and equation 2.91 into equations 2.22 and 2.23, the expression for the network contribution becomes

$$\frac{\Delta\mu_m^{el}}{k_B T} = \frac{\Delta\mu_{lc}^{el}}{k_B T} = \frac{1}{m_c} \left[1 - \frac{2}{f} \right] \phi_p = \kappa(\alpha) \frac{0.5fx - \alpha}{0.5fx \cdot \alpha} \left[1 - \frac{2}{f} \right] \phi_p \quad (2.92)$$

2.8.4 Weight of effects in the combined phase separation model

To evaluate the relative importance of the different terms in the expression of the chemical potential, the following situation is considered. Assume a theoretical sample that contains two phases with composition $\phi_{lc}^I = 0.3$, $\phi_m^I = 0.35$, $\phi_p^I = 0.35$ and $\phi_{lc}^{II} = 0.3$, $\phi_m^{II} = 0.70$. The polymer chains are assumed to be infinitely long, monomer and LC molecules are of the same size ($N_m = N_{lc} = 1$). With these assumptions, an estimate of the influence of variations in the different parameters on the numerical values of the chemical potentials has been studied.

Table 2.4: Magnitudes of the terms in the monomer and liquid crystal chemical potential for isotropic mixing.

m	phase I	phase II	lc	phase I	phase II
$\ln \phi_m$	-1.049	-0.350	$\ln \phi_{lc}$	-1.204	-1.204
χ -terms μ_m	0.045	0.045	χ -terms μ_{lc}	0.245	0.245
ϕ_p	0.350	-	ϕ_p	0.350	-
$\Delta\mu_m^M/(k_B T)$	-0.654	-0.305	$\Delta\mu_{lc}^M/(k_B T)$	-0.609	-0.959

Isotropic mixing

With the assumption that $\chi_{m-p} = 0$ and $\chi_{p-lc} = \chi_{m-lc} = 0.5$ the terms in the expression for the chemical potentials become:

$$\frac{\Delta\mu_m^M}{k_B T} = \ln \phi_m + \phi_p + \chi_{m-lc} \phi_{lc} (\phi_{lc} + \phi_p) - \chi_{p-lc} \phi_{lc} \phi_p \quad (2.93)$$

$$\frac{\Delta\mu_{lc}^M}{k_B T} = \ln \phi_{lc} + \phi_p + (\chi_{m-lc} \phi_m + \chi_{p-lc} \phi_p) (\phi_m + \phi_p) \quad (2.94)$$

Approximate values for the terms in 2.93 and 2.94 for phase I and II with a composition as described in the previous paragraph are shown in table 2.4.

The logarithmic term changes with composition, while the interaction terms remains constant. The latter is caused by the assumption that $\chi_{p-lc} = \chi_{m-lc} = 0.5$. Now the question is whether phase I and II can coexist as a consequence of isotropic mixing alone. The answer is negative since $\Delta\mu_m^I \neq \Delta\mu_m^{II}$ and $\Delta\mu_{lc}^I \neq \Delta\mu_{lc}^{II}$. In this specific case with $\phi_{lc}^I = 0.3$, $\phi_m^I = 0.35$, $\phi_p^I = 0.35$, for one component e.g. the liquid crystal, the chemical potential in the two phases can become equal, which appears when $\phi_{lc}^{II} = 0.47$. However, the chemical potential of the other component ($\phi_m^{II} = 0.53$) will never be equal in the two phases. The difference $\Delta\mu_m^I - \Delta\mu_m^{II}$ for the latter example ($\phi_m^{II} = 0.53$) is -0.073. No phase separation will be predicted by considering solely isotropic mixing for $\chi = 0.5$.

However for $\chi > 0.5$, the difference in chemical potentials $\Delta\mu^I - \Delta\mu^{II}$ can equal zero, but only for high liquid crystal contents. Additionally, an inequality of the interaction parameters between LC-monomer and LC-polymer also creates an additional contribution in the chemical potential. Even though this is a very small difference - in the order of $\Delta\mu_i^I - \Delta\mu_i^{II} = 0.01$ for $\chi_{m-lc} - \chi_{p-lc} = 0.1$ - it will give a small range of compositions in which the two phases can coexist. This will be elaborated further in section 2.8.5.

Network elasticity

The presence of the polymer network in phase I necessitates the addition of a network elasticity term to the chemical potential for that phase (equation 2.92). For the theoretical sample ($\phi_{lc}^I = 0.3$, $\phi_m^I = 0.35$, $\phi_p^I = 0.35$ and $\phi_{lc}^{II} = 0.3$, $\phi_m^{II} = 0.70$, $f = 7.2$, $\alpha = 0.5$, and $C_{eff} = 1$), its magnitude is 0.052, and it is linearly dependent on

the polymer volume fraction. Since no network is present in the second phase, the network elasticity term for phase II is 0. This induces a larger difference between the chemical potentials of the different phases, giving rise to a stronger driving force for phase separation. With decreasing polymer volume fraction of phase I, the isotropic mixing term increases, which compensates for the change in chemical potential due to network elasticity. Since this effect is a factor of 5 larger than the difference in interaction parameters will ever create (compared with the last example in the previous section), a possibility for coexistence of the two phases is expected in a large range of volume fractions.

Nematic ordering

For a liquid crystal content higher than the critical $\phi_{ni} = \frac{T}{T_{ni}}$ is ~ 0.89 for E7 at 20°C (from equation 2.38), the nematic ordering of the liquid crystal adds an extra term in the expression for the monomer and liquid crystal chemical potential. None of the two phases in the theoretical sample ($\phi_{lc}^I = 0.3$, $\phi_m^I = 0.35$, $\phi_p^I = 0.35$ and $\phi_{lc}^{II} = 0.3$, $\phi_m^{II} = 0.70$) has any contribution to the nematic ordering, since the volume fraction of LC is lower than the critical, ϕ_{ni} . For 91 volume% LCs, the nematic term for the monomer is 0.904, for the liquid crystal -0.166 (at 20°C, $T_{ni} = 58^\circ\text{C}$, using equations 2.41 and 2.40).

Again, this value is different for the two phases (since the volume fractions of LCs and monomers differ in phase I and II), therefore nematic ordering will influence the position of the phase separation line in the conversion-phase diagram. The nematic ordering only plays a role in a certain range of LC volume fractions, and the fact that network elasticity also induces phase separation, raises the idea that not a single phase separation line in the conversion-phase diagram exists, but several. This will be discussed further in the next section.

2.8.5 Simulation results: phase separation lines

In this paragraph the compositions at phase separation are studied and plotted in the ternary conversion phase diagram. The effects on the phase separation of the interaction parameter, network efficiency and nematic ordering will be discussed.

Interaction parameter: χ

The interaction parameter between two components denotes the gain in energy upon mixing of these components. Therefore, if $\chi_{ij} > \chi_{ik}$, the i-k mixing is the more stable one. Meaning that in a system containing components i,j and k, the contact between i and k is energetically more favorable than the contact between i and j. Consequently, different χ values between the components in a system could be the driving force for phase separation.

Since polymers and monomers consist of the same building blocks, the interaction parameter χ_{m-p} was assumed to be zero. However, the interactions between monomer-LC and polymer-LC were assigned non-zero χ values. Several models exist that describe the behavior of χ , as a function of composition and temperature⁵².

These will not be discussed in detail here. Generally values for the interaction parameter between polyacrylate chains and solvents are in the range of 0.4-0.6¹⁷.

It was evaluated whether phase separation is possible on the basis of differences in interactions between LC-monomer and LC-polymer, with the assumption that the LC-polymer interaction is weaker (larger χ) than that with the monomers (i.e. the LC gives preference to be near monomers). Since the difference in interaction parameters is expected to be very small, due to the similarity in size and functional groups of the monomers and the polymer-units, values of $\chi_{p-lc} = 0.55$ and $\chi_{m-lc} = 0.45$ were chosen. The resulting phase separation line is shown in figure 2.15(a). A phase separation line is observed, although in a very small volume fraction region with a high liquid crystal content.

Consequently, to simplify the interpretation of the conversion-phase diagrams, it is proposed that $\chi_{m-lc} = \chi_{p-lc} = \chi$. Chemical potentials are further simplified to:

$$\frac{\Delta\mu_m^M}{k_B T} = \ln \phi_m + \phi_p + \chi\phi_{lc}^2 \quad (2.95)$$

$$\frac{\Delta\mu_{lc}^M}{k_B T} = \ln \phi_{lc} + \phi_p + \chi(\phi_m + \phi_p)^2 \quad (2.96)$$

Using an interaction parameter of 0.5, no phase separation is predicted by the isotropic mixing described by Flory-Huggins. Increasing the value of χ , i.e. the interactions between the polymer-LC and monomer-LC are less favorable than the interactions between monomer-polymer, phase separation becomes possible (figure 2.15(b)). For $\chi = 0.55$ the phase separation line resembles that in figure 2.15(a). χ values much larger than 0.6 are not expected since the LCs and monomers used in this study are miscible.

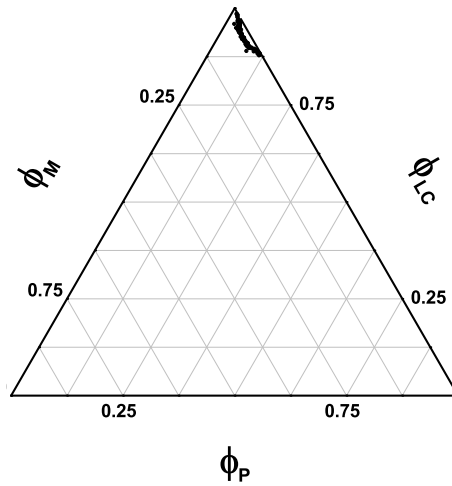
Network elasticity: $\kappa(\alpha)$

In the expression for the chemical potential due to cross-linked networks, an efficiency factor $\kappa(\alpha)(= C_{eff}\alpha)$ was introduced. This section gives an overview of the effects of an elastic network on phase separation. More substantially, variations of C_{eff} and χ are studied.

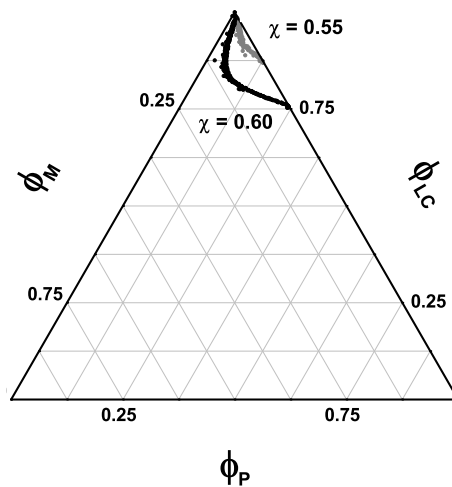
For $\chi = 0.5$, the efficiency term for cross-linked networks (C_{eff}) is varied, and its contribution is added to the Gibbs free energy (figure 2.16(a)). The elastic contribution induces the phase separation at lower liquid crystal contents than when only isotropic mixing is considered. At the intersection of the phase separation line with the ϕ_{lc} axis determines the solubility limit, a lower limit of ϕ_{lc} that will remain dissolved in the polymer network.

With decreased network strength (a lower C_{eff} value) the driving force for the phase separation is weaker. The solubility limit increases and a higher LC content is needed to obtain phase separation, which is plotted for $C_{eff} = 0.5$ in figure 2.16(a).

Next is the strength of the intermolecular interactions (χ) together with the network elasticity ($C_{eff} = 1$) examined and plotted in figure 2.16(b). When there is more interaction between LC-monomer and LC-polymer, the interaction parameter χ is lower and the phase separation line shifts upward. This signifies that for the



(a)



(b)

Figure 2.15: (a) Phase separation line with $\chi_{p-lc} = 0.55$ and $\chi_{m-lc} = 0.45$. Only at very high LC contents phase separation can occur due to a difference in interaction parameter between polymer-LC and monomer-LC contacts. (b) Phase separation line with $\chi = 0.55$ and 0.60 , when only isotropic mixing contributes to the phase separation. For $\chi < 0.5$ phase separation does not occur. The larger the χ value is, the less miscible are the liquid crystals in the polymer.

same LC content, phase separation occurs at higher conversions. For a lower value of χ , phase separation occurs later. This is plausible, since a stronger interaction is energetically more favorable. Accordingly, the system will remain in the well-mixed three-component phase up to a higher monomer conversion.

Nematic ordering

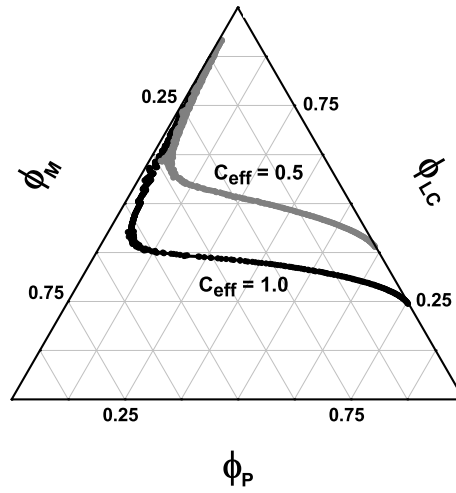
Below the nematic to isotropic transition temperature, a liquid crystal is in the ordered nematic phase. When nematic ordering is considered, together with the Flory-Huggins isotropic mixing and the network elasticity the contributions to the chemical potentials are:

$$\begin{aligned} \frac{\Delta\mu_m^M}{k_B T} + \frac{\Delta\mu_m^{el}}{k_B T} + \frac{\Delta\mu_m^N}{k_B T} \\ = \ln \phi_m + \phi_p + \chi\phi_{lc}^2 + \kappa(\alpha) \frac{0.5fx - \alpha}{0.5fx \cdot \alpha} \left[1 - \frac{2}{f} \right] \phi_p + \frac{1}{2} \nu \phi_{lc}^2 s^2 \\ \frac{\Delta\mu_{lc}^M}{k_B T} + \frac{\Delta\mu_{lc}^{el}}{k_B T} + \frac{\Delta\mu_{lc}^N}{k_B T} \\ = \ln \phi_{lc} + \phi_p + \chi(\phi_m + \phi_p)^2 + \kappa(\alpha) \frac{0.5fx - \alpha}{0.5fx \cdot \alpha} \left[1 - \frac{2}{f} \right] \phi_p - \ln Z + \frac{1}{2} \nu \phi_{lc}^2 s^2 \end{aligned}$$

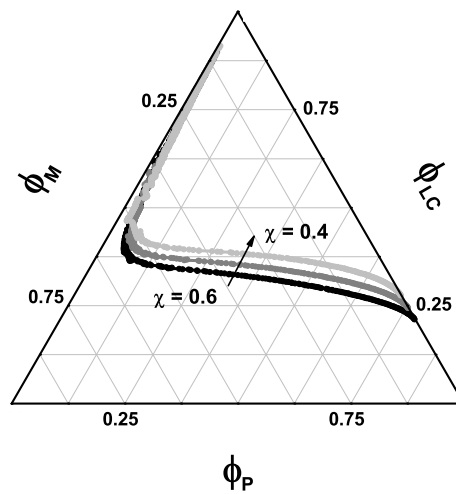
For temperatures above T_{ni} there is no contribution from the nematic ordering since the order parameter, s , is zero. For temperatures below the liquid crystal clearing temperature, a new and ordered phase appears (figure 2.17). Examining the compositions in the three separated areas of the diagram, it is found that the lower area (A) is the same phase I as before, consisting of polymers, monomers and liquid crystals. Area B is a two-phase area, containing phase I and phase II (monomers and LCs), with the liquid crystals in phase II in the isotropic phase. In area C another liquid phase, phase III, is apparent, which contains only monomers and LCs like phase II. However, the difference is that the LC volume fraction is high enough for the liquid phase to be in the nematic phase. For LC concentrations larger than ϕ_{ni} the phase is nematic.

Phase separation line for the holographic materials

Simulating the phase separation line for the holographic reaction mixture, two parameters (χ and C_{eff}) can be used to fit the curve to the experimentally measured phase separation line (figure 2.13(b)). As discussed earlier, there are experimental difficulties measuring double bond conversions at phase separation and correctly correlating it with the monomer conversions. Therefore only one experimentally measured composition can be used with confidence: That is the liquid crystal content at the intersection with the α_{max} line: $\phi_{lc} = 0.32$ (section 2.8.2). For $C_{eff} = 1$ and $\chi = 0.53$ the phase separation line crosses the α_{max} line at $\phi_{lc} = 0.32$ (figure 2.18).



(a)



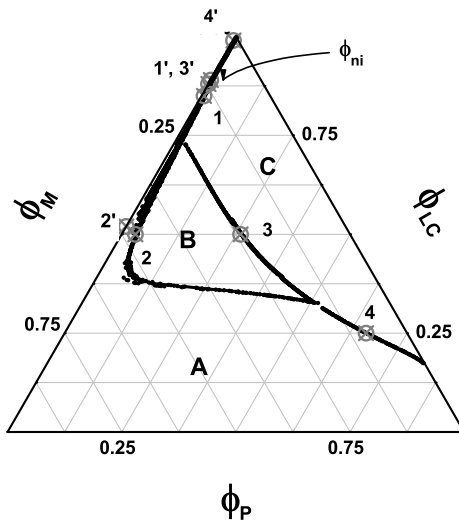
(b)

Figure 2.16: (a) Phase separation line, considering isotropic mixing ($\chi = 0.5$) and an elastic network, with elastic network efficiencies: $C_{eff} = 0.50$ and 1. (b) Shift of the phase separation line due to the interaction parameter $\chi = 0.4, 0.5$ and 0.6 . Contributions from isotropic mixing and elastic network, with $C_{eff} = 0.5$.

With $C_{eff} = 1$ the cross-linking probability becomes 1 for $x \geq 0.22$. Theoretically this indicates that cross-linking starts before all monomers are converted, which experimentally is realistic.

The interaction parameter χ was fitted to 0.53. Initially we expected the value of χ being lower than 0.5 based on the relatively similar chemical structures of the LCs and monomers and reported values in literature⁸. However, the different size and especially the bulkiness of the holographic monomers and the liquid crystals is expected to cause $\chi > 0.5$.

The nematic ordering induces a small range of compositions for which phase separation into a nematic phase is possible. The isotropic-nematic phase separation line is broken and does not enclose an area as was seen in figure 2.17. It seems plausible that complete isotropic-nematic phase separation lines only are possible below a certain temperature, which is supported with a higher contribution from the nematic ordering at lower temperatures. For our purposes the stratified PDLC grating requires nematic liquid crystals in the phase separated droplets. Therefore the holographic recording is proceeded with flood exposure converting the monomers



(a)

		Phase I	Phase II
1	ϕ_{lc}	0.85	0.89
	ϕ_m	0.145	0.11
	ϕ_p	0.005	-
2	ϕ_{lc}	0.50	0.52
	ϕ_m	0.47	0.48
	ϕ_p	0.03	-
3	ϕ_{lc}	0.50	0.89
	ϕ_m	0.24	0.11
	ϕ_p	0.26	-
4	ϕ_{lc}	0.25	0.99
	ϕ_m	0.09	0.01
	ϕ_p	0.66	-

(b)

Figure 2.17: (a) Phase separation behavior at $T = T_{ni} - 60$ K with isotropic mixing ($\chi = 0.5$), network elasticity ($C_{eff} = 1$) and nematic ordering contributing to the chemical potentials. At the critical composition ($\phi_{ni} = 0.89$) for nematic mixture of LCs and monomers, the phase separation line intersects the monomer-LC axis. Four compositions on the phase separation lines are chosen (1-4, \otimes) for which the corresponding compositions of the second phase are plotted on the M-LC axis (1'-4', \otimes). The compositions of the two phases are given in the table (b). When the liquid crystal content in phase II is larger than ϕ_{ni} ($= 0.89$), the phase separated liquid phase is nematic.

Table 2.5: Influence of isotropic mixing, network elasticity and nematic ordering on the diffusion of monomers and LCs.

effect	ϕ_p -dependence	ϕ_m -dependence	effect on M	effect on LC
mixing	linear	logarithmic	towards high	towards low
elasticity	linear	no	towards high	towards low
ordering	no	no	no	no

in the phase separated liquid phases leaving the LCs in nematic phase.

2.8.6 Simulation results: reaction-diffusion lines

Reaction-diffusion lines describe the local change in composition of monomers and liquid crystals during polymerization. In a reaction step polymer is formed, the amount of which is different in depth of the sample, giving rise to a gradient in the chemical potential. This is the driving force for diffusion, or material transport in time:

$$\frac{\partial \phi_i}{\partial t} = \frac{\partial}{\partial z} \left(\frac{D_i \phi_i}{kT} \frac{\partial \mu_i}{\partial z} \right) \quad (2.97)$$

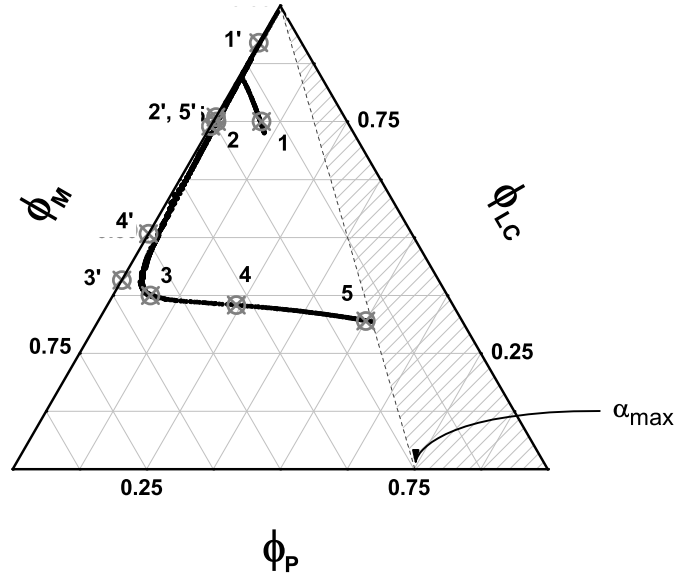
The influences on the diffusion is studied regarding the chemical potentials of isotropic mixing, network elasticity and nematic ordering and also the polymerization rate and the value of the diffusion coefficients. It was already suggested that the diffusion flux of the liquid crystals is determined by the diffusion flux of the monomers in order to fulfill the material balance (section 2.3.2). The thermodynamical effects on the diffusion will be investigated for monomer and liquid crystal transport separately.

The terms in the chemical potentials, corresponding to isotropic mixing, nematic ordering and elastic networks, and which contain ϕ_p and ϕ_m are influencing the diffusion. These terms are summarized in table 2.5. Polymer is formed more rapidly at higher light intensity sites, giving locally a higher polymer volume fraction. In the columns in table 2.5, towards high or towards low denotes that the driving force for diffusion is towards the high or low light intensity side, so towards the higher or lower polymer volume fraction. For the investigation on the effects of the different parameters this table will be used as a reference. The experimental conditions for the simulation are summarized in table 2.6.

Influence of χ on diffusion

The chemical potential for the monomer describing the isotropic mixing ($\Delta\mu_m^M$) depends linearly on the polymer volume fraction and logarithmic on the monomer volume fraction. Re-writing the term for the interaction parameter in equation 2.93 in monomer and polymer volume fractions results in:

$$\begin{aligned} \frac{\Delta\mu_m^M}{k_B T} &= \ln \phi_m + \phi_p + \chi(1 + (1 - \phi_m - \phi_m)^2) \\ &= \ln \phi_m + \phi_p + \chi(1 + (\phi_m + \phi_p)^2 - 2\phi_p - 2\phi_m - 4\phi_m\phi_p) \end{aligned}$$



(a)

		Phase I	Phase II
1	ϕ_{lc}	0.75	0.92
	ϕ_m	0.24	0.08
	ϕ_p	0.01	-
2	ϕ_{lc}	0.75	0.76
	ϕ_m	0.16	0.24
	ϕ_p	0.09	-
3	ϕ_{lc}	0.37	0.41
	ϕ_m	0.56	0.59
	ϕ_p	0.07	-
4	ϕ_{lc}	0.36	0.51
	ϕ_m	0.41	0.49
	ϕ_p	0.24	-
5	ϕ_{lc}	0.32	0.74
	ϕ_m	0.18	0.26
	ϕ_p	0.50	-

(b)

Figure 2.18: (a) Simulated phase separation line fitted to experimentally values with $\chi = 0.53$ and $C_{eff} = 1$ ($T_p = 20^\circ\text{C}$, $T_{ni} = 58^\circ\text{C}$). Five compositions on the phase separation lines are chosen (1-5, \otimes) for which the corresponding compositions of the second phase are plotted on the M-LC axis (1'-5', \otimes). The compositions of the two phases are given in the table (b). When the liquid crystal content in phase II is larger than ϕ_{ni} ($= 0.89$), the phase separated liquid phase is nematic.

The quadratic and the linear terms cancel out since the increase in polymer is the same as the decrease in monomer. However, a negative cross-term remains. Since $\phi_m\phi_p < 0.25$, $4\chi\phi_m\phi_p \leq \chi$. The contribution of the chi-terms to the chemical potential of the monomer will therefore always be positive.

The contribution of the mixing to the total chemical potential is the highest at the depth interval with a higher intensity which consequently have larger polymer volume fraction than depth intervals with lower intensity. Subsequently, the total $\Delta\mu_m^{tot}$ will be less negative at the high intensity depth intervals (compare with table 2.4). This implies that the interaction term will try to impede the diffusion of monomers to the reactive sites.

Considering the chemical potentials describing the isotropic mixing for the liquid crystals, only the quadratic term in ϕ_m and ϕ_p remains.

$$\frac{\Delta\mu_{lc}^M}{k_B T} = \ln \phi_{lc} + \phi_p + \chi(\phi_m + \phi_p)^2 \quad (2.98)$$

Therefore, the van der Waals interactions, represented by χ , do not play a role in the

Table 2.6: Reaction parameters for the simulations

T_p	Experimental temperature [K]	293	section: 2.8.1
$\phi_m(initial)$	Monomer volume fraction in reaction mix [-]	0.7	section: 2.8.1
t_p	Exposure time [s]	15	section: 2.8.1
Δz	Depth interval [nm]	5	model parameter
Δt	Polymerization step [s]	0.005	model parameter
Isotropic mixing:			
χ	Interaction parameter [-]	0.53	section: 2.8.4
Network elasticity:			
C_{eff}	Network efficiency factor [-]	1	section: 2.8.4
m_c	Network chain length [-]	eq. 2.91	section: 2.8.3
Nematic ordering:			
s	Order parameter LC phase [-]	eq. 2.35	section: 2.2.3
T_{ni}	Transition temperature of E7 [K]	331	section: 2.7.1
Photopolymerization:			
$k_p/\sqrt{k_t}$	Polymerization rate constant [$\sqrt{l \cdot mol^{-1} \cdot s^{-1}}$]	1	section: 2.7.3
$x(max)$	Maximum double bond conversion [-]	0.32	section: 2.8.2
$\alpha(max)$	Maximum monomer conversion [-]	0.75	section: 2.8.2
f	Monomer functionality [-]	7.2	section: 2.8.2
Φ_{In}	Quantum efficiency of photoinitiator [-]	0.5	section: 2.7.3
ϵ_{In}	Extinction coefficient at 351nm [$l \cdot mol^{-1} \cdot cm^{-1}$]	14000	section: 2.7.3
$[In]$	Concentration of photoinitiator [$mol \cdot l^{-1}$]	0.032	section: 2.7.1
Holographic exposure:			
$E_{photons}$	Energy of one mole photons at 351 nm [Einstein]	$3.4 \cdot 10^5$	section: 2.7.3
I_1	Intensity of incoming beam [$mW \cdot cm^{-2}$]	1.7	section: 2.8.1
I_2	Intensity of reflected beam [$mW \cdot cm^{-2}$]	$= 0.46I_1$	section: 2.8.1
V	Fringe contrast in interference pattern [-]	0.93	section: 2.8.1
Λ	Grating periodicity [nm]	150	section: 2.8.1
Diffusion:			
D_m	Diffusion coefficient of the monomer [$m^2 \cdot s^{-1}$]	$1 \cdot 10^{-10}$	section: 2.7.4
K_1	Constant in free volume theory [-]	0.21	section: 2.7.4

diffusion of the liquid crystal. Nevertheless, the $\Delta\mu_{lc}^M$ is lower in the low intensity regions than in the high intensity regions, due to the compositional entropy. It therefore induces diffusion of LCs toward the low intensity regions.

The assumption that the interaction between monomers and liquid crystals is the same as the interaction between liquid crystals and polymers, together with the assumption that a monomer-polymer interaction parameter is zero, imply that the contribution of the interaction parameter terms to the chemical potentials is the same for all possible combinations of compositions. Moreover, the contribution of the interaction parameter in the Flory-Huggins chemical potential (equations 2.17 and 2.18) is in the order of 0.05 - 0.2, while the other terms have absolute values in the order of 1 (see table 2.4). The effect on the driving force for diffusion due to interactions between subsequent depth intervals is therefore small. Subsequently only small differences can be observed between the diffusion behavior of the model with or without the incorporation of the chi-parameters. This is seen in figure 2.19 where the final depth distributions of monomers, liquid crystals and polymers for $\chi = 0.5$ and 0.6 are plotted. The compositional differences are negligible.

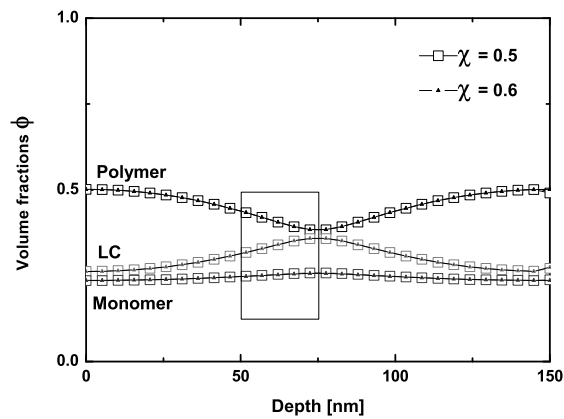
Network elasticity: κ

The network elasticity gives a contribution to the chemical potential with a driving force for diffusion that scales linearly with the polymer volume fraction. Depth-dependent polymerization induces a contrast in polymer volume fraction between subsequent layers. Since the elastic contribution always is positive ($\kappa(\alpha)$, m_c and ϕ_p in equation 2.92 are always positive), the chemical potential of both monomers and liquid crystals will be higher when more polymers are present. Therefore the network elasticity produces a driving force away from the high polymer volume fractions. Both monomers and liquid crystals experience a driving force towards the low intensity regions due to the network elasticity. Note that the diffusion of liquid crystals is therefore enhanced, while the monomer is hindered in its diffusion to the reaction sites. With a higher network efficiency (C_{eff}) the driving force is increased. However, this effect is very small and is hardly visible as can be seen in figure 2.20 in which the depth distribution of monomers, liquid crystals and polymers are plotted for $C_{eff} = 0.5$ and $C_{eff} = 1$.

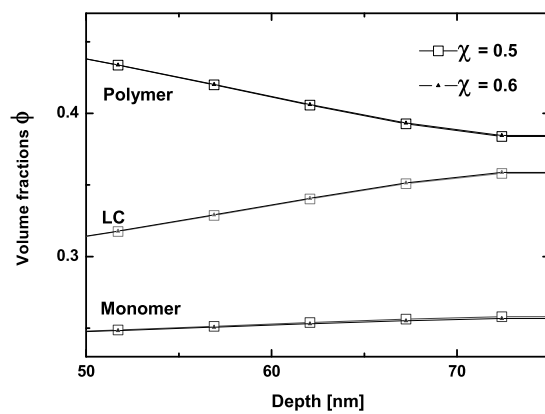
Nematic ordering

The contribution to the chemical potential due to the nematic ordering depends on the monomer and polymer volume fraction via a cross-term that is exactly the same for both monomer and liquid crystal. The nematic partition function does not depend on volume fractions, while the intermolecular interactions are characterized by a ϕ_{lc}^2 dependence. Since $\phi_{lc} = 1 - \phi_m - \phi_p$, and the monomer volume fraction decreases with the increase of formed polymer, the quadratic and linear terms cancel out. The cross-term remains.

$$\frac{1}{2}\nu\phi_{lc}^2s^2 = \frac{1}{2}\nu(1 + (\phi_m + \phi_p)^2 - 2\phi_m - 2\phi_p - 4\phi_m\phi_p) \quad (2.99)$$



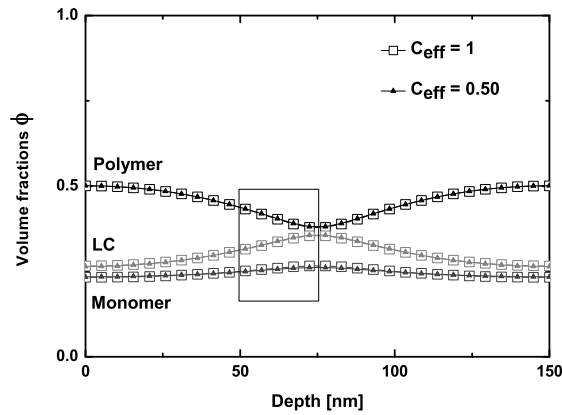
(a)



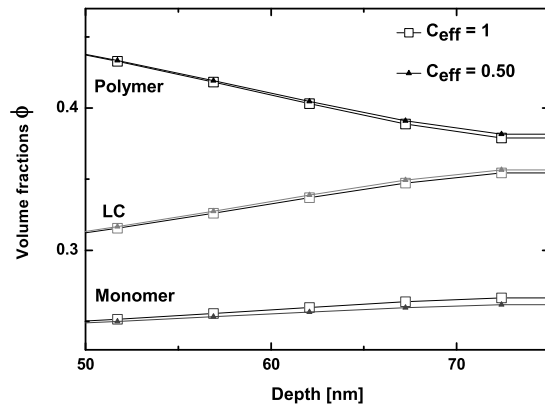
(b)

Figure 2.19: (a) Depth distributions of monomers, liquid crystals and polymers after 15 s polymerization for $\chi = 0.5$ (\square) and $\chi = 0.6$ (\blacktriangle). (b) Enlargement marked area in (a). At the lowest intensity, 75 nm, a small difference between the compositions for the χ values are seen.

Therefore the nematic ordering does not have an effect on the diffusion driven by a chemical potential (which is seen in figure 2.21). However, nematic ordering might nevertheless influence the diffusion in a different way. It is not out of the question that a nematic compound has a somewhat different diffusion coefficient, which might also be anisotropic in nature as a result of the ordering. A quantitative evaluation of this effect is beyond the scope of this thesis.



(a)



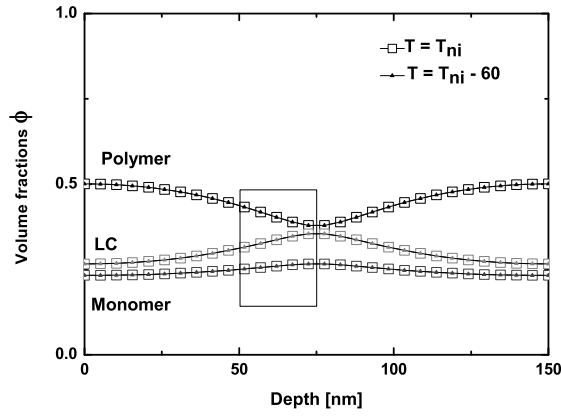
(b)

Figure 2.20: (a) Depth distributions of monomers, liquid crystals and polymers after 15 s polymerization for $C_{eff} = 0.5$ (\square) and $C_{eff} = 1$ (\blacktriangle). (b) Enlargement of the marked area in (a). The differences in diffusion behavior is small when varying the network elasticity contribution.

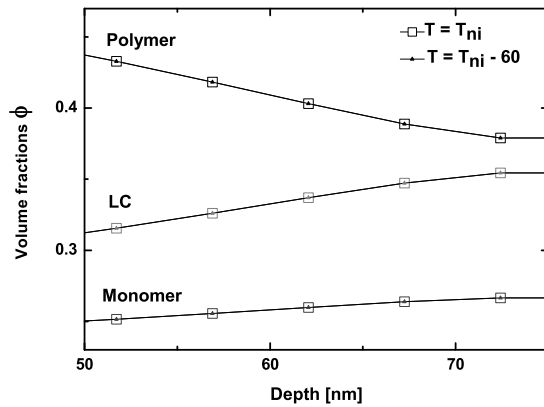
Reaction rates and diffusion coefficients

Material transport is only possible when there is a gradient in the chemical potential between two subsequent depth intervals. Assuming such a gradient, the effects on the material flux regarding the polymerization rate and value of the diffusion constants are studied.

Increasing the polymerization rate induces more polymers to be formed per time step. According to equation 2.97, a larger difference in polymer contents between two depth intervals induces larger material transport, but the influence of the dif-



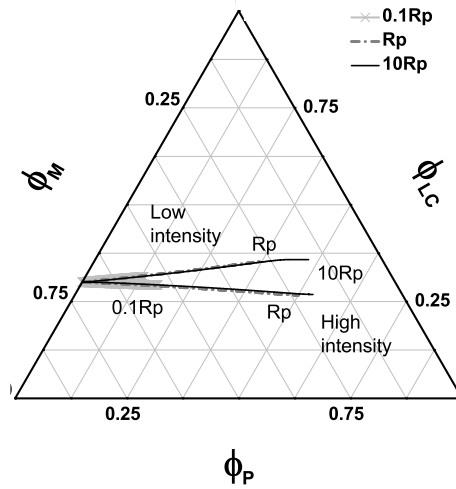
(a)



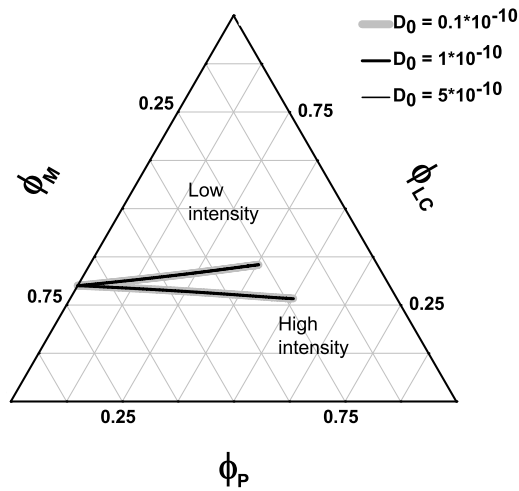
(b)

Figure 2.21: (a) Considering a change in the nematic ordering contributions at $T = T_{ni}$ (\square) and $T = T_{ni} - 60\text{K}$ (\blacktriangle), no differences in depth compositions were found. (b) Enlargement of the marked area in (a).

fusion becomes less effective, since the diffusion constant ($D(\phi_m)$) decreases with the monomer conversion (described with equation 4.3). In figure 2.22(a), reaction-diffusion lines for three reaction rates are plotted in a conversion-phase diagram. The differences between the polymerization rates for the high respectively low rates are insignificant, only more polymers are formed for the higher rates. The reaction rate can be increased by e.g. higher curing intensity, larger amount of, and/or more efficient, initiators, and possibly also higher temperatures. When polymerizing multi-functional acrylate monomers, reported rate constants varied over two orders of magnitude (as discussed in section 2.7.3). Increasing or decreasing the



(a)



(b)

Figure 2.22: (a) Reaction-diffusion lines during 15 s polymerization for different polymerization rates. The polymerization rate does not influence the shape of the reaction-diffusion lines, only the amount of formed polymer per time unit. (b) Reaction-diffusion lines during 15 s polymerization for different diffusion coefficients. No effects are simulated when varying the diffusion constants between 0.1 to $5 \cdot 10^{-10} \text{ m}^2\text{s}^{-1}$. All other experimental simulation parameters are listed in table 2.6.

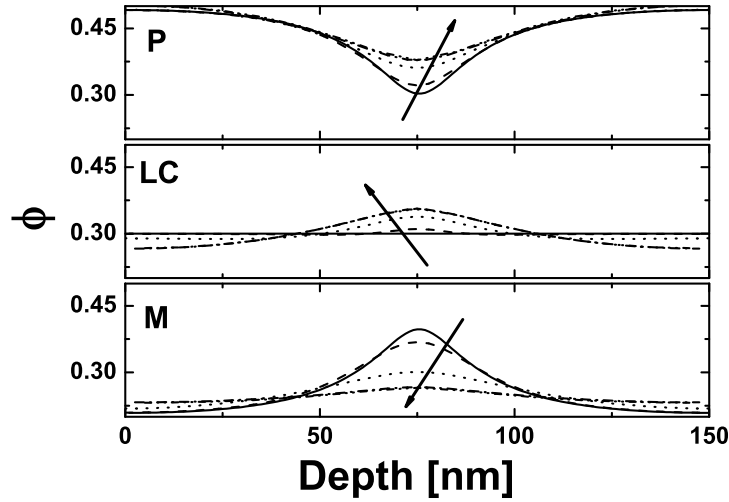


Figure 2.23: Increasing value for the diffusion constant increases the compositional differences between the depth with high intensity (at 0 and 150 nm) and low intensity (at 75 nm). The monomer concentration before polymerization, $\phi_m(\text{initial})$, was 0.7. The arrows indicate an increasing diffusion constant ($- D = 0$, $-- D = 10^{-14} \text{ m}^2\text{s}^{-1}$, $\dots D = 10^{-12} \text{ m}^2\text{s}^{-1}$, $-- D = 10^{-10} \text{ m}^2\text{s}^{-1}$, $--- D = 10^{-8} \text{ m}^2\text{s}^{-1}$). All other polymerization parameters are given in table 2.6.

polymerization rates, however, do not influence the reaction-diffusion lines.

In literature, diffusion coefficients between $0.3 - 1 \cdot 10^{-10} \text{ m}^2 \text{ s}^{-1}$ are generally applied for simulating monomer transport during polymerization^{8,28,38,50}. Simulating diffusion behaviors for diffusion constants between 0.1 to $5 \cdot 10^{-10} \text{ m}^2\text{s}^{-1}$ we found that no compositional differences were present due to diffusion constants in this range (figure 2.22(b)). It was verified that no transport of either monomers nor LCs occurred with the absence of diffusion ($D_m = 0$), which is shown in figure 2.23. By increasing the value of the diffusion constant it was found that the simulations became diffusion-independent when $D_m > 10^{-10} \text{ m}^2 \text{ s}^{-1}$, a further increase of the diffusion constant did not improve the material transport. The actual diffusion constant ($D(\phi_m)$ in equation 4.3) depends on the polymer content and is always $> D_m$. Therefore the diffusion constant (D_m) is not a limiting factor in the grating formation kinetics for the holographic samples investigated here.

2.8.7 Combination of the models

The time and composition at which the reaction-diffusion lines cross the phase separation line, are predicted by the combined phase separation and reaction-diffusion models. This is illustrated with simulations of holographic recordings and compared with the experimental PDLC gratings. Reaction-diffusion parameters that influence the structured phase separation will be evaluated and compared with experimental

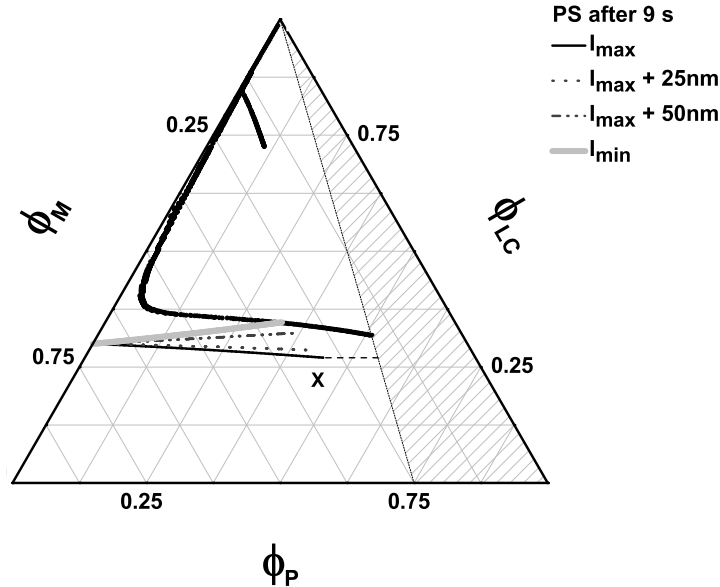


Figure 2.24: Four reaction diffusion lines at depth intervals with different light intensity are followed during polymerization. After 9 s the reaction-diffusion line at depth intervals of the lowest intensity (I_{min}) crosses the phase separation line, and the line at the highest intensity reaches point **X**. The composition of the reaction mixture (before polymerization) was 30 weight% LCs.

results from section 2.8.1.

First the phase separation and reaction-diffusion behavior during holographic exposure in a mixture with 30 weight% liquid crystals in the monomer blend is simulated. Reaction-diffusion lines from four different depth intervals are plotted in figure 2.24. All experimental parameters for the simulations are given in table 2.6, with the exposure time: 30 s. The reaction-diffusion line originating from the depth intervals of the lowest intensity (I_{min}) in the holographic interference pattern reach the phase separation line first in time; after 9 s of polymerization. When the phase separation line is crossed, the thermodynamical expressions are changed since the dynamics of the droplet formation of the phase separated liquid phase influence the thermodynamically contributions to the chemical potentials. Therefore, at the moment that one of the reaction-diffusion lines crosses the phase separation line, the modeling is stopped. The reaction-diffusion line for the depth interval with the highest intensity proceeds to point **X** in 9 s. During the resultant 21 s of the holographic exposure we assume the reaction-diffusion lines at **X** to continue to α_{max} (dashed line in figure 2.24).

The concentration of the polymer-rich layer (the depths of the highest intensity)

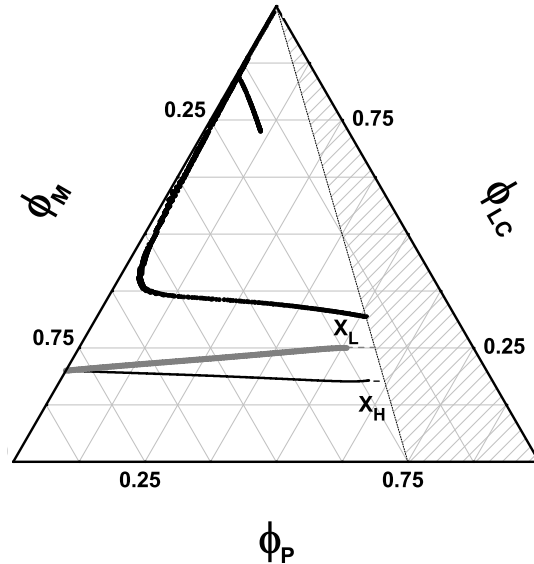


Figure 2.25: Reaction diffusion lines at the depth intervals with the highest (thin black line) and lowest (bold gray line) intensity are followed during 30 s holographic exposure on a reaction mixture containing 20 weight% LCs initially. After 30 s holographic recording the lines reach the points \mathbf{X}_H and \mathbf{X}_L . A flood exposure continues the polymerization without inducing anymore diffusion (dashed lines). None of the reaction-diffusion lines reach the phase separation line with the result that the polymerized film appears transparent.

is predicted to 27% LC by the model. The reaction-diffusion lines at the depths at lowest intensity cross the phase separation line at a concentration of 36% LC. The difference (36 - 27%LC) is low and is supported by the poor contrast in the SEM images of the cross sections of holographic reflection gratings (figure 2.9(b)).

Increasing the polymerization time will not change the grating morphology, since the phase separation line is reached after 9 s. This was experimentally verified by collecting identical reflection/transmission spectra from holographic recorded gratings with 30 respectively 60 s of exposure (figure 2.10).

Holographic recordings in reaction mixtures of 20% liquid crystal concentration resulted in fully transparent gratings. Simulation of such a grating is shown in figure 2.25. After 30s holographic exposure the reaction-diffusion lines at the depth intervals of the highest and lowest intensities reach the points \mathbf{X}_H and \mathbf{X}_L in figure 2.25. During the flood exposure the polymerization continues, and since the flood exposure is homogeneous no diffusion is induced in depth of the film. Therefore the reaction-diffusion lines continues with constant liquid crystal concentration (and are in the figure plotted as dashed lines). As a result, none of the reaction-diffusion lines

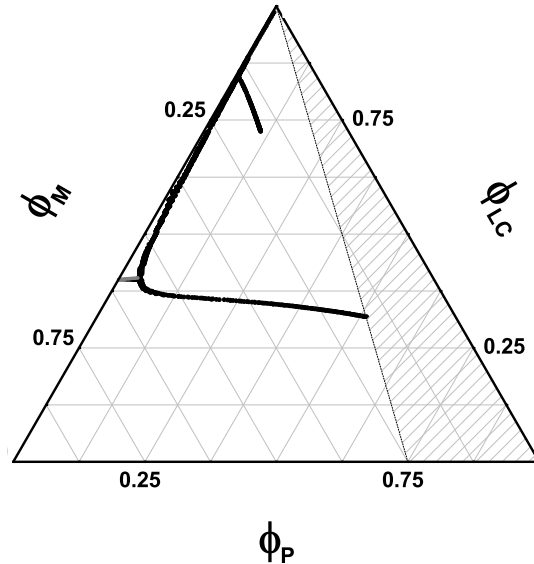


Figure 2.26: Reaction diffusion lines at the depth intervals with the highest (thin black line) and lowest (bold gray line) intensity are followed during holographic exposure on a reaction mixture containing 40 weight% LCs initially. Within a fraction of a second, the reaction-diffusion lines at all depth intervals cross the phase separation line. Therefore phase separation occurs through out the whole film with a white scattering unstructured PDLC as a result.

cross the phase separation line and the polymerized film does not experience phase separation. Instead it is a polymer network which is swollen with liquid crystals and unreacted monomers. In the polymer network a concentration profile is present, but since the concentration differences are low, and do not generate a contrast in refractive index between the depth intervals with high respectively low intensity, the grating appears transparent.

Higher concentrations of LCs in the reaction mixture moves the reaction-diffusion lines upwards in the conversion-phase diagram. Starting the polymerization in a reaction mixture containing 40% liquid crystals in the monomer mixture, the reaction-diffusion lines cross the phase separation line instantaneously, after 0.4 s (figure 2.26). As a result, unstructured phase separation occurs in the whole grating, and experimentally such a sample scattered all light in random directions.

2.9 Conclusions

Controlling photopolymerization induced phase separation to produce the desired distributions of LCs in complex structured PDLC films remains difficult but is es-

sential for the ultimate device properties. Therefore a model describing the phase separation behavior of holographic recording mixtures and a model following the reaction-diffusion behavior of a holographic recording was proposed. Modeling the chemical potentials the thermodynamical influences on the phase separation and diffusion by considering the isotropic mixing, network elasticity and nematic ordering were investigated. The effects of the polymerization rate constants and diffusion constants on the reaction-diffusion behavior was studied.

When considering only the isotropic mixing described by Flory-Huggins, neglecting the interaction enthalpy between polymer and monomer, and assuming the other interactions equal, no phase separation is predicted by the model (for $\chi \leq 0.5$). Introducing a higher interaction parameter or a small difference in the intermolecular interactions between monomer-LC and polymer-LC, this leads to phase separation, although this was found to be a very small effect.

The elasticity of a densely cross-linked network was found the most important mechanism to induce and enhance phase separation. The network efficiency factor, accounting for the elastically inactive chains, was also investigated. Less elastic networks squeeze out the liquid components less effectively with the result that the phase separation line is shifted upwards. Consequently, the network efficiency factor can be used as a fit parameter by comparing the model with experimental results. The network efficiency was assumed to be dependent on the monomer conversion, and for the holographic system C_{eff} was determined to be 1.

Investigating the effect of the Flory-Huggins interaction term in combination with an elastic network it showed that the strength of the interaction has a significant influence on the phase separation. Weaker interactions, reflected by a higher interaction parameter χ , between LC and the two other components decrease the solubility limit, i.e. the highest concentration of LC for which no phase separation can occur. Increasing the interaction parameter χ shifts the line downward, which means that for stronger interactions phase separation will take place at a lower conversion.

The contribution of the nematic ordering determines whether the phase separated phase (II) is isotropic or nematic.

The reaction-diffusion behavior during the holographic recording was modeled and the influences of Flory-Huggins isotropic mixing, network elasticity and nematic ordering were studied. The diffusion is only slightly influenced by the interaction parameter (χ), network elasticity (κ) and nematic ordering. The effects were much less than on the phase separation. The reaction-diffusion lines are diffusion independent for $D > 10^{-10} \text{ m}^2\text{s}^{-1}$, and only for lower values of diffusion constants differences in the reaction-diffusion lines were simulated. Varying the polymerization rate does not show any effects on the diffusion.

Combining the phase separation model with the reaction-diffusion behavior the morphology of the grating at the moment of phase separation can be predicted. It was found that the determining factor was the shape of the phase separation line (i.e. the lowest polymer fractions, with the respectively monomer and LC concentrations, at which phase separation occurs). Yet it is not out of question that for other monomer systems, the reaction and diffusion kinetics can influence the grat-

ing morphology more than simulated in this case. This could happen for systems generating phase separation lines including a much smaller phase separated area of compositions, e.g. due to less dense polymer network caused by lower functional monomers.

Simulated phase separation behaviors of holographic reaction mixtures were compared with experimentally prepared holographic reflection gratings. The results from the combined models agreed well with the experimental results. However, verifying the combined models with imaging techniques (as scanning electron microscopy) that depend on the contrast between the layers is difficult. Therefore, to validate the combined models, analysis technique(s) that can detect the small concentration changes in depth of the sample are assumed to be more valuable. Dynamic secondary ion mass spectrometry (SIMS) is such a method, and is examined in chapter 3, followed by in-depth analysis of holographic reflection gratings and comparison with results from the combined models (chapter 4).

2.10 References and notes

1. Qi, J. and Crawford, G. P. *Displays* **25**, 177–186 (2004).
2. Escuti, M. J. and Crawford, G. P. *Mat. Res. Soc. Symp. Proc.* **709**, 293–298 (2002).
3. Amundson, K., von Blaaderen, A., and Wiltzius, P. *Phys. Rev. E* **55**(2), 1646–1654 (1997).
4. Bowley, C. C. and Crawford, G. P. *Appl. Phys. Lett.* **76**(16), 2235–2237 (2000).
5. Wu, S.-D. and Glytsis, E. N. *J. Opt. Soc. Am. B* **20**(6), 1177–1188 (2003).
6. Qi, J., Li, L., de Sarkar, M., and Crawford, G. P. *J. Appl. Phys.* **96**(5), 2443–2450 (2004).
7. Sutherland, R. L., Tondiglia, V. P., Natarajan, L. V., and Bunning, T. J. *J. Appl. Phys.* **96**(2), 951–965 (2004).
8. Penterman, R. *Photo-enforced stratification of liquid crystal/monomer mixtures, Principle, Theory and analysis of a paintable LCD concept*. PhD thesis, Eindhoven University of Technology, Eindhoven, (2005).
9. Prenen, A. Master's thesis, Eindhoven University of Technology, Eindhoven, (2005).
10. Atkins, P. W. *Physical Chemistry*. Oxford University Press, Oxford, 5th edition, (1994).
11. Flory, P. J. *Principles of polymer chemistry*. Cornell University Press, London, (1971).
12. Huggins, M. L. *J. Chem. Phys.* **46**, 151–158 (1942).
13. Flory, P. J. *J. Chem. Phys.* **9**(8), 660–661 (1941).
14. Flory, P. J. *J. Chem. Phys.* **10**, 51–61 (1942).
15. In a regular solution the species are distributed randomly as in an ideal solution ($\Delta S_{ideal} = \Delta S_{actual}$), but have different interaction energies with each other ($\Delta H_{ideal} \neq \Delta H_{actual}$).

16. Cowie, J. M. G. *Polymer: Chemistry and Physics of Modern Materials*. Blackie Academic and Professional, an imprint of Chapman and Hall, Glasgow, 2nd edition, (1991).
17. Orwoll, R. A. *Rubber Chem. Technol.* **50**(3), 451–479 (1977).
18. Boots, H. M. J., Kloosterboer, J. G., Serbutoviez, C., and Touwslager, F. J. *Macromolecules* **29**, 7683–7689 (1996).
19. Dušek, K. and Dušková-Smrčková, M. *J. Polym. Sci. C* **25**, 1215–1260 (2000).
20. Dušek, K. *J. Polym. Sci.* , 1289–1299 (1967).
21. Moerkerke, R., Koningsveld, R., Berghmans, H., Dušek, K., and Šolc, K. *Macromolecules* **28**, 1103–1107 (1995).
22. Kelly, S. M. and O'Neill, M. *Handbook of advanced electronic and photonic materials and devices*, volume 7, chapter 1, 1–66. Academic press, London (2001).
23. Picken, S. J. *Macromolecules* **22**(14), 1766–1771 (1989).
24. Picken, S. J., van der Zwaag, S., and Northolt, M. G. *Polymer* **33**(14), 2998–3006 (1992).
25. Collings, P. J. *Liquid crystals*. IOP Publishing Ltd., Bristol, (1990).
26. Shen, C. and Kyu, T. *J. Chem. Phys.* **102**, 556–562 (1995).
27. Picken, S. J. *Macromolecules* **23**(2), 464–470 (1990).
28. de Gennes, P. G. and Prost, J. *The Physics of Liquid Crystals*. Clarendon Press, Oxford, 2nd edition, (1993).
29. To derive order parameters for highly ordered LC systems (with $s > 0.8$), another definition²⁴ of the mean field parameter is more suitable.
30. Selli, E. and Bellobono, I. R. *Radiation curing in polymer science and technology, Volume 3, Polymerization mechanisms*, volume 3, chapter 1, 1–32. Elsevier Science Publishers Ltd, London (1993).
31. Kloosterboer, J. G. *Advances in polymer science*, chapter 1, 1–61. Number 84. Springer-verlag, Berlin (1988).
32. Broer, D. J. *Liquid crystals in complex geometries, formed by polymer and porous networks*, chapter 10, 239–254. Taylor and Francis Ltd, London (1996).
33. Andrzejewska, E. *Prog. Polym. Sci.* **26**, 605–665 (2001).
34. Kloosterboer, J. G., van de Hei, G. M. M., and Boots, H. M. J. *Polym. Commun.* **25**, 354–357 (1984).
35. Anseth, K. S., Wang, C. M., and Bowman, C. N. *Polymer* **35**(15), 3243–3250 (1994).
36. Khudyakov, I. V., Legg, J. C., Purvis, M. B., and Overton, B. J. *Ind. Eng. Chem. Res.* **38**, 3353–3359 (1999).
37. Leewis, C. M. *Formation of Mesoscopic Polymer Structures for Optical Devices - a Nuclear Microprobe Study*. PhD thesis, Eindhoven University of Technology, (2002).

38. Leewis, C. M., de Jong, A. M., van IJzendoorn, L. J., and Broer, D. J. *J. Appl. Phys.* **95**(8), 4125–4139 (2004).
39. Hecht, E. *Optics*, chapter 9, 385–442. Addison Wesley, San Francisco, 4th edition (2002).
40. Sutherland, R. L., Natarajan, L. V., Bunning, T. J., and Tondiglia, V. P. *Handbook of advanced electronic and photonic materials and devices*, volume 7, chapter 2, 67–103. Academic press, London (2001).
41. Schwartz, K. *The physics of optical recording*, chapter 2, 18. Springer-Verlag, Berlin (1993).
42. Hariharan, P. *Optical holography: principles, techniques, and applications*. Cambridge studies in modern optics. Cambridge University Press, Cambridge, 2nd edition, (1996).
43. Ono, H., Kawamura, T., Frias, N. M., Kitamura, K., Kawatsuki, N., and Norisada, H. *Adv. Mater.* **12**, 143–146 (2000).
44. Brandrup, J. and Immergut, E. H., editors. *Polymer handbook*. Wiley-Interscience, London, 3rd edition, (1989).
45. Pogue, R. T., Ullett, J. S., and Chartoff, R. P. *Thermochim. Acta* **339**, 21–27 (1999).
46. Scherzer, T. and Decker, U. *Polymer* **41**, 7681–7690 (2000).
47. www.cibasc.com. Ciba speciality chemicals.
48. Mateo, J. L., Serrano, J., and Bosch, P. *Macromolecules* **30**, 1285–1288 (1997).
49. Soppera, O. and Croutxé-Barghorn, C. *J. Polym. Sci., Part A: Polym. Chem.* **41**, 831–840 (2003).
50. Kyu, T., Nwabunma, D., and Chiu, H.-W. *Phys. Rev. E.* **63**, 061802 (2001).
51. Kloosterboer, J. G., van de Hei, G. M. M., Gossink, R. G., and Dortant, G. C. M. *Polym. Commun.* **25**, 322–325 (1984).
52. Koningsveld, R., Kleintjens, L. A., and Shultz, A. R. *J. Pol. Sci. A* **8**, 1261 (1970).

Chapter 3

Secondary ion mass spectrometry and multivariate statistical analysis:

An approach to analyze concentration gradients in stratified PDLCs

3.1 Introduction

Dynamic secondary ion mass spectrometry (SIMS) is traditionally used for depth profiling in inorganic materials and is based on the detection of secondary ions sputtered from the surface of the sample by a focused primary ion source. Following the intensities of the secondary ions in time, a depth profile reflecting the composition of the sample is collected. The detection limits and depth resolution for this kind of analysis highly depend on sputter yield and ionization processes needed for peeling off fragments from the surface¹. The analysis of polymers is less obvious since a change in polymer composition does not necessarily result in unique secondary ions. Another complication is charge build-up during sputtering because of the insulating nature of most organic materials². Even though the latter can be reduced by applying low energy electrons, the ionization and sputter yield processes (matrix effects) are regarded as the main limitations of SIMS analysis of organic materials³. Nevertheless, dynamic SIMS applied on organic materials has given successful results, such as depth profiling of deuterated and brominated polymers⁴, organic solar cells⁵ and interface concentrations of ion doped thin polymer films⁶. Recently Wagner measured depth profiles of thin multilayer polymer films and identified the different polymers from large polymer-unique fragments⁷.

The identification of organic molecules and polymers becomes possible once a low current ion source with negligible sputter yield is used. Only the outermost surface is analyzed (i.e. static SIMS) and characteristic fragments from monomer repeat units and chain end-groups can be detected and pendant groups, polymer cross-linking

and branching can be identified^{8,9,10,11}. However, for depth profiling of characteristic ions, higher sputter currents are needed, which induce larger fragmentation of the sample. In this case, sample identification has to be based on a characteristic region of low molecular weight fragments, i.e. the fingerprints^{2,12}.

Generally, organic samples create complex dynamic SIMS spectra with complicated correlations between the low molecular weight fragments. Yet, the secondary ion yields sputtered from the sample surface are still believed to be specific for the material composition. However, it is commonly found that organic matrices do not induce a linear secondary ion yield compared to the concentration in the sample. Additionally, not only one but several mass channels in the spectra are required to retrieve any quantitative information from the complex SIMS fingerprints. Therefore we applied multivariate statistical analyses (MVA) to identify the compositions of our samples.

Recently MVA was introduced to analyze the complex SIMS spectra and retrieve differences in SIMS spectra based on different polymer end-groups, polymer compositions and different surface modifications^{13,14,15}. Furthermore, MVA applied on SIMS spectra identified differences between samples treated with dissimilar self-assembly methods of organic molecules^{16,17}. It also discriminated between samples with different grafting procedures for making selective polymer surfaces for e.g. biological applications¹⁸.

To our knowledge only one example is available where dynamic SIMS spectra were treated by MVA to obtain overall concentrations of solar cell materials: deuterated methoxy-carbonyl propyl-phenyl-C61 (d5-PCBM) and poly(methoxy dimethyl octyloxy-p-phenylene vinylene) (MDMO-PPV)¹⁹.

3.2 Multivariate statistical analyses

Multivariate statistical analysis enlightens sample characteristics that were not obvious in the original data set. The MVA organizes the data, summarizes it and displays it in new dimensions. Several multivariate analysis methods with different characteristics are available, e.g. reduction and structural simplification of data-sets, sorting observations and ordering them in pre-defined groups, investigation of the dependence among variables and prediction the values of one or more variables on basis of the known relationships of the others²⁰. Due to its diversity, MVA has been applied in various fields such as political sciences, engineering, medicine, chemistry, psychology, geology and recently on SIMS spectra of polymers^{20,21,22,17}.

Here, two multivariate statistical analyses have been investigated to interpret SIMS depth profiles: Principle component analysis (PCA) and discriminant function analysis (DFA). Both MVAs are based on the variance in the SIMS spectra. The analyses investigate correlations between the variables (mass channels) in order to display the information in a new coordinate system from which the sample interpretation can be facilitated. In the following paragraphs, the principles of PCA and DFA are introduced.

3.2.1 Principle component analysis

Each measured SIMS spectrum can be considered as a vector in a coordinate system of the mass channel values (m/z values), where the number of counts in each mass channel serve as the vector coefficient. The m/z values can thus be envisaged as the unit vectors of the coordinate system that describes the SIMS spectra.

The purpose of PCA is to construct an alternative coordinate system that describes the SIMS spectra in a set of unit vectors. The new unit vectors (called principle components, PCs) are ranked on the captured variance of the original data set²³. In figure 3.1 the construction of an alternative set of coordinates is visualized in a two dimensional plot of a simple sample population consisting of 50 observations ($N = 50$). Suppose that the values of the observations over two variables, p_1 and p_2 , are as shown in figure 3.1. The principle components are the unit vectors in the new coordinate system, with the axis of the first principle component (PC_1) in the direction of the largest variance. The second principle component (PC_2) is orthogonal to PC_1 . For multiple variables, $p > 2$, the same procedure applies for larger coordination dimensions. Only if the variance in the data is homogeneous in all directions, the direction of the new principle component coordinate system is arbitrary and can equal the original variables, and the principle component analysis is fruitless. For all other cases a coordination rotation can display sample characteristics not clearly visible in the original data set.

The set of new unit can be found by solving the eigenvalue problem of the sample covariance matrix (Σ):

$$\Sigma \mathbf{V} = \mathbf{V} \mathbf{D} \quad (3.1)$$

where \mathbf{V} is the matrix with the eigenvectors, and \mathbf{D} is a diagonal matrix of the eigenvalues (λ) of size $p \times p$, where p is the number of mass channels in the SIMS

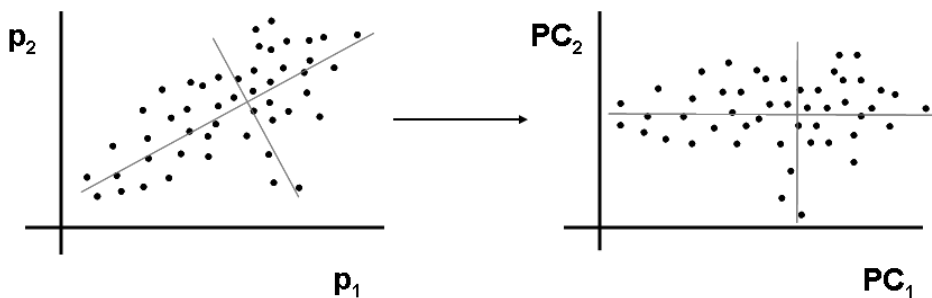


Figure 3.1: Sample observations (the dots in the graphs) are plotted for two variables, p_1 and p_2 in the left figure. The observations are spread in two main directions, indicated by the gray bars. Applying PCA on the sample observations generates an alternative coordinate system for the original data. In the right figure the principle components (PCs, the unit vectors in the new coordinate system) can graphically be seen as a rotation of the original coordinate axes (p_1 and p_2). PC_1 captures the most variance of the original data set.

spectra:

$$\mathbf{D} = \begin{bmatrix} \lambda_1 & 0 & \dots & 0 \\ 0 & \lambda_2 & \dots & 0 \\ \vdots & \vdots & \ddots & \vdots \\ 2 & 2 & \dots & \lambda_p \end{bmatrix} \quad (3.2)$$

The eigenvector matrix (\mathbf{V}), also of dimension $p \times p$, contains the p eigenvectors of the covariance matrix $\mathbf{\Sigma}$. Each eigenvector is represented as a column vector (\mathbf{A}) with length p , in the eigenvector matrix \mathbf{V} .

$$\mathbf{V} = [\mathbf{A}_1 \quad \mathbf{A}_2 \quad \dots \quad \mathbf{A}_p] \quad (3.3)$$

$$\mathbf{A}_1 = \begin{bmatrix} a_{11} \\ a_{12} \\ \dots \\ a_{1p} \end{bmatrix} \quad (3.4)$$

where a are the coefficients in the eigenvectors. The coefficients in the eigenvectors are normalized so that $(\mathbf{A})'\mathbf{A} = 1$. The eigenvectors and values are ordered in pairs, the i th eigenvector corresponds to the i th eigenvalue.

In the sample population matrix (\mathbf{S}), of dimension $p \times N$, the rows represent the N SIMS mass spectra. The column vectors (\mathbf{X}) in the sample population matrix contain the ion yields of the p number of mass channels for the N number of analyzed SIMS spectra.

$$\mathbf{S} = \begin{bmatrix} x_{11} & x_{12} & \dots & x_{1p} \\ x_{21} & x_{22} & \dots & x_{2p} \\ \vdots & \vdots & \ddots & \vdots \\ x_{N1} & x_{N2} & \dots & x_{Np} \end{bmatrix} = [\mathbf{X}_1 \quad \mathbf{X}_2 \quad \dots \quad \mathbf{X}_p] \quad (3.5)$$

The mean (\bar{x}_i) of the i :th mass channel for all SIMS spectra in the depth profile, is calculated as

$$(3.6)$$

$$\bar{x}_i = \frac{1}{N} \sum_{n=1}^N x_{ni} \quad (3.7)$$

The sample covariance matrix ($\mathbf{\Sigma}$) is computed from the sample population and its mean as:

$$\mathbf{\Sigma} = \begin{bmatrix} \mathbf{X}_1 - \bar{x}_1 \\ \mathbf{X}_2 - \bar{x}_2 \\ \vdots \\ \mathbf{X}_p - \bar{x}_p \end{bmatrix} [\mathbf{X}_1 - \bar{x}_1 \quad \mathbf{X}_2 - \bar{x}_2 \quad \dots \quad \mathbf{X}_p - \bar{x}_p] \quad (3.8)$$

The principle components (PC) are obtained as:

$$\begin{aligned}
 PC_1 &= (\mathbf{A}_1)' \mathbf{S} = a_{11} \mathbf{X}_1 + a_{12} \mathbf{X}_2 + \dots + a_{1p} \mathbf{X}_p \\
 PC_2 &= (\mathbf{A}_2)' \mathbf{S} = a_{21} \mathbf{X}_1 + a_{22} \mathbf{X}_2 + \dots + a_{2p} \mathbf{X}_p \\
 &\vdots \\
 PC_p &= (\mathbf{A}_p)' \mathbf{S} = a_{p1} \mathbf{X}_1 + a_{p2} \mathbf{X}_2 + \dots + a_{pp} \mathbf{X}_p
 \end{aligned} \tag{3.9}$$

The order of the eigenvectors is chosen so that the first PC has the maximum variance. The variance that a PC captures is reflected by the value of its corresponding eigenvalue, λ and is often given proportional to the total sample variance:

$$\text{Var}(PC_i) = \frac{\lambda_i}{\text{Var}(\mathbf{S})} = \frac{\lambda_i}{\sum_{k=1}^p \lambda_k} \tag{3.10}$$

Principle components with low variance are often discarded, since their contribution to the new coordination system is minor. Consequently PCA reduces the dimensions of the original coordination system.

The coefficients in the eigenvectors (a) are also called the loadings of the PCs. PCA generates largest loadings for the variables with the largest values and variance. To favor that all variables have the same weight when entered into the analysis, each variables ought to be standardized. Several types of standardization are possible; in this study we standardized the variables to zero mean and unit variance over the whole sample population. Using such a standardization, the eigenvalue problem is solved for the correlation matrix, \mathbf{C} (instead of the covariance matrix).

$$\mathbf{C} = \begin{bmatrix} 1 & \sigma_{12} & \dots & \sigma_{1p} \\ \sigma_{21} & 1 & \dots & \sigma_{2p} \\ \vdots & \vdots & \ddots & \vdots \\ \sigma_{p1} & \sigma_{p2} & \dots & 1 \end{bmatrix} \tag{3.11}$$

3.2.2 Discriminant function analysis

The classification analysis discriminant function analysis is commonly applied as predictive analysis in social and political sciences²¹. *A priori*, the analysis a partition of the observations into g groups is made^{21,24}. Each group represents n_g number of SIMS spectra of a specific sample composition or other group characteristics. The

sample population matrix with the pre-defined groups has the form as:

$$\mathbf{S} = \begin{bmatrix} x_{111} & x_{121} & \dots & x_{1p1} \\ x_{211} & x_{221} & \dots & x_{2p1} \\ \vdots & \vdots & \ddots & \vdots \\ x_{n_111} & x_{n_121} & \dots & x_{n_1p1} \\ x_{112} & x_{122} & \dots & x_{1p2} \\ x_{212} & x_{222} & \dots & x_{2p2} \\ \vdots & \vdots & \ddots & \vdots \\ x_{n_212} & x_{n_222} & \dots & x_{n_2p2} \\ \vdots & \vdots & \ddots & \vdots \\ x_{11g} & x_{12g} & \dots & x_{1pg} \\ x_{21g} & x_{22g} & \dots & x_{2pg} \\ \vdots & \vdots & \ddots & \vdots \\ x_{n_g1g} & x_{n_g2g} & \dots & x_{n_gpg} \end{bmatrix} \quad (3.12)$$

Similar to PCA, DFA constructs an alternative coordination system of a set of new unit vectors (called discriminant functions, F). The eigenvalue problem is solved for the matrices represented by the differences and similarities between the groups, $\mathbf{W}^{-1}\mathbf{B}$:

$$(\mathbf{W}^{-1}\mathbf{B})\mathbf{V} = \mathbf{V}\mathbf{D} \quad (3.13)$$

where \mathbf{V} is the matrix with the eigenvectors and \mathbf{D} is the diagonal matrix of the eigenvalues (λ), both of size $p \times p$.

$$\mathbf{D} = \begin{bmatrix} \lambda_1 & 0 & \dots & 0 \\ 0 & \lambda_2 & \dots & 0 \\ \vdots & \vdots & \ddots & \vdots \\ 0 & 0 & \dots & \lambda_p \end{bmatrix} \quad (3.14)$$

$$\mathbf{V} = [\mathbf{A}_1 \quad \mathbf{A}_2 \quad \dots \quad \mathbf{A}_p] \quad (3.15)$$

$$\mathbf{A}_1 = \begin{bmatrix} a_{11} \\ a_{12} \\ \dots \\ a_{1p} \end{bmatrix} \quad (3.16)$$

where a are the coefficients in the eigenvectors that are normalized to $(\mathbf{A})'\mathbf{A} = 1$. The eigenvectors and values are ordered in pairs, the i th eigenvector corresponds to the i th eigenvalue.

In equation 3.13, \mathbf{B} is the between groups matrix of sums and squares of cross products and \mathbf{W} is the within groups matrix of sums and squares of cross products. The sum of these two matrices gives the total sums and squares of cross product matrix \mathbf{T} , which is the covariance matrix $\mathbf{\Sigma}$ of the total sample population (equation

3.8). The coefficients in \mathbf{W} are calculated from the cross products of the variable's means of the specific groups. For variable 1 and 2, the coefficient is retrieved as:

$$w_{12} = \sum_{k=1}^g \sum_{m=1}^{n_{gr}} (x_{m1k} - \bar{x}_{1k})(x_{m2k} - \bar{x}_{2k}) \quad (3.17)$$

The between groups matrix of sums and squares of cross products, \mathbf{B} , is defined as:

$$\mathbf{B} = \mathbf{T} - \mathbf{W} \quad (3.18)$$

The discriminant functions (F), that are the set of unit vectors in the new coordinate system, are obtained as:

$$\begin{aligned} F_1 &= (\mathbf{A}_1)' \mathbf{S} = a_{11} \mathbf{X}_1 + a_{12} \mathbf{X}_2 + \dots + a_{1p} \mathbf{X}_p \\ F_2 &= (\mathbf{A}_2)' \mathbf{S} = a_{21} \mathbf{X}_1 + a_{22} \mathbf{X}_2 + \dots + a_{2p} \mathbf{X}_p \\ &\vdots \\ F_p &= (\mathbf{A}_p)' \mathbf{S} = a_{p1} \mathbf{X}_1 + a_{p2} \mathbf{X}_2 + \dots + a_{pp} \mathbf{X}_p \end{aligned} \quad (3.19)$$

The order of the discriminant functions (F) is chosen so that the first F has the maximum variance. The variance that the functions capture is expressed by its corresponding eigenvalue, λ , and is proportional to the total sample variance as:

$$Var(F_i) = \frac{\lambda_i}{Var(\mathbf{S})} = \frac{\lambda_i}{\sum_{j=1}^p \lambda_j} \quad (3.20)$$

Similarly to PCA, the largest loadings of the variables are obtained for the variables with the largest variance. Therefore standardization of the variables is required to allow equal weighting of the variables in the analysis. In this study we standardize the variables to zero mean and unit variance. As a consequence, the total sums and squares of cross product matrix \mathbf{T} , equals the correlation matrix \mathbf{C} (equation 3.11).

3.2.3 Significance and multivariate normal distribution

To determine the importance of the linear combinations generated by PCA and DFA, significance tests are of assistance. The chi-squared test, χ^2 , examines whether the function is, by chance or not, different compared to the other functions:

$$\chi_i^2 = (N - 1 - \frac{p+g}{2}) \ln(1 + \lambda_i), \quad (3.21)$$

where N is the total number of observations (SIMS spectra), g the number of groups, p the number of variables (mass channels) and λ_i the variance of the i :th function. Another test, the F-test investigates, per linear combination, the differences between the SIMS samples, by comparing the “between groups matrix of sums and squares of cross products”, \mathbf{B} (equation 3.18), and the “within groups matrix of sums and squares of cross products”, \mathbf{W} (equation 3.17):

$$F_i = \frac{B_{i,i}}{g-1} \cdot \frac{N-g}{W_{i,i}} \quad (3.22)$$

The level of significance is obtained by comparing the test results with the test distribution. For this the degrees of freedom for the tests are necessary. The degrees of freedom for the F-test equal the number of unique eigen vectors, which is always equal or lower than the number of variables. Regarding the chi-square test, more degrees of freedoms are allowed due to the group partitioning. For the i :th linear combination the degree of freedom is $p + g - 2i$.

A low level of significance reveals that the differences are not accidental, but represented by unique variations distinguishing sample characteristics.^{24,25}

Multi-variate normal distributions of sample populations are required for PCA and DFA. Violations to the multi-variate normal distribution can lead to false analysis results. For smaller sample populations (as analyzing some few SIMS spectra) breaches to the multivariate normal distribution might generate false results. Although, analyzing larger sample populations, which generally is the case when analyzing SIMS depth profiles, some deviation to the multi-variate normal distribution will not distort the analysis results. Additionally, large sample populations often generate low levels of significance.²¹

3.3 Predicting concentrations from SIMS spectra with PCA and DFA

For the ideal case of a blend consisting of two components, one PC would identify one of the components and another PC the second component in the blend. Consequently the two PC's would capture all variance, where one PC is enough to display the composition of the two components in the blend. However, generally a principle component explains a correlation between the two components instead of the pure component, and several PC's are needed to display all correlations necessary to give information of the concentration of the blend. The correlations can be visualized in a two dimensional plot, a score plot, using the two principle components (PC1 and PC2) that capture the largest variances. In an experiment, plotting the scores of PC1 and PC2 along the x- and y-axis, the individual SIMS spectra from samples with constant concentrations appear as a group of closely spaced dots in the graph. The order of grouped dots generates a curve which follows the concentration of the samples and can be used to identify the concentration of an unknown sample. If enough variance is captured by one PC, which also has significant different scores compared to the other PCs, then the correlations between the mass channels can be explained by a single PC. Thus the PC scores of the blends will appear in consecutive order of the concentration.

Similarly, discriminant function analysis can identify concentration differences measured in dynamic SIMS spectra.

Outline of the chapter

In this chapter we investigate the possibilities of using dynamic SIMS to identify concentration gradients in stratified samples. The multivariate statistical analyses,

principle component analysis and discriminant function analysis, are applied on the SIMS depth profiles to interpret the complex SIMS spectra and obtain information of sample compositions. The interpretation analyses are applied on polymer films made from acrylate monomers and reactive mesogens and on PDLC films. The stability of PDLC samples in SIMS environment is discussed and investigated by transmission infrared measurements. A method to derive the depth resolution by discriminant function analysis making use of depth profiles by dynamic SIMS of multilayer PDLC devices is presented.

3.4 Experimental

3.4.1 Materials

Co-polymer films of acrylates and reactive mesogens

The monomers used for the polymer films were 1-cyanobiphenyl-4'-hexyloxyacrylate (LC6A) synthesized at Philips Research (Eindhoven, NL), phenylacrylate (PhA, Polysciences Inc.), iso-bornylmethacrylate (iBMA, Aldrich), and 1H1H6H6H perfluoro-1,6-hexyldiacrylate (F-acrylate, Exflur). One weight% of the photoinitiator Ir-gacure 651 (Ciba) was added to the reaction mixtures consisting of one monomer or blends of two monomers. The structures of the chemicals are drawn in figure 3.2.

Polymer films were prepared by spin-coating reaction mixtures on silicon wafers followed by 30 min UV-curing (Philips PL-S 9W/10 at 365 nm and 3 mW/cm²) at room temperature in a nitrogen environment. We calibrated the thicknesses of the spin-coated films by measuring film thicknesses of the polymerized PhA monomers with a Tencor P-10 profilometer. Films of poly(PhA) and poly(iBMA) were prepared, as well as films of polymerized blends containing 13 weight% LC6A in PhA and 52 weight% LC6A in PhA.

The polymer films of LC6A monomer were prepared differently. Since the monomer LC6A is crystalline at room temperature an elevated temperature or sol-

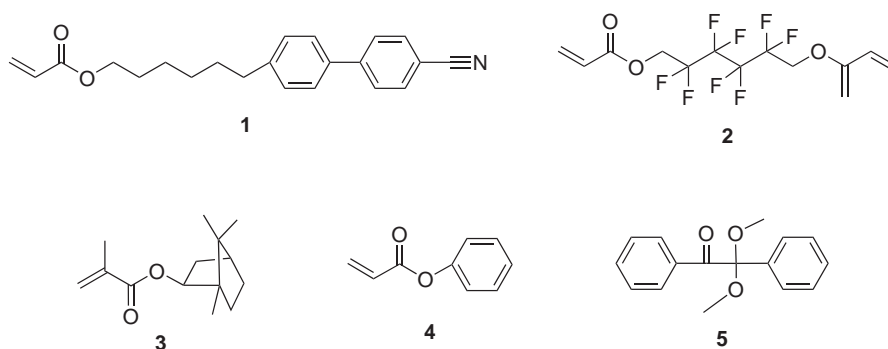


Figure 3.2: The monomers used for the co-polymer films: **1**: 1-cyanobiphenyl-4'-hexyloxyacrylate (LC6A), **2**: 1H1H6H6H perfluoro-1,6-hexyldiacrylate (F-acrylate), **3**: iso-bornylacrylate (iBMA), **4**: phenylacrylate (PhA), and **5**: photoinitiator IRG651.

vent is needed during processing. We doctor bladed the reaction mixture to a thickness of $1\ \mu\text{m}$, at 80°C onto Si-wafers. Similarly were films prepared from a blend of 39 weight% LC6A in iBMA. The UV-polymerizations were performed at 80°C in N_2 environment for 30 min.

Furthermore, two-layer samples were prepared in two steps. Reaction mixture containing the F-acrylate monomer and photoinitiator was applied in a 1 mm spaced glass cell and polymerized 30 min at room temperature. Then, the top glass-plate was removed, and on top of the poly(F-acrylate) film the reaction mixture containing iBMA monomers was spin-coated. The iBMA monomers were cured by UV-light at room temperature and in N_2 environment. The thickness of the top coating was estimated to be 20-40 nm according to the thickness calibration.

Polymer dispersed liquid crystal samples

Reaction mixtures of iso-bornylmethacrylate (iBMA, Aldrich) and blends of iBMA and the nematic LC (E7, Merck) were prepared with the addition of one weight% of the initiator Irgacure 651 (IRG651, Ciba) (figure 3.3). Thin films of homogeneous reaction mixtures were obtained by spin coating on Si-wafers. Subsequently, polymerization was induced by UV curing (Philips PL-S 9W/10 at 365nm and $3\ \text{mW}/\text{cm}^2$) during 30 min in nitrogen environment at room temperature.

The two-layer poly(iBMA)/PDLC samples were prepared by first spin casting a reaction mixture of 60 weight% E7 in iBMA followed by 30 minutes UV curing in N_2 environment. The next layer was prepared, on top of the first layer, by spin casting a reaction mixture of iBMA followed by 30 minutes UV curing in N_2 environment.

In order to investigate the quantification of LC in the vacuum system, mixtures of 60 weight% E7 in iBMA were spin coated on Si-wafers and UV cured during 30 min. These samples were capped with films of poly(vinyl alcohol) (PVA, Janssen), which were spin coated from a water solution.

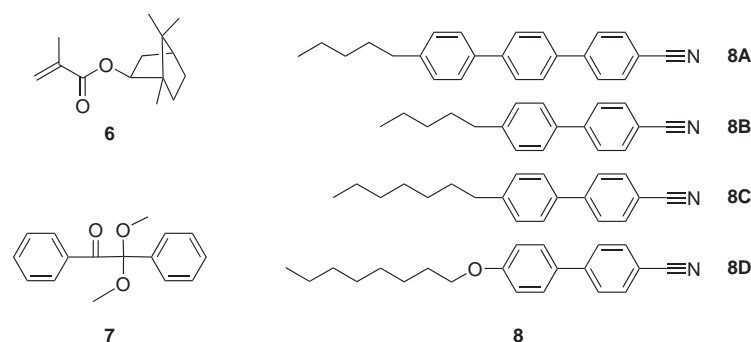


Figure 3.3: The chemicals used for the PDLC samples. **6:** iso-bornylacrylate (iBMA), **7:** photoinitiator IRG651, **8:** E7, nematic liquid crystal composed of 8% (**8A**), 51% (**8B**), 16% (**8C**) and 25% (**8D**)²⁶.

3.4.2 Analysis techniques

All dynamic SIMS measurements were obtained on a VG Ionex SIMS system, equipped with a liquid metal ion source, MIG 102, and a M12-2 s (<800 amu) quadrupole mass analyzer which measured a maximum of ten negatively charged mass fragments in consecutive order during constant sputtering. The time for measuring each of the mass channels once is called a cycle. Mass spectra were obtained by scanning the quadrupole over a range of m/z ratios during continuous sputtering. The primary ion source was operated with 10keV and 4.2nA Ga^+ , and scanned over an area of $200 \times 200 \mu\text{m}$. The secondary ion yield was, with the electronic gate, obtained from the centered 10% of the total sputtered area. In the case of measuring mass spectra, no electronic gating was possible.

Furthermore, to prevent charging of the samples during analysis we used a LEG 31F electron flood gun, additionally the samples were covered with a monolayer of conducting metal. The sputtered depths were measured by an optical profilometer (Fogale Zoomsurf 3D) and a contact profilometer (Tencor P-10). The sputter speeds were assumed constant through depth.

The infrared transmission spectroscopy (IR) was measured in transmission by a Vector 22 spectrometer (Bruker N.V.) in which the measuring chamber was flushed by nitrogen to suppress the influence of water stretch vibrations during analysis.

Prior to the multivariate statistical analysis, the dynamic SIMS spectra were normalized on the total secondary ion intensity per cycle (the time interval where the fingerprints of the m/z 's were obtained). The normalization minimizes the differences in operating conditions between the samples, such as unpredictable charging of the sample or instabilities of the primary ion source.

We used the commercial software package SPSS (release 11.0.1, SPSS Inc.) to study the DFA on the co-polymer samples. For the PDLC samples, we solved the eigenvalue problems with the programming language MatLab (The MathWorks, Inc.).

3.5 Results and discussion

The dynamic SIMS mass spectra of polymerized LC6A (poly(LC6A), figure 3.4(a)) showed low-mass fragment ions coming from six major m/z ratios: 12, 16, 24-25, and 48. All of these m/z ratios originate from common (non-specific) carbohydrate ion fragments, except m/z 16 that represents O^- (oxygen ion). The measured mass intensities of poly(PhA) also showed low mass fragments from common hydrocarbon ions (figure 3.4(b)), with the exceptions of m/z 16: O^- , and m/z 19 (F^-). The latter ion, F^- , was considered as contamination, since no fluorine should be present in the PhA polymer. The mass spectra of the poly(iBMA) (figure 3.4(c)) only showed common hydrocarbon mass-fragments. The correlations between the intensities of the m/z ratios differed between the polymers.

Even though none of the measured m/z ratios were specifically characteristic for any of the three polymers (poly(LC6A), poly(PhA) and poly(iBMA)), the fingerprints (the combinations of the m/z ratios for each individual compound that were

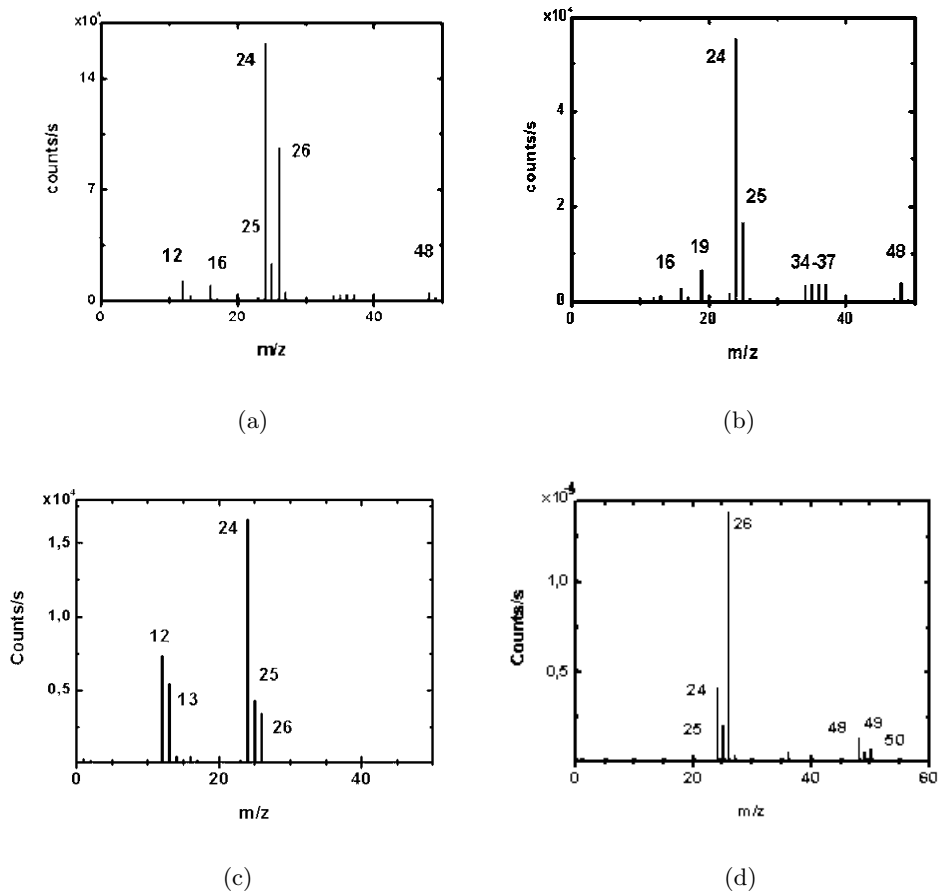


Figure 3.4: Dynamic SIMS mass spectra of (a) poly(LC6A), (b) poly(PhA), (c) poly(iBMA) and (d) the nematic liquid crystal E7. The most intense mass fragments are noted in the spectra.

measured in the SIMS mass spectra) are unique for the three different materials.

First, we analyzed several SIMS mass spectra of polymer films made from reaction mixtures containing LC6A monomers, PhA monomers and blends of LC6A and PhA monomers. We used seven common mass fragments (m/z 12, 16, 24-26 and 48) for the DFA analysis. The choice of these m/z ratios were based on the mass spectra of poly(LC6A) and poly(PhA) (figure 3.4). Each of the film compositions were defined as one group in the DFA analysis, which generated three degrees of freedom for the analysis. As a consequence, three DFA functions showed unique sample characteristics. The two first functions were significantly different below the 5% level, while the third was significantly different below the 15% level, using the chi-square test. Since the two first DFA functions were significantly different and captured most of the variance, 99,7%, we used these two in the DFA score plot (figure 3.5). In the plot the different compositions of the films were separated, as a consequence of dissimilar DFA scores. The increasing concentration of PhA in

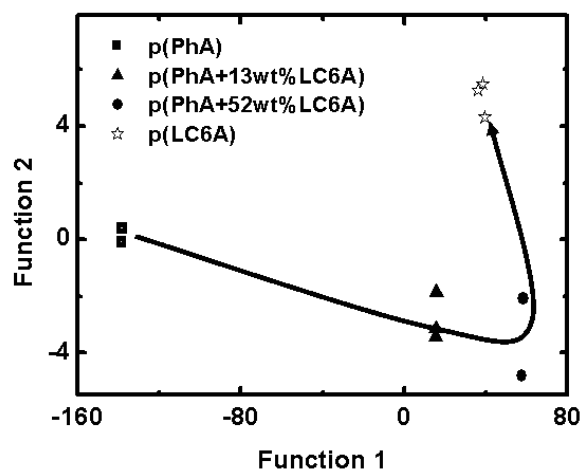


Figure 3.5: Discriminant function analysis (DFA) of poly(LC6A), poly(PhA), and two polymerized blends of LC6A and PhA. DFA creates independent functions from the SIMS spectra, with these functions DFA discriminates between the compositions in the samples. Function 1 and 2 explain significant difference between the sample compositions (at a significance level of 5%) and the functions contains 99.7% of the initial data from the SIMS spectra. As a result, the increasing concentration of LC6A in the samples is followed by the arrow in the plot.

the samples is visualized by the arrow in figure 3.5, indicating a calibration curve, following the increase of poly(LC6A) concentration. This analysis illustrates the capability of the classification analysis DFA to distinguish between samples having different composition. In this way the dynamic SIMS spectra and DFA can construct calibration curves on which prediction analysis can be applied to extract unknown sample concentrations.

Next we analyzed the samples of poly(LC6A), poly(iBMA), and a polymerized blend of LC6A and iBMA. The dynamic SIMS spectra from these samples were obtained by collecting ten m/z ratios in depth (m/z 12, 13, 16, 19, 24-26, 31, 38, and 48, figure 3.4). Of the ten mass fragments analyzed, we used four common ones (m/z 24-26 and 48) for the DFA. The four chosen mass fragments were detectable in all samples and gave stable intensities during the in-depth measurement. Each sample was divided into three groups, where every group consisted of 20 SIMS measuring cycles. In total we pre-defined 9 groups for the DFA analysis. The purpose was to investigate whether DFA could cluster the groups from the same samples as well as separate between the samples with different compositions.

The DFA analysis of the three samples generated 8 DFA functions; the two first functions contained 99.5% of the variance and were both significantly different on the 0.01% level. When plotting these functions (figure 3.6), we found the groups from the same samples clustered while the different sample compositions were separated. This visual identification is useful to recognize concentrations (in the form of a

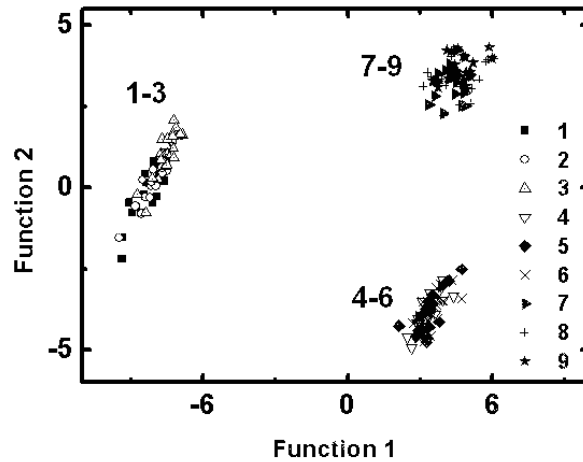


Figure 3.6: The two first DFA functions plotted for poly(LC6A), poly(iBMA), and a polymerized blend of LC6A and iBMA. The samples were divided into three groups each, where group 1-3 corresponded to poly(iBMA), group 4-6 to the blend, and group 7-9 to poly(LC6A).

calibration curve), and to identify layer compositions in layered samples.

The accuracy of the calibration curves depends on the spread of data points of the same samples in the DFA plot. We investigated possible sources of these variations and found that the scattering of the data points in the DFA plot correlated with instabilities of the SIMS yields. The instabilities in the SIMS yields might depend on local concentration variations in the samples, local charging of the sample during SIMS analysis, or other effects, which are not easy to identify. Variations of the concentrations on a scale comparable to, or larger than, the analyzed volume might be a source for instabilities. Note that we implicitly assumed that local variations, if any, were on a smaller scale than the analyzed volume.

Continuously, we analyzed samples of poly(F-acrylate) covered by poly(iBMA). Ten mass fragments (m/z 12, 13, 16, 19, 24-26, 31, 38, and 48) were followed in depth during the SIMS depth profile of such a sample (figure 3.7). The depth of the sputtered crater measured 101 nm, and since we assume the sputter speed to be constant, each cycle (the time measuring the ten masses) corresponds to 1 nm. In the SIMS spectra, the intensity of m/z 19 (F^-) represented specifically poly(F-acrylate). Surprisingly, we detected m/z 19 at the top of the sample, where no fluorine-containing polymer should be present since that mass channel is not detected in the mass spectra of poly(iBMA) (figure 3.4(c)). Furthermore, the intensity of m/z 19 gradually increased to a constant value, which was approached at the depth of approximately 60 nm.

Since the m/z ratio 19 labeled the poly(F-acrylate), this mass fragment could alone identify the pure poly(F-acrylate) film. However, we decided to study the possibility to identify polymer films by non-specific mass fragments. Therefore DFA

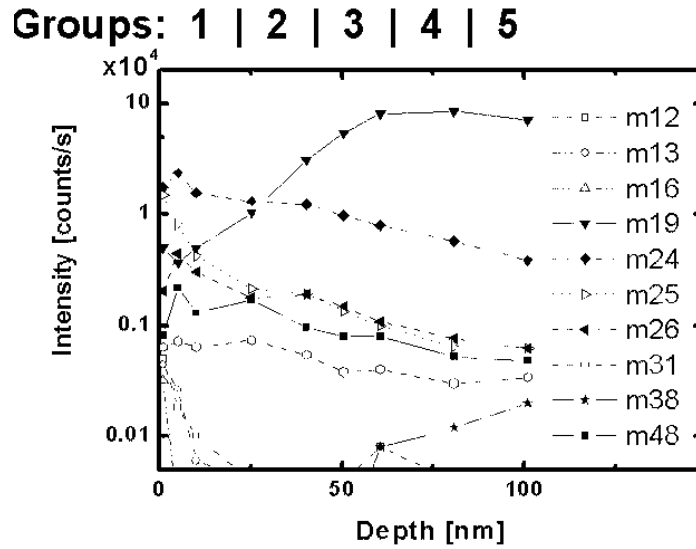


Figure 3.7: Dynamic SIMS depth profile of the poly(F-acrylate) film covered by poly(iBMA). Each group consists of 20 nm from the depth profile.

was applied on the depth profile of the two-layer sample, together with the dynamic SIMS spectra of poly(iBMA) and poly(F-acrylate). The DFA analysis was performed using four common mass fragments (m/z 24-26 and 48). The depth profile was divided into five groups, where each group consisted of a depth interval of 20 nm (20 cycles). In total we pre-defined seven groups, 5 for the layered sample and one each for poly(iBMA) and poly(F-acrylate). The statistical analysis gave six degrees of freedom and a maximum six DFA functions. From the analysis, the three first DFA functions were significant different at a level 0.01%, and the two first functions captured together 99.4% of the variance. The plot of function 1 versus function 2 separated the pure poly(iBMA) and poly(F-acrylate) samples, and spread the data points of the groups from the depth profile between them (figure 3.8). We found that group 4 and 5 coincided with the cloud of points belonging to the poly(F-acrylate). This showed that the pure poly(F-acrylate) layer in the depth profile started at around 60 nm, which was also seen from the labeled SIMS spectra. Note that the first group did not fall on the poly(iBMA) in figure 3.8. The separation between group 1 and poly(iBMA) shows that the top-coating on the two-layer sample was not pure poly(iBMA). This is in agreement with the SIMS depth profile, in which m/z 19 was detected at the top of the sample.

As a comparison with optical devices, which can be prepared by e.g. holography, the sample of poly(F-acrylate) covered by poly(iBMA) served as a model for one pitch in a layered grating. When layered electro-optical devices are produced by photopolymerization-induced phase separation, the interfaces depend on the light intensity profile curing the film, and the interfaces are unlikely to be sharp. The interface of our model sample showed a similar behavior; from the top of the sample

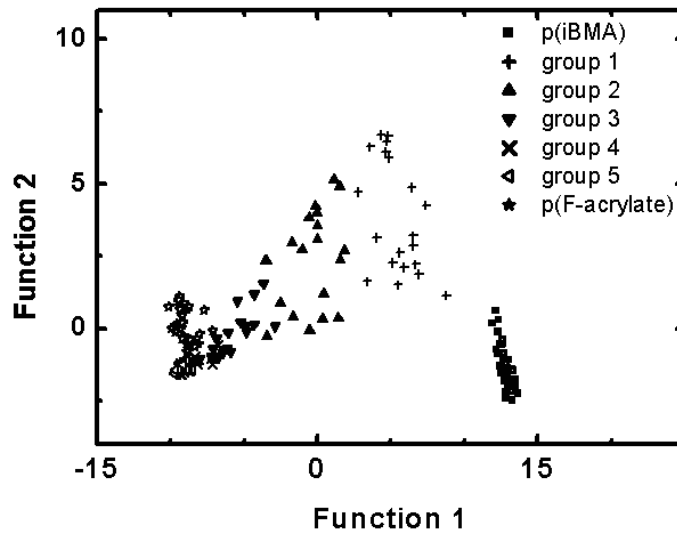


Figure 3.8: DFA of poly(iBMA), poly(F-acrylate) and sample in figure 3.7, which was divided into 5 groups, where group 1 contained the first 20 nm from the SIMS depth profile, the second group the following 20 nm, etc.

the intensities of the m/z ratios gradually changed until a depth of about 60 nm was reached. From this depth on, the intensities remained stable, and we assumed to have reached the poly(F-acrylate) film at 60 nm. Apparently the iBMA monomers migrated into the F-acrylate polymer before polymerizing, and resulted in a model for samples with a concentration gradient.

For all co-polymer samples the classification analysis DFA is useful for spectra identification. Principle component analysis was also studied on these sample, but did not simplify the interpretation of the SIMS depth profiles.

3.5.1 Polymer dispersed liquid crystal samples

Films of poly(iBMA) and E7 were identified by negative ion SIMS mass spectra (figure 3.4(c) and 3.4(d)). The largest contributions to the spectra originate from eight low mass fragments with m/z : 12, 13, 24-26, and 48-50. The detected ions originate from low mass hydrocarbons; however in the E7 spectrum m/z 26 stands out and represents apart from the common $C_2H_2^-$ fragment, also of the cyano ion CN^- . Since nitrogen is not present in poly(iBMA), CN^- is characteristic for the liquid crystal. If the contribution of CN^- to m/z 26 would have been linear related to the amount of E7 in the sample, quantification could have been derived directly from the m/z 26 peak. We did not find a linear relation of the m/z 26 peak and the concentration of E7 in blends, which indicates that the blend's matrix induces a non-linear secondary ion yield, commonly found for organic matrices. Therefore we applied MVA to identify the sample compositions.

We followed nine m/z 's in depth with dynamic SIMS, to measure the correlation

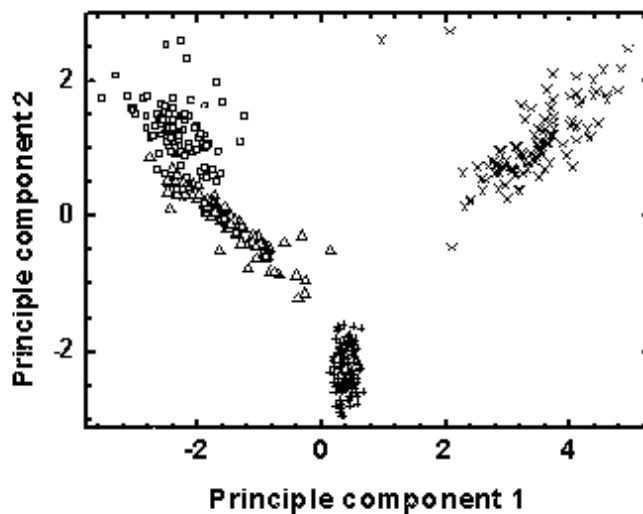


Figure 3.9: Multivariate statistical analysis, PCA applied on normalized dynamic SIMS spectra of blends □: poly(iBMA), Δ: poly(iBMA)+25 weight% E7, +: poly(iBMA)+60 weight% E7, ×: E7.

of the secondary ions from the bulk material of the blends. Added to the eight m/z 's found in the mass spectra of poly(iBMA) and E7 in figure 3.4(c) and 3.4(d), was m/z 16 (O^-); oxygen is present in both the polymer as in the LC. PCA was applied to the dynamic SIMS data to reduce the number of variables explaining the blends. In figure 3.9, the PCA values of the blends are plotted for the two first PCs, each symbol in the plot corresponds to a SIMS cycle. The first PC clearly separates the pure poly(iBMA) and E7, while the second PC mainly adds information for the 60 weight% E7 blend to be separated from the rest. The two first principle components contain 82% of the variance, which means that 18% of the initial information is not displayed in the score plot. Here, the main task is to identify the blends, therefore when a consecutive PC does not add more separation, it is not considered. With 82% of variance the centroid of the cycles corresponding to the pure E7 is separated from the other sample compositions, as is the PDLC with 60 weight% E7. Although the centroids of poly(iBMA) and the blend of 25 weight% E7 are clearly separated, the clouds corresponding to all the cycles are partly overlapping. Apparently, the low concentration blend is not fully separated from poly(iBMA), which indicates either that PCA is not capable to identify the relevant correlations of m/z 's for each cycle or that the concentrations are altered during SIMS analysis.

Since SIMS measurements are performed in vacuum (10^{-9} mbar), which can induce evaporation of volatile compounds, we investigated the stability of the blends during analysis. From a film consisting of pure E7, only 5 weight% was evaporated during 5 hours in 10^{-9} mbar, measured by weighting the sample before and after the vacuum treatment. To study the evaporation of the PDLC blends, transmission

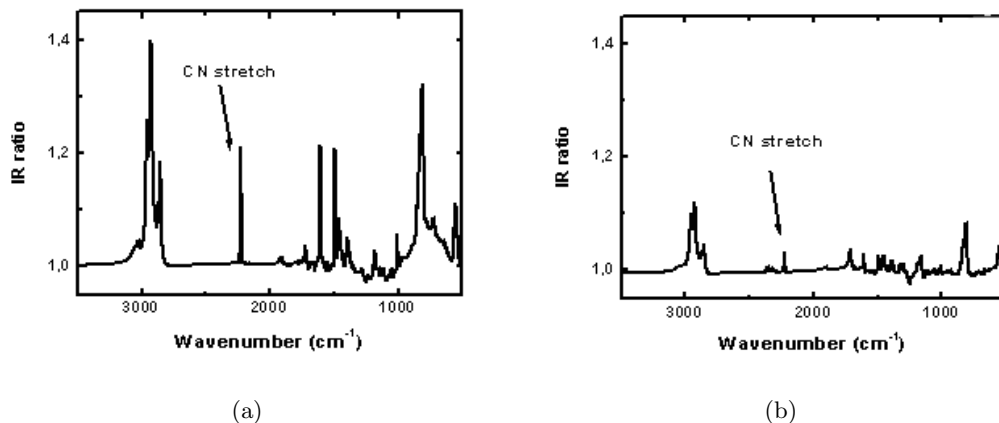


Figure 3.10: (a) Ratio of IR spectra before and after addressing PDLC samples of 60 weight% E7 in poly(iBMA) into SIMS vacuum. After one hour in vacuum, the CN⁻ stretch lost 26% of intensity, indicating evaporation of E7. (b) By capping the PDLC sample with poly(vinyl alcohol), the evaporation of E7 was reduced by 85% loss of peak intensity.

infrared (IR) spectroscopy was used. IR measurements before introducing a PDLC sample of 60 weight% E7 in a matrix of poly(iBMA) into vacuum were compared with IR measurements after one hour in SIMS vacuum environment. The ratio of the two spectra gave information of the E7 evaporation by the peak for the CN stretch at 2226 cm^{-1} , characteristic for the cyanobiphenyl component in E7²⁷. In figure 3.10(a) the CN stretch of E7 is visualized as a peak at 2226 cm^{-1} , with a loss of intensity of 26%. Therefore for quantification purposes, the effect of the evaporation cannot be neglected. To prevent evaporation, we studied with IR spectroscopy the possibility of capping PDLC samples with poly(vinyl alcohol) (PVA), which is known for its low permeability to gases. For a PDLC of 60 weight% E7 in a matrix of poly(iBMA) capped by PVA, the IR spectra were measured before entering the capped PDLC into vacuum, and after one hour in vacuum. The IR ratio of the capped PDLC (figure 3.10(b)) compared with the IR ratio of an uncapped sample, revealed a reduction of the E7 evaporation by 85% loss of peak intensity. The suppression of E7 evaporation, allows introducing PDLC samples into vacuum systems for analysis. Unfortunately, it can be envisaged that E7 will evaporate during SIMS analysis since the capping layer of PVA is broken open by the primary ion bombardment. Consequently, a better scheme for analyzing PDLC multilayer devices is capping with PVA for introducing the sample in the vacuum chamber, followed by immediate cooling to cryogenic temperatures, which prevents evaporation of the volatile LC molecules. On the cooled device SIMS analysis can be carried out with the multivariate statistical analysis for quantification.

The concentration decrease caused by evaporation of E7, prevented PCA to separate the samples with different compositions in figure 3.9. To maximize the difference between the samples and hence better separate the different compositions, DFA was applied on the SIMS spectra. The same dynamic SIMS spectra as used in PCA were utilized for DFA; the groups for the statistical analysis were based on the

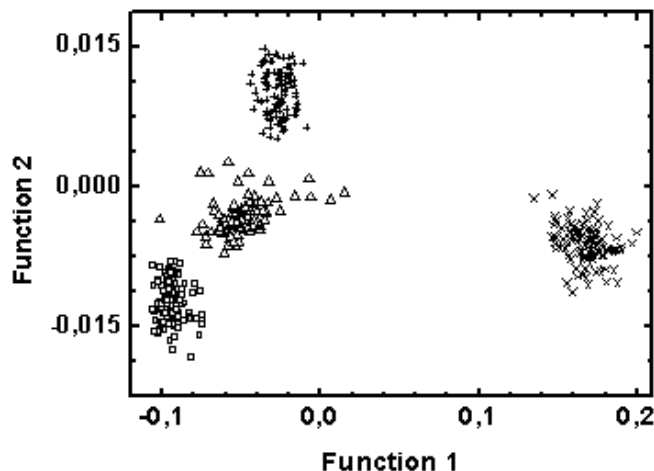


Figure 3.11: DFA on normalized dynamic SIMS spectra of blends (\square : poly(iBMA), Δ : poly(iBMA)+25 weight% E7, $+$: poly(iBMA)+60 weight% E7, \times : E7).

concentrations of the blends. Figure 3.11 shows the DFA score plot in which each point in the graph represents a SIMS spectra in depth. Two first functions captured 97% of the variance. As seen in figure 3.11, poly(iBMA) and E7 are well separated, as are the two blends. Largest separation is achieved by the first function, but also the second function reveals information of the correlation between the blends; in order to use the DFA to construct a calibration curve, both functions are needed. Additional functions do not separate blends further and are disregarded. In spite of the evaporation of E7, centroids of clusters of points from the blends lay on a curve with consecutive order in E7 concentration. Since DFA manages to separate low concentration blends, DFA is probably more efficient than PCA for identifying E7 in small concentration differences. However, to use DFA in combination with predictive analysis, first evaporation of E7 has to be prevented.

3.5.2 Depth resolution of stratified PDLC films

The minimum pitch of multilayer PDLCs that can be measured by SIMS, depends on the depth resolution of the analysis. Knowing that DFA efficiently identifies small concentration differences in layers, we explored the possibility to use DFA to derive the depth resolution. We depth profiled an uncapped two layer poly(iBMA)/PDLC sample by dynamic SIMS (figure 3.12). Nine m/z 's (m/z 12, 13, 16, 24-26, 48-50) were followed in depth. Out of the nine m/z 's, the common carbon fragment C_2^- , m/z 24, yields the largest intensity. Two m/z 's are hardly detectable; m/z 13 which represent CH^- is detected only at the surface of the top layer, while m/z 50 is only sporadically measured in the bottom layer. The SIMS spectrum in figure 3.12 shows a change in secondary ion yield at about 1 μm depth, indicating the interface of the top-and the bottom layer. To distinguish between the layers on the basis of the

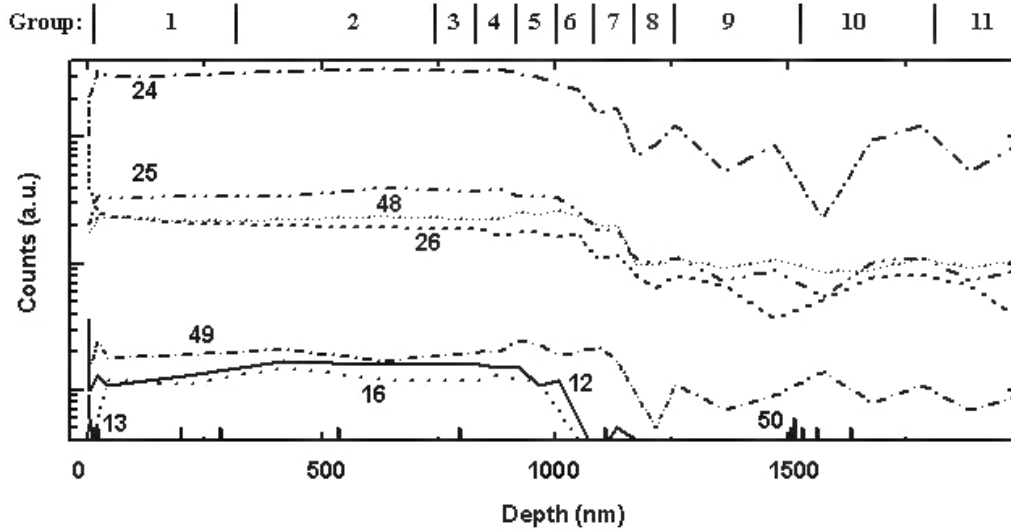


Figure 3.12: Dynamic SIMS depth profile of artificial made two layer sample of poly(iBMA) coating on a polymer dispersed liquid crystal consisting of the nematic liquid crystal (E7) and poly(iBMA). Nine masses, m/z 12, 13, 16, 24, 25, 26, 48, 49, and 50, were followed in depth. The eleven groups are used by the multivariate statistical analysis DFA to distinguish between the two layers.

change in the measured mass fragments, DFA was applied to the depth profile. The SIMS depth profiles were divided into eleven groups, displayed in top of figure 3.12. The top and bottom layers were assigned four and three groups respectively; to label the position of the interface it was divided into four groups with small depth intervals. In figure 3.13(a), the DFA of the artificial two-layer PDLC is shown, groups with equal correlations between the mass channels are located at the same position in the plot, while the groups from the interface are spread between the top and bottom layer positions. The separation of the two layers is clearly visible by, and highly dependent on, the first function, the second function is not adding more separation between the layers. Since function 1 yields 93% of the variance and displays significant differences between the groups (table 3.1), it contains enough information to derive the depth resolution. In figure 3.13(b), where the first DFA function is plotted versus the SIMS cycles, an S shaped curve is obtained. At 16-84% (corresponding to σ) of the height of the curve, the depth resolution was determined to 130 nm. At a shallower depth a lower depth resolution would be obtained since

Table 3.1: The statistical information as cumulative eigenvalue and the significance for the first DFA function of the depth profile of poly(iBMA)/PDLC sample.

DFA function	Eigenvalue	Eigenvalue [weight%]	Chi-square	Degrees of freedom	Significance
1	17.6	93.1	2454	18	0.1% level

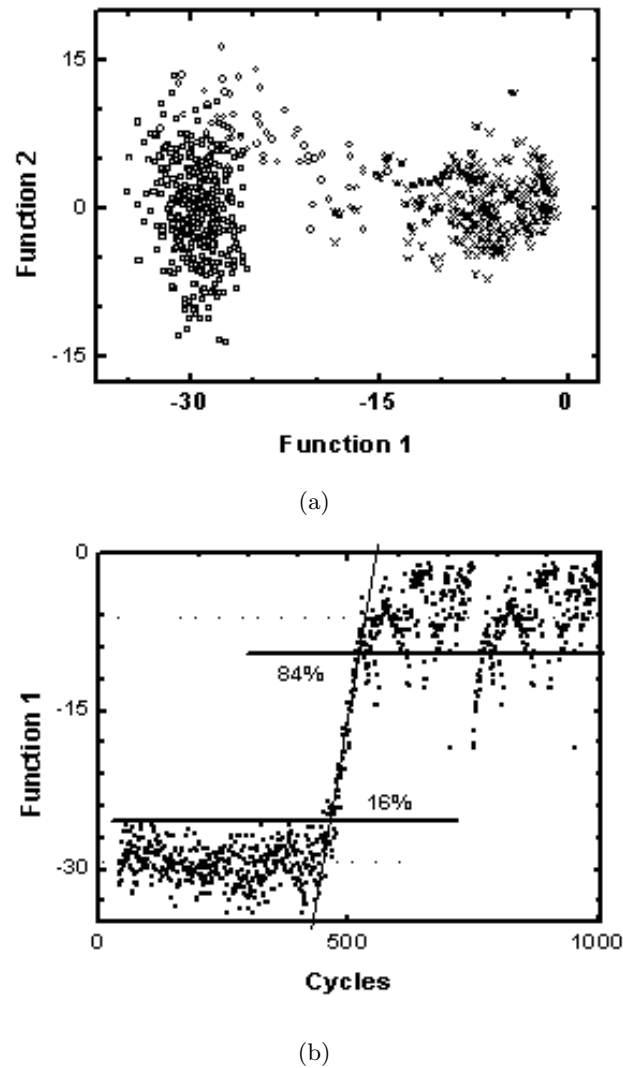


Figure 3.13: (a) DFA on the SIMS spectrum of poly(iBMA)/PDLC, \square : group 1-4, \circ : group 5-6, \times : group 7-11, the groups for the analysis is displayed in fig. 5. (b) DFA function 1 from the analysis in fig 6a, plotted versus SIMS cycles to determine the depth resolution of the SIMS measurement. After converting the cycles to depth units of 2,1 nm, the depth resolution was determined to 130 nm.

the depth resolution relies on roughness of the crater surface, which increases by sputtering and thus degrades the resolution with depth^{28,29}. Therefore, using SIMS to distinguish between concentration differences in grating pitches reflecting visible light, the analysis should be performed at small depths in the samples.

3.6 Conclusions

Dynamic SIMS depth profiles result in complex fingerprint spectra. By applying multivariate statistical analysis to the SIMS spectra, we could identify different polymers and their blends. We have shown that discriminant function analysis efficiently distinguishes between films with different compositions, both for co-polymer samples as for PDLC films. Furthermore concentrations can be derived using calibration curves calculated by the multi-variate statistical analyses.

Quantification of the concentrations of E7 in PDLCs was complicated by evaporation of the nematic liquid crystals. Evaporation was suppressed by capping the PDLC samples with poly(vinyl alcohol) before inserting samples into the SIMS vacuum system.

The separation of the compositions by DFA can be utilized to derive the depth resolution of SIMS depth profiles. The depth resolution of a sample of a poly(iBMA) coating on a polymer dispersed liquid crystal consisting of the nematic liquid crystal (E7) and poly(iBMA) was found to be 130 nm, which is comparable to the grating pitch of a violet reflecting stratified PDLC film.

3.6.1 Improvements to interpret SIMS depth profiles of stratified polymer dispersed liquid crystals

To quantify LC concentrations in stratified PDLCs, the interpretation of SIMS spectra has to be improved by developing the experimental conditions. First, slower sputtering than used in this study (1 - 2.1 nm/s) will improve the depth resolution. It is essential that the depth resolution is superior to the grating periodicity. A slower sputtering rate is obtained by lowering the current on the primary ion source, also a faster detection system than the quadrupole analyzer is favorable. Such a detector is the time-of-flight, which simultaneously measures all secondary ions sputtered from the sample surface. In this way a larger number of ions are detected per time unit, which is favorable for the multivariate statistical analysis.

Secondly, the stability of the PDLC samples has to be controlled during SIMS analysis. Capping the sample with poly(vinyl alcohol) and performing the SIMS analysis at cryogenic temperatures should suppress the evaporation of LCs. SIMS spectra from cooled and capped stratified PDLC films are believed cogent for quantification purposes.

If larger and component unique fragments are sputtered from the sample surface with e.g. cluster ions as primary ion source, sample identification can directly be obtained from the SIMS depth profile. In that case, statistical analysis would not supply additional information. However, depth profiling generally induces polymer fragmentation with the result that spectra identification can only be based on the fingerprint region of low mass fragments. In the latter case, MVA is a useful tool.

Quantification of liquid crystal concentrations in PDLC gratings from SIMS depth profiles are presented and discussed in chapter 4. The depth profiles were obtained at cryogenic temperatures using slow sputter rates to collect characteristic secondary ions representing the concentrations in the layered PDLC films.

3.7 References and notes

1. Zalm, P. C. *Vacuum* **45**, 753–772 (1994).
2. Wien, K. *Nucl. Instr. And Meth. In Phys. Res. B* **131**, 38–54 (1997).
3. Benninghoven, A. *Surf. Sci.* **299/300**, 246–260 (1994).
4. Rysz, J., Ermer, H., Budkowski, A., Lekka, M., Bernasik, A., Wróbel, S., Brenn, R., Lekki, J., and Jedliński, J. *Vacuum* **54**, 303–307 (1999).
5. Bulle-Lieuwma, C. W. T., van Duren, J. K. J., Yang, X., Loos, J., Sieval, A. B., Hummelen, J. C., and Janssen, R. A. J. *Appl. Surf. Sci.* **231/232**, 274–277 (2004).
6. Mattsson, J., Forrest, J. A., Krozer, A., Södervall, U., Wennerberg, A., and Torell, L. M. *Electrochim. Acta* **45**, 14531461 (2000).
7. Wagner, M. S. *Anal. Chem.* **77**(3), 911–922 (2005).
8. Mahoney, C. M., Yu, J., and Jr, J. A. G. *Anal. Chem.* **77**, 3570–3578 (2005).
9. Eynde, X. V. and Bertrand, P. *Appl. Surf. Sci.* **141**, 1–20 (1999).
10. Li, L., Chan, C.-M., Ng, K.-M., Lei, Y., and Weng, L.-T. *Polymer* **42**, 6841–6849 (2001).
11. Delcorte, A., Bertrand, P., Arys, X., Jonas, A., Wischerhoff, E., Mayer, B., and Laschewsky, A. *Surf. Sci.* **366**, 149–165 (1996).
12. Bernasik, A., Rysz, J., Budkowski, A., Kowalski, K., Camra, J., and Jedliński, J. *Macromol. Rapid Commun.* **22**, 829–834 (2001).
13. Eynde, X. V. and Bertrand, P. *Surf. Interface Anal.* **25**, 878–888 (1997).
14. Coullerez, G., Léonard, D., Lundmark, S., and Mathieu, H. G. *Surf. Interface Anal.* **29**, 431–443 (2000).
15. Canteri, R., Speranza, G., Anderle, M., Turri, S., and Radice, S. *Surf. Interface Anal.* **35**, 318–326 (2003).
16. Graham, D. J., Price, D. D., and Ratner, B. D. *Langmuir* **18**, 1518–1527 (2002).
17. Wagner, M. S., Graham, D. J., Ratner, B. D., and Castner, D. C. *Surf. Sci.* **570**, 87–106 (2004).
18. McArthur, S. L., Wagner, M. S., Hartley, P. G., McLean, K. M., Griesser, H. J., and Castner, D. C. *Surf. Interface Anal.* **33**, 924–931 (2002).
19. van Gennip, W. J. H. *The analysis of polymer interfaces*. PhD thesis, Eindhoven University of Technology, (2003).
20. Johnson, R. A. and Wichern, D. W. *Applied multivariate statistical analysis*. Prentice-Hall Inc., New Jersey, 5th edition, (2002).
21. Klecka, W. R. *Discriminant analysis*. Number 07-019 in Sage university paper series on Quantitative applications in the social sciences. Sage Publications, Inc., London, (1987).
22. Wold, S., Esbensen, K., and Geladi, P. *Chemom. Intell. Lab. Syst.* **2**, 37–52 (1987).

23. Anderson, T. W. *An introduction to multivariate statistical analysis*, chapter 11, 451–479. John Wiley and sons, Inc., New York, 2nd edition (1984).
24. Manly, B. F. J. *Multivariate statistical methods: A primer*. Chapman and Hall, Ltd., Bristol, (1988).
25. Maisel, L. *Probability, statistics and random processes*, chapter 7, 129–161. Simon and Schuster, Inc., New York (1971).
26. Ono, H., Kawamura, T., Frias, N. M., Kitamura, K., Kawatsuki, N., and Norisada, H. *Adv. Mater.* **12**, 143–146 (2000).
27. Urano, T. I. and Hamaguchi, H.-O. *Chem. Phys. Let.* **195**, 278–292 (1992).
28. Wöhner, T., Ecke, G., Rössler, H., and Hofman, S. *Surf. Interface Anal.* **26**, 1–8 (1998).
29. Gray, K. H., Gould, S., Leasure, R. M., Musselman, I. H., Lee, J. J., Meyer, T. J., and Linton, R. W. *J. Vac. Sci. Technol. A* **10**, 2679–2684 (1992).

Chapter 4

Liquid crystal concentrations in stratified PDLCs Simulations and experiments

4.1 Introduction

Stratified liquid crystal-polyacrylate films have shown great importance in switchable electro-optical devices such as reflective displays^{1,2}. Periodic concentration differences in polymer dispersed liquid crystals (PDLCs) are obtained by photopolymerization induced phase separation from a homogeneous blend of multi-functional monomers and liquid crystals (LCs)^{3,4}. By altering the light intensity in depth, with e.g. laser beam holography, multilayer films can be produced⁵. The holographic interference pattern induces a position dependent reaction rate, which creates local distortions in the compositional equilibrium causing diffusion of the reactive materials to the high intensity sites. Non-reactive materials, i.e. the liquid crystals, are transported towards the low intensity sites. For a certain LC concentration, phase separation takes place at a critical monomer conversion. The liquid components separate from the polymer forming periodic layers of LC droplets in the polymer matrix.

Phase separation during photopolymerization can be considered as the process where a liquid phase, containing only liquid components (monomers and liquid crystals) emerges from the three-component phase of polymers, monomers and liquid crystals. The latter phase is created during the polymerization of the monomer-LC mixture. The two phases can coexist when the system is in thermodynamically equilibrium, expressed as a minimum in Gibbs free energy. Three effects are assumed to contribute independently to the free energy of the system: isotropic mixing, network elasticity and nematic ordering. First, the isotropic mixing takes into account the relative size of the molecules and the van der Waals interactions between different species⁶. Secondly, the elasticity of a cross-linked network can affect the phase separation considerably, dense cross-links can lead to phase separation at low conversions⁷. Thirdly, the theory of Maier and Saupe for nematic ordering is adopted

to account for the extra term originating from the nematic ordering of the liquid crystals⁸. A model simulating the phase separation was introduced in chapter 2. Combining it with the reaction-diffusion kinetics characteristic for the holographic recording, the morphology, e.g. the concentration of LCs in the layers, of the grating can be predicted.

Controlling photopolymerization-induced phase separation to produce the desired concentration gradients of LCs in complex structured PDLC films is essential for the ultimate device properties. One major reason is that we do not have any satisfactory way to accurately identify when and where the phase separation takes place. Experimentally, imaging techniques such as spectroscopy and scanning electron microscopy usually characterize the devices in respect of reflected/transmitted wavelength and grating periodicity. However, these analysis techniques are dependent on the contrast between the layers. Moreover they do not provide quantitative information on the composition of layers. An analysis technique that identifies phase separation and measures the local concentrations would aid in our development of structured PDLC films.

In our preliminary studies (in chapter 3) we investigated multivariate statistical analyses (MVA) to interpret secondary ion mass spectrometry (SIMS) spectra in order to get information of LC concentrations in polymer matrices^{9,10}. Analyzing PDLCs by SIMS is difficult due to the volatility of the LC molecules. To overcome this problem it was suggested to apply an evaporation barrier of poly(vinyl alcohol) which allows introduction of the sample into the high vacuum, followed by performing the SIMS analysis at cryogenic temperatures to prevent evaporation during sputtering⁹.

Traditionally, quantification from SIMS spectra is retrieved by the relative peak intensities (RPI) of two characteristic ion intensities¹¹. Normally, RPI is applied to quantify two-component blends, where the investigated ion intensity ratio originates from two mass channels that both uniquely represents one of the two components in the blend. However, this technique requires that the sputter process is independent of the sample composition (i.e. sample matrix), and that the two ion fragments correctly reflect the concentration differences in the samples. This is not always the case when depth profiling polymer matrices.

Recently, the multivariate regression analysis, partial least square (PLS), was applied on SIMS spectra to predict surface concentrations of polymer blends and adsorbed proteins^{12,13,14}. PLS can be applied directly on the ion yields from the SIMS spectra, or the input data can be pre-treated by e.g. multivariate statistical analysis as principle component analysis (then the regression analysis is called principle component regression, PCR). As is normal in regression analysis, parts of the data are regarded as errors and are discarded from the analysis. In order to control this error selection and to understand the interpretation analysis we have chosen to perform the analysis in two steps: First we interpret the SIMS depth profiles by MVA, continued by a regression analysis to create calibration curves to predict concentrations in the layered PDLC films. This approach allows a qualified selection of the data for which the predictive analysis is applied.

Outline of the chapter

This chapter reports the first successful attempt to measure LC concentrations in depth of multilayer LC-polyacrylate films. The samples were covered with poly(vinyl alcohol) to enable vacuum processing without LC evaporation. Consequently, dynamic SIMS spectra of PDLC reflection gratings were obtained at cryogenic temperatures to suppress evaporation of the LCs. Multivariate statistical analyses are applied on the dynamic SIMS spectra to interpret the spectra, and regression analysis to obtain the LC concentrations in depth of the gratings.

The experimental measured concentrations are compared with simulations of the holographic grating formation. The simulations are based on a combined phase separation and reaction-diffusion model introduced in chapter 2.

4.2 Experimental

Multilayer samples were prepared from a mixture of 29.9 weight% liquid crystals (E7, Merck) mixed with 70.1 weight% of a monomer blend consisting of 65.9 weight% dipentaerythritolhydroxy pentacrylate (DPHPA, Polysciences Inc.), 14.1 weight% N-vinyl-2-pyrrolidone (NVP, Aldrich) and 19.0 weight% hexafluoro bisphenol A diacrylate (6F-bisA, Polysciences Inc.) and 1.0 weight% of the UV-sensitive photoinitiator Irgacure 369 (IRG369, Ciba Speciality Chemicals). Figure 4.1 shows the chemical structures of the materials.

Reflection gratings were recorded with the interference pattern of an Ar⁺ laser at a wavelength of 351 nm. The reaction mixture was sandwiched between a Si wafer coated with 150 nm Ag and a cover glass slide. The interference pattern was gener-

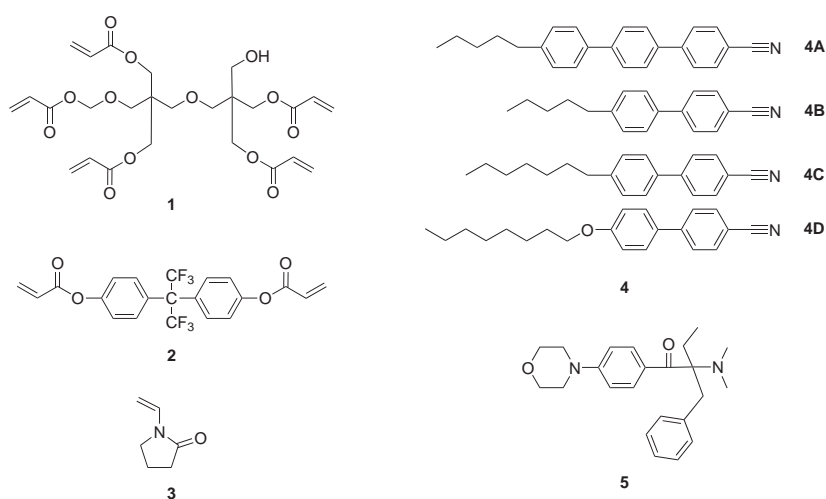


Figure 4.1: Molecular structures of **1**: dipentaerythritolhydroxy pentacrylate (DPHPA), **2**: hexafluoro bisphenol A diacrylate (6F-bisA), **3**: N-vinyl pyrrolidone (NVP), **4**: E7, components (composition of E7 mix¹⁵: 8% (**4A**), 51% (**4B**), 16% (**4C**) and 25% (**4D**)), **5**: photoinitiator Irgacure 369.

ated by an incoming and a reflected laser beam. The periodicity of the interference pattern and thus the grating pitch was controlled by the angle of incidence of the laser beam to the sample. We coupled the laser beam onto the sample with a prism, using cyclohexane as contact liquid to reduce losses from total internal reflections. The intensity of the laser beam was 1.7 mW cm^{-2} , and the illumination time was 30 s. After recording of the interference patterns, the samples were flood exposed by 0.3 mW cm^{-2} (Philips Cleo 15 W) for 20 min in order to fix the grating.

The layer periodicities were analyzed by scanning electron microscopy (SEM, XL 30 ESEM-FEG, Philips) of the cross section of the holographic sample. Thereto the samples were broken in liquid nitrogen, followed by removal of the liquid crystal at the cross section by washing with methanol. Prior to the SEM analysis, a conducting layer of 15 nm gold was sputter coated (K575 XD Turbo sputter coater, Emitech, Ltd.) on the remaining polymer layers of the cross section.

Calibration samples with different concentrations of E7 were prepared with the same monomer blend as for the layered samples (65.9 weight% DHPA, 14.1 weight% NVP, and 19.0 weight% 6F-bisA and 1.0 weight% IRG369). Six calibration concentrations were made by mixing 0, 19.3, 29.9, 39.7, 44.9, and 60.7 weight% E7 into the monomer blend. The calibration mixtures were sandwiched between two cover glass plates and polymerized during 30 s at 1.7 mW cm^{-2} . The light source (ORIEL Lamp model 66902, ORIEL Instruments Ltd.) was non-coherent in order to obtain uniform polymerization over the whole sample, and so avoid any kind of interference patterns. Continually, the calibration samples were flood exposed by 0.3 mW cm^{-2} (Philips Cleo 15W) for 20 min.

Prior to the SIMS analysis, three additional preparation steps were made. First one cover glass was removed. In the case of the holographic samples, the silver coated Si wafer was detached from the films and the part of the sample polymerized by the most uniform interference pattern was facing upwards.

Secondly, an evaporation barrier of poly(vinyl alcohol) (PVA, Aldrich) was spin-coated from a water solution (5 weight% PVA in H_2O) on the samples. The water solution was not expected to swell or affect the LC-polyacrylate samples during spincoating. The spincoating process was calibrated to give PVA films of 80-120 nm thickness. Thirdly, we applied a 9 nm layer of gold (K575 XD Turbo sputter coater, Emitech, Ltd.) on top of the samples, to facilitate charge mobilization during SIMS analysis and thus diminish charge build-up due to the insulating behavior of polymers. After introduction into the vacuum chamber, we also cooled the samples to -60°C to further diminish any possible evaporation of the LCs during the SIMS analysis.

The dynamic SIMS profiling measurements were performed on a time of flight (ToF) SIMS apparatus (ION-TOF TOF-SIMS IV)¹⁶, which detector saturates at 10^5 counts. Dual beam mode was applied with the sputtering source of 30 nA 500 eV Cs^+ at 45° rastered over $200 \mu\text{m} \times 200 \mu\text{m}$ and a pulsed 15 keV Ga^+ beam (2 pA ac) at 45° rastered over $50 \mu\text{m} \times 50 \mu\text{m}$ for analysis. The analyzed volume was assumed to be larger than local (and lateral) variations, if any, of LCs in the polymer matrix. The SIMS analyses were performed at temperatures below -60°C generated by cooling the sample holder by liquid nitrogen (Eurotherm cooling unit).

Effective charge compensation was obtained by the thin Au film and additionally in the sputtered crater by use of an electron flood gun (20 eV), which was carefully adjusted so that no secondary ions were generated by the flood gun source. This was controlled multiple times for every sample analyzed. All depth profiles were accomplished in the negative mode and mass calibrated on negatively charged C_xH_y fragments. The mass resolution of the ToF-SIMS analysis was sufficient to identify the secondary ion peaks in the negative spectra ($m/\Delta m > 5000$).

To obtain the SIMS sputter rates of the LC-polymer samples the depths of the sputtered craters were measured by a contact profilometer (DekTak 6M, Veeco). The sputtered depths of the polymer-LC samples were calculated by subtracting the known layer thicknesses of the Au coatings and PVA films from the total crater depths. For each polymer-LC sample the sputter rate was determined from the sputter time and the depth of the crater. Since the measured sputter rates of all SIMS calibration samples were similar, the sputter rate was assumed constant: 0.24 nm/s. This value of the sputter rate was used to approximate the layer pitches from the SIMS depth profile of the holographic samples.

Detailed descriptions of the multivariate statistical analyses are found in chapter 3. The eigenvalue problems for the statistical analyses were solved in the programming language MatLab (The MathWorks, Inc.).

4.2.1 Combined phase separation and reaction-diffusion model

The phase separation behavior of the holographic reaction mixture and the holographic characteristic reaction-diffusion kinetics were introduced and discussed in chapter 2, and a phase separation model was proposed.

Upon polymerization of the LC-monomer mixture the monomers are converted into polymers and at a certain monomer conversion, phase separation occurs and a second phase (phase II) emerges from the three component (polymers, monomers and LCs) phase (phase I). The phase separation occurs when the chemical potentials ($\Delta\mu$) of the two phases are equal: $\Delta\mu_m^I = \Delta\mu_m^{II}$ and $\Delta\mu_{lc}^I = \Delta\mu_{lc}^{II}$. Three effects are assumed to contribute independently to the chemical potentials: isotropic mixing, network elasticity and nematic ordering^{6,7,7}. The expressions then become:

$$\begin{aligned} \frac{\Delta\mu_m^{tot}}{k_B T} &= \frac{\Delta\mu_m^M}{k_B T} + \frac{\Delta\mu_m^{el}}{k_B T} + \frac{\Delta\mu_m^N}{k_B T} \\ &= \ln \phi_m + \phi_p + \chi \phi_{lc}^2 + \kappa(\alpha) \frac{0.5fx - \alpha}{0.5fx \cdot \alpha} \left[1 - \frac{2}{f} \right] \phi_p + \frac{1}{2} \nu \phi_{lc}^2 s^2 \\ \frac{\Delta\mu_{lc}^{tot}}{k_B T} &= \frac{\Delta\mu_{lc}^M}{k_B T} + \frac{\Delta\mu_{lc}^{el}}{k_B T} + \frac{\Delta\mu_{lc}^N}{k_B T} \\ &= \ln \phi_{lc} + \phi_p + \chi(\phi_m + \phi_p)^2 + \kappa(\alpha) \frac{0.5fx - \alpha}{0.5fx \cdot \alpha} \left[1 - \frac{2}{f} \right] \phi_p - \ln Z + \frac{1}{2} \nu \phi_{lc}^2 s^2 \end{aligned}$$

where ϕ_i is the volume fractions of the species: monomers (m), polymers (p) or liquid crystals (lc). The interaction parameter (χ) describes the van der Waals interactions between the lc-m and lc-p. The monomers and polymers are assumed

to mix perfectly ($\chi_{m-p} = 0$). The network elasticity is dependent on the cross-linking probability, which is estimated by considering the number of converted double bonds that are not required to convert the monomers. x is the double-bond conversion, α is the monomer conversion and f the functionality of the monomers. An efficiency factor accounts for the inelastic network chains, and is approximated to a linear function of the monomer conversion: $\kappa(\alpha) = C_{eff}\alpha$.

The nematic ordering contribution is different for the monomers and the liquid crystals since the monomers used here are not liquid crystalline by nature. However, they are influenced by the nematic ordering of the LCs. $\Delta\mu^N$ is expressed in the LC order parameter (s) and the nematic quadrupole parameter: $\nu = 4.54 \frac{T_{ni}}{T}$, with T_{ni} being the nematic-isotropic transition temperature of the LCs. The nematic partition function (Z) expresses the total number of possible states of the nematic system.

The reaction-diffusion kinetics for holographic reflection gratings were modeled and discussed in chapter 2. The reaction rate (R_p) during radical photopolymerization is expressed in the decreasing concentration of un-reacted double bonds ($[C = C]$) as

$$-\frac{\partial[C = C]}{\partial t} = R_p = \frac{k_p}{\sqrt{k_t}} \left(1 - \frac{\alpha}{\alpha_{max}}\right) \sqrt{\Phi_{In} I_a(z)} [C = C] \quad (4.1)$$

where k_p and k_t are the kinetic constants for propagation and termination. At a certain monomer conversion (α_{max}) the polymerization is assumed to terminate due to vitrification effects. The initiation of the polymerization is dependent on the amount and properties of the photoinitiator; the quantum yield (Φ_{In}), the concentration (In), the extinction (ϵ_{In}) and the absorbed light intensity (I_a). The intensity in depth of the film ($I_a(z)$) is generated by the holographic interference pattern:

$$I_a = \int_0^z 2.3 (I_1 + I_2) \left(1 + V \cos \left[\frac{2\pi}{\Lambda} z \right]\right) \epsilon_{In} [In] z dz \quad (4.2)$$

where I_1 and I_2 are the intensities of the interfering laser beams, V is the fringe contrast and Λ the fringe periodicity of the interference pattern.

The diffusion is described by applying Fick's law and assuming the diffusion to decrease with increasing polymer content. This is expressed with a diffusion constant (D) as a function of the monomer volume fraction (ϕ_m):

$$D(\phi_m) = D_p \cdot e^{\frac{1}{K_1(\frac{1}{\phi_m} + K_2)}} \quad (4.3)$$

where D_p is the monomer diffusion coefficient in the pure polymer, and K_1 and K_2 are positive constants described in the free volume theory. The diffusion flux of the LCs is assumed to be determined by that of the monomers':

$$\frac{\partial \phi_m}{\partial t} = -\frac{\partial \phi_{lc}}{\partial t} = \frac{\partial}{\partial z} \left(\frac{D_m \phi_m}{kT} \frac{\partial \mu_m}{\partial z} \right) \quad (4.4)$$

All values of the parameters used for the simulations are listed in table 4.1.

Table 4.1: Values of simulation parameters for the combined phase separation and reaction-diffusion models.

T_p	Experimental temperature [K]	293
$\phi_m(initial)$	Monomer volume fraction in reaction mix [-]	0.7
t_p	Exposure time [s]	30
Δz	Depth interval [nm]	4
Δt	Polymerization step [s]	0.005
Isotropic mixing:		
χ	Interaction parameter [-]	0.53
Network elasticity:		
C_{eff}	Network efficiency factor [-]	1
Nematic ordering:		
s	Order parameter of LC phase [-]	eq. 2.35
T_{ni}	Transition temperature of E7 [K]	331
Photopolymerization:		
$k_p/\sqrt{k_t}$	Polymerization rate constant [$\sqrt{l \cdot mol^{-1} \cdot s^{-1}}$]	1
x_{max}	Maximum double bond conversion [-]	0.32
α_{max}	Maximum monomer conversion [-]	0.75
f	Monomer functionality [-]	7.2
Φ_{In}	Quantum efficiency of photoinitiator [-]	0.5
ϵ_{In}	Extinction coefficient at 351nm [$l \cdot mol^{-1} \cdot cm^{-1}$]	14000
$[In]$	Concentration of photoinitiator [$mol \cdot l^{-1}$]	0.032
Holographic exposure:		
$E_{photons}$	Energy of one mole photons at 351 nm [Einstein]	$3.4 \cdot 10^5$
I_1	Intensity of incoming beam [$mW \cdot cm^{-2}$]	1.7
I_2	Intensity of reflected beam [$mW \cdot cm^{-2}$]	$= 0.46I_1$
V	Fringe contrast in interference pattern [-]	0.93
Λ	Grating periodicity [nm]	164
Diffusion:		
D_m	Diffusion coefficient of the monomer [$m^2 \cdot s^{-1}$]	$1 \cdot 10^{-10}$
K_1	Constant in free volume theory [-]	0.21
K_2	Constant in free volume theory [-]	0

4.3 Results and discussion

4.3.1 Analyzed LC concentrations

Mass spectra of positive and negative secondary ions were collected for both the reflection gratings and the calibration samples. Both the monomers and the liquid crystals contribute to electronegative fragments (as e.g. oxygen, flour, cyano-groups and carboxyl groups). Furthermore, the negative ion mass spectra were found to yield higher, and more diverse, ion intensities than the positive spectra. Consequently, we continue our analysis by considering only the negative ion spectra.

Negative ToF-SIMS spectra were collected of all samples, while the experimental measuring conditions were kept constant. Even though all masses over charge, m/z , are specific for the samples, it is useful to make a qualified selection of mass

channels based on the composition of the samples (and common contaminations). For the statistical analysis we choose to filter out the low intensity mass channels and contamination ions (as Cl^- and S^-) due to intensities close to the noise level or since they were not part of the chemical structure of the organic sample. Secondly, only the m/z exceeding 500 counts per measuring cycle, in the LC-polymer samples, were entered in the statistical methods (table 4.2). For all SIMS spectra we strictly used the same selection procedure.

The remaining mass channels after the selection were all representative for common organic material, C_x^- ions, C_xH^- ions, O^- , and OH^- , but also present was the specific label for the polymer: F^- . The ions CN^- and C_3N^- could be regarded as labels for the LC, but since one of the monomers (NVP) also contains nitrogen, these ions can also be formed during the sputter process from NVP.

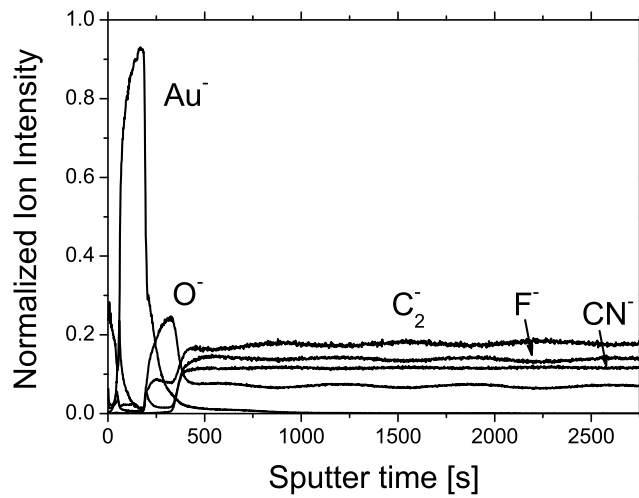
A depth profile of the multilayer sample is shown in figure 4.2. The spectra in figure 4.2(a) shows three main regions; first the charge neutralization layer of gold (Au^-), followed by the evaporation barrier of poly(vinyl alcohol), which is represented by a high O^- intensity. The third and main region, starting at 370 s, is attributed to the multilayer sample. The F^- and O^- ions, that are assumed to represent the polymer, counter oscillated with the CN^- and C_2^- ions that were believed to characterize the LCs. The periodicity of the oscillations is clearly demonstrated in figure 4.2(b) and was estimated to 164 nm. The periodicity of the layers was confirmed by a SEM analysis of the cross section of the film. The pitch measured in the SEM images was 160 nm, only 4 nm less than the pitch from the SIMS depth profile. The slightly smaller pitch measured by SEM is probably due to a SEM sample treatment which may deform the layer structure due to cleavage and LC extraction (discussed in chapter 2, section 2.8.1).

In order to accurately measure the concentrations in the multilayer samples, calibration samples with concentrations of 0, 19.3, 29.9, 39.7, 44.9, and 60.7 weight% LC were prepared and analyzed by dynamic SIMS until the ion intensities reached equilibrium.

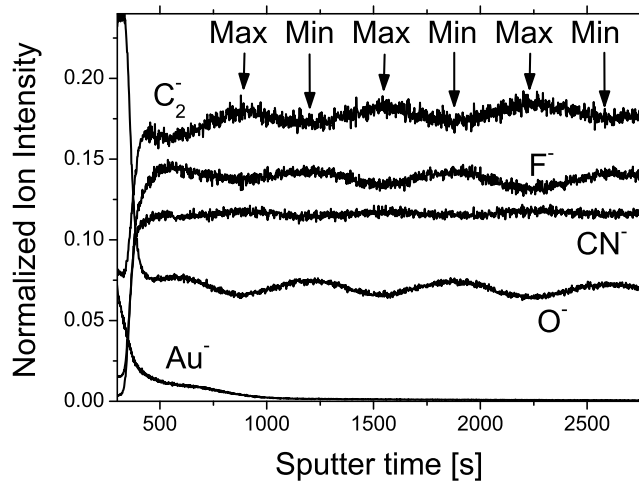
SIMS depth profiles for three concentrations (0, 29.9, and 44.9 weight% LC) are shown in figure 4.3. Five mass channels (Au^- , O^- , C_2^- , F^- , and CN^-) are plotted versus sputter time of the three samples. The samples had a charge neutralization top-coating of gold (visualized by the Au^- peak), followed by an evaporation barrier of PVA (identified by the O^- peak); similar to the multilayer sample in figure 4.2(a).

Table 4.2: The selected fifteen mass channels (m/z) from the dynamic ToF-SIMS analysis to be used in the statistical analysis.

m/z	identified as	m/z	identified as	m/z	identified as
1.0093	H^-	18.9987	F^-	37.0092	C_3H^-
12.0001	C^-	24.0015	C_2^-	47.9995	C_4^-
13.0081	CH^-	25.0078	C_2H^-	49.0080	C_4H^-
15.9950	O^-	26.0033	CN^-	50.0089	C_3N^-
17.0038	OH^-	36.0017	C_3^-	72.0077	C_6^-



(a)



(b)

Figure 4.2: (a) SIMS depth profile in negative mode of a multilayer sample showing five sample representative ion intensities in depth. On the surface of the multilayer sample two top-coatings were applied, first the charge neutralization layer of gold (marked with high intensity of Au^- ion) and secondly the evaporation barrier of poly(vinyl alcohol) marked by the peak of O^- ion intensity. In (b) the spectrum of the multilayer sample is enlarged. In depth of the sample, the ions that are assumed to represent the liquid crystal (C_2^- and CN^-) counter oscillate with the ions assumed to represent the polymer (F^- and O^-). The oscillations are constant with a pitch of 164 nm. Six depth intervals of 40s or 9.6nm at high respectively low LC content (Max respectively Min) were chosen for the quantification of LC concentration of the layers.

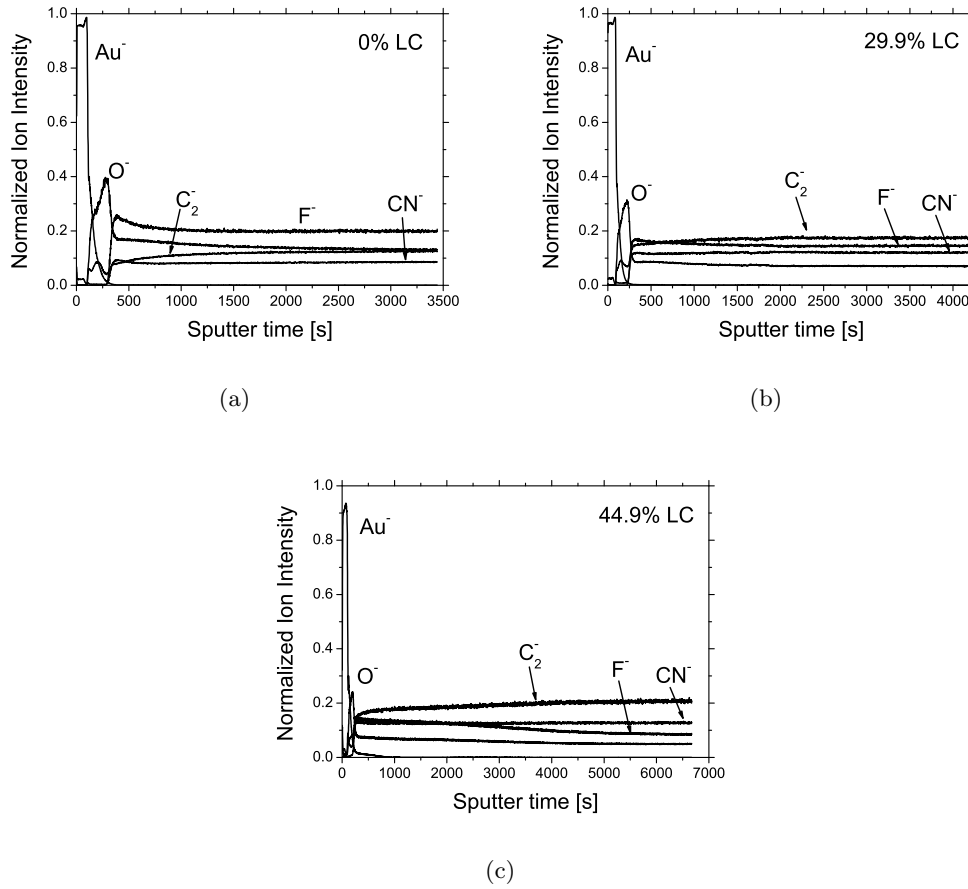


Figure 4.3: SIMS depth profiles, with five representative ion intensities, of three samples with different concentrations of LC: a) 0 weight%, b) 29.9 weight% and c) 44.9 weight%. Each sample has two top-coatings; a charge neutralization layer of gold (marked by the Au^- peak) and an evaporation barrier of PVA (marked by the O^- peak). Depth profiling was continued until the ion yield is stable in time. This occurred when sputtering reached 2440s for 0 weight% LC (a), 3200s for 29.9 weight% LC (b) and 5700s for 44.9 weight% LC (c).

Depth profiling was continued until a stable ion yield is reached which is assumed to represent the bulk composition of the calibration samples.

Note that the F^- signal decreases with increasing LC content, while C_2^- and CN^- behave oppositely. With this information one could try to extract a calibration curve from relative peak intensities of two characteristic ion intensities. In appendix A, a detailed comparison is given for the construction of calibration curves with the RPI, PCA and DFA methods. Clearly DFA turns out to be the preferable method that is able to discriminate convincingly between the slight differences in concentrations as measured for the reflection gratings.

Consequently, discriminant function analysis was used to analyze all calibration samples and the SIMS data from the multilayer sample. In the first step, inter-

vals from the depth profile of the multilayer sample were chosen for the analysis. We decided to determine the maximum (LC-rich) and minimum (polymer-rich) LC concentrations of the layers. SIMS data were selected from narrow intervals (40 s or 9.6 nm) at the peaks and valleys of the oscillating part of the spectra in figure 4.2(b). The intensities of the mass channels of these 22 SIMS spectra in the depth interval were inserted into the DFA together with the depth intervals at equilibrium from the calibration SIMS spectra. Note that the layered sample has to be treated in the statistical analysis together with the calibration samples. This is required since the statistical analysis enlightens differences between the samples. As a result we ended up with 12 groups: six groups from the multilayer sample together with 6 groups consisting of the six concentrations of the calibration samples. The DFA plot shows a successful discrimination between the concentrations of the calibration samples and the concentrations of the layers (figure 4.4(a)). The plot of F1 versus F2 shows that the three groups from the polymer-rich layers are centered on top of each other, as are the three groups from the LC-rich layers. Even though DFA maximizes differences between the groups; it also recognizes similarities of groups containing equal concentrations which is seen in figure 4.4(a) for the groups of the polymer-rich layers as well as for the groups of the LC-rich layers.

The ability of the first DFA function (F1) to separate between the concentrations of the calibration samples was described by the loadings of F1 (figure 4.4(b) and 4.4(c)) that showed anti-correlations of ions assumed to represent the polymer (F^- and O^-) and the ions believed to characterize the LC (CN^- and C_2^-). F2 on the other hand does not show such anti-correlations. Apparently it contains other, non concentration specific, correlations. F1 captured 93% of variance and has low levels of significance for the chi-square test (0.01 level) meaning that F1 is uniquely different from the other DFA functions. The significance for the F-test is also low (0.001 level), indicating that it explains true differences between the concentrations.

A calibration curve was calculated by linear regression analysis on the F1 scores of the calibration concentrations (figure 4.5), with error bars representing the standard deviations of the F1 scores of the measured ion intensities for the equilibrated intervals from the SIMS depth profiles. The equation for the calibration curve is:

$$LC \text{ concentration} \pm 1.9 = -5.1 \cdot F1 + 29.8 \quad [weight\%] \quad (4.5)$$

From the regression analysis (equation A.5) and the F1 scores of the layers, we calculated the concentration of the LC-rich layers to 32.9 ± 3.4 weight% LC and 28.8 ± 2.7 weight% LC for the polymer-rich layers. The error bars represent the standard deviations of the F1 scores of all measured ion intensities in the depth intervals (Max/Min) from the layered sample. These concentrations are centered round the concentration of the reaction mixture (29.9 weight% LC) from which the layered samples were prepared, supposing DFA correctly depicts the correlation between all mass channels.

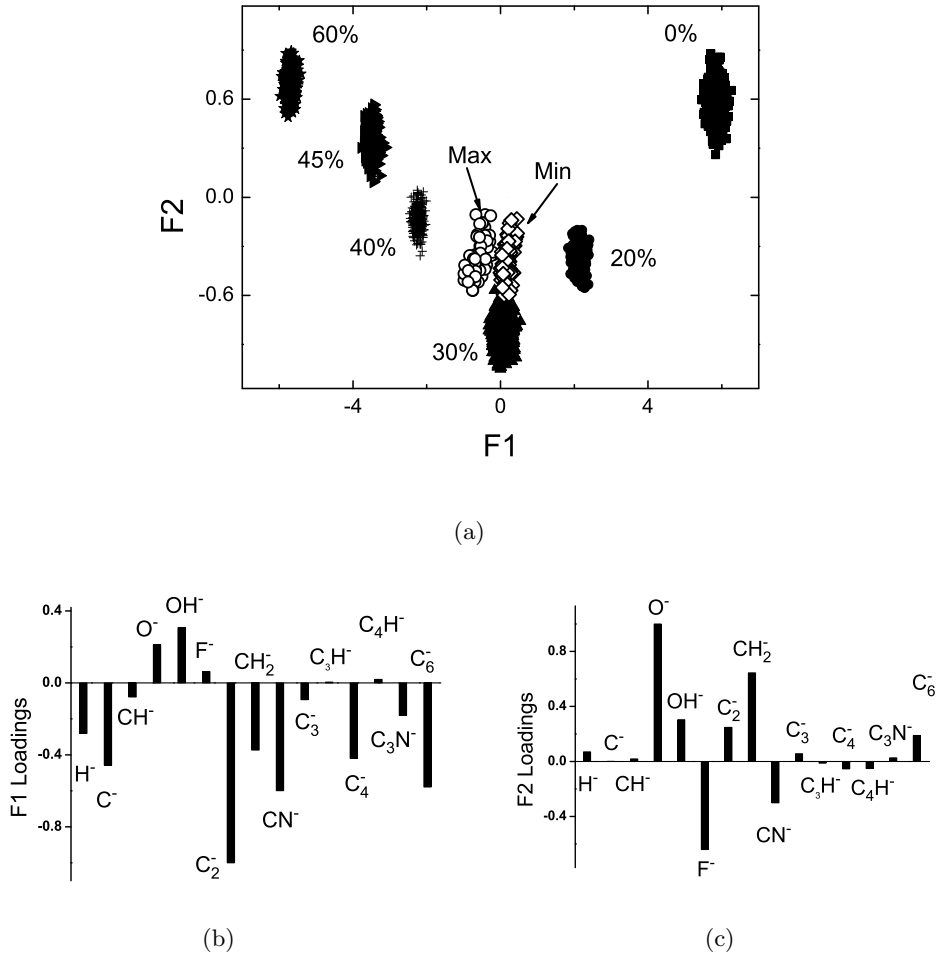


Figure 4.4: a) Score plot of F1 and F2 (together 98% of the variance) from the discriminant function analysis of the six calibration concentrations (0 weight% (■), 19.3 weight% (●), 29.9 weight% (▲), 39.7 weight% (+), 44.9 weight% (►) and 60.7 weight% LC (★) LC), and the depth intervals from the multilayer sample. The DFA scores from the depth intervals assumed to have highest LC content (Max, ○) are separated in F1 on the concentration from the depth intervals assumed to have lower LC content (Min, ◇). b) The loadings of F1 (93% of the variance) and F2 (5% of the variance) show different correlations. F1 is assumed to be related to the LC concentration differences since an anti correlation between the ions representing the polymer (F^- and O^-) and the ions assumed to represent the LC (CN^- and C_2^-) is present. c) F2 expresses other properties assumed not to correlate to the concentration of LC. Hence F1 is assumed to express the concentration differences and therefore chosen to determine the LC concentrations in the layered sample.

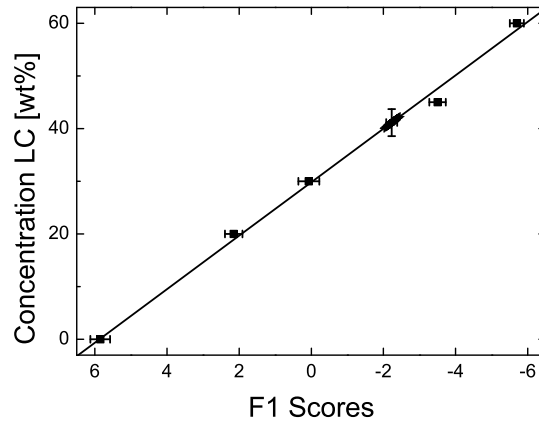


Figure 4.5: Calibration curve made from regression analysis on the F1 scores of the five calibration concentrations (■). The applicability of the calibration curve was tested with the F1 scores of the sixth calibration concentration (39.7% LC, +) that was deliberately left out of the calculations of the calibration curve. The concentration was determined to 41.3 ± 2.7 weight%. The calibration curve was used to calculate the concentrations of the layers in the multilayer samples. The error bars represent the standard deviations of the F1 scores of all measured ion intensities in the depth intervals.

4.3.2 Simulated liquid crystal concentrations

The time and composition at which the reaction-diffusion lines cross the phase separation line are predicted by the combined phase separation and reaction-diffusion models. The phase separation behavior during holographic exposure in a mixture with 29.9 weight% liquid crystals in the monomer blend was simulated and discussed in chapter 2. The reaction-diffusion lines from different depth intervals are plotted in figure 4.6 (all experimental parameters for the simulations are given in table 4.1). The reaction-diffusion line originating from the depth interval of the lowest intensity in the holographic interference pattern reaches the phase separation line first in time; after 9 s of polymerization. When the phase separation line is crossed, the thermodynamical expressions are changed since the dynamics of droplet formation of the phase separated liquid phase influences the thermodynamically contributions to the chemical potentials. Therefore, at the moment that one of the reaction-diffusion lines crosses the phase separation line, the modeling is stopped. The reaction-diffusion line for the depth interval with the highest intensity proceeds to point A in 9 s. After 9 s we assume the line to continue to α_{max} (dashed line in figure 4.6) since the corresponding depth interval is physically separated from the low intensity region where phase separation occurs.

Consequently, the concentration of the polymer rich layers is predicted by the reaction-diffusion lines at the highest intensity to 27 % LCs. Due to the changed thermodynamical expressions after phase separation, the concentration at the LC

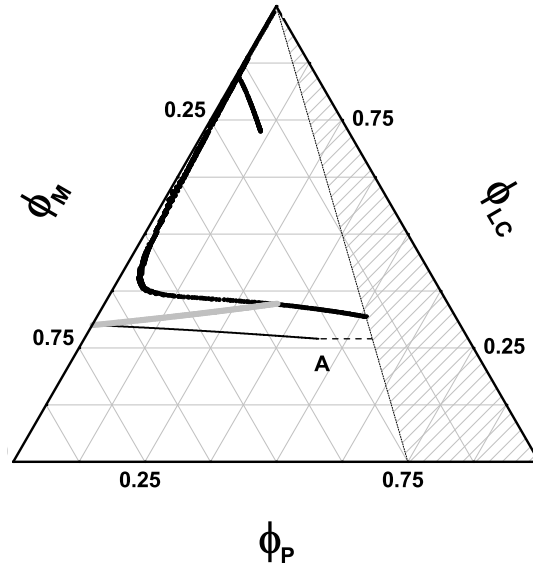


Figure 4.6: Reaction diffusion lines at depth intervals with the highest light intensity (black line) and the lowest intensity (gray line) are followed during polymerization. After 9 s the reaction-diffusion line at depth intervals of the lowest intensity (gray line) crosses the phase separation line, and the reaction-diffusion line for the highest intensity reaches point A. After 9 s we assume the line to continue to α_{max} (dashed line). The composition of the polymer rich layers at the high intensity reaction-diffusion lines is predicted to 27 % LC.

rich layers can not be determined. If the phase separated droplets are small, as in this case, the concentration of the LC rich layers can be estimated around the composition at which the phase separation line is crossed: 35 % LC.

4.4 Conclusions

For the first time, layer concentrations of liquid crystal-polyacrylate reflection gratings have been measured by dynamic ToF-SIMS.

We suppressed evaporation of the mobile liquid crystals in the SIMS vacuum environment by adding an evaporation barrier of poly(vinyl alcohol), and during SIMS analysis by performing the analysis at cryogenic temperatures. All dynamic SIMS spectra were obtained following strictly the same SIMS analysis procedures.

With DFA we could reliably determine the LC concentrations of the layers of the reflection grating. As expected the concentrations fluctuated round 30 weight%LC, which was the concentration of the reaction mixture of the multilayer samples. The concentration of the LC-rich layers was determined to 32.9 ± 3.4 weight% LC and for the polymer-rich layers: 28.8 ± 2.7 weight% LC. The concentration of the polymer

rich layers are confirmed by the combined phase separation and reaction-diffusion model.

The concentration differences between the layers are low and consequently also the refractive index contrast between the layers is low. Nevertheless, efficient reflections from the gratings can be obtained as long as a sufficient number of layers is present¹⁷.

The SIMS analysis verified the small concentration differences between the layers in the holographic recorded gratings which are in agreement with the model results. This supports further use of the simulation models to be applied on the cholesteric self-stratification process.

4.5 References

1. Qi, J. and Crawford, G. P. *Displays* **25**, 177–186 (2004).
2. Bunning, T. J., Natarajan, L. V., Tondiglia, V. P., and Sutherland, R. L. *Annu. Rev. Mater. Sci.* **30**, 83–115 (2000).
3. Doane, J. W., Vaz, N. A., Wu, B.-G., and Žumer, S. *Appl. Phys. Lett.* **48**, 269–271 (1986).
4. Amundson, K., von Blaaderen, A., and Wiltzius, P. *Phys. Rev. E* **55**(2), 1646–1654 (1997).
5. Escuti, M. J. and Crawford, G. P. *Mat. Res. Soc. Symp. Proc.* **709**, 293–298 (2002).
6. Flory, P. J. *Principles of polymer chemistry*. Cornell University Press, London, (1971).
7. Moerkerke, R., Koningsveld, R., Berghmans, H., Dušek, K., and Šolc, K. *Macromolecules* **28**, 1103–1107 (1995).
8. de Gennes, P. G. and Prost, J. *The Physics of Liquid Crystals*. Clarendon Press, Oxford, 2nd edition, (1993).
9. Kjellander, B. K. C., van IJzendoorn, L. J., de Jong, A. M., Broer, D. J., van Gennip, W. J. H., de Voigt, M. J. A., and Niemantsverdriet, J. W. *Proc. SPIE* **5289**, 94–101 (2004).
10. Kjellander, B. K. C., van IJzendoorn, L. J., de Jong, A., Broer, D. J., and Niemantsverdriet, J. W. *Mol. Cryst. Liq. Cryst.* **434**, 171–182 (2005).
11. Thompson, P. M. *Anal. Chem.* **63**(21), 2447–2456 (1991).
12. Wagner, M. S., Graham, D. J., Ratner, B. D., and Castner, D. C. *Surf. Sci.* **570**, 87–106 (2004).
13. Chilkoti, A., Ratner, B. D., and Briggs, D. *Anal. Chem.* **65**, 1736–1745 (1993).
14. Pérez-Luna, V. H., Horbett, T. A., and Ratner, B. D. *J. Biomed. Mater. Res.* **28**, 1111–1126 (1994).
15. Ono, H., Kawamura, T., Frias, N. M., Kitamura, K., Kawatsuki, N., and Norisada, H. *Adv. Mater.* **12**, 143–146 (2000).

16. The ToF-SIMS measurements were performed at Philips Research (Eindhoven, NL). The author acknowledges Dr. Corrie Bulle-Lieuwma for her kind assistance.
17. Bowley, C. C. and Crawford, G. P. *Appl. Phys. Lett.* **76**(16), 2235–2237 (2000).

Chapter 5

Cholesteric self-stratification process: Simulations

5.1 Introduction

The cholesteric self-stratification process is a novel and alternative route to produce stratified optical switches. Unlike methods based on two opposing interfering laser beams (holographic recordings) to produce Bragg gratings, it has the advantages of unlimited device size and a tunable pitch. The layer formation process is based on photopolymerization-induced phase separation, and the layer periodicity is determined by a periodic modulation of the reaction rate in depth of the reaction mixture. This is similar to the holographic recording however the underlying procedure to obtain the stratified films is different. While holographic layer formation is based on an intensity profile of interfering laser beams, the cholesteric self-stratification process makes use of an absorbed intensity profile in depth of a cholesteric reaction mixture.

The principle of the cholesteric self-stratification process is based on the self-organization of chiral nematic liquid crystals. All components in the reaction mixture, including a dichroic photoinitiator, align in the cholesteric LC phase. The absorbed intensity profile is created with linearly polarized light and the dichroic photoinitiators, which consist of elongated, rod-like molecules with their transition dipole moment for UV absorption parallel to the molecular long axis. The initiators mainly absorb the linearly polarized light at every depth where the light polarization direction is parallel to the molecular long axis. If the polarization of the curing light remains unaffected by the optical anisotropy of the cholesteric LCs, absorption maxima are obtained at every half cholesteric pitch (figure 5.1). The periodicity of the absorption profile relies on the cholesteric pitch, which is easily manipulated before polymerization by adding chiral dopants to the reaction mixture.

In order to realize the stratified PDLC switch by the cholesteric self-stratification process the reaction mixture has to fulfill certain demands. The requirements that were listed in chapter 1 are:

- allowing curing light to propagate through the reaction mixture without change in polarization to initiate the dichroic photoinitiator at every half cholesteric

pitch

- having perfect miscible components in the cholesteric LC phase to align the dichroic photoinitiator and obtain the absorption profile
- favoring the polymerization-induced phase separation starting from the LC phase (in contrast to ordinary PDLC formation which involves phase separation from an isotropic phase)
- producing isotropic polymer layers with refractive index matching to one of the refractive indices of the aligned LCs

In this chapter we will focus on the absorption profile and the phase separation mechanism, by simulating the curing light propagation and the layer formation processes. First, the light absorption profile is predicted by simulating the propagation of the curing UV light through the cholesteric reaction mixture. Light propagating through anisotropic media experiences retardation which can differ in the x- and y-components of the electric field vectors. Depending on the birefringence and the cholesteric pitch, chiral nematic liquid crystals can reflect the light, transmit it unaffected, or fully guide the electric field vectors along with the cholesteric pitch. Here, the polarization and the guiding of the light will be studied by light propagation simulations. At the depths where the curing light polarization is parallel to the transition dipole moment, i.e. parallel to the long axis, of the dichroic

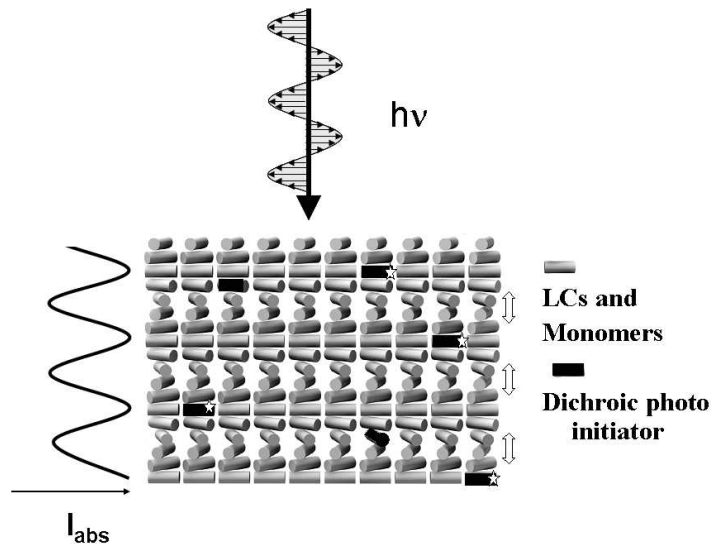


Figure 5.1: The principles of the cholesteric self-stratification process. A mixture of monomers, liquid crystals and dichroic photoinitiators are all in the chiral nematic phase (ordered in the cholesteric helices). Applying linearly polarized light on the cholesteric mixture, the dichroic photoinitiators aligned with the polarized light will most efficiently absorb the light; an absorption profile is created in depth. Polymers are predominantly formed at every half cholesteric pitch due to the absorption profile; this favors phase separation into stratified PDLCs. (Image kindly provided by Chris van Heesch).

photoinitiators, maximum absorption is obtained. The amount of absorbed light is determined by the extinction coefficient, additionally the absorption profile depends on the dichroism and the alignment of the initiators. Three photoinitiators are investigated experimentally and the dichroic ratio is measured. As input for the light propagation simulations, the refractive indices of the cholesteric reaction mixture are required at the wavelengths of the curing UV light. These were measured by ellipsometry.

Furthermore the layer formation process is studied by simulating the phase separation mechanisms during polymerization. We adapt the phase separation and the reaction-diffusion models (that were introduced in chapter 2) to the cholesteric self-stratification process. The temperature effects on the phase separation are discussed. The simulation results will be used to design experimental conditions to obtain multilayer large area optical switches.

5.2 Absorbed intensity profile

Aiming for stratified films reflecting visible light in the wavelength range of $400 < \lambda_{ref} < 650$ nm, and assuming that the layer formation process is initiated at every half cholesteric pitch, the corresponding cholesteric pitch (P_{chol} , figure 5.2) is calculated as^{1,2}

$$P_{chol} = \frac{\lambda_{ref}}{n_{average}} \quad (5.1)$$

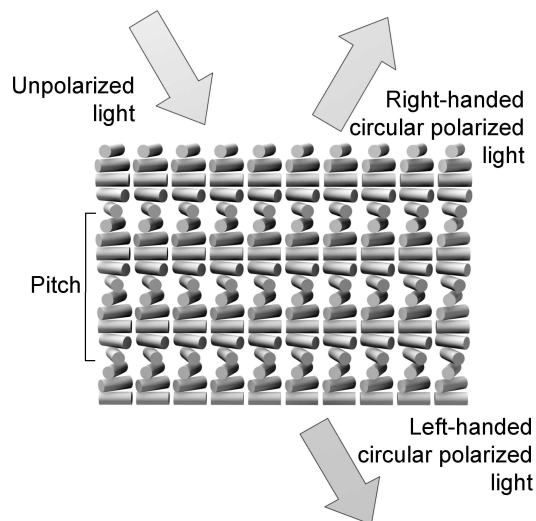


Figure 5.2: Cholesteric liquid crystals are aligned in planes that rotate in depth of the film. The distance at which the director has rotated 360° is called the cholesteric pitch. Cholesteric liquid crystals reflect one handedness of circularly polarized light, the same handedness as the rotation of the cholesteric pitch. The other handedness is transmitted. (Image kindly provided by Chris van Heesch).

Estimating the average refractive index ($n_{average}$) to ~ 1.55 , the cholesteric pitches reflecting visible wavelengths are between 270 to 430 nm.

For cholesteric reaction mixtures that reflect wavelengths much larger than the wavelength of the curing light (λ), the Mauguin regime is approached ($\lambda \ll P_{chol}$)¹. In this regime the curing light is completely guided along with the cholesteric pitch (this effect is used in some LCDs). The Mauguin parameter indicates whether the polarization direction of the propagating light remains unaffected or is rotated with the cholesteric helix as:

$$\frac{\pi \Delta n d}{\lambda \omega} \quad (5.2)$$

d is the thickness of the film, Δn is the birefringence ($\Delta n = n_e - n_o$) and ω is the cumulative angle of rotation of the molecules ($\omega = \frac{\pi}{180} \frac{360 n_{average} d}{\lambda_{ref}}$), expressed in radians. When the Mauguin parameter is large, $\gg 1$, the light is guided along with the helix. For a typical cholesteric reaction mixture reflecting in green ($\lambda_{ref} = 550$ nm, $\Delta n \approx 0.17$, $d = 10 \mu\text{m}$ and $\omega \approx 170$ radians), the Mauguin parameter for $\lambda = 351$ nm is approximately 0.09. The value of the Mauguin parameter indicates that the curing light ($\lambda = 351$ nm) is only slightly rotated with the cholesteric pitch.

The optical rotation of cholesteric liquid crystals increases enormously when approaching the cholesteric reflection band. This is explained by not only the macroscopic properties as the birefringence of the LCs but also the optical activity of the chiral dopants, which are chiral liquid crystals inducing the cholesteric pitch. Isotropic dispersions of chiral molecules of a single handedness give rise to optical activity and it increases significantly at wavelengths close to the absorption of the molecules³. In general with the applied concentrations and film thicknesses, optical rotation of chiral LCs in isotropic phase is very small and can be neglected. However, when aligned in the cholesteric phase the optical activity becomes particularly important at the edges of the reflection band, yielding light rotation of hundreds of degrees per μm (figure 5.3). The optical rotation (φ) in cholesteric liquid crystals can be predicted based on de Vries' theories on cholesteric rotary powers^{4,5}.

$$\varphi = -\frac{\pi \beta^2}{4 P_{chol} \lambda'^2 (1 - \lambda'^2)} \quad (5.3)$$

$$\beta = \frac{n_e(\lambda) - n_o(\lambda)}{\frac{1}{2} [n_e(\lambda) + n_o(\lambda)]} \quad (5.4)$$

$$\lambda' = \lambda / \lambda_{ref} \quad (5.5)$$

The optical rotation is dependent on the helical pitch (P_{chol}), the central wavelength of reflection (λ_{ref}), and the refractive indices (n_e and n_o). To avoid severe optical rotation, photopolymerizations of the cholesteric films should be initiated with light having wavelengths at least 100 nm from the reflection band⁶.

The linear curing light may not only be rotated but also elliptically polarized when propagating through the birefringent cholesteric liquid crystals. To predict the polarization direction of the propagating light we simulate the propagating electric field vectors for the curing UV-light through the depth of the cholesteric film. There

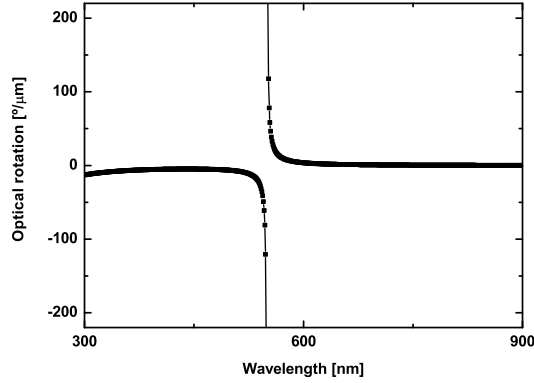


Figure 5.3: Optical rotation simulated using equation 5.3 for a cholesteric film with reflection maximum at 550 nm. Close to the reflection band, the optical rotation approaches $\pm\infty$.

are several methods to simulate light propagation, however only the Berreman's 4x4 matrix method is generalized to be applied on light propagation in any birefringent media, and especially cholesteric films^{7,8,9,1}. It treats the multiple reflections at all interfaces and gives exact solutions to the Maxwell wave equations (description in experimental section). Berreman's 4x4 matrix method is generally used to predict reflection and transmission of cholesteric films, such a simulation is shown for a right handed cholesteric film in figure 5.4(a). We use Berreman's 4x4 matrix method to simulate the electric field vectors of the propagating curing light. Electric field vectors can be written in Stokes parameters, from which the polarization direction and ellipticity can be deduced.

All light can be regarded as waves with an elliptical polarization. By studying the shape of the polarization ellipse, the polarization direction and state are obtained and can be expressed by the Stokes parameters. The four Stokes parameters are real quantities describing the polarization ellipse in terms of intensities^{10,11}:

$$S_0 = E_x E_x^* + E_y E_y^* \quad (5.6)$$

$$S_1 = E_x E_x^* - E_y E_y^* \quad (5.7)$$

$$S_2 = E_x E_y^* + E_y E_x^* \quad (5.8)$$

$$S_3 = i(E_x E_y^* - E_y E_x^*) \quad (5.9)$$

with the electric field vector in the x and y components as:

$$E_x(t) = E_{0x} e^{i(\omega t - kx)} \quad (5.10)$$

$$E_y(t) = E_{0y} e^{i(\omega t - ky)} \quad (5.11)$$

S_0 expresses the total intensity of the light. For completely polarized waves, $S_0^2 = S_1^2 + S_2^2 + S_3^2$ while partially polarized and unpolarized beams have a larger total

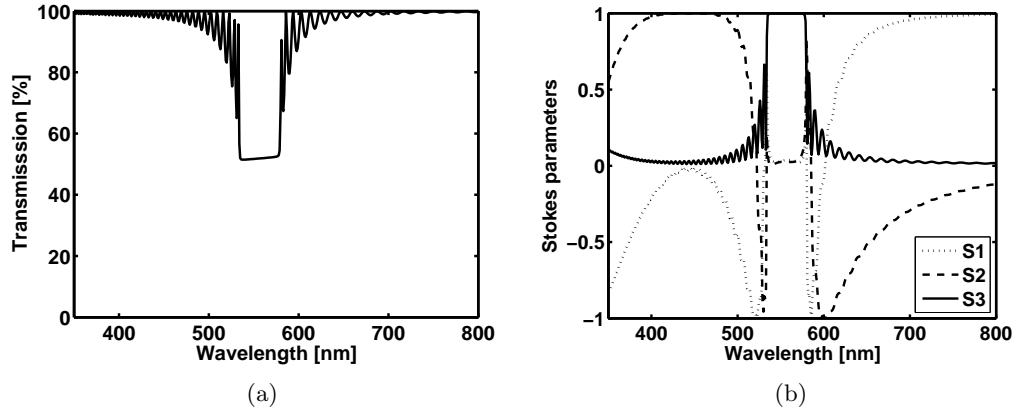


Figure 5.4: Berreman's 4x4 matrix simulations of transmitted light that propagated through a righthanded cholesteric film reflecting 550 nm. Transmission spectra (a), and Stokes parameters (b); S_1 and S_2 indicate the polarization direction and S_3 reflects the amount of circularly polarized light of the transmitted light. The total intensity (S_0 is assumed to be constant).

intensity than the sum of the intensities of the polarized components (S_1, S_2, S_3). The directionality of the polarization is described by S_1 in vertical and horizontal directions and by S_2 in $+45^\circ$ and -45° directions to the horizontal axis (figure 5.5). The last parameter, S_3 , explain the ellipticity of the light with the value -1 representing right circularly polarized light and +1 representing left circularly polarized light. Light polarizations can be visualized on the Poincaré sphere where each point on the sphere represents a state of polarization of the light. S_1 and S_2 are placed as two orthogonal vectors describing the direction of linearly polarized light, and S_3 is orthogonal to the S_1 and S_2 plane.

The azimuth angle (ξ) describes the polarization direction compared to the $S_1 = 1$ (horizontal) direction and is defined as:

$$\tan(2\xi) = \frac{S_2}{S_1} \quad -\pi/4 \leq \xi \leq \pi/4 \quad (5.12)$$

The ellipticity parameter, S_3 , explains how much of the light is circularly polarized. In the case of perfect linearly polarized light, $S_3 = \text{zero}$. Studying the Stokes parameters of the propagating light, the polarization direction, and the ellipticity at the wavelengths of the curing light in depth of the reaction film is obtained. In order to simulate the propagation of light that addresses the photoinitiators, the refractive indices at the UV wavelengths are required. Refractive indices increase when approaching the maximum absorption wavelength, which is above 200 nm for molecules having conjugated multiple bonds³. For liquid crystals, the extraordinary and/or the ordinary refractive indices (n_e, n_o) can differ as much as 0.15 units between 600 and 350 nm¹². To simulate the light propagation correctly, n_e and n_o are required as a function of wavelength, which can be measured by ellipsometry.

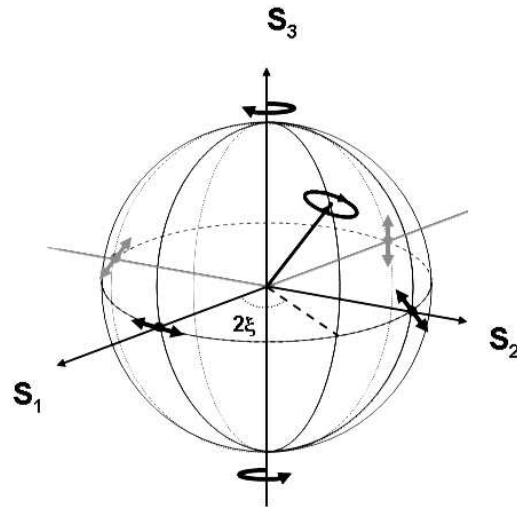


Figure 5.5: Poincaré's sphere showing polarization directions (arrows) and polarization angle (ξ).

The absorbed light intensity profile in depth can be calculated from the angle between the molecular axis (which is obtained by the cholesteric helix) and the polarization direction of the light. Obviously, the photoinitiators are required to align with the cholesteric liquid crystals in order to obtain a periodic absorption profile. Due to the molecular structure and molecular dimension of dichroic photoinitiators it is assumed that they align with the liquid crystals. The preferential absorption along the molecular length axes of the initiator can be measured by absorption spectroscopy using incident light polarized in the extraordinary (A_{\parallel}) respectively in the ordinary (A_{\perp}) directions in uniaxially aligned, non-chiral, liquid crystals. The dichroic ratio is calculated as: A_{\parallel}/A_{\perp} . The ratio must be large enough to induce modulating reaction rates in depth of the film. Recently, this was achieved in a cholesteric mixture of two LC monomers, and during polymerization the modulating reaction rates induced diffusion of one of the monomers to the highest absorbed intensity which resulted in a deformed cholesteric pitch^{13,6}.

5.3 Phase separation mechanisms

The phase separation mechanisms induced by photopolymerization were introduced in chapter 2 for isotropic reaction mixtures. Phase separation can be considered as the process where a liquid phase, containing only liquid components (monomers and liquid crystals) emerges from the polymer network (consisting of polymer, monomers and liquid crystals). The latter phase is created during the polymerization of the monomer-LC mixture. Two phases can coexist when the system is in thermodynamically equilibrium, expressed as a minimum in Gibbs free energy. Three effects are assumed to contribute independently to the free energy of the system: isotropic mixing, network elasticity and nematic ordering. The isotropic mixing¹⁴ takes into

account the relative size of the molecules and the van der Waals interactions between different species. The elasticity of a cross-linked network can affect the phase separation considerably: dense cross-links can lead to phase separation at low monomer conversions¹⁵. The theory of Maier and Saupe for nematic ordering is adopted to account for the contribution to the Gibbs free energy originating from the nematic ordering of the reactive and unreactive liquid crystalline molecules¹⁶.

The expressions for the isotropic mixing and network elasticity that were derived in chapter 2 for holographic reaction mixtures can also be applied for the cholesteric self-stratification process. Using the approximations that the monomers and LCs have equal size ($N_{lc} = N_m = 1$), and that the interaction parameter χ is zero for the monomer-polymer interactions, the chemical potentials for the mixing term are:

$$\frac{\Delta\mu_m^M}{k_B T} = \ln \phi_m + \phi_p + \chi_{m-lc} \phi_{lc} (\phi_{lc} + \phi_p) - \chi_{p-lc} \phi_{lc} \phi_p \quad (5.13)$$

$$\frac{\Delta\mu_{lc}^M}{k_B T} = \ln \phi_{lc} + \phi_p + (\chi_{m-lc} \phi_m + \chi_{p-lc} \phi_p) (\phi_m + \phi_p) \quad (5.14)$$

where ϕ_i is the volume fraction of the monomers (m), liquid crystals (lc) or polymer (p).

The elastic network contribution is

$$\frac{\Delta\mu_m^{el}}{k_B T} = \frac{\Delta\mu_{lc}^{el}}{k_B T} = \frac{1}{m_c} \left[1 - \frac{2}{f} \right] \phi_p \quad (5.15)$$

with f the monomer functionality and m_c the average chain length between cross-links. The latter can be expressed in the cross-linking probability ($P(\text{cross})$) as:

$$m_c = \frac{\alpha}{P(\text{cross}) \cdot \kappa(\alpha)} = \frac{\alpha}{\frac{0.5fx - \alpha}{0.5fx} \cdot \kappa(\alpha)} \quad (5.16)$$

where α is the monomer conversion and x is the double bond conversion. $\kappa(\alpha)$ is an efficiency factor accounting for the ineffective elastic network chains, the cross-linking efficiency is assumed to increase with the monomer conversion as: $\kappa(\alpha) = C_{eff} \cdot \alpha$.

The expressions for the nematic ordering contribution are different for the cholesteric self-stratification process compared to the holographic system in chapter 2. The cholesteric self-stratification starts from a chiral nematic phase, where the monomers are aligned with the LCs and have LC properties. Thus, the monomers contribute also to the nematic ordering, and the chemical potentials become¹⁷:

$$\frac{\Delta\mu_m^n}{kT} = \frac{1}{2} \nu_{mm} s_m^2 \phi_m^2 + \frac{1}{2} \nu_{lclc} s_{lc}^2 \phi_{lc}^2 + \nu_{mlc} s_m s_{lc} \phi_m \phi_{lc} - \ln Z_m \quad (5.17)$$

$$\frac{\Delta\mu_{lc}^n}{kT} = \frac{1}{2} \nu_{mm} s_m^2 \phi_m^2 + \frac{1}{2} \nu_{lclc} s_{lc}^2 \phi_{lc}^2 + \nu_{mlc} s_m s_{lc} \phi_m \phi_{lc} - \ln Z_{lc} \quad (5.18)$$

where s_m and s_{lc} are the order parameters of the (liquid crystalline) monomers and (unreactive) LCs. The nematic partition functions ($\ln Z$) are calculated using equation 2.35. The influence on the order parameter when mixing isotropic molecules

with liquid crystals is known. However, when mixing two liquid crystalline components, the effect on the order parameter is difficult to simulate. Therefore we assume $s_m = s_{lc} = 0.6$ for the liquid crystals, the monomers, and mixtures of the two, in agreement with experimental observations. Finally, the nematic interaction terms (ν) are obtained as:

$$\nu_{mm} = 4.54 \frac{T_{ni,M}}{T}, \quad \nu_{lclc} = 4.54 \frac{T_{ni,LC}}{T} \quad (5.19)$$

$$\nu_{mlc} = c \sqrt{\nu_{mm} \nu_{lclc}} \quad (5.20)$$

where c is a proportionability constant characterizing the relative strength of the interactions¹⁷. If the mixture of the monomers and LCs are azeotropic, i.e. have compositions at which both the nematic and the isotropic phase are in equilibrium, the value of the constant c can be determined. Low values of c (< 1) means that the nematic interactions are weak and the two components are more stable in their pure states than mixed. Strong nematic interactions ($c > 1$) exhibits well mixed nematic phase. Here we assume $c = 1$, which means that the (liquid crystalline) monomers and the unreactive LCs interact with equal magnitude.

5.4 Reaction-diffusion mechanisms

Photopolymerization kinetics for radical photopolymerization was described in chapter 2, and can be applied to derive the reaction rate for the cholesteric self-stratification process.

$$-\frac{\partial[C=C]}{\partial t} = \frac{k_p}{\sqrt{k_t}} \left(1 - \frac{\alpha}{\alpha_{max}}\right) \sqrt{\Phi_{In} I_a(z)} [C=C] \quad (5.21)$$

$-\frac{\partial[C=C]}{\partial t}$ is the polymerization rate converting double bonds ($[C=C]$). k_p and k_t are the rate constants for the propagation and termination reactions. The polymerization rate decreases with increasing monomer conversion (α), and terminates when α_{max} is reached. Φ_{In} is the quantum efficiency of the photoinitiator, and $I_a(z)$ is the light absorption profile:

$$I_a(z) = 2.3 I_0 \epsilon_{In}(z) [In] z \quad (5.22)$$

that depends on the light intensity (I_0), the photoinitiator concentration ($[In]$), the film thickness (d) and the extinction coefficient ($\epsilon_{In}(z)$). The intensity loss in depth of the film is assumed negligible since the photoinitiators absorb only a small fraction of the light.

The absorbed intensity profile is assumed to follow a periodic change in extinction ($\epsilon(z)$): from maximum to minimum absorption (with the absorption contrast, V_{abs}), and with an absorption pitch (Λ_{abs}) corresponding to the periodic depth at which the long axis of the initiator is aligned with the polarization direction of the curing light.

$$\epsilon_{In}(z) = \int_0^d \epsilon_0 \left(1 + V_{abs} \cos \left[\frac{2\pi}{\Lambda_{abs}} z \right] \right) dz \quad (5.23)$$

where ϵ_0 is the isotropic extinction coefficient. The dichroic contrast (V_{abs}) is determined from the absorption parallel and perpendicular to the molecular long axis:

$$V_{abs} = \frac{A_{\parallel} - A_{\perp}}{A_{\parallel}} \quad (5.24)$$

A_{\parallel} and A_{\perp} can be measured by absorption spectroscopy. Λ_{abs} is predicted by light propagation simulations in depth of the cholesteric film.

The diffusion during polymerization was described in chapter 2 and can be applied on the cholesteric self-stratification process. The diffusion flux of the LCs is assumed to be determined by that of the monomers¹⁸:

$$\frac{\partial \phi_m}{\partial t} = \frac{\partial}{\partial z} \left(\frac{D_m \phi_m}{kT} \frac{\partial \mu_m}{\partial z} \right) \quad (5.25)$$

$$\frac{\partial \phi_{lc}}{\partial t} = -\frac{\partial \phi_m}{\partial t} \quad (5.26)$$

where the diffusion constant D_m decreases with increased monomer conversion:

$$D(\phi_m) = D_p \cdot e^{-\frac{K_1}{\phi_m + K_2}} \quad (5.27)$$

D_p is the monomer diffusion coefficient in pure polymer, and K_1 and K_2 are positive constants described in the free volume theory¹⁹.

5.5 Experimental

5.5.1 Materials

Nematic planar aligned polymer films were prepared from the reactive mesogen RM257 (LC-diacrylate, Merck), with the addition of 2 weight% of the photoinitiator Irgacure 369 (IRG369, Ciba) and 1 weight% of the inhibitor hydroquinone (HQ, Aldrich), reaction mixture A in table 5.1(a). The latter was used to suppress thermal polymerization when keeping the mixture in nematic LC phase at 85°C. The chemical structures of the molecules are shown in figure 5.6. Cells with anti-parallel planar alignment layer of rubbed polyimide (AL1454, JSR), the cell gaps, and thus the thickness of the polymer films, were controlled by microscopic spacers to 5-30 μm . The cells were filled by capillary forces with the reaction mixture at 85°C (in nematic LC phase) continued by UV polymerization (0.3 mW cm^{-2} , Philips Cleo 15W) for 20 min at 85°C.

Chiral nematic polymer films were prepared by polymerizing chiral nematic mixtures of the reactive mesogen RM257 (Merck), the chiral dopant Palicolor LC756 (BASF) and the isotropic photoinitiator Irgacure 369 (IRG369, Ciba). The chemical structures are shown in figure 5.6 and the compositions of the reaction mixture used are given in table 5.1(a).

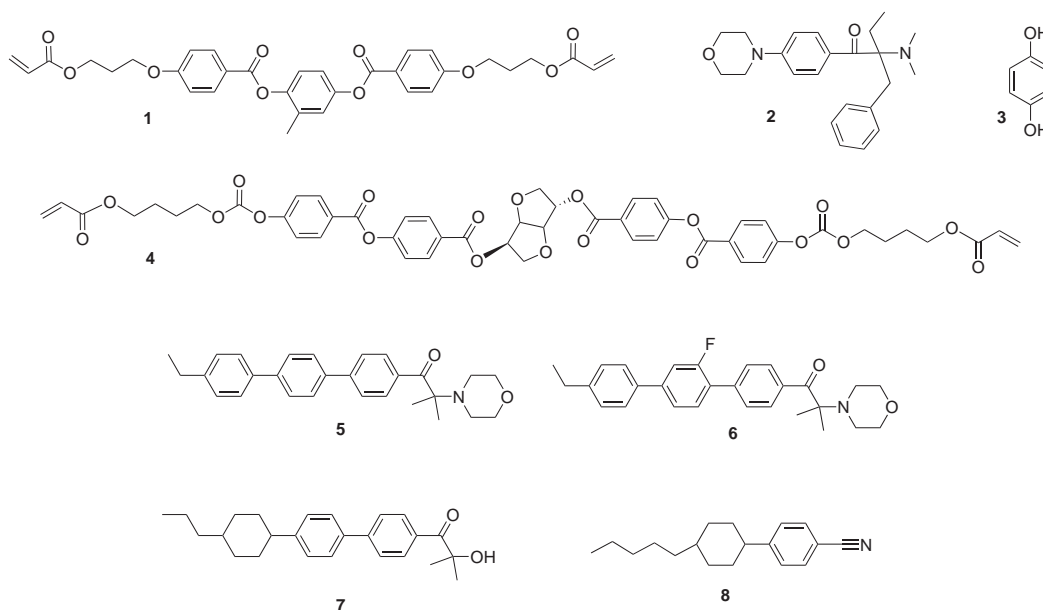


Figure 5.6: Chemicals used for the liquid crystalline polymer films for refractive index measurements and light propagation experiments. **1** reactive mesogen RM257, **2** isotropic photoinitiator IRG369, **3** inhibitor hydroquinone, and **4** chiral dopant LC756. Photoinitiators (**5-7**) and the nematic host (**8**) 5-PCH.

Glass cells were prepared with planar alignment layers of rubbed polyimide (AL1454, JSR), the rubbing directions in the cells were perpendicular with respect to each other. The latter in order to average out the retardation effects of the alignment layers (or rather the closest molecular LC layers at the interfaces of the alignment layers). The cell gaps were controlled by microscopic spacers to 17 and 26 μm . The cells were filled by capillary forces with the reaction mixture at 85°C (in chiral nematic phase). The samples were polymerized by UV light (0.3 mW cm^{-2} , Philips Cleo 15W) for 20 min at 85°C (in chiral nematic phase). The reflected wavelengths of the films were measured by UV-vis scanning spectro-

Table 5.1: (a) Compositions of reaction mixtures for nematic and cholesteric films used to experimentally determine the refractive indices and the light propagation. (b) Films of the dichroic photoinitiators with the nematic host 5-PCH.

(a)						(b)				
Mixture	A	B	C	D			E	F	G	
RM257	97	93.5	95	96	wt%	5-PCH	98.5	98.5	98.0	wt%
LC756	-	5.5	4	3	wt%	5	1.5	-	-	wt%
IRG369	2	1	1	1	wt%	6	-	1.5	-	wt%
HQ	1	-	-	-	wt%	7	-	-	2.0	wt%
						cell thickness	8.7	9.6	8.1	μm

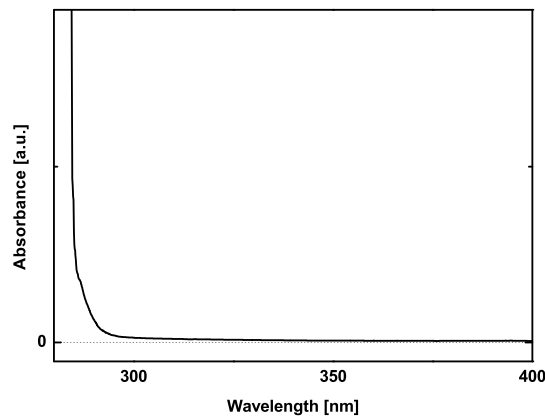


Figure 5.7: The absorption of the nematic host 5-PCH. (Graph kindly provided by Blanca Serrano Ramón).

tometer (Shimadzu UV-3102PC equipped with MPC-3100) in transmission. The loss in transmission describes reflection from the film for wavelengths that are not absorbed or scattered by the sample itself (or its supporting glass plates with the polyimide coating). The transmission as a function of wavelength was measured at normal incidence.

Three photoinitiators (**5-7** in figure 5.6) were investigated on their dichroism and alignment when mixed with the nematic liquid crystal 5-PCH (**8** in figure 5.6). 5-PCH was chosen as nematic host due to its low absorbance above 300 nm (figure 5.7). Mixtures with 1.5-2 weight% of the photoinitiators in 5-PCH were prepared. Cells of anti-parallel planar alignment layers of rubbed polyimide (AL1454, JSR) on quartz glasses were made with cell gaps controlled by microscopic spacers to approximately 8 μm . The mixture compositions and cell gaps are listed in table 5.1(b).

The absorption of linearly polarized light parallel and perpendicular to the molecular alignment direction was measured by spectroscopy (Shimadzu UV-3102PC equipped with MPC-3100). The absorbance of 5-PCH was subtracted from the absorption spectra of the initiators.

5.5.2 Ellipsometry and birefringence measurements

The extraordinary and the ordinary refractive indices as a function of wavelength can be measured by ellipsometry. The change in polarization state, detected as the change of the light intensity ratio ($|R^p|/|R^s|$) of the orthogonal electric field vectors, and the phase difference of the light after interacting with the sample are measured by ellipsometry²⁰. The polarization state and the phase difference of the reflected and transmitted light beams were measured by a Wollam VASE system (equipped with rotating analyzer and a sequential scanning xenon light source)²¹. From the

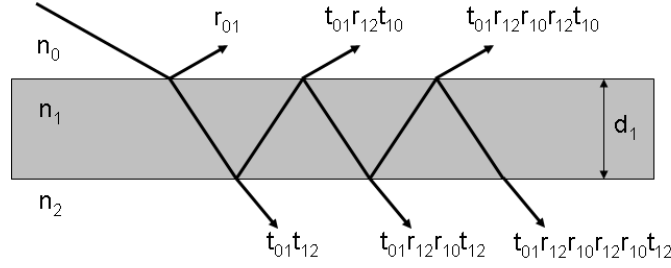


Figure 5.8: Fresnel coefficients for reflection and transmission through a material with average refractive index n_1 and thickness d_1 .

change in polarization and phase of the light beam when transmitted or reflected from the sample surface (figure 5.8), the refractive indices can be extracted using the Fresnel reflection and transmission coefficients^{1,22}:

$$r_{01}^s = \frac{n_0 \cos \theta_0 - n_1 \cos \theta_1}{n_0 \cos \theta_0 + n_1 \cos \theta_1} \quad (5.28)$$

$$r_{01}^p = \frac{n_1 \cos \theta_0 - n_0 \cos \theta_1}{n_1 \cos \theta_0 + n_0 \cos \theta_1} \quad (5.29)$$

$$r_{12}^s = \frac{n_1 \cos \theta_1 - n_2 \cos \theta_2}{n_1 \cos \theta_1 + n_2 \cos \theta_2} \quad (5.30)$$

$$r_{12}^p = \frac{n_2 \cos \theta_1 - n_1 \cos \theta_2}{n_2 \cos \theta_1 + n_1 \cos \theta_2} \quad (5.31)$$

$$t_{01}^s = \frac{2n_0 \cos \theta_0}{n_0 \cos \theta_0 + n_1 \cos \theta_1} \quad (5.32)$$

$$r_{01}^p = \frac{2n_0 \cos \theta_0}{n_1 \cos \theta_0 + n_0 \cos \theta_1} \quad (5.33)$$

$$t_{12}^s = \frac{2n_1 \cos \theta_1}{n_1 \cos \theta_1 + n_2 \cos \theta_2} \quad (5.34)$$

$$r_{12}^p = \frac{2n_1 \cos \theta_1}{n_2 \cos \theta_1 + n_1 \cos \theta_2} \quad (5.35)$$

where n_0, n_1 and n_2 are the refractive indices of the media (here the sample is medium 1, while the media with notations 0 and 2 are of air). The angles (θ_i) are interrelated by the Snell's law:

$$n_0 \sin \theta_0 = n_1 \sin \theta_1 = n_2 \sin \theta_2 \quad (5.36)$$

The sum of all reflection coefficients:

$$r_{tot} = r_{01} + t_{01}r_{01}t_{10}e^{(-2i\beta)} + t_{01}r_{12}r_{10}r_{12}t_{10}e^{(-4i\beta)} + \dots \quad (5.37)$$

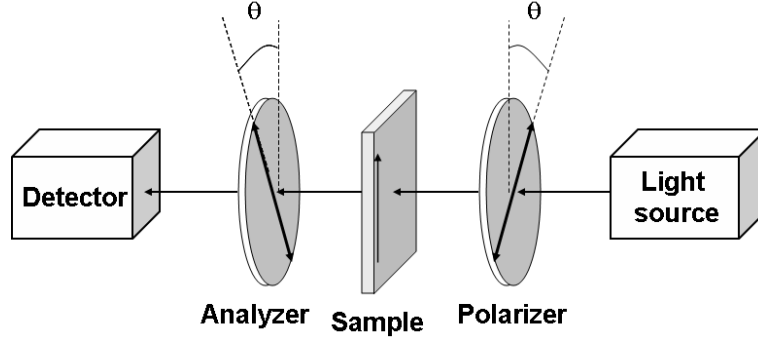


Figure 5.9: Experimental setup for measuring the birefringence with transmission spectroscopy. The polarizer and analyzer are 45° in respect to the aligned liquid crystals in the polymer film.

where d is the film thickness and $\beta = 2\pi \frac{d}{\lambda} n_1 e^{\theta_1}$, converges into Fresnel reflection coefficients for light of the two polarization directions (p and s) as:

$$R^p = \frac{r_{01}^p + r_{12}^p e^{-i2\beta}}{1 + r_{01}^p r_{12}^p e^{-i2\beta}} \quad (5.38)$$

$$R^s = \frac{r_{01}^s + r_{12}^s e^{-i2\beta}}{1 + r_{01}^s r_{12}^s e^{-i2\beta}} \quad (5.39)$$

Similarly, the Fresnel transmission coefficients can be obtained. Measuring then polarization direction and phase while rotating both the polarizer and the analyzer, and varying the angle of incidence, the refractive indices of the anisotropic nematic LCs are obtained.

The refractive indices at 589 nm were measured by an Abbe refractometer (T2) by placing a free-standing planar aligned polymer film on the measuring crystal.

The polarization of a light beam passing through anisotropic media changes due to the birefringence of the anisotropic material. The birefringence (Δn) as a function of wavelength (λ) was measured on the planar nematic polymer films by transmission spectroscopy (Shimadzu UV-3102PC equipped with MPC-3100, optical setup in figure 5.9). The detected transmittance ($T(\lambda)$) depends on the birefringence (Δn) and sample thickness as²³:

$$T(\lambda) = T_0 \sin^2(2\theta) \sin^2\left(\frac{\pi \Delta n(\lambda) d}{\lambda}\right) \quad (5.40)$$

where θ is the angle between the polarizer or analyzer and the molecular direction of the LCs (always 45° in our setup). d is the thickness of the polymer film. We express the birefringence with Cauchy's dispersion equation²³:

$$\Delta n(\lambda) = C_1 + \frac{C_2}{\lambda^2} \quad (5.41)$$

where C_1 and C_2 are constants. C_1 can be regarded as the birefringence at large wavelengths (Δn_∞). Inserting equation 5.41 into equation 5.40 and fitting the simu-

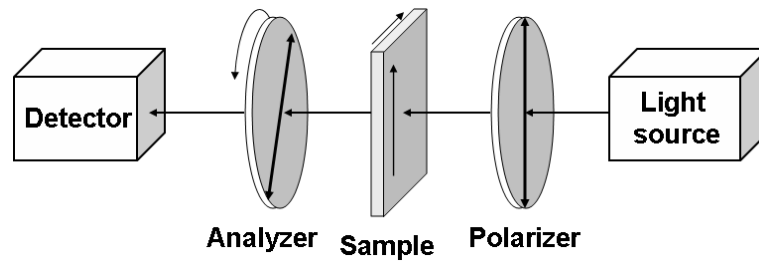


Figure 5.10: Experimental setup for transmission spectroscopy measuring polarization direction of the light that propagated through the cholesteric film. The first polarizer is parallel to the molecular alignment direction at the first glass plate. The analyzer is rotated and the transmitted light is collected by the detector.

lation to the experimentally measured transmission by using d , C_1 and C_2 as fitting parameters, $\Delta n(\lambda)$ can be obtained.

5.5.3 Light propagation through cholesteric films

Light rotation of the cholesteric films was investigated by measuring the direction of the (linear) polarized light exiting the cholesteric polymerized film by transmission spectroscopy using the setup shown in figure 5.10. Linearly polarized light enters the cholesteric film and the direction at which it leaves the sample is measured by rotating the analyzer. The intensity of light (per wavelength) leaving the sample is plotted as a function of the angle of the rotated analyzer (θ). The transmitted light (T) is fitted by:

$$T = \cos^2 \theta \quad (5.42)$$

From equation 5.42, the experimentally measured polarization directions of the transmitted light are obtained.

Berreman's 4x4 matrix method

Simulations of light propagation through cholesteric polymer films were computed using the Berreman's 4x4 matrix method. It simulates how plane electromagnetic waves ($\Psi(z)$) propagate through stratified and nonmagnetic dielectric media^{7,8,9,1} (figure 5.11). Reducing the Maxwell equations we obtain

$$\frac{\partial}{\partial z} \Psi(z) = \frac{\omega}{c} D(z) \Psi(z) \quad (5.43)$$

where c is the speed of light and ω is the angular frequency. $D(z)$ is the differential propagation matrix including material characteristic properties as the dielectric

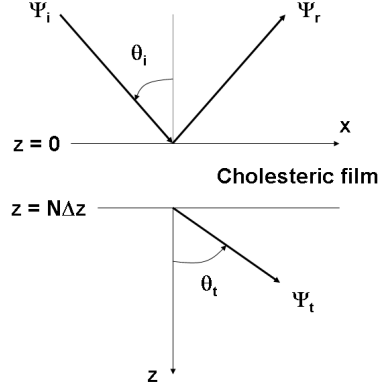


Figure 5.11: The reflected and transmitted electric field vectors calculated by Berreman's 4x4 matrix method for light propagating in depth through a cholesteric liquid crystal.

constants (ϵ):

$$D(z) = \begin{bmatrix} -i \left(\frac{kc}{\omega} \right) \frac{\epsilon_{xz}}{\epsilon_{zz}} & 1 - \frac{1}{\epsilon_{zz}} \left(\frac{kc}{\omega} \right)^2 & -i \left(\frac{kc}{\omega} \right) \frac{\epsilon_{yz}}{\epsilon_{zz}} & 0 \\ -\epsilon_{xx} + \frac{\epsilon_{xz}^2}{\epsilon_{zz}} & -i \left(\frac{kc}{\omega} \right) \frac{\epsilon_{xz}}{\epsilon_{zz}} & \frac{\epsilon_{xz}\epsilon_{yz}}{\epsilon_{zz}} - \epsilon_{xy} & 0 \\ 0 & 0 & 0 & 0 \\ \frac{\epsilon_{xz}\epsilon_{yz}}{\epsilon_{zz}} - \epsilon_{xy} & -i \left(\frac{kc}{\omega} \right) \frac{\epsilon_{yz}}{\epsilon_{zz}} & \frac{\epsilon_{yz}^2}{\epsilon_{zz}} - \epsilon_{yy} + \left(\frac{kc}{\omega} \right)^2 & 0 \end{bmatrix} \quad (5.44)$$

The x and y directions are in the plane perpendicular to the depth direction (z) of the media and $\epsilon = n^2$, k is the wave vector.

For very small depth intervals Δz for which the change in material properties negligible, the differential propagation matrix can be assumed constant. Then equation 5.43 can be approximated by:

$$\Psi(z + \Delta z) = e^{[(\omega/c)\Delta z D(z)]} \Psi(z) \quad (5.45)$$

Repeated matrix multiplications over the small steps of Δz over the whole sample thickness ($N\Delta z$) results in the general propagation matrix F . Using F , the electromagnetic waves from one side of the cholesteric film ($\Psi_{N\Delta z}$) to the other (Ψ_0) can be calculated.

$$\Psi_{N\Delta z} = e^{[(\omega/c)\Delta z_N D(z_N)]} \cdot e^{[(\omega/c)\Delta z_{N-1} D(z_{N-1})]} \dots e^{[(\omega/c)\Delta z_1 D(z_1)]} \Psi_0 = F \Psi_0 \quad (5.46)$$

The electric field vectors for the transmitted and reflected light are obtained from the following relations:

$$\begin{aligned} \Psi_0 &= \Psi_i + \Psi_r \\ \Psi_{N\Delta z} &= \Psi_t \\ \Psi_t &= F (\Psi_i + \Psi_r) \end{aligned}$$

The polarization direction and ellipticity of the light at every depth in the film are obtained by analyzing the electric field vectors after each multiplication step in equation 5.46.

5.5.4 Phase separation and reaction-diffusion model parameters

Simulations of the phase separation and reaction diffusion behavior for the cholesteric self-stratification process were performed for diacrylate monomers (with functionality $f = 4$). We assume the polymerization to proceed towards completion, giving $\alpha_{max} = 1$ and $x_{max} = 1$, and use the mean-field theory to link α to x (chapter 2). Since we use cross-linking monomers we assume $C_{eff} = 1$.

Diffusion coefficients for material transport parallel to the molecular long axis have been measured to be 1.4 times larger than perpendicular²⁴. Reported values of diffusion coefficients (parallel to the LC long axis) for liquid crystals in the nematic LC phase are similar to those in the isotropic phase^{25,18,26,27}, and values are generally in the range of $10^{-10} m^2s^{-1}$. Since the diffusion in depth of the film is perpendicular to the length axis of the molecules, the lower diffusion constant has to be considered in the simulations. The monomer diffusion is assumed to be dominant over the diffusion of the non-reactive materials (discussed in chapter 2) and determines material flux. Table 5.2 shows the simulation parameters.

Table 5.2: Values of simulation parameters for the combined phase separation and reaction-diffusion models.

T_p	Experimental temperature [K]	298
Δz	Depth interval (fraction of Λ) [nm]	1-10
Δt	Polymerization step [s]	<0.0005
χ	Isotropic mixing: Interaction parameter [-]	0.5
C_{eff}	Network elasticity: Network efficiency factor [-]	1
s_{lc}	Nematic ordering: Order parameter of LCs [-]	0.6
s_m	Order parameter of M [-]	0.6
$k_p/\sqrt{k_t}$	Photopolymerization: Polymerization rate constant [$\sqrt{l \cdot mol^{-1} \cdot s^{-1}}$]	1
x_{max}	Maximum double bond conversion [-]	1
α_{max}	Maximum monomer conversion [-]	1
f	Monomer functionality [-]	4
Φ_{In}	Quantum efficiency of photoinitiator [-]	0.5
$\epsilon_{In}(z)$	Extinction coefficient at 351 nm [$l \cdot mol^{-1} \cdot cm^{-1}$]	eq. 5.23
$[In]$	Concentration of photoinitiator [$mol \cdot l^{-1}$]	0.01
$E_{photons}$	Exposure: Energy of one mole photons at 351 nm [Einstein]	$3.4 \cdot 10^5$
I_0	Intensity of incoming light [$mW \cdot cm^{-2}$]	0.05-250
V_{abs}	Absorption contrast [-]	section 5.6.1
Λ_{abs}	Absorption pitch [nm]	200
D_m	Diffusion: Diffusion coefficient of the monomer [$m^2 \cdot s^{-1}$]	$0.7 \cdot 10^{-10}$
K_1	Constant in free volume theory [-]	0.21
K_2	Constant in free volume theory [-]	0

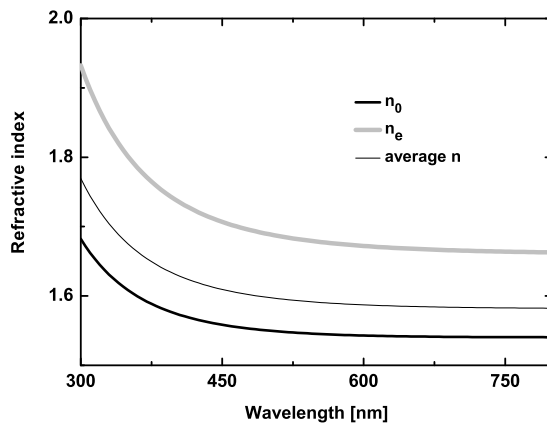
5.6 Results and discussion

5.6.1 Absorbed light intensity profile

Ordinary and extraordinary refractive indices

The wavelength dependent refractive indices ($n_e(\lambda)$ and $n_o(\lambda)$) of the cholesteric reaction mixtures are required for the light propagation simulations. It is assumed that the refractive indices of the cholesteric reaction mixtures B, C and D (table 5.1(a)) resemble those of the nematic LC reaction mixture A, since only small amounts of the chiral dopant is present in B, C and D. Also it is assumed that the refractive indices of mixture A - before polymerization - resemble those of the polymerized films. The ordinary refractive index of planar aligned poly(RM257) (from mixture A) was measured to be 1.546 at 589 nm with the Abbe refractometer. Since the optical properties of the liquid crystal polymer films are wavelength dependent, the refractive indices increases drastically, n_e more than n_o , at wavelengths approaching to the absorption maximum of molecules. The wavelength of the curing UV light is close to the absorption of the molecules, and the refractive indices in this wavelength region needs to be measured.

Ellipsometry measurements on the polymerized planar aligned LC films yielded n_o and n_e in the wavelength range of 300–800 nm (figure 5.12). Good agreements of the birefringence are obtained for wavelengths between 400-800 nm when comparing the ellipsometry measurements with the transmission measurements (figure 5.13(a)). The transmission of the planar aligned nematic polymer films were measured using the optical setup shown in figure 5.9. The birefringence was obtained by fitting the



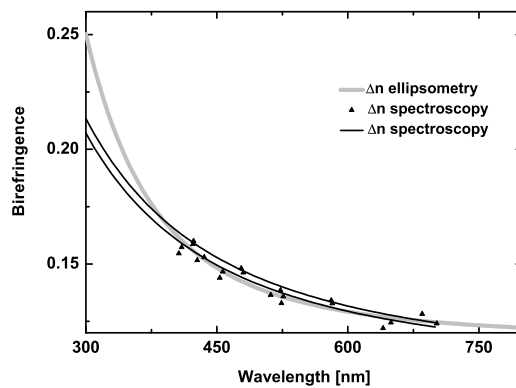
(a)

λ [nm]	n_e	n_o	Δn
351	1.80	1.61	0.19
365	1.78	1.60	0.18
589	1.67	1.54	0.13

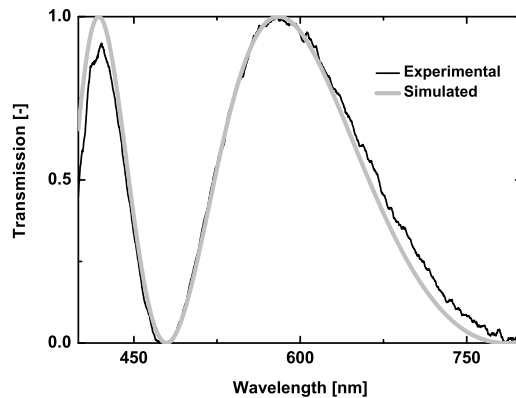
(b)

Figure 5.12: (a) Refractive indices of polymerized planar aligned RM257 measured by ellipsometry. n_e (gray line), n_o (black line) and the average refractive index (black thin line). (b) Refractive indices and birefringence at 351, 365 and 589 nm.

transmission measurements with equations 5.40 and 5.41 using two Cauchy constants (C_1 and C_2) and the film thickness as fitting parameters, figure 5.13(b) shows such a fit. The intensity of the transmitted light decreases at low wavelengths due to absorption and/or scattering of light by the sample itself. This complicates the fitting procedure and the interpolation (lines in figure 5.13(a)) of the birefringence obtained from the transmission data gives lower Δn than the ellipsometry measured birefringence (gray line in figure 5.13(a)). The mathematical approximation, the Cauchy function (equation 5.41), used to fit the transmission data is obviously not sufficient to predict refractive indices close to the absorption band.



(a)



(b)

Figure 5.13: (a) Birefringence measurements of polymerized RM257: ellipsometry data (gray line), transmission spectroscopy data (\blacktriangle) and interpolation of the spectroscopy data (black line). (b) The transmission of planar aligned polymerized RM257 using the optical setup in figure 5.9. Black line: experimental measured transmission, gray line: fitted curve with equations 5.40 and 5.41.

Light propagation simulations

Four polymerized cholesteric films were prepared to verify the light propagation simulations. The two first cholesteric films (1 and 2) were prepared from reaction mixture B (table 5.1(a)) and the central wavelength (λ_{ref}) in the reflectance band for the two films is 490 nm (figure 5.14(a)). Sample 1 has a thickness of 17 μm and the thickness of sample 2 is 26 μm . The other two cholesteric films (3 and 4) were polymerized from mixture C and D, with $\lambda_{ref} = 710$ nm and 930 nm, respectively. The sample thicknesses of 3 and 4 are 17 μm . The reflected wavelengths were

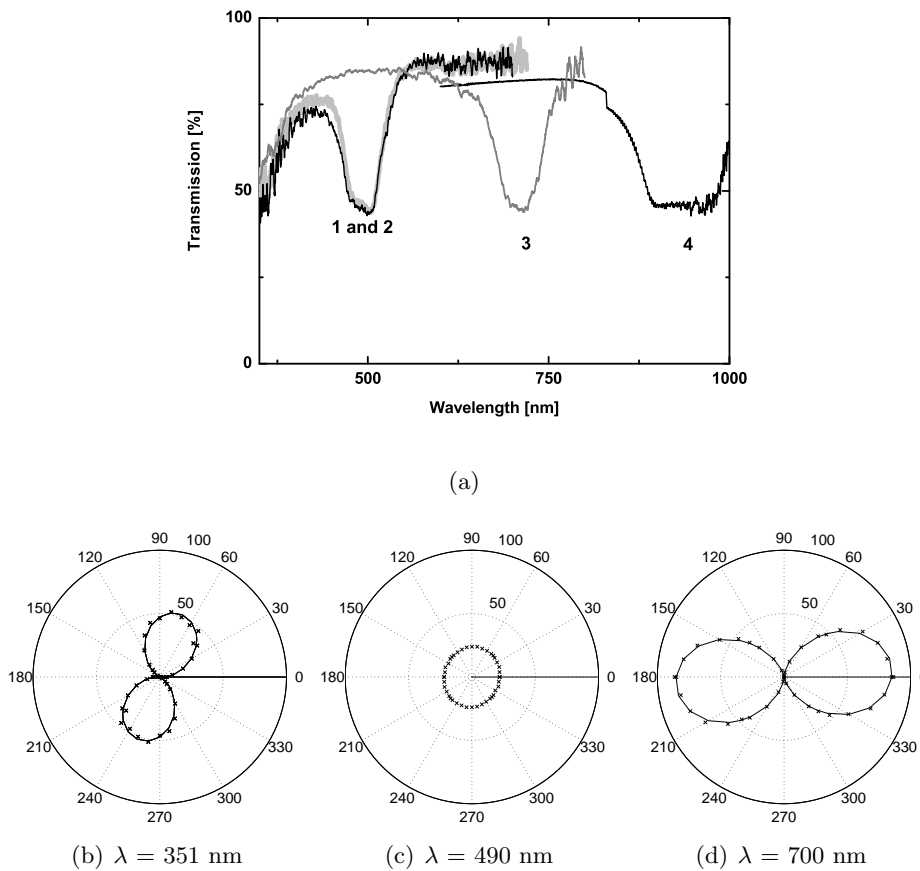


Figure 5.14: Transmission measurements of the four polymerized test samples, the loss in transmission visualizes the reflection band of the cholesteric films. Sample 1 and 2 are prepared from the same reaction mixture and the central wavelength in the resonance band (λ_{ref}) is 490 nm. Sample 3 reflects at red with $\lambda_{ref} = 710$ nm, and sample 4 reflects outside the visible range with $\lambda_{ref} = 930$ nm. (b) - (d): Measured intensities of transmitted linearly polarized light as a function of polar angle providing the polarization direction of the transmitted light of the cholesteric 1 for wavelengths 351 nm (b), in the reflection band at $\lambda = \lambda_{ref} = 490$ nm (c) and for 700 nm (d). The measurements are fitted with equation 5.42 (black line). The incident light was polarized in the horizontal, 0° , direction.

measured by spectroscopy in transmission mode. At low wavelengths (< 400 nm) the transmission is decreased in the spectra due to absorption by the materials, but also scattering. The latter decreases the transmitted intensity at all measured wavelengths.

Light simulations of the polarization directions of the propagating light are compared with the experimental measured polarization directions of the transmitted linearly polarized light of four test samples. The transmitted light polarization from the films was measured with transmission spectroscopy using the optical setup in figure 5.10. At each wavelength the intensities were collected in all directions by rotating the analyzer, and the polarization direction was obtained by fitting the transmission data with equation 5.42. In figure 5.14 the polarization directions of the transmitted light at 351, 490 and 700 nm are shown for sample 1. Inside the reflection band of the cholesteric film (at 490 nm) part of the light is reflected as righthanded circularly polarized light, and part of the light is transmitted as lefthanded circularly polarized light which is detected as equal intensities in all directions.

To simulate the light propagation through the cholesteric films, the wavelength dependent refractive indices were applied (figure 5.12). We assume that the optical properties remain constant when adding (low amounts of) chiral dopants (LC756) to the nematic monomer RM257 to obtain cholesteric LC phase. Using linearly polarized incident light ($S_1 = 1$, $S_2 = 0$ and $S_3 = 0$), the Stokes parameters of the transmitted light were simulated with Berreman's 4x4 matrix method for the four cholesteric test samples. In figure 5.15, the Stokes parameters for the transmitted

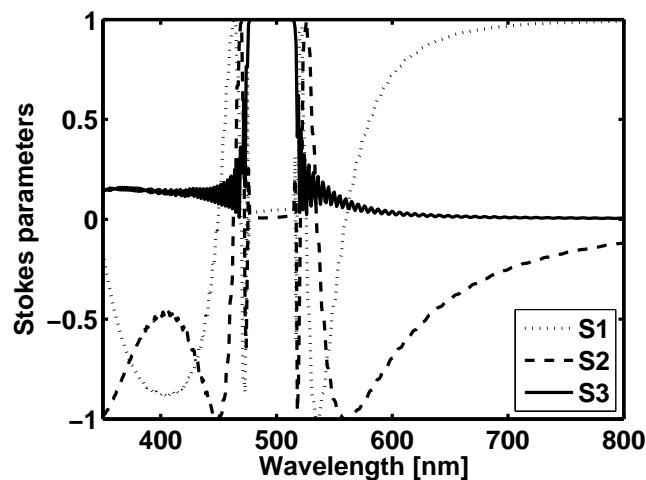


Figure 5.15: Simulated Stokes parameters of the transmitted light that entered as linearly polarized in the horizontal direction ($S_1 = 1$, $S_2 = 0$ and $S_3 = 0$). The cholesteric pitch and sample thickness equals that of the cholesteric test sample 1 ($\lambda_{ref} = 490$ nm, $d = 17$ μm). The transmitted light in the reflection band is left circularly polarized ($S_3 = +1$ and $S_1 = S_2 = 0$). Outside the reflection band the transmitted polarization direction remains mainly linearly polarized (since $S_3 \approx 0$), and the polarization direction can be retrieved from S_1 and S_2 .

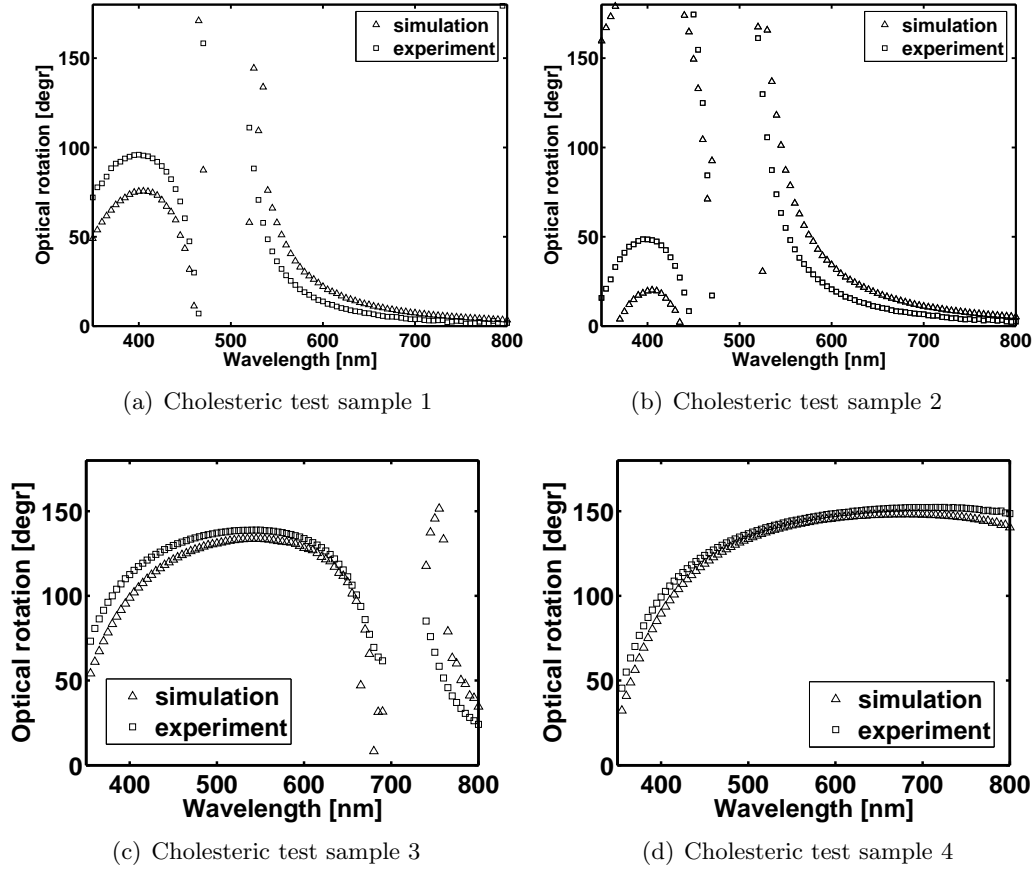


Figure 5.16: Polarization directions of the transmitted light obtained from simulations (\triangle) and experiments (\square).

light are plotted for sample 1. Left circularly polarized light ($S_3 = +1$) is transmitted through the reflection band of the right handed cholesteric film. Close to the reflection band the Stokes parameters change rapidly in value due to the increased optical rotation. For wavelengths lower and higher than the reflection band, the transmitted light is only slightly elliptical polarized ($S_3 \approx 0$).

Comparisons between experimentally measured and simulated transmitted polarization directions yield good agreements for all test samples (figure 5.16). At low wavelengths ($\lambda < 450$ nm) deviations of 10 to 35 degrees between the measured and simulated polarization directions are measured. The deviation in this region (350 nm $< \lambda < 450$ nm) is larger for sample 1 and 2, similar behavior has been noted elsewhere²⁸ and can be explained by the proximity of the reflection band ($\lambda_{ref} = 490$ nm) which gives additional optical rotation. Close to the band edges of the reflection band, all samples show large deviations between the measured and simulated polarization directions, due to the increased optical rotation that is not simulated in the Berreman's light propagation method.

The Stokes parameters in depth of the samples were simulated using the Berre-

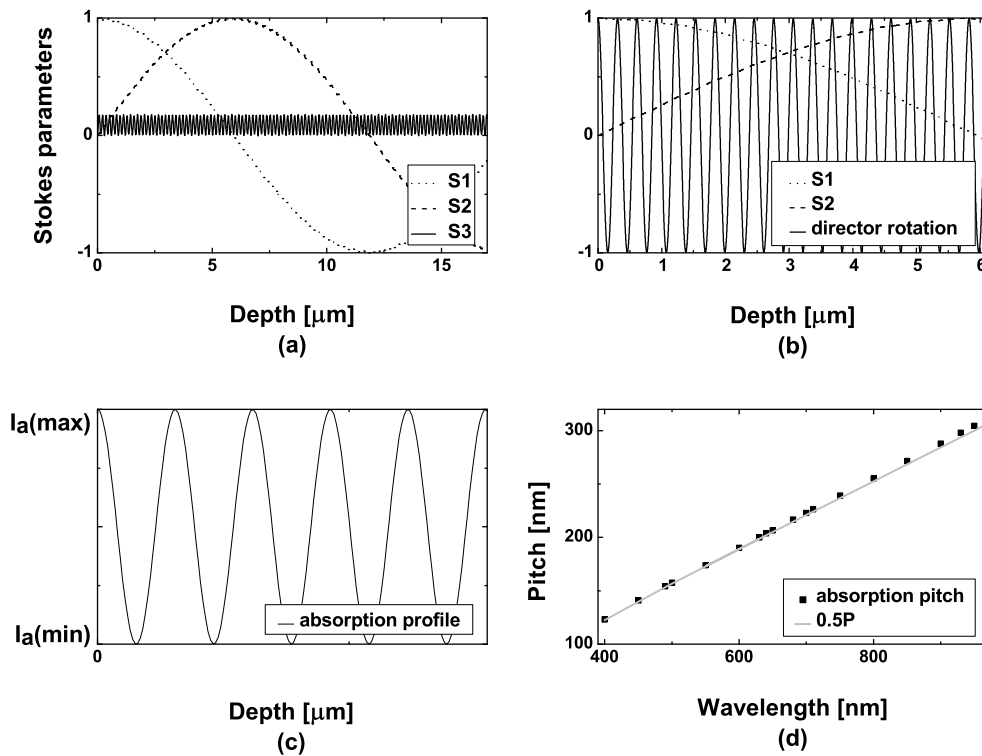


Figure 5.17: (a) Simulated Stokes parameters for the propagating wavelength 351 nm in depth of sample 1. (b) The rotating molecular direction (thin line) and the simulated rotated polarization of the propagating light represented by the Stokes parameters: S_1 (dashed line) and S_2 (dotted line) in sample 1. (c) The absorption profile, with maximum absorption where the director is parallel to the polarization and minimum where they are orthogonal. The absorption pitch (V_{abs}) is the distance between the minimum and maximum. (d) The small difference between the half cholesteric pitch (black line) and the simulated initiation pitch (■) increases with the cholesteric pitch, to 5 nm deviation for cholesteric films reflecting at 900 nm.

man's 4x4 matrix formulation. Such a simulation is shown in figure 5.17 for a 17 μm cholesteric film reflecting at 490 nm (comparable to test sample 1). By knowing the polarization direction of the propagating light and the dichroic photoinitiators alignment, we can predict the absorption pitch (Λ_{abs}) of the absorbed light intensity profile. At every depth that the light polarization direction is parallel with the molecular length direction of the initiator, absorption maximum is obtained (figure 5.17). From simulations of light propagation through cholesteric films reflecting between 400 to 900 nm, we find that the ellipticity of the propagating light remains low (< 0.25), and a small maximum deviation (less than 5 nm) between the simulated absorption pitch and half of the cholesteric pitch is detected. The deviation increases

Table 5.3: Simulated Stokes parameters at the curing wavelength (351 nm) for cholesteric reaction mixtures reflecting light at different wavelengths (λ_{ref}), the cholesteric pitch is calculated using wavelength dependent refractive indices in figure 5.12.

λ_{ref} [nm]	400	500	600	700	800	900	1000	1100
Cholesteric pitch [nm]	490	626	756	884	1010	1136	1264	1390
S_0	1	1	1	1	1	1	1	1
S_1	0.88	-0.29	-0.35	-0.16	0.19	0.54	0.77	0.91
S_2	0.44	-0.94	-0.91	-0.96	-0.94	-0.79	-0.54	-0.18
S_3	0.18	0.18	0.21	0.24	0.27	0.30	0.34	0.37

with the cholesteric pitch (figure 5.17). The light guiding of the propagating light is much slower than the rotation of the cholesteric pitch. For the simulation sample in figure 5.17, the light polarization is rotated ca 45° at a depth of $6 \mu\text{m}$, while the cholesteric director rotate $20 \times 360^\circ$ (figure 5.17). The influence of the rotating light is therefore small, and the absorption pitch can therefore be approximated to half of the cholesteric pitch.

When the cholesteric film reflects light of wavelengths above 900 nm, the ellipticity of the propagating curing light exceeds 30% (table 5.3). Elliptical light will not favor the preferential absorption of the dichroic photoinitiators, and should be omitted. To avoid elliptical propagating light for obtaining larger layer pitches, dichroic photoinitiators absorbing light of larger wavelengths, but below the reflection wavelength of the reaction mixture, are required.

Dichroic ratio²⁹

The absorption spectra of the three photoinitiators (figure 5.6) show that the initiators have larger absorption of light polarized along the long axis (extraordinary direction) than along the short axis (ordinary direction, figure 5.18, the absorption of the nematic host 5-PCH is subtracted from the spectra). The contrast in absorption in the parallel respectively perpendicular direction indicates that the photoinitiators are aligned with the nematic host. The dichroic ratio (A_{\parallel}/A_{\perp}) was measured to 4.5–5.6, averaged over the wavelength for which absorption in both polarization directions were detected (table 5.4). From other studies, a dichroic ratio = 6.7 of photoinitiator **7** was reported²⁸. The dichroic ratio is dependent on the order of the nematic host (5-PCH), with a host having higher order parameter ($s > 0.5$) the dichroic ratio is also increased. For all three initiators the absorption of light polarized in the ordinary direction is low at 351 nm, and very low at 365 nm, which improves the absorption contrast. In general the absorption is low at the curing wavelengths (350 – 365 nm) and is preferable for the polymerization reaction in order not to decrease the intensity significantly in depth of the film. The absorption contrast (V_{abs}) corresponding to dichroic ratios between 4.5–5.6 are 0.78–0.82 (using equation 5.24).

The isotropic extinction coefficients (ϵ_0) for the photoinitiators **5** and **6** were measured by absorption spectroscopy of isotropic dispersed initiator in a solvent

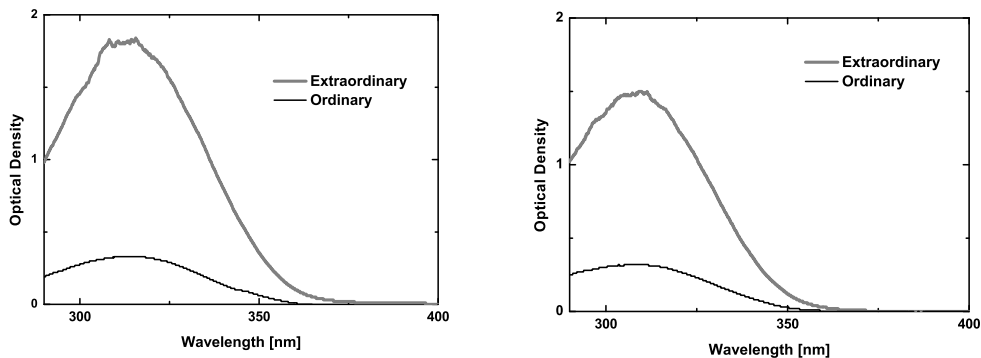
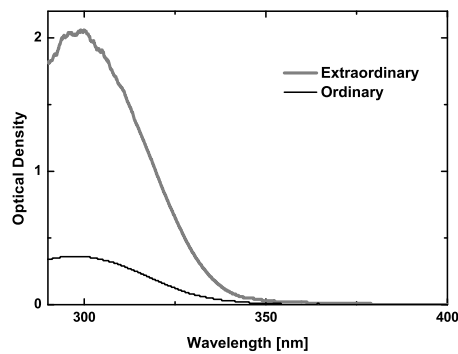
(a) Photoinitiator, **5**(b) Photoinitiator, **6**(c) Photoinitiator, **7**

Figure 5.18: The absorption parallel and perpendicular to the molecular direction measured by spectroscopy on the three photoinitiators: (a) Dichroic photoinitiator **5**, (b) dichroic photoinitiator **6** and (c) dichroic photoinitiator **7**. (Graphs kindly provided by Blanca Serano Ramón).

Table 5.4: Dichroic ratio, absorption contrast (V_{abs}) and extinction coefficients (ϵ) for the dichroic photoinitiators **5**, **6** and **7**.

photoinitiator	dichroic ratio	V_{abs}	ϵ_{351}	ϵ_{365}
5	5.6	0.83	3330	560
6	4.5	0.78	4900	830
7	5.3	0.81	340 [†]	64 [†]

[†] Extinction coefficients estimated using $\epsilon = \frac{2A_{perp} + A_{parallel}}{cl}$. A_{perp}/l and $A_{parallel}/l$ from figure 5.18(c). l is the thickness of the cell, and $c = 0.054$ moles/l (molar concentration of **7** in 5-PCH).

(tetrahydrofuran). The extinction coefficients for 351 and 365 nm are given in table 5.4. The extinction coefficients for **7** are estimated from the absorption spectra in figure 5.18(c).

5.6.2 Combined phase separation - reaction diffusion model

In chapter 2 the parameters that influence the phase separation mechanisms from an isotropic reaction mixture were studied: the interaction between the molecules (χ), the network elasticity ($\kappa(\alpha)$) and the nematic ordering. For the cholesteric self-stratification process the reaction mixture is in the chiral nematic phase, i.e. both the unreactive LCs and the monomers are ordered in the liquid crystalline phase and the nematic ordering contribution arises from both compounds in the mixture. Even though the monomers do not necessarily need to be liquid crystalline, they are required not to disturb the cholesteric phase. The magnitude of the nematic ordering contribution depends on the reaction temperature relative to the clearing temperature of the mixture. A liquid crystalline phase is guaranteed by choosing the polymerization temperature (T_p) below the clearing temperature of the monomers and that of the unreactive LCs. For temperatures above the clearing temperature, in the isotropic phase, no nematic ordering is present (and also not simulated). This is also the case for isotropic monomers that do not have a clearing temperature.

Additionally, the reaction-diffusion mechanisms need to be understood, and controlled in order to favor a reaction rate gradient in depth of the sample that induces phase separation into polymer- and LC-rich layers. The difference in reaction rate at the low and high absorbed intensities induces diffusion of monomers to the reactive sites (primarily at the highest absorbed intensity depths), and counter diffusion of unreactive LCs towards the depths with lower intensity. Combining the phase separation properties of the system with the reaction-diffusion kinetics, the grating morphology can be predicted (chapter 2 and 4 for holographic reflection gratings). Ideally, the reaction-diffusion lines at the lowest absorbed intensities should cross the phase separation line, while the reaction-diffusion lines at the highest absorbed intensities should not.

The phase separation behavior for the cholesteric reaction mixtures is simulated to predict the PS qualities of the cholesteric systems, followed by simulations of the reaction-diffusion behavior to predict the final grating morphology. The phase separation modeling predicts the photopolymerization-induced phase separation that forms stratified PDLCs.

Phase separation lines

The clearing temperature of the reaction mixtures of LC monomers and unreactive LCs ($T_{n^*i(mix)}$) is approximated by

$$T_{n^*i(mix)} = \phi_{lc} \cdot T_{n^*i(LC)} + (1 - \phi_{lc}) \cdot T_{n^*i(M)}$$

The linear behavior of $T_{n^*i(mix)}$ may not be true for all real mixtures, but serves as an approximation for the clearing temperature. The clearing temperature of the

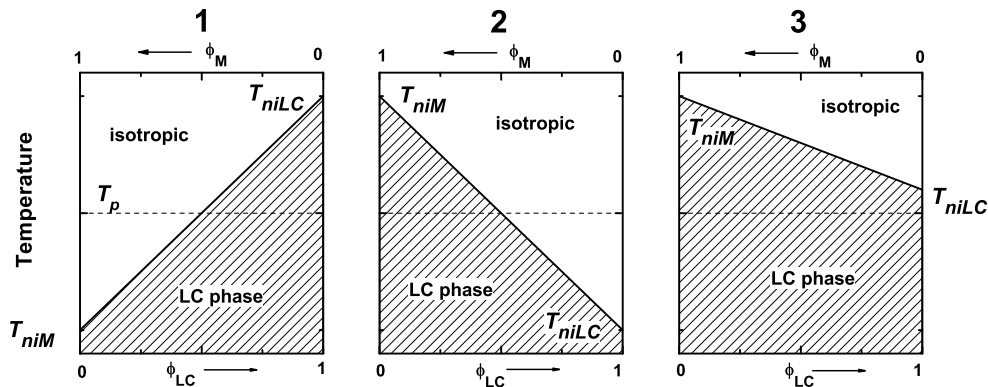


Figure 5.19: Approximated clearing temperatures of reaction mixtures of monomers and unreactive LCs with different clearing temperatures.

reaction mixtures compared to the reaction temperature determine whether a certain concentration of a reaction mixture is in the LC phase or is isotropic (see figure 5.19). From such a comparison the concentrations of the reaction mixture in order to be LC can be estimated. The exact clearing temperatures of the mixtures have to be experimentally determined. Also, $T_{n^*i(mix)}$ indicates below which temperatures the nematic ordering contributes to the phase separation mechanisms. Polymerization temperatures (T_p) can be chosen so that:

1. T_p is below the clearing temperature of the unreactive LCs, but above the clearing temperature of the monomers: $T_{n^*i(LC)} > T_p > T_{n^*i(M)}$. This is equivalent to using isotropic monomers (replacing $T_{n^*i(M)}$ with $T_{m(M)}$ = melting temperature).
2. T_p is above the clearing temperature of the unreactive LCs, but below the clearing temperature of the monomers: $T_{n^*i(LC)} < T_p < T_{n^*i(M)}$.
3. T_p is below the clearing temperature of both the unreactive LCs and the monomers: $T_{n^*i(LC)} > T$, and $T_{n^*i(M)} > T$.

The phase separation simulations are performed without considering crystallization of the mixtures. At reaction temperatures below the clearing temperature, crystallization is possible and may be experimentally verified. Liquid crystal mixtures can remain chiral nematic even at temperatures below the crystallization temperatures, i.e. when mixtures become supercooled and remain the liquid crystalline phases. Due to the retarded crystal nucleation and decreased mobility in the supercooled mixtures the ordered phases remain. Eventually the mixtures will crystallize. Supercooled reaction mixtures might generate well ordered cholesteric LC phases and thus stable absorption profiles, but the decreased mobility does not favor the

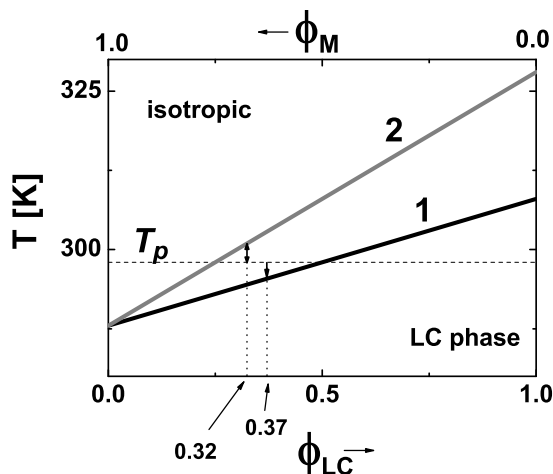


Figure 5.20: Case 1. Clearing temperatures of reaction mixtures determines the phase (isotropic or liquid crystalline phase) of the mixture. **1:** The reaction temperature is chosen in between the clearing temperature of the unreactive LCs and the monomers ($T_p = T_{n^*i(M)} + 10$ and $T_p = T_{n^*i(LC)} - 10$). **2:** The reaction temperature is closer to the clearing temperature of the monomers ($T_p = T_{n^*i(M)} + 10$ and $T_p = T_{n^*i(LC)} - 30$).

diffusion during the polymerization. For the simulations in this chapter, we assume that crystallization and supercooling are not present.

For a reaction temperature exactly between $T_{n^*i(LC)}$ and $T_{n^*i(M)}$ (**1** in figure 5.20), the reaction mixture changes from isotropic to liquid crystalline at $\phi_{lc} = 0.5$. A reaction temperature closer to $T_{n^*i(M)}$ than $T_{n^*i(LC)}$ (**2** in figure 5.20) needs less unreactive LCs to ensure the liquid crystalline state ($\phi_{lc} = 0.25$). The latter allows a larger range of concentrations for reaction mixtures in the LC phase. The phase separation mechanisms are shown in the ternary conversion-phase diagram in figure 5.21. Due to larger contributions from nematic ordering for reaction temperatures closer to $T_{n^*i(M)}$ than $T_{n^*i(LC)}$ (**2** in figure 5.21), phase separation occurs at smaller amounts of polymer (lower monomer conversions).

In figure 5.21, the solubility limit for **1** is found to be $\phi_{lc} = 0.37$, however a reaction mixture at that polymerization temperature (dotted line in figure 5.20) 37% LCs of mixture **1** is isotropic and is thus not suitable for the cholesteric self-stratification process. Only at $\phi_{lc} > 0.5$ the reaction mixture of **1** becomes liquid crystalline, but starting with 50% LC in the reaction mixture requires a decrease in the concentration by 13% in order not to cross the phase separation line by the reaction-diffusion lines from the high absorbed intensity depths.

For **2** (in figure 5.21) the solubility limit is lower, at $\phi_{lc} = 0.32$. A reaction mixture with 32% LC for **2**, is liquid crystalline. Starting with a reaction mixture composed of $\phi_{lc} > 0.25$, the reaction-diffusion lines at the depths with the highest absorbed intensities can enter the isotropic state, while the reaction-diffusion lines

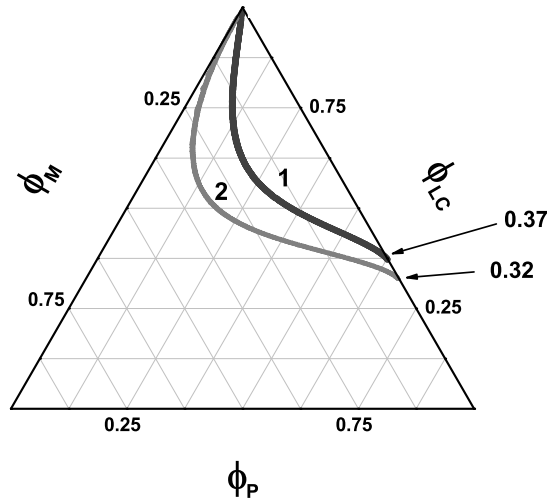


Figure 5.21: Phase separation lines of **1** and **2** from figure 5.20.

at the lowest absorbed intensities stays in the liquid crystalline state. In this way, the polymer-rich layers could be assumed becoming isotropic.

Next the second case of reaction temperatures: T_p is above the clearing temperature of the unreactive LCs, but below the clearing temperature of the monomers (case 2, figure 5.19)

$$T_{n^*i(LC)} < T_p < T_{n^*i(M)}$$

The clearing temperatures of reaction mixtures (figure 5.22) show the reversed state compared to the former case. Since the chosen temperature T_p is higher than the clearing temperature of the unreactive LCs, the reaction mixtures with high contents of unreactive LCs are isotropic. The solubility limit of LCs in the polymer network is $\phi_{lc} = 0.39$ (figure 5.23). A reaction mixture with 39% unreactive LCs is in the LC phase (figure 5.21). The formed polymer will remain anisotropic (and not become isotropic) since the polymerization temperature is below the clearing temperature of the monomers ($T_p < T_{n^*i(M)}$). Another disadvantage is that the compositions at the low intensity regions may become isotropic. Without the LC order, the dichroic photoinitiators are also disordered with a lost absorption profile giving less contrast between the polymer rich and LC rich layer as a result.

In figures 5.21 and 5.23, one phase separation line per set, is found, and no nematic-isotropic phase separation lines are present (as was the case for the holographic reaction mixtures in chapter 2). Examining the state of the phase separated liquids (phase II), it was found that all possible compositions of phase II were either nematic (figure 5.21) or isotropic (5.23). Therefore only one phase separation line is present.

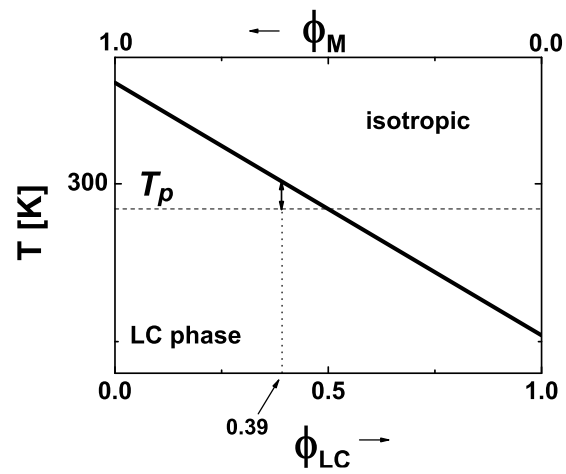


Figure 5.22: Case 2. Clearing temperatures of reaction mixtures determines the phase (isotropic or liquid crystalline phase) of the mixture for a reaction temperature between the clearing temperature of the unreactive LCs and the monomers ($T_p = T_{n^*i(M)} - 10$ and $T_p = T_{n^*i(LC)} + 10$).

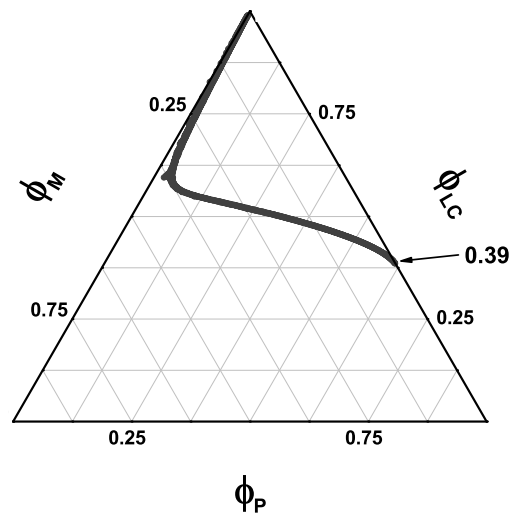


Figure 5.23: Phase separation line of the reaction mixture in figure 5.22.

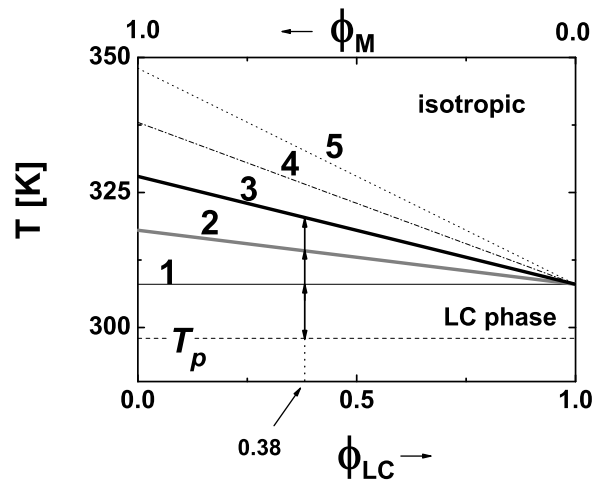


Figure 5.24: Case 3. Clearing temperatures of liquid crystalline reaction mixtures: **1:** $T_p = T_{n^*i(LC)} - 10$ and $T_p = T_{n^*i(M)} - 10$, **2:** $T_p = T_{n^*i(LC)} - 10$ and $T_p = T_{n^*i(M)} - 20$, **3:** $T_p = T_{n^*i(LC)} - 10$ and $T_p = T_{n^*i(M)} - 30$, **4:** $T_p = T_{n^*i(LC)} - 10$ and $T_p = T_{n^*i(M)} - 40$, and **5:** $T_p = T_{n^*i(LC)} - 10$ and $T_p = T_{n^*i(M)} - 50$.

For the last of the three temperature cases, T_p is below the clearing temperatures of both the unreactive LCs and the monomers,

$$T_{n^*i(LC)} > T \quad \text{and} \quad T_{n^*i(M)} > T$$

all composition of reaction mixtures are liquid crystalline (figure 5.24). Increasing the difference between the clearing temperatures, the phase separated area increases. At a certain difference, $T_{n^*i(M)} \geq T_{n^*i(LC)} + 40$ (**4** and **5** in figure 5.25), miscible and homogeneous mixtures are found at two isolated positions in the conversion phase diagram: in the top left part of the diagram - for large LC and low polymer contents, and in the bottom right corner of the diagram - for low LC and large polymer contents. In the other parts of the diagram the polymer network can not hold unreactive liquids and instantaneous phase separation occurs. The miscible phase in the bottom right corner of the diagram is only accessible from right to left: by swelling a polymer network with monomers and LCs, because of phase separation of the monomers and LCs.

Reaction-diffusion lines

Material transport is only possible when there is a gradient in the chemical potential between two subsequent depth intervals. In chapter 2 the effects on the material flux regarding the polymerization rate and value of the diffusion constants were studied for the holographic exposures. There are some differences in material properties of the holographic and cholesteric self-stratification processes that can influence the

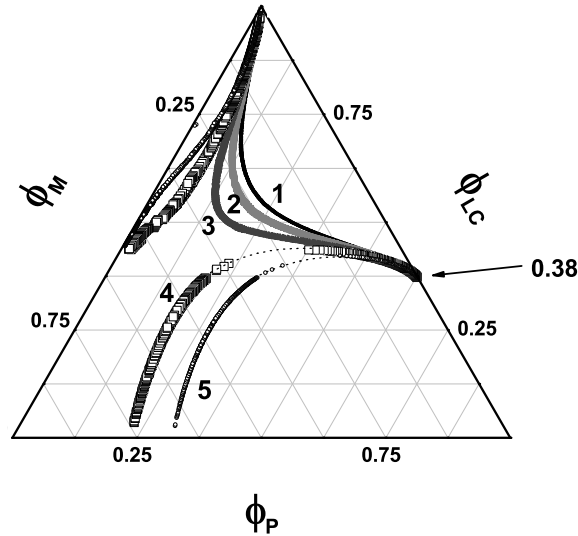


Figure 5.25: Phase separation lines for 1-5 from figure 5.24.

reaction-diffusion kinetics: the monomer functionality, the extinction coefficient of the photoinitiator and the diffusion constant.

While the holographic reaction mixtures contained high-functional monomers, the cholesteric self-stratification process requires lower functional reactive species in order not to disrupt the liquid crystalline phase with bulky multi-functional monomers. Lowering the functionality of the monomers may decrease the polymerization rate and change the elastic properties of the network formed. The extinction coefficients of the dichroic monomers were found to be four times lower than the extinction coefficient of the isotropic PI used for the holographic recordings. Since the reaction rate is proportional to the square root of the extinction coefficient, using the dichroic photoinitiators reduces the rate to the half.

The influences of the diffusion coefficients on the reaction-diffusion behavior in isotropic reaction mixtures were investigated in chapter 2. It was found that the small changes of the initial value of the diffusion coefficient did hardly affect the diffusion during polymerization (for 150nm grating pitches). For ordered liquid crystalline systems, it is known that the diffusion in the length direction of the LC molecule is larger than diffusion in the direction perpendicular to the long axis. However, the differences are small (1 respectively $0.7 \cdot 10^{-10}$), and are not expected to largely influence the simulations.

Experimentally the polymerization rate can easily be altered by the intensity of the curing light, and by the amount of photoinitiators. In the reaction-diffusion simulations, the light intensity is varied while the amount of photoinitiator is kept

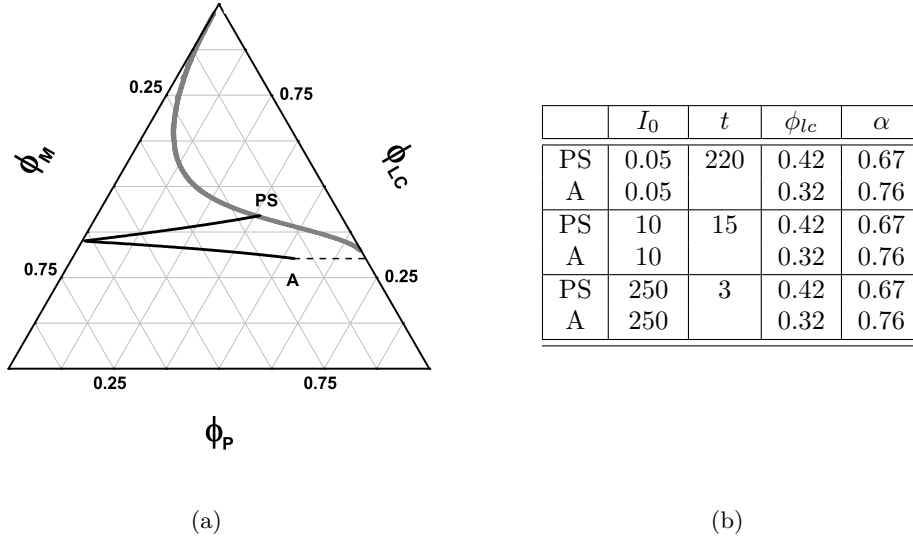


Figure 5.26: (a) Reaction-diffusion lines for the depth intervals with the lowest (top) and highest (bottom) absorbed intensities for $T_{n^*i(LC)} = T_p - 30$ and $T_{n^*i(M)} = T_p + 10$. At a certain time the depth intervals with the lowest intensity crosses the phase separation line (**PS**). At the same time, the depth intervals with the highest intensity reach point **A**. Varying the curing intensity between 0.05 – 250 mW/cm² results in identical reaction-diffusion lines. (b) The time (t [s]) to reach phase separation, and the composition (ϕ_{lc}) and the monomer conversion (α) at that time for different curing intensities (I_0 [mW/cm²]).

constant. Recalling equations 5.21 and 5.22, it is easy to understand that increasing the photoinitiator concentration will generate the same simulation results as long as the light intensity is decreased with the same amount.

Reaction-diffusion simulations were performed for the three temperature cases:

1. $T_{n^*i(LC)} > T_p > T_{n^*i(M)}$: $T_{n^*i(LC)} = T_p - 30$, $T_{n^*i(M)} = T_p + 10$
2. $T_{n^*i(LC)} < T_p < T_{n^*i(M)}$: $T_{n^*i(LC)} = T_p + 10$, $T_{n^*i(M)} = T_p - 10$
3. $T_{n^*i(LC)} > T$, and $T_{n^*i(M)} > T$: $T_{n^*i(LC)} = T_p - 10$, $T_{n^*i(M)} = T_p - 30$

The simulated intensities of the curing light was varied between 0.05 and 250 mWcm⁻², to cover intensities of a magnitude lower than what is generally used for UV-polymerization (~ 0.3 mWcm⁻²) with powerful lasers.

For the first temperature case, the reaction-diffusion mechanisms were simulated starting from a reaction mixture with 35% LC (figure 5.26(a)). The initial reaction concentration is liquid crystalline (according to figure 5.20 the liquid crystalline phase is remained in the reaction mixtures until 75% monomers). The time for the reaction-propagation lines to reach the phase separation line, the LC compositions (ϕ_{lc}) at this time and the monomer conversion (α) are given in table 5.26(b).

The effects on reaction-diffusion lines were identical for all curing intensities. This agrees with the results in chapter 2 (figure 2.22(a)) for the holographic record-

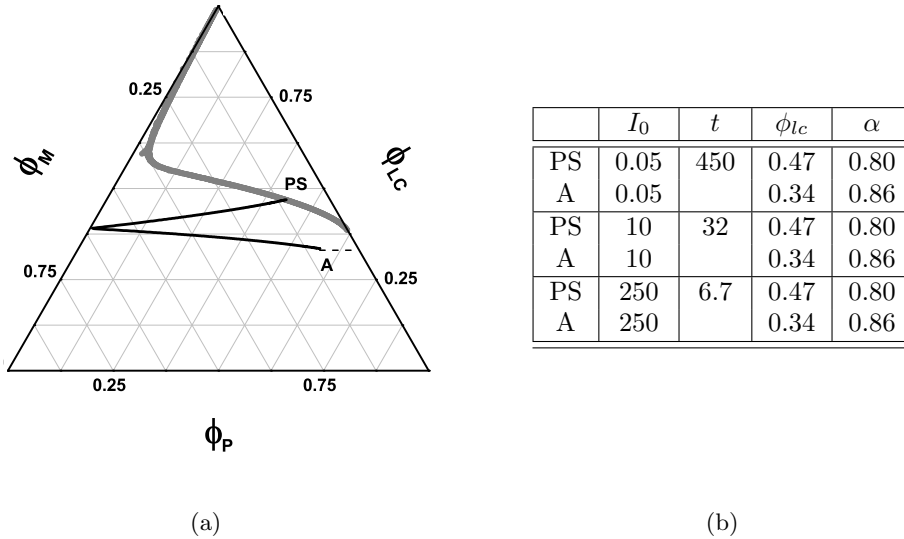


Figure 5.27: (a) Reaction-diffusion lines for the depth intervals with the lowest (top) and highest (bottom) absorbed intensities for $T_{n^*i(LC)} = T_p + 10$ and $T_{n^*i(M)} = T_p - 10$. At a certain time the depth intervals with the lowest intensity crosses the phase separation line (**PS**). At the same time, the depth intervals with the highest intensity reach point **A**. Varying the curing intensity between 0.05 – 250 mW/cm² results in identical reaction-diffusion lines. (b) The time (t [s]) to reach phase separation, and the composition (ϕ_{lc}) and the monomer conversion (α) at that time for different curing intensities (I_0 [mW/cm²]).

ings, for which it was found that the reaction-diffusion lines were independent on the diffusion constant. The polymerization kinetics of the holographic reaction mixture differs from the lower functional cholesteric reaction mixture. However, it was stated in chapter 2 that the reaction-diffusion lines were unaltered when changing the reaction rates; only the amount of polymer formed per time unit decreased with slower polymerization.

The other two temperature cases show very similar behavior: reaction-diffusion behaviors were identical for all intensities of the curing light. For the second temperature case, the reaction-diffusion mechanisms were simulated starting from a reaction mixture with 39% LC (figure 5.27(a)). The time for the reaction-propagation lines to reach the phase separation line, the LC compositions (ϕ_{lc}) at this time and the monomer conversion (α) are given in table 5.27(b).

The third and last temperature case, the reaction-diffusion mechanisms were simulated starting from a reaction mixture with 40% LC (figure 5.28(a)). Since the reaction temperature is chosen to be below all clearing temperatures, all compositions in the phase diagram are liquid crystalline. The time for the reaction-propagation lines to reach the phase separation line, the LC compositions (ϕ_{lc}) at this time and the monomer conversion (α) are given in table 5.28(b).

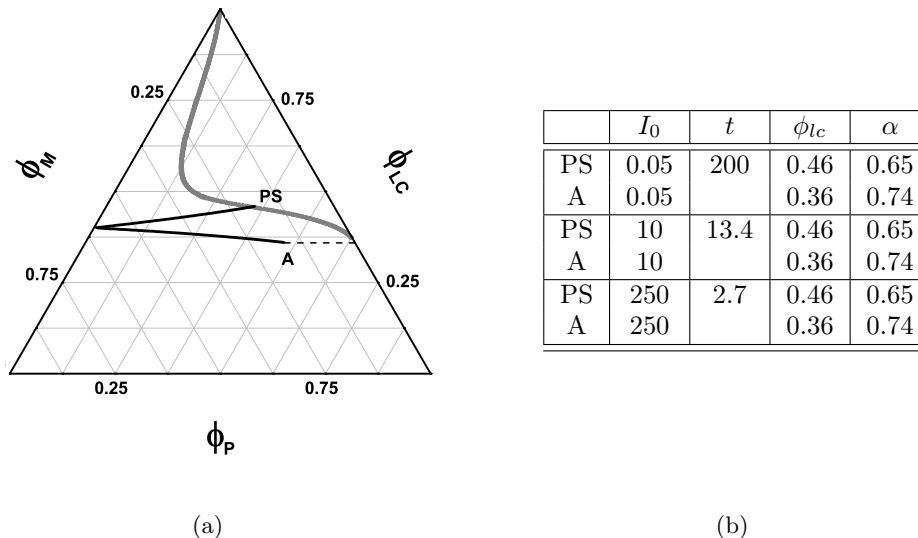


Figure 5.28: ((a) Reaction-diffusion lines for the depth intervals with the lowest (top) and highest (bottom) absorbed intensities for $T_{n^*i(LC)} = T_p - 10$ and $T_{n^*i(M)} = T_p - 30$. At a certain time the depth intervals with the lowest intensity crosses the phase separation line (**PS**). At the same time, the depth intervals with the highest intensity reach point **A**. Varying the curing intensity between 0.05 – 250 mW/cm² results in identical reaction-diffusion lines. (b) The time to reach phase separation, and the composition (ϕ_{lc}) and the monomer conversion (α) at that time for different curing intensities.

5.7 Conclusions

The absorbed light intensity profile was simulated using Berreman's 4x4 matrix method. For the simulations the birefringence at the wavelengths of the curing light are necessary, and was measured by ellipsometry on a model sample. The absorption pitch can be approximated to half of the cholesteric pitch for cholesteric pitches below 1100 nm (reflecting light below 900 nm). Simulations revealed that light propagation through reaction mixtures with larger cholesteric pitches (> 1100 nm) the ellipticity of the propagating light became important ($> 30\%$). Since elliptic curing light initiates the photoinitiators at all depth, the pitch of the cholesteric reaction mixture should not exceed 1100 nm, or other photoinitiators excited by larger curing wavelengths are required.

Photoinitiators have been experimentally tested on their preferential light absorption (along the long axis) and their alignment with the chiral nematic liquid crystals. Three suitable candidates were found.

The reaction temperature is critical for the phase separation properties of the reaction mixtures. Experimentally, the reaction mixture must be chiral nematic therefore the temperature needs to be below the clearing temperature of the reaction mixture. For the simulations it means that the chemical potentials gain

contributions from the nematic ordering of both the non-reactive LCs as well as from the monomers, but only when the mixtures are liquid crystalline.

Reaction-diffusion simulations reveal that the reaction kinetics does not play an important role in the layer formation; by altering the curing light intensity from 0.05 to 250 mW/cm² identical reaction-diffusion lines are simulated. However the time for the reaction-diffusion lines to reach the phase separation line differ (from 7.5 min to 3 s).

The phase separation and reaction-diffusion simulations help us in defining suitable material properties and choosing experimental conditions for the cholesteric self-stratification process. From the phase separation simulations the reaction temperature and composition of the reaction mixture can be estimated. The composition of the reaction mixture, before polymerization, should preferably have a LC concentration corresponding to the solubility limit (i.e. the highest LC concentration of that can be held by the polymer network). Nor the reaction rate neither the diffusion constants (for the values studied here) influence the reaction-diffusion lines. Therefore it was found that only the time determines when the phase separation is reached; as long as the absorbed intensity profile remains constant.

5.8 References and notes

1. Yeh, Y. and Gu, C. *Optics of liquid crystal displays*. John Wiley and Sons, Inc., New York, (1999).
2. van de Witte, P., Brehmer, M., and Lub, J. *J. Mater. Chem.* **9**, 2087–2094 (1999).
3. Solomons, T. W. G. *Organic chemistry*. John Wiley and Sons, Inc., New York, 6th edition, (1996).
4. Stegemeyer, H. *Ber. Bunsenges. Phys. Chem.* **78**, 860–869 (1974).
5. de Vries, H. *Acta Cryst.* **4**(219) (1951).
6. Broer, D. J. *Curr. Opin. Solid State Mat. Sci.* **6**(553-561) (2002).
7. Berreman, D. W. and Scheffer, T. J. *Phys. Rev. Lett.* **25**, 577 (1970).
8. Berreman, D. W. and Scheffer, T. J. *Mol. Cryst. Liq. Cryst.* **11**, 395 (1970).
9. Berreman, D. W. *J. Opt. Soc. Am.* **63**, 1374 (1973).
10. Levi, L. *Applied optics*, volume 1. John Wiley and Sons, (1968).
11. Collett, E. *Polarized light*. Marcel Dekker, Inc., New York, (1993).
12. Li, J. and Wu, S.-T. *J. Appl. Phys.* **95**(3), 896–901 (2004).
13. Broer, D. J., Mol, G. N., van Haaren, J. A. M. M., and Lub, J. *Adv. Mater.* **11**(7), 573–578 (1999).
14. Flory, P. J. *Principles of polymer chemistry*. Cornell University Press, London, (1971).

15. Moerkerke, R., Koningsveld, R., Berghmans, H., Dušek, K., and Šolc, K. *Macromolecules* **28**, 1103–1107 (1995).
16. Shen, C. and Kyu, T. *J. Chem. Phys.* **102**, 556–562 (1995).
17. Chiu, H.-W. and Kyu, T. *J. Chem. Phys.* (1995).
18. Penterman, R. *Photo-enforced stratification of liquid crystal/monomer mixtures, Principle, Theory and analysis of a paintable LCD concept*. PhD thesis, Eindhoven University of Technology, Eindhoven, (2005).
19. Leewis, C. M. *Formation of Mesoscopic Polymer Structures for Optical Devices - a Nuclear Microprobe Study*. PhD thesis, Eindhoven University of Technology, (2002).
20. Hecht, E. *Optics*, chapter 4, 86–148. Addison Wesley, San Francisco, 4th edition (2002).
21. The ellipsometry measurements were performed at Philips Research (Eindhoven, NL). The author acknowledges Toon de Win for his kind assistance.
22. Azzam, R. M. A. and Bashara, N. M. *Ellipsometry and polarized light*. North-Holland publishing company, Amsterdam, (1977).
23. Escuti, M. J., Cairns, D. R., and Crawford, G. P. *J. Appl. Phys.* **95**(5), 2386–2390 (2004).
24. de Gennes, P. G. and Prost, J. *The Physics of Liquid Crystals*. Clarendon Press, Oxford, 2nd edition, (1993).
25. Bowley, C. C. and Crawford, G. P. *Appl. Phys. Lett.* **76**(16), 2235–2237 (2000).
26. Leewis, C. M., de Jong, A. M., van IJzendoorn, L. J., and Broer, D. J. *J. Appl. Phys.* **95**(8), 4125–4139 (2004).
27. Kyu, T., Nwabunma, D., and Chiu, H.-W. *Phys. Rev. E.* **63**, 061802 (2001).
28. Broer, D. J., Mol, G. N., van Haaren, J. A. M. M., Lub, J., and Huck, N. *Polym. Preprints* **43**(2), 526 (2002).
29. Ramón, B. S. PhD thesis to be published. experimental results and discussions.

Chapter 6

Materials selection for the cholesteric self-stratification process

6.1 Introduction

Optical switches with periodic and alternating polymer and liquid crystal layers formed by the cholesteric self-stratification process involve photopolymerization-induced phase separation from a cholesteric liquid crystalline reaction mixture. In this chapter, materials for such cholesteric reaction mixture are investigated.

Reaction mixtures for the cholesteric self-stratification process need to include monomers that are miscible with the LCs without disturbing the cholesteric phase. Cross-linking monomers are necessary for phase separation to occur; it was simulated in chapter 2 that a polymer network favors the phase separation properties. Ideally isotropic phase separated polymer layers should be formed upon polymerization, and the unreactive liquid crystals should have large birefringence to allow large contrast differences when switching the multilayer grating. These properties can be hard to combine in two components only (one monomer and one LC), but blending monomers and non-reactive liquid crystals with different specific properties (e.g. liquid crystalline monomers, small isotropic monomers, and cross-linking monomers, one or several non-reactive LCs) the miscibility and phase separation properties might be tailored for the cholesteric self-stratification process.

The chirality of the reaction mixture can be incorporated by a chiral dopant, which can be a chiral unreactive LC or a chiral reactive molecule. By tuning the chiral dopant concentration the cholesteric pitch can be modified and thus also the absorption pitch and the layer periodicity. The helical twisting power (HTP) of the chiral dopant determines the handedness and twisting of the cholesteric helix. A positive and large HTP indicates that the dopant tightly winds the helix and produces a righthanded cholesteric film with the nematic host. Helical twisting powers of chiral dopants are determined from the central reflecting wavelength (λ_{ref})

as:

$$HTP = \frac{1}{c \cdot P_{chol}} = \frac{n_{average}}{c \cdot 2\lambda_{ref}} \quad (6.1)$$

where c is the concentration of the chiral dopant, P_{chol} is the cholesteric pitch, and $n_{average}$ is the average refractive index^{1,2,3}.

The temperature of the reaction mixture can also affect the cholesteric pitch, depending on the materials properties, P_{chol} can e.g. increase or decrease with increased temperature⁴. Above the clearing temperature the cholesteric LC phase is lost and the mixture becomes isotropic. At low temperatures, on the other hand, the reaction mixture crystallizes. The phase transition to or from the crystalline state occurs at a temperature which is not as well defined as the nematic-isotropic transition, since the former require nucleation centers. A fast cooling of the cholesteric mixture can delay the nucleation and the liquid crystalline state can be remained at temperatures below the melting temperature. This supercooling phenomena enables processing the mixture in its liquid crystalline state at temperatures sometimes far below the melting temperature.

Polymerization-induced phase separation and reaction-diffusion simulations for the cholesteric self-stratification process in chapter 5 predicted periodic layer formation when using reaction mixtures of more than 50% reactive materials. Polymerizing reaction mixtures with less monomers phase separation will be induced at the depths of both the high and low absorbed intensities (comparable to figure 2.26, in chapter 2).

Isotropic monomers polymerize into isotropic polymers, while LC-monomers can remain anisotropic after polymerization. Cross-linking LC monomers do in general remain anisotropic, while other LC monomers that are sterically restricted, i.e. have short aliphatic chains between the reactive group and the LC moiety may produce isotropic polymer. The phase separated polymer and LC layers need to fulfill the conditions for Bragg reflection⁵, i.e. having a refractive index modulation in depth of the stratified PDLC great enough to reflect light. Layers of isotropic polymer in the grating allow polarization independent reflection, which is preferable for e.g. display and ambient lighting applications.

Outline of chapter

In this chapter liquid crystals and monomers for typical reaction mixtures are investigated as single component and in mixtures of different concentrations of the compounds. The study of the compounds is concentrated in four categories:

1. Liquid crystalline nematic host (non-reactive)
2. Chiral dopant (polymerizable or non-reactive)
3. Cross-linker (polymerizable)
4. Difunctional monomers (polymerizable)

In each category one or several compounds are proposed and are analyzed on their liquid crystalline ordering and miscibility, their chirality and reflectance, and their phase separation properties upon photopolymerization.

6.2 Experimental

6.2.1 Materials

Four mono-acrylates were used in the study: 2-phenoxyethyl acrylate (PEA, **1**, Aldrich), isobornyl methacrylate (iBMA, **2**, Aldrich), biphenyl methacrylate (BiPhMA, **3**, J&W PharmLab), cyanobiphenyl acrylate (LCA, **4**, synthesized by Philips Research, NL). As cross-linker the reactive mesogen RM257 (**5**, Merck) was used. The chiral dopant, with high positive twisting power, Palicolor LC756 (**6**, LC756, BASF) also acts as cross-linker due to its two acrylate groups. The non-reactive nematic liquid crystals used in this study were 4'-pentyl-4-cyanobiphenyl (K15, **7**), 4'-hexyl-4-cyanobiphenyl (K18, **8**), and 4'-heptyl-4-cyanobiphenyl (K21, **9**), 4''-pentyl-4-cyanoterphenyl (**10**, 5CT), and 4'-octyloxy-4-cyanobiphenyl (M24 or 8OCB, **11**), all from Merck. The nematic LC mixture E7 consists of a blend⁶ of 51% (**7**), 16% (**9**), 8% (**10**) and 25% (**11**) and is commercial available at Merck). Two initiators

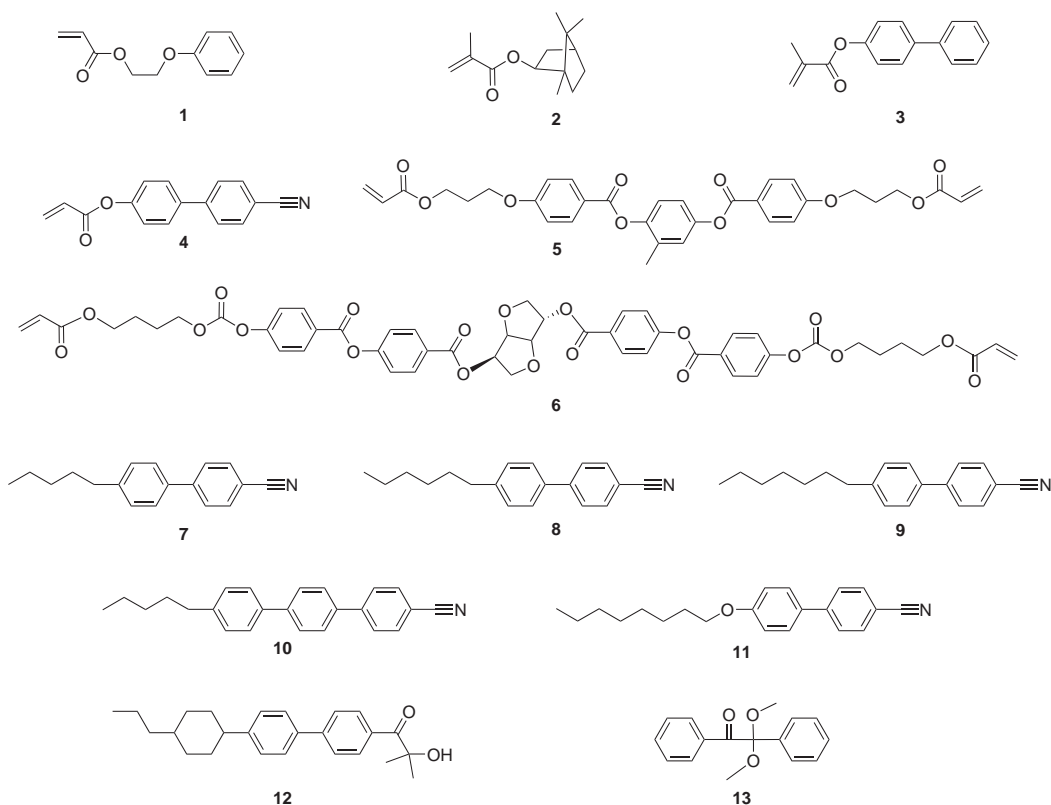


Figure 6.1: Chemicals used in this study: **1** 2-phenoxyethyl acrylate (PEA), **2** isobornyl methacrylate (iBMA), **3** biphenyl methacrylate (BiPhMA), **4** cyanobiphenyl acrylate (LCA), **5** reactive mesogen RM257, **6** chiral dopant LC756, **7** 4'-pentyl-4-cyanobiphenyl (K15), **8** 4'-hexyl-4-cyanobiphenyl (K18), **9** 4'-heptyl-4-cyanobiphenyl (K21), **11** 4'-octyloxy-4-cyanobiphenyl (M24), **10** 4''-pentyl-4-cyanoterphenyl (5CT), **12** dichroic photoinitiator and **13** isotropic photoinitiator IRG651.

are used with different purposes: a dichroic photoinitiator (**12**) and an isotropic photoinitiator: 2,2-Dimethoxy-1,2-diphenylethanone (IRG651, **13**, Ciba). The isotropic photoinitiator is applied when uniform polymerization is required for the reaction mixture investigations, while the dichroic photoinitiator, which consists of elongated, rod-like molecules with its transition dipole moment for UV absorption parallel to its molecular long axis, is primarily used for creating the absorbed intensity profile in depth of the film. Reaction mixtures consisting of at least one reactive molecule (**1-6**), at least one non-reactive liquid crystal (**7-11**) and one of the photoinitiators (**12-13**) were prepared. Films were analyzed after introduction into anti-parallel planar aligned glass cells ($5\mu\text{m}$ cell gap, Linkam) or between polyimide (AL1454, JSR) coated and rubbed glass plates. Polymerizations were performed with non-coherent UV-light (0.3 mW cm^{-2} , Philips Cleo 15W) for 15-120 min.

6.2.2 Experimental techniques

Miscibility studies and transition temperatures were measured by differential scanning calorimetry (DSC, Q2000 DSC, TA Instruments). During the DSC measurements the mixtures in the sample pans were cooled and heated ($5\text{-}10^\circ\text{C}/\text{min}$) in a temperature range including the clearing temperature of the mixture. At the peak of the heat flow measured by the DSC, the clearing temperature is obtained. Information of miscibility is obtained from the shape of the peak. A sharp peak represents a well ordered liquid crystalline phase in which all components are miscible. A broad peak informs that the transition occurs over a range of degrees, which is characteristic for less miscible systems.

The miscibility of the reaction mixtures, and transition temperatures were also analyzed by optical microscopy (Axioplan 2, Zeiss) equipped with temperature regulating stage (THMS 600, TMS 94 and LNP, Linkam). Reaction mixtures in planar aligned cells were analyzed between crossed polarizers while heating and cooling the samples. The temperature at which the reaction mixture becomes isotropic (and all light is blocked by the crossed polarizers) is the clearing temperature. The homogeneity of the reaction mixture is studied at room temperature and at the transition temperatures.

The reflected wavelengths of the mixtures were measured by UV-vis scanning spectrophotometer (Shimadzu UV-3102PC equipped with MPC-3100) in transmission. The loss in transmission describes reflection from the film for wavelengths that are not absorbed by the sample itself (or its supporting glass plates with the polyimide coating). The transmission as a function of wavelength was measured at normal incidence.

Sample morphologies were analyzed by scanning electron microscopy (SEM, XL 30 ESEM-FEG, Philips) of the cross section of polymerized films. Thereto the samples were broken in liquid nitrogen, followed by removal of the liquid crystal at the cross section by washing with methanol. Prior to the SEM analysis, a conducting layer of 15 nm gold was sputter coated (K575 XD Turbo sputter coater, Emitech) on the remaining polymer structures of the cross section.

6.3 Results and discussion

6.3.1 Nematic liquid crystal host

A suitable nematic host for the cholesteric self-stratification process should keep its liquid crystalline phase when monomers are added. Furthermore it should favor phase separation into periodic layers upon polymerization and preferably have large birefringence to display optical contrast between the switched and non-switched state. A single LC compound can be used or a mixture of several, the latter is often applied in devices since it generally improves the properties of the nematic host. There are many different types of liquid crystals, in this study we focus on nematic cyanobiphenyls as they represent liquid crystal phases at relatively modest temperatures.

Three nematic hosts were studied. First, as a single component nematic host the cyanobiphenyl K18 (**8** in figure 6.1) was used. K18 is nematic at room temperature; the crystalline–nematic and the nematic–isotropic transitions were measured to 15 and 29 °C. Its birefringence is given to 0.189⁷. To widen the temperature window for processing, a second nematic host was prepared by mixing equal parts of K18 with the cyanobiphenyl K21 (**9** in figure 6.1, Cr30N44I °C and $\Delta n = 0.199$ ⁷). The nematic phase of the mixture was measured to be present between -4 to 37 °C. The melting temperature is suppressed when mixing nematic LCs with concentration at the eutectic point.

The commercial available nematic liquid crystal mixture E7 (Merck) contains three biphenyls (**7**, **9**, and **11** in figure 6.1) and a terphenyl (**10** in figure 6.1). The mixture enables qualities as large optical and dielectrical anisotropy ($\Delta n = 0.225$), and a broad temperature range of the nematic LC phase⁷. Furthermore

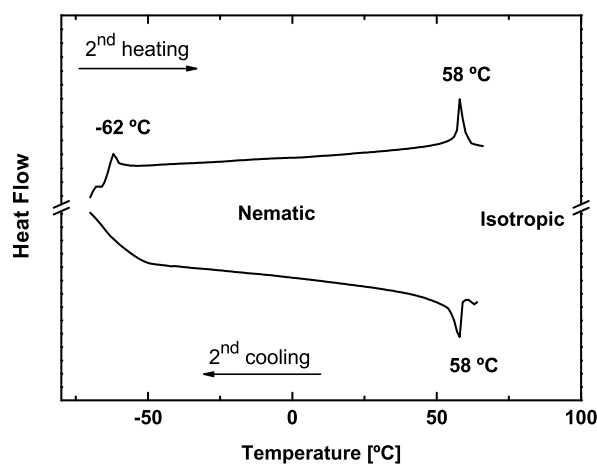


Figure 6.2: Phase transitions of E7 during the 2nd cooling and heating runs measured by differential scanning calorimetry.

it has been applied in reaction mixtures to produce photopolymerization-induced phase separated PDLC devices with random distributed LC droplets or droplets confined in layers^{8,9,10,11,12}. E7 has also been used in photopolymerization-enforced stratification where phase separated E7 is covered by a polymer top coating^{13,14}.

The large nematic window of E7 spans from -62 °C to +58 °C (measured by DSC, figure 6.2). At +58 °C the sharp peak in the DSC curve indicates that E7 change phase from nematic to isotropic, or vice versa. The phase transition and the phases (nematic LC and isotropic phase) were confirmed by analyzing E7 in the temperature range by polarization microscopy. Upon cooling, the E7 rather forms a glassy nematic phase than crystallizes; the phase transition at the lower temperature in the figure (-62 °C) is therefore generally assumed to be the glass temperature of the mixture^{15,16} than the crystallization temperature. The large nematic window is an advantage when adding extrinsic species that may decrease the clearing temperature (which is the case when e.g. adding isotropic molecules).

6.3.2 Chiral dopants

Chiral dopants are molecules with chiral centers that induce the cholesteric phase in the nematic host. The advantage of a chiral dopant with a large twisting power is that small concentrations of the dopant modify the cholesteric pitch without significantly varying the other properties of the mixture. The chiral dopant Palicolor LC756 (BASF, **6** in figure 6.1) melts at 100-110 °C and crystallizes at 80-90 °C, measured by temperature regulated optical microscopy and DSC. Despite the calamitic nature, the molecule by itself was not found to be liquid crystalline, concluded from microscopy studies. Also addition of LC756 suppressed the clearing temperatures of the nematic hosts. If LC756 would have been liquid crystalline, in the super-cooled state at temperatures above the clearing temperature of the nematic host the clearing temperature would most likely have been increased (such a behavior will be displayed for the liquid crystalline cross-linker in the next section).

However, LC756 does not disturb the nematic phase; instead it induces the cholesteric LC phase in the nematic hosts. Cholesteric films reflecting in visible wavelengths were prepared by adding 3-13 weight% LC756 to the hosts. The cholesteric films reflected right-handed circularly polarized light of the matching wavelengths to the cholesteric pitch, $\lambda_{ref} = P_{chol}n_{average}$ (figure 6.3). The reflection of right-handed circularly polarized light reveals that the chiral dopant is right-handed.

The chiral dopant needs to be miscible in the nematic host to form a stable and homogeneous cholesteric LC phase. Only then, the inverse of the cholesteric pitch (and thus the reflection) is linear proportional to the concentration of chiral dopant. The slope, the helical twisting power (HTP), is influenced by the nematic host (or rather the miscibility of the chiral dopant with the nematic host). The reflection and helical twisting power for LC756 in E7, in the eutectic mixture of K18 and K21, and in the nematic liquid crystal monomer RM257 (**5** in figure 6.1) were investigated. It was observed that cholesteric mixtures with higher concentrations of LC756 reflected light of a larger wavelength than expected (e.g. 11 weight% in E7 or 8 weight% in the mixture of K18 and K21, figure 6.3 and 6.4(b)). For these

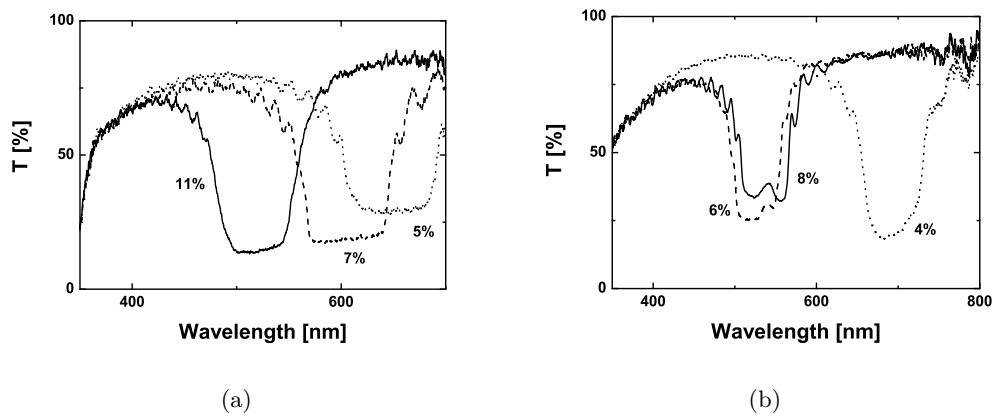
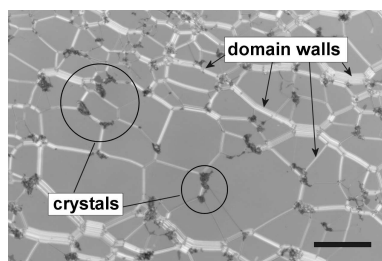
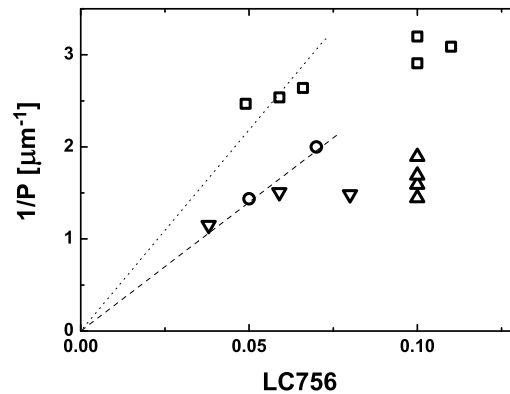


Figure 6.3: Transmission spectroscopy with right-handed circularly polarized light of cholesteric LC mixtures with the chiral dopant LC756. (a) In the nematic host E7 (5 weight% LC756 dotted line, 7 weight% LC756 broken line, and 11 weight% LC756 black line), (b) in the nematic mixture of K18 and K21 (4 weight% LC756 dotted line, 6 weight% LC756 broken line, and 8 weight% LC756 black line).



(a)



(b)

Figure 6.4: (a) Crystallization of LC756 in E7, some crystals (darker spots) are circled in the optical microscopy image of the cholesteric film. The domain walls (lighter lines) between the cholesteric LC domains, the “oily streaks”, are characteristic for chiral nematic LCs. The measure bar is $100 \mu\text{m}$. (b) The helical twisting power of LC756 in E7 (\square) was calculated to $44 \mu\text{m}^{-1}$ (dotted line), and for the other nematic hosts $\text{HTP} = 28 \mu\text{m}^{-1}$ (broken line, ∇ : mixture K18 and K21, \circ : RM257). The solubility limit for LC756 in the hosts is assumed to be exceeded for concentrations ≥ 8 weight%. The concentrations of LC756 in the mixtures of E7 and RM257 (\triangle) are all above the solubility limit.

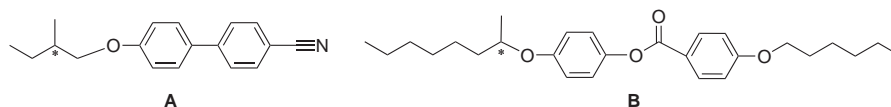


Figure 6.5: Non-reactive chiral dopants: **A** right-handed CB15 and **B** left-handed ZLI811.

mixtures the solubility limit was reached, at which LC756 phase separates from the nematic host and crystallizes (figure 6.4(a)). The decreased concentration of LC756 in the hosts due to crystallization explains the larger cholesteric pitches. The helical twisting power depends on the nematic host, which was also observed here. The twisting power for LC756 in the hosts are calculated for concentrations below the solubility limit <0.08 . The twisting power in E7 is larger ($\text{HTP} = 44 \mu\text{m}^{-1}$, dotted line in figure 6.4(b)), than that for the other two hosts: RM257 and the mix of K18 and K21 ($\text{HTP} = 28 \mu\text{m}^{-1}$, broken line in figure 6.4(b)).

Since the chiral dopant is a diacrylate, it also acts as a cross-linker creating a polymer network upon polymerization, which is favorable for the phase separation process. A combination of an unreactive chiral dopant and a cross-linker is also possible. Two examples of unreactive chiral dopants are the right-handed CB15 or the left-handed ZLI811 (figure 6.5), both commercial available from Merck. The helical twisting powers of ZLI811 and CB15 are approximately 4 times lower than that of LC756^{17,7}, therefore large concentrations (20-60%) are required for cholesteric LC mixtures to reflect in the visible wavelength range. In the end result there is an essential difference between devices made by reactive or non-reactive chiral dopants. Polymerizing mixtures containing non-reactive chiral dopants the phase separated LCs remain chiral after the polymerization, instead of incorporating the chirality into the polymer network (as is the case using LC756) and the phase separated LCs becomes nematic.

6.3.3 Cross-linking monomers

The network elasticity strongly influences the phase separation properties of a system (chapter 2). Polymer networks can be created by polymerizing cross-linking monomers, therefore are cross-linking monomers a necessary ingredient in the reaction mixtures for the cholesteric self-stratification process. Those monomers should have two or more reactive groups, be miscible with the other components in the reaction mixture and should not deteriorate the cholesteric LC phase.

The cross-linking monomer RM257 (Merck, **5** in figure 6.1) was chosen as candidate for the cholesteric self-stratification process based on its documented polymerization-induced phase separation properties in mixtures with liquid crystalline cyanobiphenyls¹⁸. The reactive mesogen is a diacrylate with nematic–isotropic phase transition at 127 °C, measured in the DSC graph of the first cooling and consecutive heating cycles (figure 6.6). During the first cooling the RM257 did not show any crystallization due to a relative stable supercooled nematic LC phase that was caused by a fast cooling rate hindering the mixture to relax and form crystals. The

melting temperatures, at 39 and 70 °C, detected during the heating cycle revealed that the sample had crystallized during the 5 minutes at 0 °C. The clearing temperature was detected to be at 127 °C. After the first heating, the mixture polymerized when kept at 140 °C, during the following cooling and heating cycles the polymer did not show any phase transitions due to the cross-linked polymer restricting the mobility of the liquid crystal moieties and the reorganization of the molecular rods.

Adding the chiral dopant LC756 in the nematic host RM257 creates cholesteric liquid crystals that reflect light of shorter wavelengths than when added to E7 as nematic host. Transmission measurements showed that a cholesteric mixture with 5 weight% LC756 in RM257 reflected the central wavelength of 550 nm and the cholesteric pitch was estimated to $550/1.58 = 348$ nm (average refractive index of the monomer RM257 is 1.58). Polymerizing the same film, the cholesteric structure was remained in the cross-linked polymer. From scanning electron micrographs of the cross-section of such a polymerized cholesteric film (figure 6.7), the cholesteric pitch was estimated to 344 nm ($= 2 \cdot 172$). The measured cholesteric pitch agrees with the cholesteric pitch obtained from transmission spectroscopy. Comparable SEM images of cross-sectioned polymerized cholesteric materials have been reported elsewhere¹⁹.

Replacing parts of the nematic host RM257 with E7 while keeping the concentration of LC756 constant, decreases the nematic–isotropic transition temperatures (table 6.1). Also the wavelengths of reflection are affected of the composition of the host. The more E7 that is present in the mixture cause reflection at larger wavelengths (table 6.1). After one day at room temperature, the reflection shifted to larger wavelengths, table 6.1, due to phase separation and crystallization of the chi-

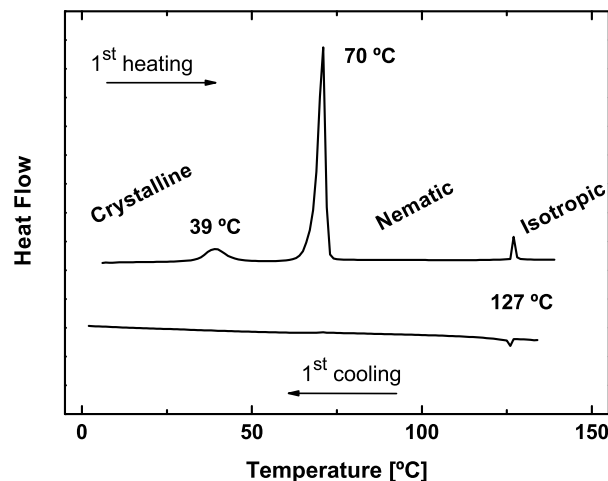


Figure 6.6: Phase transitions of RM257 during the 1st cooling and heating curves measured by differential scanning calorimetry.

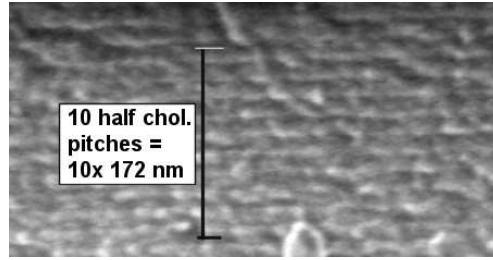


Figure 6.7: Scanning electron micrograph of the cross-section of a polymerized chiral nematic film with composition: 5 weight% LC756 and 1 weight% photoinitiator IRG651 in RM257.

ral dopant. For the cholesteric self-stratification process the control of the cholesteric pitch is necessary, therefore it is important to have a well miscible system. This can be favored by heating up the reaction mixture above the clearing temperature where the mixing is facilitated, continued by slowly cooling down the mixture to chiral nematic phase just before the polymerization. The temperature control of the mixture is crucial since the cholesteric pitch is increased by temperatures approaching the clearing temperature¹⁹.

The polymerization-induced phase separation properties of RM257 in E7 (without the chiral dopant) were studied by polymerizing planar aligned reaction mixtures of 10 and 20 weight% RM257 in E7 and 1 weight% photoinitiator IRG651 (**13** in figure 6.1). The films were polymerized by $0.3\text{mW}/\text{cm}^2$ UV-light during 120 min. The polymerized films did not display optical phase separation. This behavior has been reported for similar systems²⁰ and is explained by the similar birefringence of E7 and

Table 6.1: Reflection from cholesteric films of the cross-linker RM257 in the chiral nematic host (10 weight% LC756 in E7). Chiral nematic–isotropic transition temperatures (T_{n^*i}) for mixtures of RM257 in the chiral–nematic host(6 weight% LC756 in E7).

RM257 in chiral–nematic host [weight%]	after 1 h λ_{ref} [nm]	after 24 h λ_{ref} [nm]
45	UV	420
25	420	470
0	500	550

RM257 in chiral–nematic host [weight%]	T_{n^*i} (heating) [°C]	T_{n^*i} (cooling) [°C]
100	127.4	126.5
30.4	72.3	70.6
19.3	64.2	62.7
9.8	60.6	59.1
0	55.2	54.6

poly(RM257) combined with the alignment of the formed polymer, poly(RM257), and the non-reactive E7 after polymerization. Due to these two matters the optical contrast is low between the polymer and non-reactive LCs. In the coming paragraph one alternative to increase the optical contrast will be discussed.

6.3.4 Difunctional monomers

Monomers that favor the polymerization-induced phase separation and simultaneously increase the optical contrast between their polymers and the phase separated anisotropic liquid crystals are suitable for the cholesteric self-stratification process. Preferable the monomers are isotropic and polymerize into isotropic polymers. In addition the monomers must be miscible in the cholesteric reaction mixture without disturbing the liquid crystalline phase. Four monoacrylates (which are difunctional, i.e. the monomers by them-self polymerize into linear polymers) are investigated to fulfill the needs of the cholesteric self-stratification process.

Phenoxyethyl acrylate

On the basis of similarity of parts of the LC diacrylate RM257, the phenyl group in the monomer PEA (**1** in figure 6.1) is assumed to facilitate the miscibility and alignment with E7. The monomer did not show any liquid crystalline behavior as was expected from the molecular structure. At room temperature the monomer PEA is an isotropic liquid, which viscosity is increased by decreasing temperatures. Due to its lack of anisotropy, the PEA monomer will create isotropic polymers upon polymerization. Adding PEA to nematic or chiral nematic hosts decreased the nematic–isotropic transition temperatures of the hosts significantly. With K18 as nematic host the mixtures became isotropic at room temperature caused by a drastic decrease of the nematic–isotropic transition temperatures. Decreasing the temperature, an instable nematic phase was obtained below the crystallization temperature of K18, with the result that K18 spontaneously crystallized. To overcome crystallization of the nematic host a larger nematic window is required; hence the host was replaced with a mixture of K18 and K21. Addition of LC756 and PEA to the mixture of K18 and K21, also decreased the nematic–isotropic transition temperatures (figure 6.8(a)), contrary the cross-linker RM257 increased the mixtures T_{ni} . A chiral nematic host consisting of 20 weight% RM257 and 6 weight% LC756 allowed up to 15 weight% PEA to be added while still remaining the liquid crystalline phase. More PEA turned the mixtures instable and isotropic.

Instable mixtures were also observed mixing PEA in the nematic host E7 (figure 6.8(b)). Above 13 weight% PEA in a nematic host consisting of RM257 and E7, the mixture becomes instable and phase separates into nematic and isotropic regions which is seen in the polarizing micrograph between crossed polarizers in figure 6.9.

To conclude, only small amounts (< 15%) of the isotropic monomer PEA can be added to the cholesteric reaction mixture without disturbing the cholesteric phase.

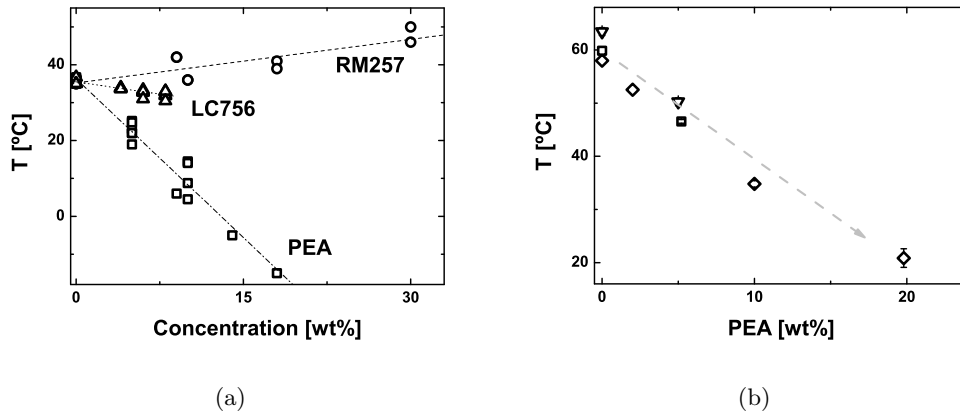


Figure 6.8: (a) Phase transition temperatures of the (chiral) nematic mixtures of K18/K21 (50/50 w/w) after addition of the isotropic monomer PEA (□), the LC cross-linker RM257 (○) or the chiral dopant LC756 (△). The transition temperatures are measured by DSC and temperature regulated microscopy during both heating and cooling of the samples. (b) The (chiral) nematic–isotropic phase transition temperature is drastically decreased by addition of PEA to nematic (E7 ◇, E7 and 20 weight% RM257 ∇) or chiral-nematic (E7 and 5-6 weight% LC756 and 10 weight% RM257 □) reaction mixtures. The dashed line indicates the decreased transition temperatures with increasing content of PEA.

Isobornyl methacrylate

Isobornyl methacrylate (iBMA, **2** in figure 6.1) is an isotropic monomer that has documented phase separation properties in E7 for photopolymerization enforced stratification processes^{13,21}. The main difference between the photo-enforced stratification and cholesteric self-stratification processes is that the former starts in isotropic phase, while the cholesteric self-stratification process requires a cholesteric liquid crystalline phase. So, for iBMA to serve in reaction mixture for the cholesteric self-

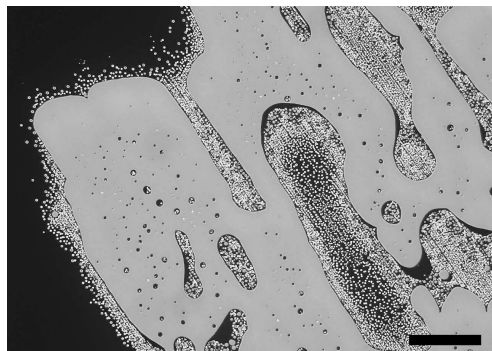


Figure 6.9: Optical microscopy image between crossed polarizers of phase separated reaction mixture of 14 weight% PEA and 19 weight% RM257 in E7, measured at room temperature.

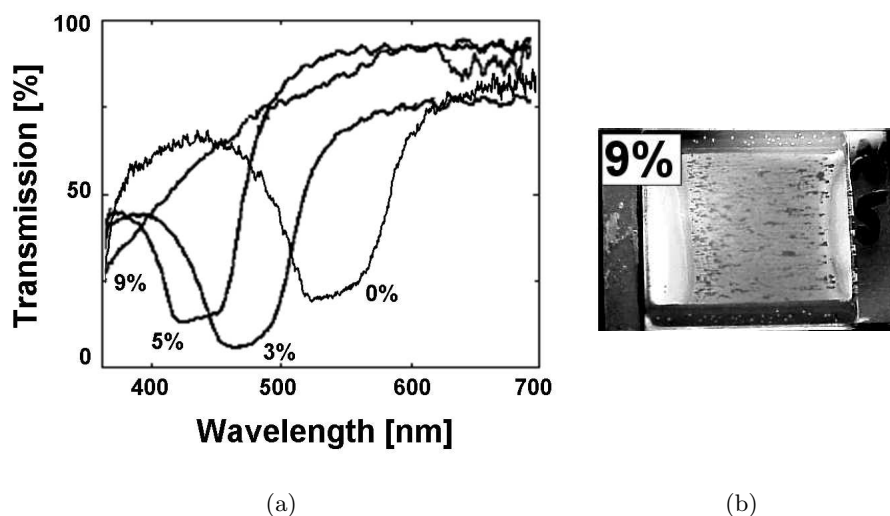


Figure 6.10: (a) Reflected wavelengths decrease when adding larger amounts of the isotropic monomer isobornyl methacrylate (0, 3, 5 and 9 weight% iBMA) to a chiral nematic mixture of 10 weight% LC756 in E7 (measurements 1 h after sample preparation). (b) Photo (1 day after preparation) of a cholesteric mixture of 9 weight% iBMA and 5 weight% LC756 in E7 between crossed polarizers. Going inwards from the edges the color changes from yellow to green to blue, the large region in the middle reflects red color and contains isotropic stripes (black stripes). The chiral nematic–isotropic transition temperature of the mixture was measured to 32 °C, the photograph was taken at room temperature.

stratification process, it must not only display good phase separation properties but also favor a stable cholesteric LC phase in the reaction mixture.

The monomer iBMA was found to tighten the pitch in cholesteric mixtures of E7 and 10 weight% LC756, as was indicated by the decrease of the reflected wavelength with increased amount iBMA (figure 6.10(a)). These results were surprising regarding the molecular structure and isotropy of the monomer, since it was expected that isotropic molecules would instead increase the cholesteric pitch. On the other hand, iBMA might improve the solubility of the chiral dopant and thereto decrease the cholesteric pitch. When analyzing the unpolymerized samples below the clearing temperatures of the mixtures in polarization microscopy, isotropic phase separated regions were observed and the pitch was continually changing over the sample (figure 6.10(b)). Additionally, the mixtures were unstable in time. After some days the reflected wavelengths had increased, equivalent with LC756 mixtures with E7 and RM257, in which LC756 crystallized.

Due to the instability of cholesteric phase, it is not advisable to use iBMA as isotropic monomer in the reaction mixtures studied here.

Biphenyl methacrylate

The monomer biphenyl methacrylate (BiPhMA, **3** in figure 6.1) has a biphenyl group which was assumed to increase the miscibility with the biphenyl containing nematic

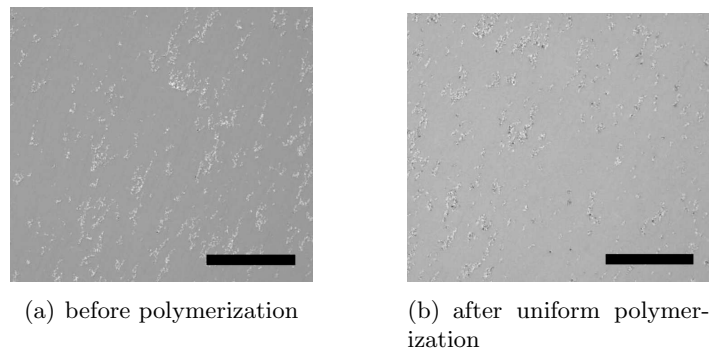


Figure 6.11: Optical microscopy images of BiPhMA containing samples between crossed polarizers. (a) The reaction mixture contained 2 weight% BiPhMA, 19 weight% RM257, 1 weight% IRG651 and 78 weight% E7. (b) After uniform polymerization (0.3 mW/cm^2 during 30 min at room temperature) the phase separated crystals are still present and unchanged. No additional phase separation occurred.

hosts.

The monomer BiPhMA is solid at room temperature and did not show any liquid crystalline properties during polarization microscopy or DSC. The monomer exhibits two melting temperatures, at $96 \text{ }^\circ\text{C}$ and $108 \text{ }^\circ\text{C}$.

The transition temperatures of nematic hosts were decreased by adding the isotropic monomer BiPhMA (table 6.2). Even though DSC analysis of the mixtures revealed miscible liquid crystalline phases, microscopy investigations of cells filled with the same mixtures showed the opposite. Micrographs revealed that cells with planar alignment layers filled with mixtures containing BiPhMA were not homogeneous for any concentration of BiPhMA. Instead crystals of BiPhMA were detected in the hosts (figure 6.11), indicating that processing or storage in room temperature is not possible.

Cyanobiphenyl acrylate

A monomer with a cyanobiphenyl group is very similar to the nematic hosts and therefore assumed to exhibit good miscibility. The cyanobiphenyl acrylate (LCA, 4 in figure 6.1) is presumed to show liquid crystalline behavior but to polymerize into an isotropic polymer because of steric hindrance of the liquid crystal moiety (the

Table 6.2: Nematic–isotropic transition temperatures (T_{ni}) for mixtures with BiPhMA in nematic mixture of E7 and in E7 + 10 weight%RM257.

BiPhMA [weight%]	host	T_{ni} (heating) [$^\circ\text{C}$]	T_{ni} (cooling) [$^\circ\text{C}$]
-	E7	58	58
10	E7	56	54
10	E7 + 10 weight% RM257	53	51

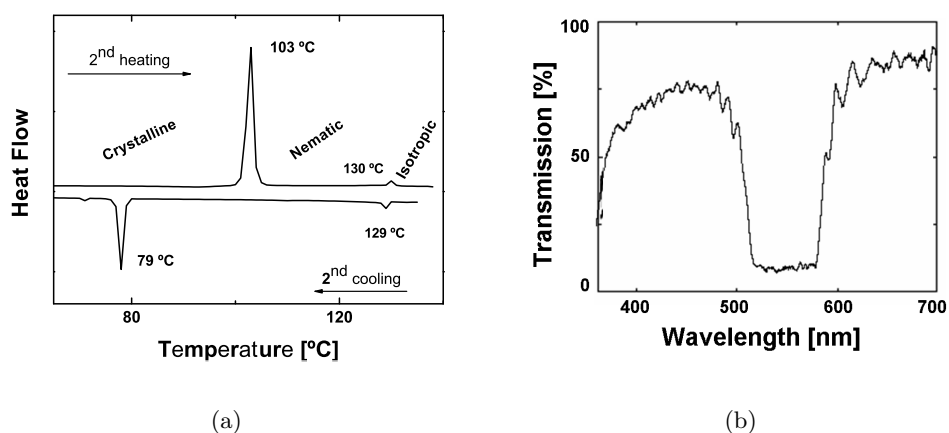


Figure 6.12: (a) Phase transition temperatures measured by the second cooling and heating during DSC measurements. The monomer LCA melts into a nematic phase at 103 °C and becomes isotropic at 130 °C. Upon cooling a broader nematic temperature range is found, from 129 °C to 79 °C where the monomer crystallizes. (b) Transmission spectroscopy for right-handed circularly polarized light of a mixture containing 11 weight% LCA and 6 % LC756 in E7. The reflection is almost 100% and the reflection band, with the central wavelength of 540 nm, is rectangular shaped which is characteristic for cholesteric mixtures.

cyanobiphenyl group) by the polymer main chain. The steric hindrance is due to the absence of a flexible spacer between the rodlike unit (the cyanobiphenyl group) and the polymer main chain.

Microscopy and DSC measurements revealed that LCA have a nematic phase below 130 °C (figure 6.12(a)). During cooling the LCA crystallized at 79 °C and is solid at room temperature. The melting temperature was found to be 103 °C.

LCA increased the transition temperatures of the chiral nematic host (table

Table 6.3: Liquid crystalline phase transition temperatures for mixtures with LCA in nematic and/or chiral nematic hosts.

LCA [weight%]	host nematic or chiral-nematic	Clearing temperature [°C]
100	-	130
-	E7	58
9	E7	62
-	E7 + 6 weight% LC756	55
9	E7 + 6 weight% LC756	58
-	E7 + 6 weight% LC756 + 10 weight% RM257	61
5	E7 + 5 weight% LC756 + 10 weight% RM257	62
-	E7 + 6 weight% LC756 + 20 weight% RM257	64
5	E7 + 5 weight% LC756 + 20 weight% RM257	69

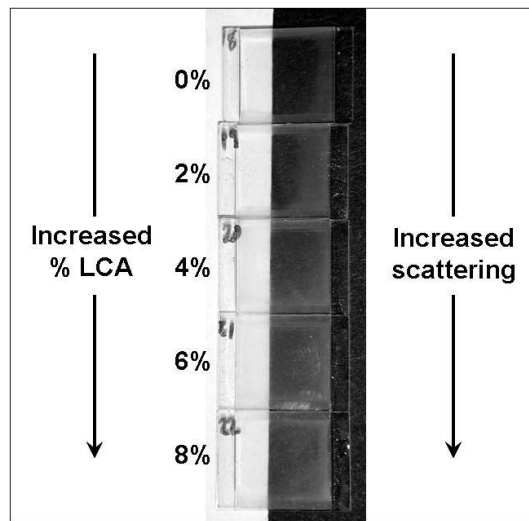


Figure 6.13: Optical visible phase separation in form of white scattering samples after polymerization (0.3 mW/cm^2 UV-light during 15 min) at $50 \text{ }^\circ\text{C}$, which is just below the clearing temperature of the mixtures.

6.3), similarly to the liquid crystalline cross-linker RM257. The mixtures are homogeneous and stable in time, this is reflected by well defined cholesteric reflection bands (figure 6.12(b)).

The polymerization-induced phase separation properties of LCA mixtures were investigated by homogeneous polymerization (0.3 mW/cm^2 UV-light during 15 min) of planar aligned nematic mixtures of LCA in E7 and the cross-linker RM257. At room temperature no optical phase separation was observed after polymerization (analogous to what was found for RM257 mixtures, section 6.3.3). Increasing the polymerization temperature to $50 \text{ }^\circ\text{C}$, which is ca $10 \text{ }^\circ\text{C}$ below the nematic-isotropic transition temperatures of the mixtures, phase separation was observed as white scattering films (figure 6.13). The increased polymerization temperature allows reorganization of the aligned reaction mixture to formed polymer networks differing in optical properties (refractive indices) compared to the phase separated unreactive LCs. Due to the low contents of LCA in the samples in figure 6.13, the intensity of the white scattered light is low.

6.3.5 Towards photopolymerization-induced stratified films

The simulations in chapter 5 predicted polymerization-induced phase separation into layers for reaction mixtures containing large amounts of monomers ($> 50\%$). Based on the materials in the previous paragraphs, we are left with two choices for the cholesteric self-stratification process:

- reaction mixtures containing LCA monomers and polymerizing at elevated temperatures
- reaction mixtures with some ($< 15\%$) PEA, and increase the monomer content with the liquid crystalline cross-linker RM257.

Table 6.4: Refractive indices of the materials in the reference samples and the samples polymerized with linearly polarized light.

non-reactive	reactive		[weight%]	n_o	n_e
K18		nematic	19.5	1.523	1.711
K21		nematic	19.5	1.520	1.719
	RM257	nematic, diacrylate	45	1.549 [†]	1.688 [†]
	LC756	chiral dopant, diacrylate	5	isotropic	
	PEA	isotropic, monoacrylate	10	isotropic	
	12	dichroic photoinitiator	1	isotropic	

[†] The refractive indices for liquid crystalline monomers can change upon polymerization, and are generally decreased due to restricted ability of the LC moieties to align themselves along the director.

In this paragraph experimental results will be discussed for the latter alternative.

Reaction mixtures with high contents of RM257 were prepared: 45 weight% RM257, 10 weight% PEA, 5 weight% LC756, 1 weight% dichroic photoinitiator (**12** in figure 6.1) in the nematic host of equal parts of K18 and K21 (table 6.4). Such a reaction mixture has a clearing temperature at 28-33 °C and is reflecting in green at room temperature. First, reference samples were prepared. Reaction mixtures were polymerized in the cholesteric LC phase with circularly polarized light (0.3 mW/cm² UV-light during 15 min) to avoid an absorption profile in depth of the film. These samples showed optical properties for liquid crystal swollen cholesteric polymers (figure 6.14(a)) which was expected due to the large amount of the anisotropic monomers (45% RM257). At room temperature the films reflected right-handed circularly polarized light and reflected the other handedness. Reflection of linearly

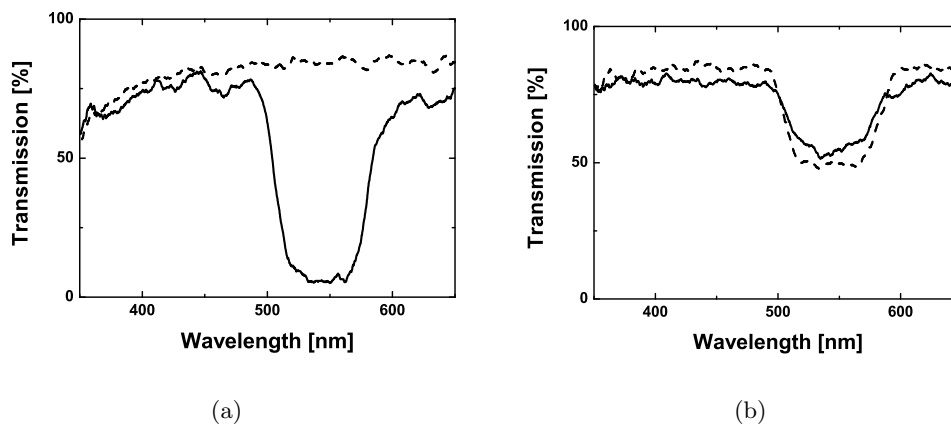


Figure 6.14: Transmission spectroscopy at room temperature of polymerized reference sample made from a cholesteric reaction mixture with the composition in table 6.4: (a) circularly polarized light (right-handed: line, left-handed: broken line) and (b) linearly polarized light (+45° to the LC alignment direction: line, and -45° to the LC alignment direction: broken line).

polarized light of the reference sample was as expected hardly influenced by the polarization direction (figure 6.14(b)). The reflection bands are typical for cholesteric films: rectangular shaped. From the spectroscopy measurements it is clear that the cholesteric pitch is remained in the polymerized network since the polymerized film reflects one handedness of circularly polarized light.

Next, polymerizing the reaction mixture 15 min with linearly polarized light (linear polarizer in front of the UV-light source of 0.3 mW/cm^2), the transmission spectra differ from the reference sample (figure 6.15(a)). The film remained reflecting in green but at lower wavelength compared to the reference sample ($\Delta\lambda = \text{nm}$). The reflection band is narrower, but still only one handedness of circularly polarized light is reflected. Examining the polymerized film by polarizing microscopy, it showed that the cholesteric phase was present since oily streaks, appearing from the domain walls in the cholesteric LC phase, were observed (figure 6.16(a)). The transmission spectra with linearly polarized light were however remarkably different from the reference samples. The linearly polarized polymerized film reflected more than 50% of linearly polarized light in one polarization direction (figure 6.15(b)). Light linearly polarized in the orthogonal direction showed low reflection.

Whether the additional reflection appeared from Bragg layers, cross sections of the sample were studied by SEM imaging (figure 6.16(b)). A layer periodicity was clearly visible, and the pitch was measured in the SEM images to 163 nm. This value is similar to that of the half cholesteric pitch (P_{chol}) calculated from the central reflected wavelength (λ_{ref}) and the average refractive index ($n_{average}$):

$$P_{chol} = \lambda_{ref} \cdot n_{average} = 513 \cdot 1.59 = 322 \text{ nm} (= 2 \cdot 161 \text{ nm})$$

The cross-section in figure 6.16(b) is comparable to the cross-sections of the periodically stratified holographic gratings in chapter 2 (figure 2.9(b)), where periodic layers were produced from isotropic reaction mixtures. On the other hand it also resembles SEM graphs of cholesteric polymers (figure 6.7). It cannot be concluded unambiguously whether the periodicity is solely from phase separated layers or from cholesteric polymer network. It is obvious that more and advanced analyses are necessary. The polarization dependent reflection of the sample could be the result of several optical structures that are integrated in the cholesteric network:

- Bragg gratings of anisotropic polymer layers and phase separated LCs (ideally polarization independent reflection of linearly polarized light depending on the refractive index contrast)
- optical retardation layers of e.g. phase separated non-chiral nematic LCs

Most probably these effects are present simultaneously. An attempt to discriminate between these effects is using temperature regulated transmission spectroscopy, where the optical properties of the non-reactive phase separated liquid crystals can be tuned by the temperature.

Heating the reference sample to $60 \text{ }^\circ\text{C}$, the layer periodicity may increase slightly because of thermal expansion which causes reflection at larger wavelengths¹⁹. By

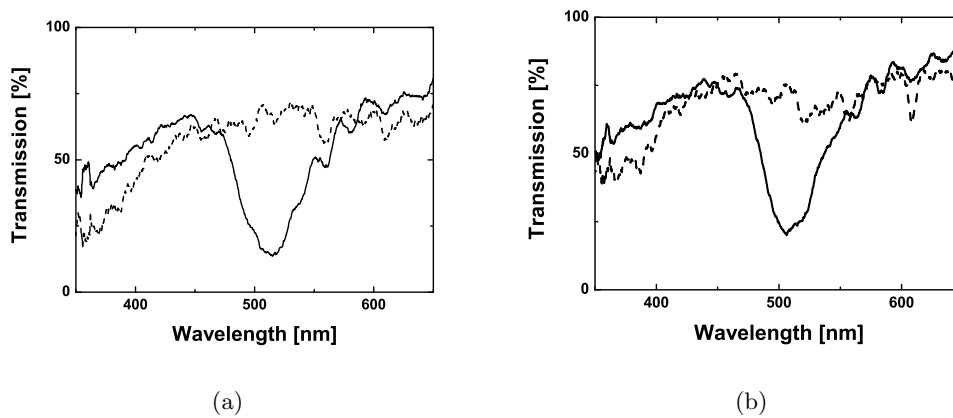


Figure 6.15: Transmission spectroscopy of polymerized cholesteric reaction mixture (cured with linearly polarized light, composition in table 6.4). (a) The polymerized film reflects circularly polarized light of the right handedness (line), and transmits the left handedness (broken line). (b) Transmission of linearly polarized light $+45^\circ$ to the LC alignment direction: line, and -45° : broken line.

the elevated temperature, which is above the clearing temperature of the mixture of K18 and K21 ($T_{ni} = 37^\circ\text{C}$), the unreactive liquid crystals become isotropic and lose their anisotropy. Therefore, at 60°C the reflection band edges are determined by the birefringence of the anisotropic polymer network. Due to the similar refractive indices of the polymer and nematic host, the reflection band shifts only marginally by increased temperature (figure 6.17(a)). Linearly polarized light in any polarization

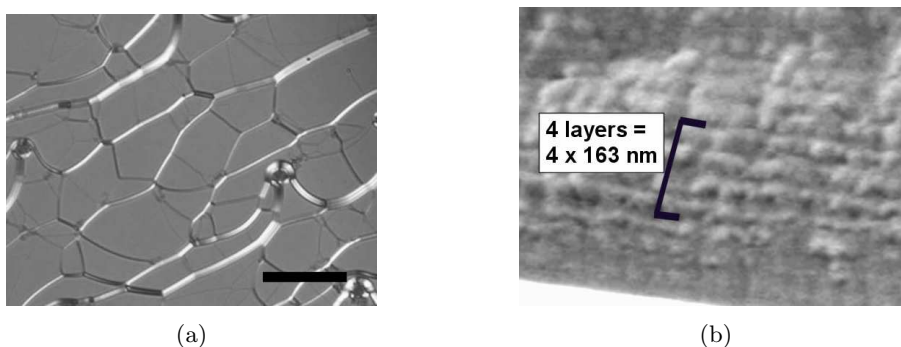
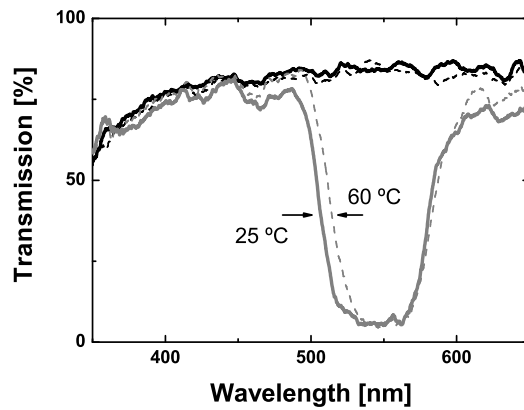
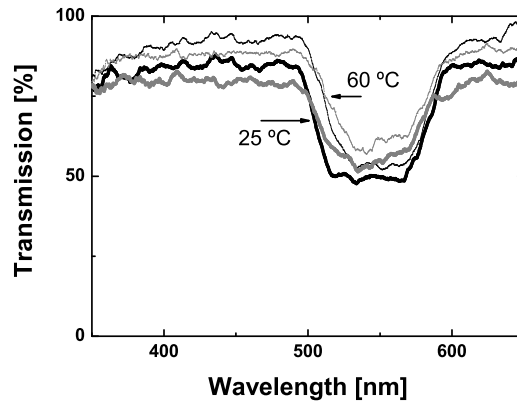


Figure 6.16: (a) Polarization microscopy image of the same polymerized film. Oily streaks witness of a remained cholesteric phase after polymerization (the bar measures $50\ \mu\text{m}$). (b) Cross-section of the same film from which the unreacted liquid crystals been washed away.



(a)



(b)

Figure 6.17: Transmission spectroscopy at 25 °C (lines) and 60 °C (broken lines) of polymerized reference sample made from a cholesteric reaction mixture with the composition in table 6.4: (a) circularly polarized light (left-handed: black lines, and right-handed: gray lines) and (b) linearly polarized light (-45° to the LC alignment direction: black lines, and +45° to the LC alignment direction: gray lines).

direction and temperature was reflected to 50% (figure 6.17(b)), the band shift was identical to that experienced by circularly polarized light. The shifts of the reflection band edges were reversible.

Unlike the reference sample that changed its reflection properties only marginally with increasing temperatures, the linearly polarized polymerized samples exhibits remarkable temperature effects (table 6.5). The first observation is that the intensity of the right-handed reflection band increases. This indicates that the state of polarization of circularly polarized light is less affected at elevated temperatures. The second observation is that the difference in reflection between the two states

Table 6.5: Intensity of the reflection band from the sample polymerized with linearly polarized light.

T [°C]	⊙ right-handed	⊙ left-handed	↑ lin. pol.	↔ lin. pol.
25	78	0	74	8
60	88	0	38	46

of linearly polarized light vanishes at elevated temperatures. Both phenomena can be explained by the disappearance of optical retardation as caused by the isotropic phase of a non-chiral nematic liquid crystal that phase separated into one or more layers.

The optical properties of anisotropic films are very dependent on the alignment of the liquid crystals; therefore it is difficult from these measurements to draw unambiguous conclusions regarding the sample morphology. A larger optical contrast between the polymer and the phase separated liquid crystals would facilitate the interpretation of the spectra; an isotropic polymer is preferable for these optical measurements.

6.4 Conclusions

The reaction mixture for the cholesteric self-stratification must keep a stable, ordered and liquid crystalline phase before polymerization. For the materials investigated here, the nematic hosts E7 and the mixture of equal parts of K18 and K21 that have nematic phases over large temperature regions were more suitable than the single component nematic host K18.

One of the components in E7 (the cyanoterphenyl molecule) absorbs light in UV region; this hinders the selection of wavelengths in the absorption band of the dichroic photoinitiator. Preferably only the photoinitiator absorbs at the curing wavelengths, and generates the periodic absorption profile in depth of the reaction mixture. Else, if the LCs also absorb the light, the intensity decreases in depth of the film and an additional profile over the film thickness appears and materials transport over the whole grating might be induced.

The isotropic right-handed chiral dopant LC756 has a high twisting power (HTP = $44 \mu\text{m}^{-1}$ in E7 and HTP = $28 \mu\text{m}^{-1}$ in RM257 and in the mixture K18 and K21), with small concentration changes of the dopant (3-8 weight%) the cholesteric pitch was modified to reflect over the visible spectra of wavelengths. However, larger concentrations of LC756 (≥ 8 weight%) induced crystallization which also occurred in all mixtures after some days. Even though crystallization is not a desired property, it can to a certain amount be controlled by improving the miscibility by heating the reaction mixture above the clearing temperature, continued by slowly cooling down the mixture to chiral nematic phase just before the polymerization.

The liquid crystalline cross-linker RM257 stabilized the reaction mixtures by increasing the clearing temperatures. Even though polymerization-induced phase

separation of this monomer in cyanobiphenyls is documented¹⁸, no optical phase separation was observed in the reaction mixtures.

The isotropic monomers studied here (PEA, iBMA and BiPhMA) disturbed the cholesteric order in the reaction mixture, observed as phase separation and crystallization. The miscibility in the reaction mixture is critical for the cholesteric self-stratification process, and was improved only when monomers were added that were liquid crystalline in nature.

The liquid crystal monomer LCA increased the clearing temperature of the mixtures and aligned in the cholesteric reaction mixture. Phase separation was only observed when polymerizing at temperatures close to the clearing temperature of the mixture. Besides its mixing properties in the monomeric state, LCA has also an additional favorable property. The molecular structure of LCA, with the cyanobiphenyl group directly attached to the acrylate group, hinders the packing of the molecules after polymerization because of steric reasons. As a result the monomer forms an isotropic polymer when polymerized as a single component. In a blend of anisotropic monomers it destabilizes the liquid crystal phase of the polymer and will decrease the optical anisotropy. Other monomers with similar qualities (liquid crystal monomer forming isotropic polymer due to steric hindrance) are also interesting alternatives to the cholesteric self-stratification process.

The simulations in chapter 5 revealed that large amounts of monomers (> 50 %) in the cholesteric reaction mixture are required to obtain polymerization-induced phase separated layers. Based on the materials studied in this chapter two alternatives are possible: reaction mixtures with large contents of the liquid crystalline monomer LCA, or reaction mixtures with the isotropic monomer PEA (10%) in which the monomer content is increased by the LC cross-linker RM257. Cholesteric reaction mixtures with dichroic photoinitiators were polymerized by linearly polarized light. Due to the large content of reactive anisotropic material, it was not possible to conclude unambiguously whether the cholesteric LC phase was remained in the polymerized film, whether Bragg gratings were created, or a combination of the two. A larger optical contrast between the polymer and the phase separated liquid crystals would facilitate the interpretation of the spectra.

Further recommendations

A good contrast between the layers remains a challenge for the cholesteric self-stratification process. It was shown with simulations that neither the reaction rates nor the diffusion constants influence the composition profile in depth (chapter 2 and 5), instead the temperature and concentration of the reaction mixture are critical parameters for the phase separation process (chapter 5). In chapter 2 simulations revealed that small periodicity in the absorption profile (< 500 nm) favors material transport and generates large concentration differences between the depths with high and low absorbed intensity. The absorption profile depends mainly on materials parameters as the extinction of the photoinitiator, concentration and the absorption contrast. The latter, the absorption contrast (V_{abs}), influences the reaction-diffusion

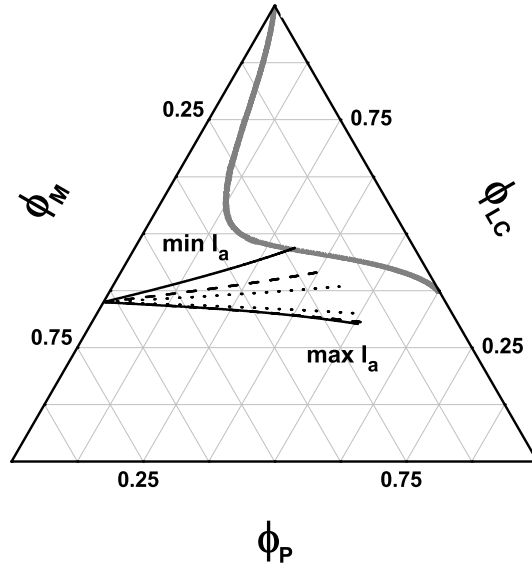


Figure 6.18: Large contrast in absorption ($V_{abs} = 1$, i.e. no absorption at the I_a depths) provides a large difference in concentration between the reaction-diffusion lines (black lines) after 15 s polymerization. Lower contrasts ($V_{abs} = 0.83$ broken lines, $V_{abs} = 0.5$ dotted lines) show less separation of the reaction-diffusion lines.

lines significantly (figure 6.18). This behavior was investigated for a cholesteric reaction mixture with $T_{n^*i(LC)} = T_p - 10$ and $T_{n^*i(M)} = T_p - 30$, initial monomer content = 60%, and UV-light intensity = 10 mWcm^{-2} . After 15 s of polymerization the phase separation line is crossed by the reaction-diffusion lines for the simulation with a perfect contrast, $V_{abs} = 1$ (i.e. polymerization is not allowed at the depths with “low absorbed” intensity, black lines in the figure). Larger contrasts, $V_{abs} = 0.83$ as was determined for the dichroic photoinitiators used in this study, and $V_{abs} = 0.5$, influence the composition differences between the reaction-diffusion lines less. Logically, the line at the lowest I_a is strongest influenced, since the all other parameters were constant.

The absorption contrast is dependent on the order in the cholesteric reaction mixture. A perfect ordered cholesteric reaction mixture would increase the absorption contrast, however in normal practice the order parameter in chiral nematic systems is 0.6-0.7. Moreover, in this chapter it was shown that by introducing several reactive components the order tends to decrease. Another possibility might be the addition of radical scavengers. Radical scavengers react with (photo-induced) radicals and compete with the monomers in the polymerization reaction. Since the radical combination rate with the scavengers is faster than that with the monomers the polymerization becomes inhibited at locations with relatively low levels of free

radicals²². Examples of radical scavengers that inhibit the polymerization and retard it, are hydroquinones²³. Such inhibitors in the cholesteric self-stratification reaction mixture are believed to inhibit the polymerization at the positions with low absorbed light intensity, while at the depths with high intensity the scavengers are consumed faster and polymerization starts. In this way the contrast increases between the layers, as shown in the simulations in figure 6.18. With an improved separation between the reaction-diffusion lines, the layer formation process becomes less dependent on the concentration of the reaction mixture and the temperature. A large absorption contrast is favorable for the experimental verification of the cholesteric self-stratification process.

Finally it is also useful to note that nucleation centers for the phase separation process are believed to influence the grating formation. One alternative to control the shape of the phase separation, and improve the mechanical properties, is by forming *in situ* the reaction mixture by a lithography step before the stratification process²¹. This technique was suggested¹⁴ and applied^{13,21} for the photo-enforced stratification. The presence of nucleation centers could improve the phase separation possibilities for the cholesteric self-stratification process, since the nucleation centers could destabilize the supercooled chiral nematic LC state (which was discussed in section 5.6.2).

6.5 References

1. Wilson, M. R. and Earl, D. J. *J. Mater. Chem.* **11**, 26722677 (2001).
2. Lub, J., van de Witte, P., Doornkamp, C., Vogels, J. P. A., and Wegh, R. T. *Adv. Mater.* **15**, 1420–1425 (2003).
3. Kurihara, S., Yoshioka, T., Zahangir, A. M., Ogata, T., and Nonaka, T. *J. Appl. Polym. Sci.* **92**, 2577–2580 (2004).
4. Lub, J., van de Witte, P., and Broer, D. J. *Progr. Organic Coatings* **45**, 211217 (2002).
5. Hecht, E. *Optics*, chapter 10, 443–. Addison Wesley, San Francisco, 4th edition (2002).
6. Ono, H., Kawamura, T., Frias, N. M., Kitamura, K., Kawatsuki, N., and Norisada, H. *Adv. Mater.* **12**, 143–146 (2000).
7. EM Industries, Hawthorne NY, An Associate of Merck KGaA, Germany. data sheets of liquid crystals.
8. Pogue, R., Natarajan, L., Siwecki, S., Tondiglia, V., Sutherland, R., and Bunning, T. *Polymer* **41**, 733741 (2000).
9. Sutherland, R. L., Tondiglia, V. P., Natarajan, L. V., Bunning, T. J., and Adams, W. W. *Appl. Phys. Lett.* **64**(9), 1074–1076 (1994).
10. Sutherland, R. L., Natarajan, L. V., Tondiglia, V. P., and Bunning, T. J. *Chem. Mater.* **5**, 1533–1538 (1993).

11. Urbas, A., Klosterman, J., Tondiglia, V., Natarajan, L., Sutherland, R., Tsutsumi, O., Ikeda, T., and Bunning, T. *Adv. Mater.* **16**(16), 1453–1456 (2004).
12. Natarajan, L. V., Sutherland, R. L., Tondiglia, V. P., Siwecki, S., Pogue, R., Schmitt, M., Brandelik, D., Epling, B., Berman, G., Wendel, C., Riter, M., Stallings, M., and Bunning, T. J. *Mat. Res. Soc. Symp. Proc.* **559**, 109–116 (1999).
13. Penterman, R., Klink, S. I., de Koning, H., Nisato, G., and Broer, D. J. *Nature* **417**, 55–58 (2002).
14. Vorflusev, V. and Kumar, S. *Science* **283**, 1903–1905 (1999).
15. van Boxtel, M. C. W., Janssen, R. H. C., Broer, D. J., Wilderbeek, H. T. A., and Bastiaansen, C. W. M. *Adv. Mater.* **12**(10), 753–756 (2000).
16. Roussel, F., Buisine, J.-M., Maschke, U., Coqueret, X., and Benmouna, F. *Phys. Rev. E* **62**(2), 2310–2316 (2000).
17. Cao, W., Muñoz, A., Palffy-Muhoray, P., and Taheri, B. *Nature Mater.* **1**, 111–113 (2002).
18. Wilderbeek, H., Koning, H. D., Vorstenbosch, J., Chlon, C., Bastiaansen, K., and Broer, D. J. *Jpn. J. Appl. Phys. Part 1* **41**(4A), 21282138 (2002).
19. Broer, D. J. *Liquid crystals in complex geometries, formed by polymer and porous networks*, chapter 10, 239–254. Taylor and Francis Ltd, London (1996).
20. Hikmet, R. A. M. *Liquid crystals in complex geometries, formed by polymer and porous networks*, chapter 3, 53–82. Taylor and Francis Ltd, London (1996).
21. Penterman, R. *Photo-enforced stratification of liquid crystal/monomer mixtures, Principle, Theory and analysis of a paintable LCD concept*. PhD thesis, Eindhoven University of Technology, Eindhoven, (2005).
22. Moad, G. and Solomon, D. H. *The chemistry of free radical polymerization*. Elsevier Science Ltd., Oxford, (1995).
23. Odian, G. *Principles of polymerization*. John Wiley and Sons, Inc., Singapore, 4th edition, (2004).

Appendix A

SIMS spectra identification:

A study of multivariate statistical analysis to obtain liquid crystal concentrations in stratified polymer dispersed liquid crystals.

Three methods to predict the liquid crystal concentration of the layers from the SIMS depth profile in chapter 4, figure 4.2 were studied: the relative peak intensity method (RPI) which is a regression method, and the two spectrum identification techniques principle component analysis (PCA) and discriminant function analysis (DFA) combined with linear regression analysis.

SIMS depth profiles of six samples with homogeneous LC concentrations were used for calibration. Three spectra of the calibration samples are shown in chapter 4, figure 4.3. Note that the F^- signal decreases with increasing LC content, while C_2^- and CN^- behave oppositely. With this information one could try to extract a calibration curve from relative peak intensities (RPI) of two characteristic ion intensities. We investigated the intensity ratio between the F^- ion that uniquely represents the polymer and CN^- . A calibration curve was calculated by applying linear regression on the intensity ratios I_{F^-}/I_{CN^-} from the SIMS depth profiles at equilibrium of the calibration samples (figure A.1). The error bars represent the standard deviations of the measured ion intensities for each equilibrated intervals of the SIMS depth profiles. From the regression analysis we derived an equation for the concentration of LC from the I_{F^-}/I_{CN^-} ratio:

$$LC \text{ concentration} \pm 4.0 = -29.8 \cdot \frac{I_{F^-}}{I_{CN^-}} + 68.5 \quad [weight\%] \quad (A.1)$$

The applicability of the calibration curve was tested by a calibration sample with a concentration of 39.7 weight% LC that was deliberately left out of the linear regression analysis. The concentration of the 39.7 weight% LC sample was determined to be 42.2 ± 5.1 weight% LC, with error bars representing the standard deviations of the measured ion intensities for each equilibrated intervals of the SIMS depth pro-

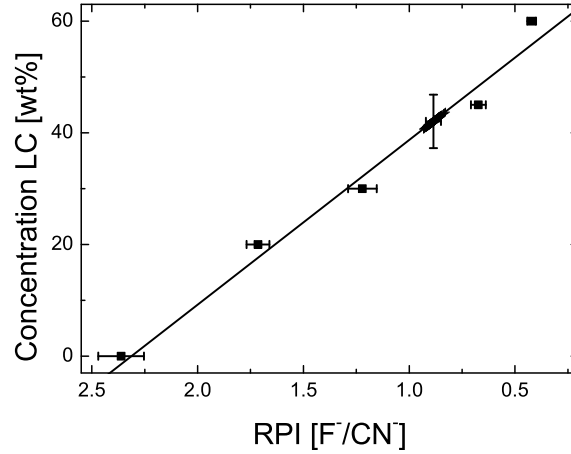


Figure A.1: Calibration curve made from regression analysis on the relative peak intensities of the intensity ratio F^-/CN^- of five calibration concentrations (■). The error bars represent $\pm 34\%$ deviation from the mean of the ratios from all SIMS depth units. The applicability of the calibration curve was tested with the F^-/CN^- ratio of one calibration concentration (39.7% LC, +) that was on purpose not used for the calculations of the calibration curve. Its concentration was determined to 42.2 ± 5.1 weight%.

files. Continuously, the concentrations of the layers in the multilayer sample were calculated from the I_{F^-}/I_{CN^-} ratio from narrow depth intervals (40 s or 9.6 nm) at the peaks and valleys of the oscillating part of the SIMS depth profile in figure 1b. The concentrations of the ratios were calculated to 34.5 ± 5.7 weight% LC for the layers with high content of LC (Max) and to 31.9 ± 5.3 weight% LC for the polymer-rich layers (Min). The error bars represent the standard deviations of the measured ion intensities for each equilibrated intervals of the SIMS depth profiles.

Principally, we expected the concentrations of the layers to fluctuate round 30 weight% LC, which was the concentration from which the multilayer sample was prepared. Due to the relatively large errors in the obtained concentrations, RPI is apparently not suitable to accurately determine the concentration fluctuations present in our layered LC-polymer samples. Obviously the concentration differences cannot be related to the correlation between only two ion fragments. Investigating RPI ratio's consisting of more mass channels, e.g. the sum of the F^- and O^- intensities divided by the sum of the CN^- and C_2^- intensities, diminished the fluctuations for the calculated concentrations of the layers to ± 4.2 weight% LC. Also the concentrations of the layers are more efficiently separated: 37.1 weight%LC for the LC-rich layers and 33.9 weight% LC for the layers mainly consisting of polymers. However, the calculated concentrations do not fluctuate round 30 weight% LC, as required. Therefore multivariate statistical analyses are required to investigate the correlations between all mass channels for each concentration.

The multivariate statistical analysis PCA was first studied to investigate whether

it is a suitable analysis technique to extract the information of sample compositions from the SIMS depth profiles. This was analyzed by applying PCA on the equilibrated parts of the SIMS depth profiles of the calibration samples. In figure A.2(a) the scores of principle component 1 (PC1) and 2 (PC2) are plotted, in which groups of dots representing the chosen depth units of each concentration are seen. PC1 and PC2 captured together 93% of the variance. PCA successfully separated the six concentrations by the PC1 scores, while PC2 contained information of other properties than concentration which was seen in the spread of the data points without correlation to the increasing concentrations of the samples. This interpretation was supported by the loadings (the normalized eigenvectors) obtained from the PCA (figure A.2(b) and A.2(c)). The loadings of PC1 clearly have an anti-correlation between the ions assumed to represent the polymer (F^- and O^-), and those imagined to correspond to the LC (CN^- and C_2^-). PC1 contains 85% of the variance. Additionally it has low levels of significance of both the chi-squared (on the 0.01 level) and F (on the 0.001 level) tests, which means that PC1 is truly different from the other PCs (chi-squared test) and that it represents unique variations between the concentrations (F-test). Thus PC1 can alone be selected to discriminate between the concentrations.

Figure A.3 shows the relation between the PC1 scores and the concentrations of LC of the calibration samples. We applied linear regression analysis to obtain a calibration curve of the calibration samples from the PC1 scores. The error bars in figure A.3 represent 68% of the PC1 scores for each concentration. The applicability of the calibration curve to attain the concentration of an unknown sample was tested by with the sample containing 39.7 weight% LC, which was deliberately left out the calculations of the regression analysis. The test sample's concentration obtained from the calibration curve,

$$LC \text{ concentration} \pm 4.4 = 5.7 \cdot PC1 + 29.6 \quad [weight\%] \quad (A.2)$$

was 39.1 ± 6.1 weight% LC. The mean of the test sample's concentration determined by PCA is closer to its real concentration, compared with the RPI analysis (of the ratio I_{F^-}/I_{CN^-}).

Next, we used PCA to determine the concentrations of the multilayer sample. First intervals from the depth profile of the multilayer sample were chosen for the analysis. We decided to determine the maximum (LC-rich) and minimum (polymer-rich) LC concentrations of the layers. SIMS data were selected from narrow intervals (40 s or 9.6 nm) at the peaks and valleys of the oscillating part of the spectra in figure 4.2(b). These 22 SIMS spectra in the depth interval were inserted into the PCA together with the depth intervals at equilibrium from the calibration SIMS spectra. Note that the layered sample has to be treated in the statistical analysis together with the calibration samples. This is required since the statistical analysis enlightens differences between the samples.

The scores of PC1 and PC2 in figure A.4(a) show a separation between the calibration samples, and also between the LC-rich and polymer-rich layers of the multilayer sample. As for the calibration samples in figure A.2(a), PC1 successfully separates the concentrations, while PC2 apparently represents other unknown

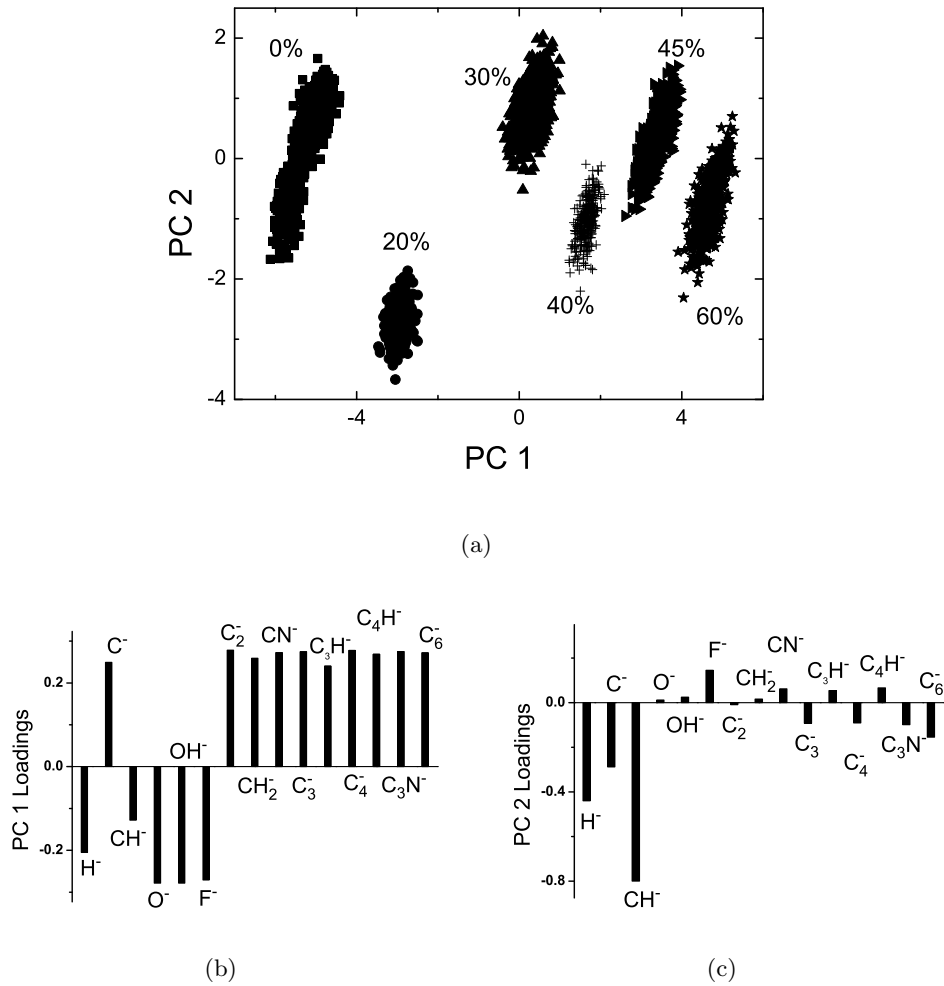


Figure A.2: Score plot of PC1 and PC2 from principle component analysis of the six calibration concentrations. a) The plot of the two first PCs (together 93% of the variance) shows separation of six grouped clouds of dots representing depth units at equilibrium sputter processes from six calibration concentrations: 0 weight% (■), 19.3 weight% (●), 29.9 weight% (▲), 39.7 weight% (+), 44.9 weight% (▶) and 60.7 weight% LC (★). b) The loadings of PC1 (85% of the variance) show anti correlation between the mass channels representing the polymer (F^- and O^-) and the ions assumed to represent the LC (CN^- and C_2^-). c) The loadings of PC2 (8% of the variance) express other properties assumed not to correlate to the concentration of LC.

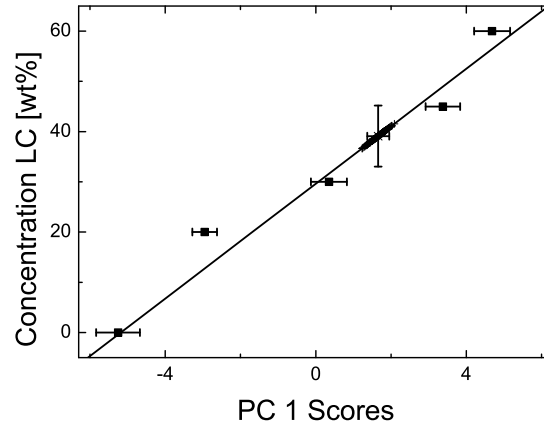


Figure A.3: Calibration curve of the calibration sample concentrations determined by regression analysis of the PC1 scores (■) and the concentrations. The applicability of the calibration curve was tested with the sigma distribution of the PC1 scores of one concentration (39.7% LC, +) that was deliberately left out of the calculations of the calibration curve. Its concentration was determined to 39.2 ± 6.2 weight%. The error bars represent the standard deviation of the PC1 scores for each concentration.

properties of the samples. The loadings of PC1 (figure A.4(b) and A.4(c)) confirm anti-correlation between the ions assumed to represent the polymer (F^- and O^-), and the ions assumed to represent the LC (CN^- and C_2^-), while the non-specific ions CH^- , C^- and H^- show the largest loadings for PC2. The choice of PC1 to discriminate between the concentrations for the calibration curve was justified by the high variance (85%) of PC1 and its low levels of significance for the chi-square (on the 0.01 level) and F (on the 0.001 level) tests. The low levels of significance implies that PC1 is uniquely different compared to the other PCs (chi-squared test) and that it displays unique differences between the concentrations (F-test).

The concentrations of LC for the calibration samples are plotted versus the PC1 scores obtained from the last PCA analysis. A calibration curve (figure A.5) was obtained by applying linear regression analysis on the PC1 scores of the calibration samples (figure A.4(a)), the error bars represent the standard deviations of the PC1 scores of the measured ion intensities of the equilibrated intervals from the SIMS depth profiles of the calibration samples. Similarly to the former analysis, the applicability of the calibration curve to obtain the concentration of an unknown sample was tested with the sample containing 39.7 weight% LC, which was deliberately left out the calculations of the regression curve. The equation of the calibration curve was:

$$LC \text{ concentration} \pm 4.5 = 5.7 \cdot PC1 + 30 \quad [weight\%] \quad (\text{A.3})$$

The test sample's concentration was determined by the calibration curve to 39.2

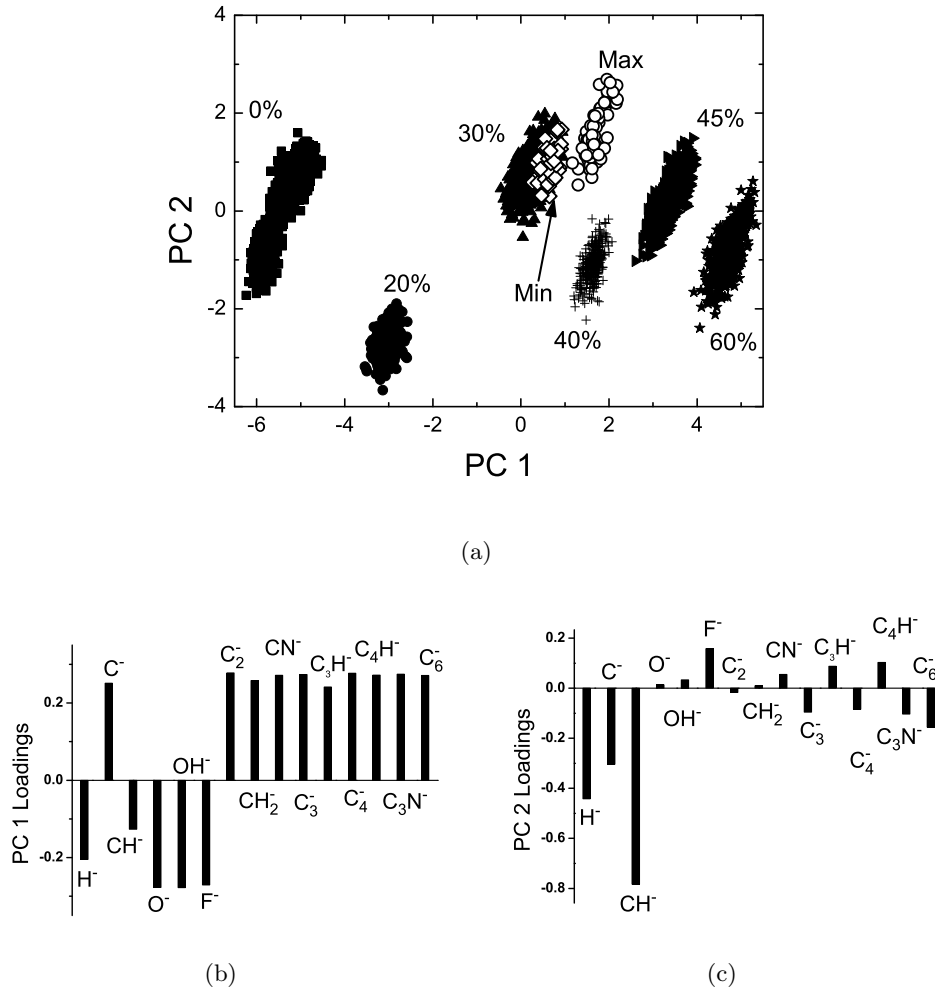


Figure A.4: a) Score plot of PC1 and PC2 (together 93% of the variance) from the principle component analysis of six calibration concentrations (0 weight% (■), 19.3 weight% (●), 29.9 weight% (▲), 39.7 weight% (+), 44.9 weight% (►) and 60.7 weight% LC (★) LC), and six depth intervals from the multilayer sample. The scores from the depth intervals assumed to have highest LC content (Max, ○) are separated in PC1 on the concentration from the depth intervals assumed to have lower LC content (Min, ◇). b) The loadings of PC1 (85% of the variance) and PC2 (8% of the variance) show different correlations. PC1 is assumed to be related to the LC concentration differences since an anti correlation between the ions representing the polymer (F^- and O^-) and the ions assumed to represent the LC (CN^- and C_2^-) is present. c) PC2 expresses other properties assumed not to contribute to the discrimination of LC concentrations in the samples.

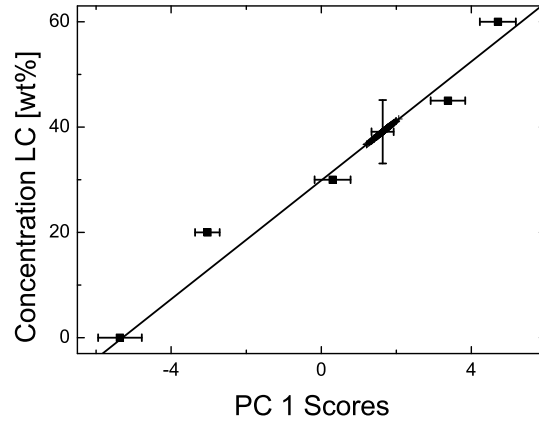


Figure A.5: Calibration curve made from regression analysis of the PC1 scores (from figure A.4(a)) of five calibration concentrations (■). The applicability of the calibration curve was tested with the sigma distribution of the PC1 scores of the sixth calibration concentration (39.7% LC, +) that was on purpose not used for the calculations of the calibration curve. The concentration was determined to 39.2 ± 6.1 weight%. This calibration curve was used to calculate the concentrations of the layers in the multilayer samples. The error bars represent the standard deviation of the PC1 scores of the measured ion intensities of the equilibrated intervals from the SIMS depth profiles of the calibration samples.

± 6.2 weight% LC. This value is similar to the one obtained when only the calibration samples (without the layered sample) was treated by the statistical analysis (figure A.3). We used the calibration curve (equation A.3) to obtain the concentrations of the layers in the multilayer sample. The concentration of the LC-rich layers was calculated to 39.6 ± 6.5 weight% LC, and the polymer-rich layers to 33.6 ± 3.9 weight% LC.

Similar to the RPI, the layer concentrations calculated from PCA were higher than 30 weight% LC, this was not expected since that is a higher LC concentration than the one from which the layered sample was prepared. Apparently neither RPI nor PCA are suitable to extract information from the SIMS spectra in order to determine the concentration fluctuations present in our layered LC-polymer samples. A classification analysis, that maximizes the differences between the concentrations, is assumed to more accurately identify sample compositions. Subsequently discriminant function analysis (DFA) was applied to identify the LC concentrations in the dynamic SIMS spectra.

At first we investigated how DFA interprets the calibration samples by applying the analysis on the same SIMS data of the calibration samples as for the PCA. The main difference to the latter analysis is that each calibration concentration in DFA was grouped already when inserted in the analysis model, and the grouping is used by DFA to maximize the differences between the concentrations. The plot of the

two DFA functions with the highest variance (F1 and F2) is seen in figure A.6(a). The clouds of points, in which each point corresponds to a SIMS spectra at a certain depth, are separated by the concentrations. The loadings of the functions (figure A.6(b) and A.6(c)) show that F1 expresses anti-correlation of the ions assumed to represent the polymer (F^- and O^-) and the ions believed to characterize the LC (CN^- and C_2^-). The loadings of F2 showed other anti-correlations; apparently F2 contains other information apart from discriminating between concentrations. Therefore we used F1 to distinguish between the concentrations; this is supported by the high variance (93%) of F1 and its true ability to express differences between F1 and the other functions (chi-square test, with significance on the 0.01 level), as well as differences between the calibration samples within F1 (F-test, with significance on the 0.001 level).

The LC concentrations of the calibration samples were plotted against the scores of F1 (figure A.7), the error bars that represent the standard deviations of the F1 scores of the measured ion intensities for the equilibrated intervals from the SIMS depth profiles. As for the PCA, linear regression analysis was applied on the F1 scores to obtain a calibration curve. Again, the applicability of the calibration curve to determine concentrations of unknown samples was tested with the sample containing 39.7 weight% LC, which was on purpose left out the calculations of the regression curve. The equation of the calibration curve is:

$$LC \text{ concentration} \pm 1.9 = -36.3 \cdot F1 + 29.8 \quad [weight\%] \quad (A.4)$$

The test sample's concentration was calculated from the calibration curve, by inserting the F1 scores, to 41.2 ± 2.7 weight% LC. Compared to the PCA and RPI results, the error for the test sample was considerably lowered, implying that DFA better resolves concentration differences (which was expected).

Subsequently, we performed discriminant function analysis on all calibration samples and the SIMS data from the multilayer sample. The same intervals (40 s or 9.6 nm at each peak and valley of the oscillations in figure 4.2) of the SIMS spectra of the multilayer sample as used for the PCA were also chosen for this analysis, and each interval was linked to a separate group in the analysis. As a result we ended up with 12 groups: six groups from the multilayer sample together with 6 groups consisting of the six concentrations of the calibration samples. The DFA plot shows a successful discrimination between the concentrations of the calibration samples and the concentrations of the layers (figure A.8(a)). The plot of F1 versus F2 shows that the three groups from the polymer-rich layers are centered on top of each other, as are the three groups from the LC-rich layers. Even though DFA maximizes differences between the groups; it also recognizes similarities of groups containing equal concentrations which is seen in figure A.8(a) for the groups of the polymer-rich layers as well as for the groups of the LC-rich layers.

The ability of the first DFA function (F1) to separate between the concentrations of the calibration samples was described by the loadings of F1 (figure A.8(b) and A.8(c)) that showed anti-correlations of ions assumed to represent the polymer (F^- and O^-) and the ions believed to characterize the LC (CN^- and C_2^-). F2 on the other hand does not show such anti-correlations. Apparently it contains other,

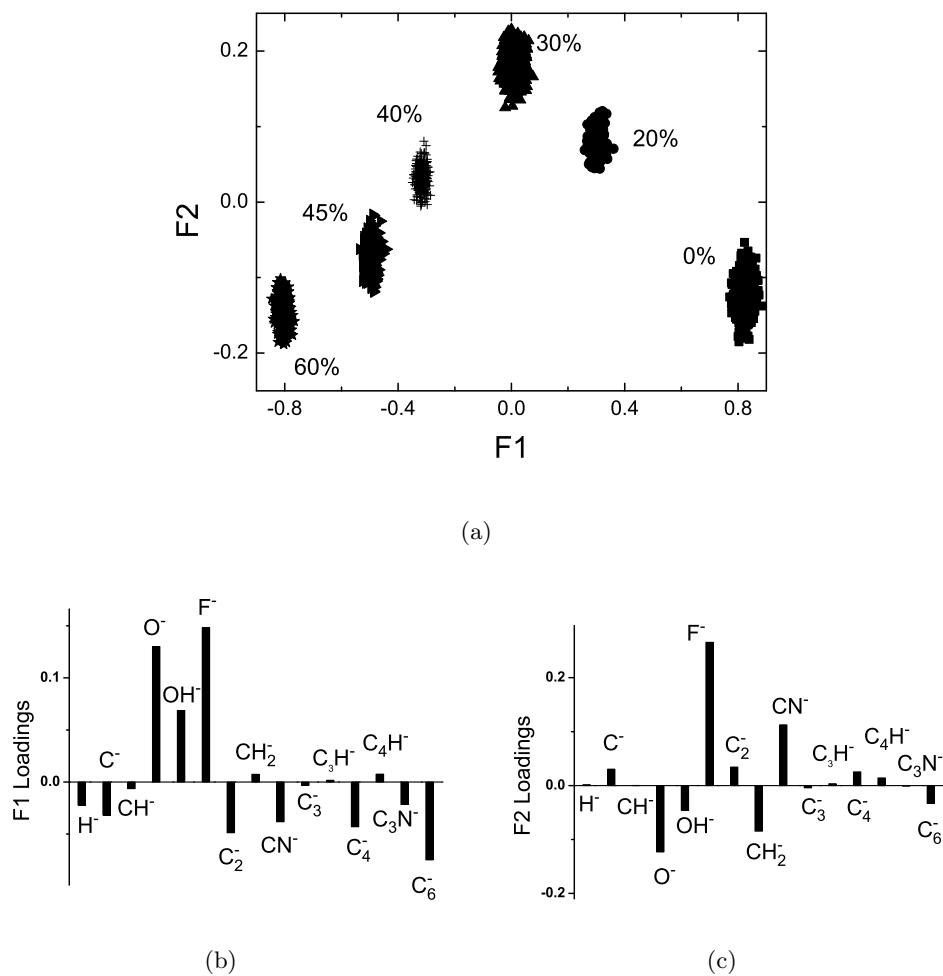


Figure A.6: a) Score plot of F1 and F2 from discriminant function analysis of the six calibration concentrations (0 weight% (■), 19.3 weight% (●), 29.9 weight% (▲), 39.7 weight% (+), 44.9 weight% (►) and 60.7 weight% LC (★) LC). The plot of the two first functions (together 99% of the variance) shows better centering, than PCA, of the grouped dots representing the concentrations. b) F1 (93% of the variance) has anti correlated loads concerning the mass channels representing the polymer (F^- and O^-) and the ions assumed to represent the LC (CN^- and C_2^-). c) The loadings of F2 (5% of the variance) express other properties assumed not to correlate to the concentration of LC.

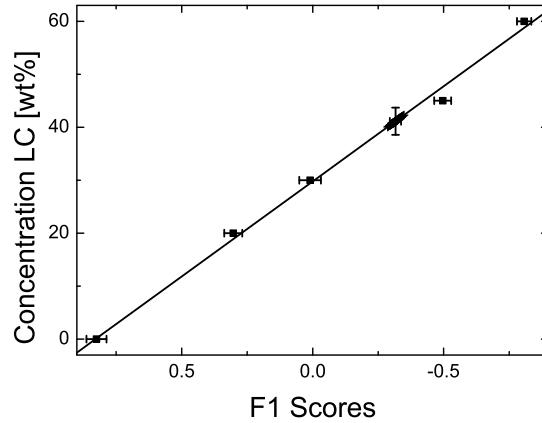


Figure A.7: Calibration curve from regression analysis of five calibration concentrations, calculated from the F1 scores (■). The applicability of the calibration curve was tested with the F1 scores of one concentration (39.7% LC, +), on purpose left out of the calculations of the calibration curve. The concentration was determined to 41.3 ± 2.7 weight% LC. The error bars represent the standard deviation of the F1 scores for each concentration.

non concentration specific, correlations. F1 captured 93% of variance and has low levels of significance for the chi-square test (0.01 level) meaning that F1 is uniquely different from the other DFA functions. The significance for the F-test is also low (0.001 level), indicating that it explains true differences between the concentrations.

A calibration curve was calculated by linear regression analysis on the F1 scores of the calibration concentrations (figure A.9), with error bars representing the standard deviations of the F1 scores of the measured ion intensities for the equilibrated intervals from the SIMS depth profiles. The equation for the calibration curve is:

$$LC \text{ concentration} \pm 1.9 = -5.1 \cdot F1 + 29.8 \quad [weight\%] \quad (\text{A.5})$$

The equation for this calibration curve differ from that based on the DFA analysis of the calibration samples only (equation A.4), but the appearance of the score plots are similar (figures A.6(a) and A.8(a)). This was also seen for the analysis made by PCA (equations A.2 and A.3, and figures A.2(a) and A.4(a)), even though the values of the PC1 and PC2 scores did not vary as much as the F1 and F2 scores did, when adding the layered samples depth intervals into the MVA. This illustrates the necessity to treat all the samples simultaneously by the MVA in order to retrieve information of the differences between the samples.

The feasibility of DFA to determine the concentrations of an a priori unknown sample concentration was tested by the 39.7 weight% LC calibration sample which was on purpose left out of the linear regression analysis. Using the test sample's F1 scores, its concentration was determined to 41.3 ± 2.7 weight% LC, equal to the

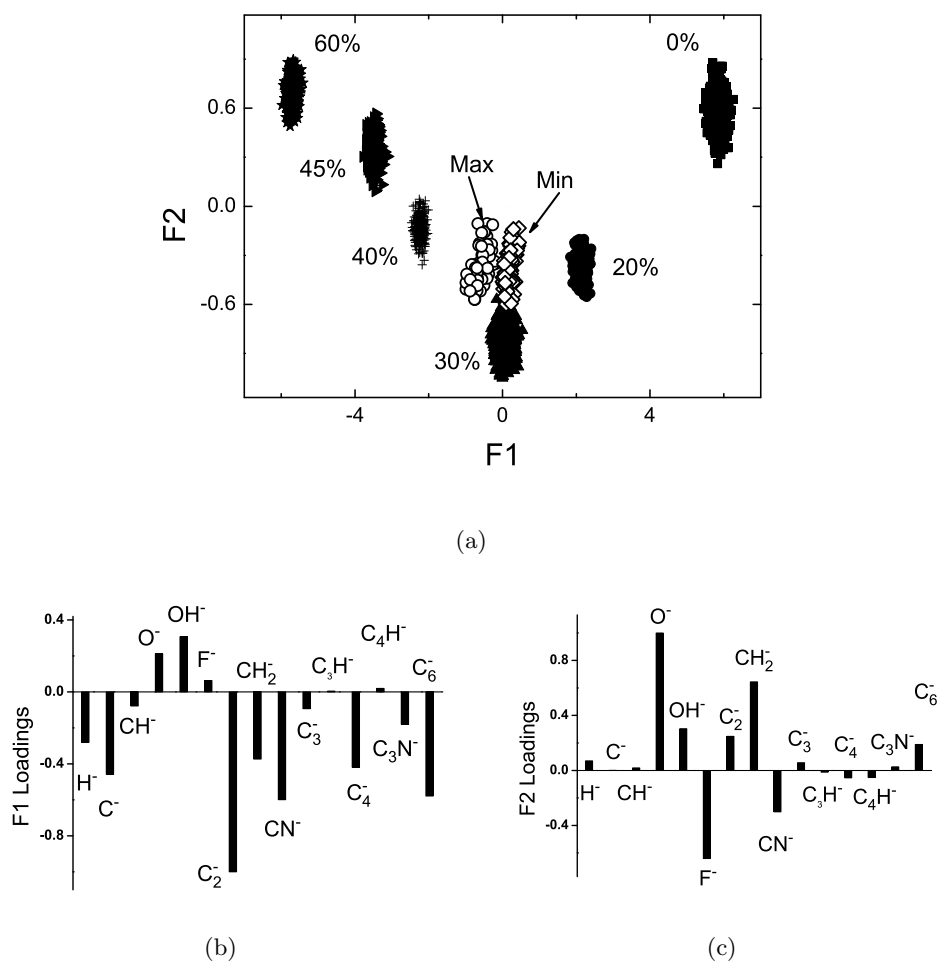


Figure A.8: a) Score plot of F1 and F2 (together 98% of the variance) from the discriminant function analysis of the six calibration concentrations (0 weight% (■), 19.3 weight% (●), 29.9 weight% (▲), 39.7 weight% (+), 44.9 weight% (►) and 60.7 weight% LC (★) LC), and the depth intervals from the multilayer sample. The DFA scores from the depth intervals assumed to have highest LC content (Max, ○) are separated in F1 on the concentration from the depth intervals assumed to have lower LC content (Min, ◇). b) The loadings of F1 (93% of the variance) and F2 (5% of the variance) show different correlations. F1 is assumed to be related to the LC concentration differences since an anti correlation between the ions representing the polymer (F^- and O^-) and the ions assumed to represent the LC (CN^- and C_2^-) is present. c) F2 expresses other properties assumed not to correlate to the concentration of LC. Hence F1 is assumed to express the concentration differences and therefore chosen to determine the LC concentrations in the layered sample.

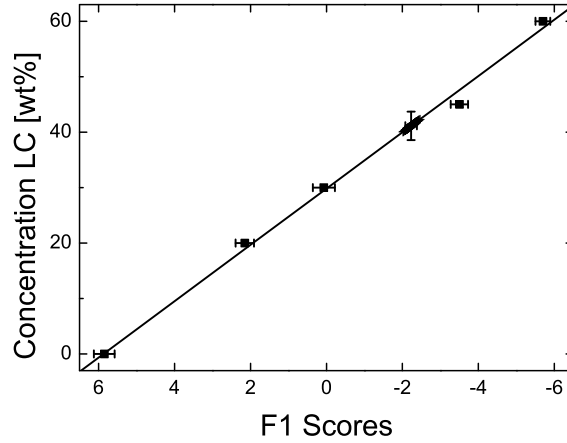


Figure A.9: Calibration curve made from regression analysis on the F1 scores of the five calibration concentrations (■). The applicability of the calibration curve was tested with the F1 scores of the sixth calibration concentration (39.7% LC, +) that was deliberately left out of the calculations of the calibration curve. The concentration was determined to 41.3 ± 2.7 weight%. The calibration curve was used to calculate the concentrations of the layers in the multilayer samples. The error bars represent the standard deviation for the measured ion intensities of the equilibrated intervals from the SIMS depth profiles of the calibration samples.

former DFA analysis. From the regression analysis (equation A.5) and the F1 scores of the layers, we calculated the concentration of the LC-rich layers to 32.9 ± 3.4 weight% LC and 28.8 ± 2.7 weight% LC for the polymer-rich layers. The error bars represent the standard deviations of the F1 scores of all measured ion intensities in the depth intervals (Max/Min) from the layered sample. These concentrations are centered round the concentration of the reaction mixture (29.9 weight% LC) from which the layered samples were prepared, supposing DFA correctly depicts the correlation between all mass channels.

To conclude, careful interpretation of the SIMS depth profiles are important in order to extract the useful information of the sample composition to construct calibration curves. Of the three studied methods only DFA could efficiently identify the small concentration differences in the depth profile of the layered PDLC grating, resulting in reliable LC concentrations.

Technology Assessment

In our present society there is a market for wider, lighter and thinner electro-optical switches to be used as e.g. cost-effective large privacy windows (in homes and offices), as wall coverage (ambient intelligence), or for large area wall-sized displays and television sets. Effective and reasonably fast responding switches can be made by using liquid crystals, e.g. by switching the state of polarization of polarized light as is done in the present flat panel liquid crystal displays (LCDs). For most of the applications mentioned it is beneficial to find operational solutions using unpolarized light in order to enhance the brightness, weight and energy efficiency and to find production methodologies to make the switches larger and cheaper. For instance current LCDs are fabricated in batch wise processes using cell-technology. Rigid glass substrates in rectangular form are stacked as cells which are filled by the anisotropic and switchable liquid crystals (LCs). The cell-technology is a multistep and complex manufacturing method leaving little space to tailor the dimensions of the displays. Recently, a new approach to produce flexible single-substrate devices was introduced: the paintable LCD technology¹. Using the concept of photopolymerization-induced phase separation, a matrix of LC cells are created by exposing a mixture containing monomers and liquid crystals to ultra violet (UV) light. Standard coating processes are suitable to manufacture paintable LCDs which potentially enable continuous production lines.

The next generation optical switches will include additional functionalities. For many applications it has advantages to switch light by reflection rather than by absorption, e.g. to increase the energy efficiency and to avoid heating. The wavelength selective reflection is based on the principles of Bragg reflection. Periodic layers of polymer and liquid crystals with different refractive indices generate the wavelength selective reflection. By realigning the LCs with e.g. an electrical field and matching the ordinary refractive index of the aligned LC molecules to that of the polymer, the grating becomes transparent. By tuning the layer periodicity and refractive indices so that the device reflects light to a narrow band of red, green or blue, the device is interesting for color display applications. Such wavelength specific switchable grating can replace not only the LC cell and the color filters in a display, but also the polarizers, resulting in an increased energy efficiency of the device. Another application of switchable wavelength selective films is temperature regulators, i.e. multilayer films reflecting only infrared (IR) wavelengths. Switching the anisotropic LCs, the temperature regulator transmits the heat waves. Furthermore, incorporating a gradient in layer periodicity in depth of the film a large band

optical switch is obtained controlling light over a wide wavelength range. When the range of wavelengths that are switched corresponds to the visible light, a switchable sunscreen is obtained. Combining such wavelength specific switches with a large area production technique would allow these narrow and broad band switches to be applied on large surfaces for private use (ambient intelligence and wall-sized displays), temperature regulating windows and sunscreens for especially agricultural and automotive applications where temperature and sun light regulation are issues to solve.

In literature electro-optical switches are proposed that fulfill most of the optical requirements such as, polarization non-selective narrow reflection bands that switch within milliseconds by using <100 V electrical fields^{2,3}. They are made by holographic means using interference pattern of two interfering laser beams to initiate a multilayer phase separation of polymer and liquid crystals^{4,5}. The phase separated liquid crystals form droplets at periodic depths in the multilayered polymer dispersed liquid crystal (PDLC) film. Holography is however difficult to upscale to large sizes and large production quantities. The cholesteric self-stratification process, a novel method presented in this thesis⁶, is approaching the goals of large, light and flat device, and simultaneously providing an easily varied wavelength specific reflection and device shape. The advantage of the cholesteric self-stratification process is the self-organization of cholesteric liquid crystals which offers unlimited device size and easily manipulated layer periodicity, stretching from reflecting light in the deep UV to in the far IR. Furthermore the processing is simple, only a normal UV-light source combined with a polarizer are required. With the cholesteric self-stratification method difficulties with localized polymerization shrinkage blurring the refractive index contrast (which is often noticed for holographic reflection gratings^{7,8}) are surmounted by the cholesteric ordering. During the polymerization-induced shrinkage the absorbed intensity profile remains with the relative position of the aligned photoinitiators although the absolute periodicity might shift. The cholesteric order act as a spring that when being compressed the positions that initially have the highest absorption intensity remain the highest intensity and only change their periodicity. The positions with low absorbed intensity will not be subjected to higher absorbed intensity. However, the reaction method for the cholesteric self-stratification is considerably complicated. In spite of the understanding of the phase separation mechanism as studied in this thesis, still experimental parameters are difficult to control. In particular the construction of a functional device based on switchable selective reflection by periodic layers of polymers and LCs remains to be proven. Solving the final intricacy of the cholesteric self-stratification process offers versatile multilayered optical switches.

Furthermore, the phase separation mechanism combined with the liquid crystalline self-organization control not only the layer periodicity but also the porosity of the polymer film. By extracting the liquid crystals from the polymer film, a whole new area of applications is approached: membranes. Creating membranes with controlled pore sizes combined with optical effects as wavelength specific reflection would not only allow separation but simultaneously also detection. The latter since the responsive reflection is sensitive to the sort of fluid that passes through

the membrane or more specifically the amount of swelling (e.g. increased layer periodicity) of the Bragg grating-membrane caused by the fluid. Since the cholesteric self-stratification process provides unlimited sample sizes, not only large but also small devices can be produced. In that case the light-induced phase separation process is easy to combine with lithographic techniques such that both top-down and bottom-up structuring becomes possible. Top-down in this case stands for the formation of structures in the micrometer range by techniques such as lithography or printing followed by the light-induced phase separation. Bottom-up stands for the formation of sub-micrometer structures by means of self-organization of the system, in our case the chiral order in the liquid crystals. Top-down/bottom-up approaches make easy device integration possible. Therefore can membranes that are prepared by the cholesteric self-stratification process find applications in micro- and nanoscopic reactors, labs-on-a-chip and biosensors.

References

1. Penterman, R. *Photo-enforced stratification of liquid crystal/monomer mixtures, Principle, Theory and analysis of a paintable LCD concept*. PhD thesis, Eindhoven University of Technology, Eindhoven, (2005).
2. Sutherland, R. L., Tondiglia, V. P., Natarajan, L. V., Bunning, T. J., and Adams, W. W. *Appl. Phys. Lett.* **64**(9), 1074–1076 (1994).
3. Bunning, T. J., Natarajan, L. V., Tondiglia, V. P., and Sutherland, R. L. *Annu. Rev. Mater. Sci.* **30**, 83–115 (2000).
4. Sutherland, R. L., Natarajan, L. V., Tondiglia, V. P., and Bunning, T. J. *Chem. Mater.* **5**, 1533–1538 (1993).
5. Qi, J. and Crawford, G. P. *Displays* **25**, 177–186 (2004).
6. Kjellander, B. K. C., Broer, D. J., de Jong, A. M., and van IJzendoorn, L. *Patent PCT Int. Appl.* **WO 2006059895 A1**, 21 pp. 20060608 (2006).
7. Sutherland, R. L., Tondiglia, V. P., Natarajan, L. V., and Bunning, T. J. *J. Appl. Phys.* **769**(10), 1420–1422 (2001).
8. Natarajan, L. V., Shepherd, C. K., Brandelik, D. M., Sutherland, R. L., Chandra, S., Tondiglia, V. P., Tomlin, D., and Bunning, T. J. *Chem. Mater.* **15**, 2477–2484 (2003).

Acknowledgements

I had the advantage of being member in several groups at the applied physics and the chemistry departments. This stimulated me to look at my research from different perspectives. I have plenty of people to thank for these wonderful and learning years in Eindhoven: without you this book would never have been finalized. Thanks!

I would like to acknowledge some persons more in detail. First I want to thank my first supervisor Dick; your exciting ideas initiated my curiosity of and passion for cholesteric liquid crystals. Thanks for the stimulating discussions, your confidence in me and your never lasting patience that guided me in the project, I learnt enormously from you. Next, Leo my co-supervisor; your logical and critical thinking was extremely useful for structuring and presenting research. Thanks for all the long discussions at the many difficult times, you always had time to help solving yet another tricky problem and that always with the same enthusiasm. Hans, my second supervisor, thanks for straightening out the difficult calibration curves from the SIMS and statistical analysis. Arthur, my “almost co-supervisor”. Thanks for the help and discussions with the SIMS and IR spectroscopy. I’ll miss the excursions to the van der Waals pub. Christian, thanks for all lab and programming tricks you showed me the first year. Thanks Wouter van G. for teaching me the (delicate) handling of the quadropole SIMS, and Tiny for your always helpful support with the same machine.

I have had the opportunity to guide three students in my PhD project. Jurrian: the three months SIMS pre-work you studied finally (some years later) led to some nice quantification results. Veronique: your “stage” project was pretty frustrating since nothing worked as expected, however the results were important for my further work. Good luck with your PhD studies! An: without the results from your “stage” and “afstudeer” projects this book would look quite different. Thanks for all (often late evening) discussions over the phase separation mechanisms, polymerization kinetics and matlab programming (just to mention some). But also thanks for the laughs during the squash, tennis and biking sessions. All my best for your PhD period!

I wish to thank several persons at Philips Research in Eindhoven for the good scientific collaborations. Thanks Roel, Steve and Joris for the phase separation discussions and the help with the DSC experiments. Corrie, thanks for your help with the many cryo-SIMS measurements that finally turned out to give very nice results. Thanks Toon and Roy for the ellipsometry measurements. Titie, your cholesteric tricks were very useful. Hugo and Nina, thanks for your input the first

years of my PhD project.

Chris, I'm grateful for all your help, not only the support with my thesis book (cover and images), but also for the assistance with the laser holography work, the many discussions, for the daily coffebreak(s) and for sure for your patience and relaxed attitude. Blanca, my travel- and conference-hotelroom-mate; a conference without you will never be the same. Thanks for letting me use your research results (especially those with the dichroic photoinitiators) in my thesis.

I surly enjoyed the collaboration with the photonic crystal group at the applied physics department filling photonic crystals with polymers and LCs. Thanks Rob, Robbie, Juri, Carl-Fredrik, Harm and Huub for the fun work which also led to several publications.

All my thanks to the PICT group that adopted me and gave me full freedom in the UV-labs: Thanks! Cees B., Pit, Carmen (my optical course mate), Joost, Ko, Mike D., Casper, An, Mike E. (thanks for the MatLab code of the "Berreman's simulations" and for the start-up discussions), Carlos (always with a smile), Ken and Anastasia (finally someone to discuss REAL hockey with), Soney, David, Greg, Matt, Jim, Hans, Anja, Thijs, Robbert, Nico. And thanks all guys from SKT: Jules K., Jules H., Irina, Roy, Mark, Maya, Marjolein, Luigi, Wouter G., Pauline, Anne, Cees W., Martijn, Zhou Ting, Esther, Ann, Chris H.

During the last year I could join Arthur and Leo to a new group: Molecular biosensors for medical diagnostics; thanks all of you (Menno, Xander, Francis, Petra, Loes, Betty, Machteld, Mirjam, Kim, Jaap, Lindy and Carolien) for introducing me to the biosensor world. A special thanks to my office-mates Francis and Xander for the patience and support during my last tough months, and for being there when I needed to ventilate the built-up frustration from writing.

All surface science friends at the third floor: Thanks for the encouragements during the long days of measurements! Abdool (for sharing my passion for chocolate), Armando, Peter, Thérèse-Anne, Dani, Bruce, Sander, Eero, Emiel, Davy, Wei Han, Adelaida and Prabashini.

I also want to thank my groups at the cyclotron building (FTV and former TIB) jullie hebben me de Nederlandse taal geleerd. Bedankt Martien, Jom, Jimi, Jan, Peter, Jaap, Seth, Inge, Ria, Betty, Ruben, Ray, Willem, Thijs, Bas en Marieke, Marnix, Harry, Ad, Eddy, Wim, Eric, Frits, Cyrile, Gianluca, Fred en Walter voor de gezellige koffiepauzes, leuke groepsuitjes and etentjes. Speciale dank aan Mirjam: ik (en mijn Nederlands) heb je echt gemist het laatste halve jaar.

Ett stort tack to my parents and sister for all mental support and encouragement to finalize this project, even though I chose to move "so far from home". Heel erg bedankt Lieve, Francy en tante Lea voor de hartelijke verwelkoming in België en het opnemen van mij in uw familie. And last, the honorary place to Kurt - my very best supporter. Thanks for your love and your endless confidence in me. With this book finally finished, I look forward to new adventures together with you.

Curriculum Vitae

Charlotte Kjellander was born in Hässleholm (Sweden) September 10, 1974. After finishing secondary school in 1994 (Lundsbergs skola, Storfors, Sweden), she studied chemical engineering at Lund Institute of Technology, Lund University (Sweden). With polymer technology as main subject (Prof. Dr. Frans Maurer, Lund Institute of Technology) she deepened her materials knowledge with six months studies at the Swiss Federal Institute of Technology (Ecole Polytechnique Fédérale de Lausanne, EPFL, Switzerland). Her Master's thesis included polymer characterization and rheology research and was carried out at DSM Research in Geleen (the Netherlands) supervised by Dr. Paul Steeman and Ton Loontjens. In December 2001 Charlotte obtained her Master of Science degree in Chemical Engineering (Civilingenjör) at Lund Institute of Technology.

Five months later Charlotte started her PhD project at Eindhoven University of Technology (the Netherlands) in the group of Physics and Applications of Ion Beams (Prof. Dr. Martien de Voigt, Dr. Leo van IJzendoorn) at the Department of Applied Physics. During the PhD project she had close collaboration within the groups of Polymers for Information and Communication Technology (Prof. Dr. Dick Broer) and Surface Sciences and Catalysis (Prof. Dr. Hans Niemantsverdriet) at the Department of Chemical Engineering and Chemistry. The four years of doctoral studies on optical switches were continued by a five months research contract at Eindhoven University of Technology, both projects were financially supported by the Dutch Polymer Institute (DPI, the Netherlands).

Starting on October 15, 2006, Charlotte continues her career at Philips Research (the Netherlands) specializing in thin film analysis by time of flight secondary ion mass spectrometry.

List of publications**Towards measuring concentration gradients in polymer dispersed liquid crystals with secondary ion mass spectrometry.**

B. K. C. Kjellander, L. J. van IJzendoorn, A. M. de Jong, D. J. Broer, W. J. H. van Gennip, M. J. A de Voigt, and J. W. Niemantsverdriet. Proc. SPIE, 5289:94-101, 2004.

Mesoscopic concentration variations analyzed by secondary ion mass spectrometry.

B. K. C. Kjellander, L. J. van IJzendoorn, A.M. de Jong, D. J. Broer, and J. W. Niemantsverdriet. Mol. Cryst. Liq. Cryst., 434:171-182, 2005.

Switchable narrow band reflectors produced in a single curing step.

B. K. C. Kjellander, D. J. Broer, A. M. de Jong, and L.J. van IJzendoorn. Patent. PCT Int. Appl., WO 2006059895 A1:21 pp., 20060608, 2006.

Quantification of liquid crystal concentrations in periodically stratified polymer dispersed liquid crystal films by dynamic secondary ion mass spectrometry and multivariate statistical analysis.

B. K. C. Kjellander, C. W. T. Bulle-Lieuwma, L.J. van IJzendoorn, A. M. de Jong, J.W. Niemantsverdriet, and D. J. Broer. submitted to J. Phys. Chem., 2006.

Photopolymerization-induced phase separation for holographic stratified films: modeling and experiments.

B. K. C. Kjellander, A. M. Prenen, L.J. van IJzendoorn, and D. J. Broer. in preparation, 2006.

InP-based two-dimensional photonic crystals filled with polymers.

R. van der Heijden, C. F. Carlström, J. A. P. Snijders, R. W. van der Heijden, F. Karouta, R. Nötzel, H. W. M. Salemink, B. K. C. Kjellander, C. W. M. Bastiaansen, D. J. Broer, and E. van der Drift. Appl. Phys. Lett., 88:161112, 2006.

Two-dimensional photonic crystals from semiconductor material with polymer filled holes.

R. van der Heijden, C. Kjellander, C.-F. Carlström, J. Snijders, R. W. van der Heijden, K. Bastiaansen, D. Broer, F. Karouta, R. Nötzel, E. D. van Drift, and H. W. M. Salemink. Proceedings of SPIE, 6182, 2006.

InP-based planar photonic crystals infiltrated with solid polymers and liquid crystals.

R. van der Heijden, C. Kjellander, C.-F. Carlström, J. Snijders, H. Kicken, R. W. van der Heijden, C. Bastiaansen, D. Broer, F. Karouta, R. Nötzel, E. D. van Drift, and H. W. M. Salemink. Proceedings of SPIE, 6322, 2006.

Stellingen

behorende bij het proefschrift

Multilayer optical switches by photopolymerization-induced phase separation

van

Charlotte Kjellander

1. Polymerization-induced phase separation is independent of diffusion for optical switches with grating periodicities below 200 nm, reflecting visible colors.
this thesis, chapter 2.
2. An elastic polymer network is crucial for phase separation.
this thesis, chapter 2; Boots et al., Macromolecules, 29 (1996).
3. Apparently, stratified switches are easier to obtain with phase separation simulations than by experimental methods.
this thesis, chapters 5 and 6.
4. Not any multivariate statistical analysis can solve every quantification issue.
this thesis, chapters 3 and 4; M. S. Wagner et al., Surf. Sci., 570 (2004).
5. Periodic structures from non-phase separated, but multi-step lithographic systems also serve as optical switches when infiltrated by liquid crystals.
J. Martz et al., J. Appl. Phys., 99 (2006); R. van der Heijden, PhD thesis, Eindhoven University of Technology (2006).
6. Without entropy there would be no need to clean up the mess.
7. Thermotropic liquid crystals and the European population have clear similarities: following the temperature gradient from north to south they change from being quiet and ordered to more chaotic.
P. J. Collings, J. S. Patel, in Handbook of liquid crystal research, Oxford University Press, Oxford (1997); own experiences.
8. Waiting for nothing takes very long time.
Especially when nothing is close to 10^{-9} bar.
9. The top-down and bottom-up approaches are the main differences between a chemist and a physicist.
10. “Platteland” is the correct word for the Dutch countryside.